UNCLASSIFIED

AD NUMBER
ADB036406
LIMITATION CHANGES
TO: **Approved for public release; distribution is unlimited.**
FROM: **Distribution authorized to U.S. Gov't. agencies only; Test and Evaluation; APR 1979. Other requests shall be referred to Arnold Engineering Development Center, Arnold AFB, TN .**
AUTHORITY
AEDC ltr 15 Aug 1980

THIS PAGE IS UNCLASSIFIED

AEDC-TR-79-10

cy 1 Vol I

ARCHIVE COPY
DO NOT LOAN

WIND TUNNEL RESULTS FROM A NOZZLE AFTERBODY TEST OF A 0.2-SCALE FIGHTER AIRCRAFT IN THE MACH NUMBER REGIME OF 0.6 TO 1.5

Volume I
TEST TECHNIQUE EVALUATION

Ernest J. Lucas
ARO, Inc., a Sverdrup Corporation Company

PROPULSION WIND TUNNEL FACILITY
ARNOLD ENGINEERING DEVELOPMENT CENTER
AIR FORCE SYSTEMS COMMAND
ARNOLD AIR FORCE STATION, TENNESSEE 37389

This document has been approved for public release and sale; its distribution is unlimited. per AF letter dated 15 Aug 80.

April 1979

Final Report for Period July 1977 — September 1978

~~Distribution limited to U.S. Government agencies only; this report contains information on test and evaluation of military hardware; April 1979; other requests for this document must be referred to Arnold Engineering Development Center/OIS, Arnold Air Force Station, Tennessee 37389.~~

Prepared for

AIR FORCE AERO-PROPULSION LABORATORY/TBA
WRIGHT-PATTERSON AIR FORCE BASE, OHIO 45433

and

ARNOLD ENGINEERING DEVELOPMENT CENTER/DOTA
ARNOLD AIR FORCE STATION, TENNESSEE 37389

NOTICES

APPROVAL STATEMENT

This report has been reviewed and approved.

Russell B. Sorrells III

RUSSELL B. SORRELLS, III
Project Manager, Analysis and Evaluation Division
Directorate of Test Engineering

Approved for publication:

FOR THE COMMANDER

Robert W. Crossley

ROBERT W. CROSSLEY, Lt Colonel, USAF
Acting Director of Test Engineering
Deputy for Operations

REPORT DOCUMENTATION PAGE	READ INSTRUCTIONS BEFORE COMPLETING FORM
1 REPORT NUMBER AEDC-TR-79-10 Volume I	2 GOVT ACCESSION NO.
	3 RECIPIENT'S CATALOG NUMBER
4 TITLE (and Subtitle) WIND TUNNEL RESULTS FROM A NOZZLE AFTERBODY TEST OF A 0.2-SCALE FIGHTER AIRCRAFT IN THE MACH NUMBER REGIME OF 0.6 TO 1.5 - VOLUME I TEST TECHNIQUE EVALUATION	5 TYPE OF REPORT & PERIOD COVERED Final Report-July 1977 - September 1978
	6 PERFORMING ORG. REPORT NUMBER
7 AUTHOR(s) Ernest J. Lucas, ARO, Inc., a Sverdrup Corporation Company	8 CONTRACT OR GRANT NUMBER(s)
9 PERFORMING ORGANIZATION NAME AND ADDRESS Arnold Engineering Development Center/DOTA Air Force Systems Command Arnold Air Force Station, Tennessee 37389	10 PROGRAM ELEMENT, PROJECT, TASK AREA & WORK UNIT NUMBERS Program Element 65807F and 62203F
11 CONTROLLING OFFICE NAME AND ADDRESS Arnold Engineering Development Center/OIS Arnold Air Force Station, Tennessee 37389	12 REPORT DATE April 1979
	13 NUMBER OF PAGES 242
14 MONITORING AGENCY NAME & ADDRESS(if different from Controlling Office)	15 SECURITY CLASS. (of this report) UNCLASSIFIED
	15a DECLASSIFICATION DOWNGRADING SCHEDULE N/A

16 DISTRIBUTION STATEMENT (of this Report)

Distribution limited to U.S. Government agencies only; this report contains information on test and evaluation of military hardware; April 1979; other requests for this document must be referred to Arnold Engineering Development Center/OIS, Arnold Air Force Station, Tennessee 37389.

17 DISTRIBUTION STATEMENT (of the abstract entered in Block 20, if different from Report)

18 SUPPLEMENTARY NOTES

Available in DDC

19 KEY WORDS (Continue on reverse side if necessary and identify by block number)

wind tunnels	scale	Mach numbers
tests	models	Reynolds numbers
nozzle closures	fighter aircraft	
afterbodies	YF-17 aircraft	

20 ABSTRACT (Continue on reverse side if necessary and identify by block number)

An investigation was conducted in the Propulsion Wind Tunnel (16T) to determine the effect of throttle-dependent parameters (nozzle closure and nozzle pressure ratio) on the aft end surface pressures of a 0.2-scale model of a twin-engine fighter prototype (YF-17). The data are part of a data base to be used in a wind tunnel/flight correlation to define the validity of current wind tunnel test techniques to provide data for full-scale flight

DD FORM 1 JAN 73 1473 EDITION OF 1 NOV 65 IS OBSOLETE

PREFACE

The investigation reported herein was conducted by the Arnold Engineering Development Center (AEDC), Air Force Systems Command (AFSC), Arnold Air Force Station, Tennessee, by ARO, Inc., AEDC Division (a Sverdrup Corporation Company), operating contractor for the AEDC. The work was accomplished under sponsorship of the Air Force Aero-Propulsion Laboratory (AFAPL/TBA), Wright-Patterson Air Force Base, Ohio, and AEDC/DOT. The test programs were conducted in the Propulsion Wind Tunnel Facility (PWT), Propulsion Wind Tunnel (16T), under ARO Projects Nos. P41T-L8 and P41T-09. The supporting analysis was accomplished under ARO Project No. P43T-71. The Air Force project manager was Mr. R. B. Sorrells, III, AEDC/DOTA, and the manuscript was submitted for publication on January 2, 1979.

CONTENTS

ILLUSTRATIONS

TABLES

1.0 INTRODUCTION

In general, the aerodynamic loads obtained with wind tunnel force models have to be extrapolated to predict the performance of the full-scale flight vehicle. The current test technique used in prototype aircraft development or configuration optimization studies obtains airframe data on a sting-supported model with jet effects simulated by, at best, a flow-through, altered aft end. Throttle-dependent effects are then either estimated or obtained on a support system that would allow proper aft end geometry and jet flow simulation. Thus, data (afterbody shell balance loads or integrated surface pressure loads) can be obtained to provide the change in vehicle loading produced by afterbody configuration and jet exhaust plume interaction with the local flow field.

The investigation of the 0.2-scale YF-17 aircraft model reported herein was conducted in three phases as part of an effort to verify the current wind tunnel test techniques. The model was wingtip-supported in Phase I to determine the throttle-dependent (jet exhaust) effects on the model afterbody and nozzle pressure distributions, supported by a large twin-sting system in Phase II to define the wingtip support interference, and supported by a small twin-sting system in Phase III to determine the validity of the sting-supported annular-jet plume simulation technique. This report contains the results from the support system interference and annular-jet simulation studies with the twin-engine model. The effects of model configuration variables are presented in Volume II for conditions other than those presented in the support system and simulation analysis. The pressure data obtained during the investigations will be used, along with previously acquired wind tunnel data from a 0.1-scale model investigation (Ref. 1) and data from a flight test program with the YF-17 prototype aircraft, in a wind tunnel-to-flight correlation study. The study is being conducted to validate or indicate regions requiring improvement in the current subscale model testing techniques.

2.0 APPARATUS

2.1 TEST FACILITY

The AEDC Propulsion Wind Tunnel (16T) is a variable density, continuous flow tunnel that can be operated at Mach numbers from 0.2 to 1.6 and stagnation pressures from 120 to 4,000 psfa. The maximum attainable Mach number may be limited slightly depending on the tunnel pressure ratio requirements for the particular test installation. Maximum stagnation pressure is a function of Mach number and available electrical power. Tunnel stagnation temperature is controlled over the range from 80 to 160°F. The test section is 16 ft square by 40 ft long and is enclosed by 60-deg inclined-hole perforated walls of six-percent porosity. A more complete description of the tunnel and its operational characteristics is contained in Ref. 2

2.2 Test Article

2.2.1 Wingtip Support Model (Phase I)

The initial wind tunnel test of the 0.2-scale YF-17 model was conducted with the wingtip support system shown in Fig. 1. The model basic dimensions and its axial location in the test section are illustrated in Fig. 2. This installation provided an unobstructed jet exhaust region (see Fig 3) which allowed definition of throttle-dependent effects. Effects of nozzle closure, associated with the throttle movement, were investigated by use of the four interchangeable nozzles shown in Fig. 4. The nozzle external contours simulated closures from dry power through partial afterburning. Internally, the nozzle exit-to-throat area was simulated although the total flow duct was not simulated.

Simulated jet flow for the nozzle closures was provided by high-pressure air heated to 560°R to prevent icing on the flow mixing screens and was supplied through the wingtip support booms to an internal model plenum. The high-pressure air was ducted through right- and left-side diffusers Choke plates and screens were used to ensure a uniform subsonic flow upstream of each nozzle throat. Instrumentation was provided in each duct to determine the total-pressure profiles.

Wing modification for structural support and high-pressure air passages altered the main wing planform outboard of the 55-percent semispan station (see Fig. 2). Because of the change incorporated in the planform, no attempt was made to simulate the wing leading-edge or trailing-edge flaps. Twin vertical tails with the rudder fixed at zero degrees and horizontal tails were located as shown in Fig. 2. The horizontal tail root chord extends from fuselage station 122.4 (X/L = 0.86) to 137.8 (X/L = 0.97). Horizontal tail deflection angles from 0.5 to -4.0 deg could be set manually by rotating the tails about fuselage station 129.6 (X/L = 0.92). Positive horizontal tail angles are defined as leading edge up.

The influence of the aircraft on the static pressure reading from the pitot boom was determined with a scaled version of the pitot probe and support boom. However, the probe static orifices were incorrectly located (compared to the flight probe) on the contractor-supplied probe during Phases I and II. A scaled version of the flight test probe, as shown in Fig. 5, was built and used during Phase III.

The engine bay purge flow system was simulated by using an inlet in the main engine inlet fairing (see Fig. 1) and scaled top and bottom exists on each engine compartment as illustrated in Fig. 6. The flow system was isolated side to side in the model, but both the top and bottom exhaust exists on each side were open to a common bay area. The exhaust flow distribution was thus dependent on the local surface pressure at the exhaust exists. When the bay purge effect was not being investigated cover plates were provided to seal the inlet and exhaust ports.

Model surface pressures were obtained from 239 surface pressure orifices located on the forebody (48), afterbody (130), and nozzle (61). Pressure orifice locations are indicated in Figs. 7a, b, and c for the forebody, afterbody, and nozzle, respectively. The locations are defined in Table 4.

A simulated sting support system shown in Fig. 8 was used to provide data for the support system interference study. The simulated sting diameter and taper location X_s could be varied. The configurations tested are defined in Table 1.

2.2.2 Large-Sting Support System (Phase II)

Phase II of the 0.2-scale test program was conducted on the sting support system shown in Fig. 9. The stings were designed to support the model at high aerodynamic loading resuting from the simulation of flight Reynolds numbers. The required sting diameters filled the exit of the cruise nozzle (see Fig. 9c) which precluded jet exhaust simulation.

To determine the interference effects of the supports on data obtained during Phase I (wingtip support), the wingtip support mechanism was simulated as shown in Fig. 10. The simulated boom supports were removed from the wing glove (Fig. 10b) so that the effects of the wing modification and adaptor could be assessed. Model variables and pressure orifice locations were the same as on the wingtip-supported model.

2.2.3 Small-Sting Support System (Phase III)

The annular-jet model, shown in Fig. 11, was tested to determine if a properly simulated jet plume would mask the sting support system interference effects. This sting-supported model utilized high-pressure air supplied through the stings which exhausted through the annulus between the sting and the internal flow duct as shown in Fig. 11b. The jet exhaust region for the largest nozzle opening tested (A8 = 360-in.^{2} full scale) is shown in Fig. 11c. Choke plates and flow straightener screens were used with this system. Model nozzle changes were accelerated by using split nozzles (Fig. 11d). This arrangement allowed configuration changes to be made while the main model-sting support remained intact. The seal along the nozzle split was maintained by using machine surfaces coated with RTV® sealant and sufficient screws to allow a total pressure of 135 psia in the nozzles. The annular-jet nozzle contours are defined in Fig. 12.

Wingtip support simulators, previously used during the Phase II entry, were also utilized during this phase with a horizontal blade simulator (see Fig. 13) to define the total wingtip support interference. The horizontal blade simulator was positioned axially at the Phase I location of 94.9 in. aft of the model nozzle reference station (FS 137.8) and at one location 19 in. closer to the model. However, location of the blade relative to the nozzle exit varies depending on the nozzle configuration being investigated since the nozzle length decreases as the nozzle exit area increases (see Fig. 12).

Simulated wingtip missiles and underwing flap actuator fairings, shown in Fig. 11c, were used on the sting-supported models to closely simulate the actual flight vehicle. The configurations tested with this simulation are defined in Tables 2 and 3.

2.3 INSTRUMENTATION

Model surface pressures were measured using six multiport scanning valves with 15-psid transducers. The forty-eight port valves were controlled by a facility computer in a step pause mode which monitored each pressure to ensure stabilization before advancing to the next port.

Jet exhaust simulation flow was monitored by internal duct pressure and temperature rakes. Standard facility pressure transducers of the appropriate range were used to measure the pressure at known flow duct areas. Temperatures were measured at the same locations with copper-constantan thermocouples.

Model attitude was obtained with a model-mounted angular position indicator.

3.0 TEST DESCRIPTION

3.1 TEST CONDITIONS AND PROCEDURES

Test data were acquired on the 0.2-scale YF-17 model within the Mach number range of 0.6 to 1.5 at Reynolds numbers from 1.4×10^6/ft to 5.6×10^6/ft. Model surface pressure data were obtained for the various configurations during the three-phase program at test conditions defined in the test summaries presented in Tables 1, 2, and 3.

Each model configuration was assembled and the surface pressures leak checked immediately before testing to identify valid instrumentation. After tunnel conditions were established, data were obtained by varying the model angle of attack at a pre-established nozzle pressure ratio (NPR) or by varying the NPR at a constant angle of attack.

The annular-jet concept refined by Price (Ref. 5) was investigated with the small-sting support system. This technique allows for the simulation of a conventional jet by using an annular jet around a solid core (sting support). The equivalent nozzle pressure ratio (NPRE), which generally differs from the actual NPR, used with the annular jet produces a plume that matches the isentropic expansion maximum plume diameter of the conventional jet. The actual plume shape and the axial location of the maximum diameter, however, are not exactly simulated.

3.2 DATA REDUCTION TECHNIQUE

Model surface pressures were used to calculate the pressure coefficients referenced to free-stream static pressure (P), calculated from the free-stream Mach number and total pressure measured in the stilling chamber, and the free-stream dynamic pressure (Q). Nozzle and afterbody integrated pressure loads were calculated by using the axial and normal projected areas (Ai) in an area times pressure summation. Each pressure was assumed to act over areas assigned by the engine manufacturer. The calculated axial and normal force loads were converted to coefficients based on the wing-fuselage planform area (S = 2,020 in.^{2}) and the free-stream static and dynamic pressures. The normal and axial pressure loads were resolved into the wind axis to define the nozzle plus afterbody lift and drag. Empennage loads were not included in the calculated loads since pressure instrumentation was not included on the tails. The tails, however, were on the model throughout these investigations thus influencing the calculated integrated pressure loads.

Jet exhaust simulation mass flow was measured for the wingtip support and annular-jet test (Phases I and III) with the facility venturi system. Flow rates were calculated using a turbulent flow discharge coefficient based on the venturi throat Reynolds number. Additional corrections were applied for compressibility and real gas effects.

3.3 UNCERTAINTY OF MEASUREMENTS

Uncertainties (combinations of systematic and random errors) of the basic tunnel parameters, shown in Fig. 14, were estimated from repeat calibration of the instrumentation and from the repeatability and uniformity of the test section flow during tunnel calibration. Uncertainties in the instrumentation systems were estimated from repeat calibration of the systems against secondary standards whose uncertainties are traceable to the National Bureau of Standards calibration equipment. The instrument uncertainties are combined using the Taylor series method of error propagation described in Ref. 3 to determine the pressure coefficient uncertainties at the typical test conditions shown below.

M	Re x 10^{-6}/ft	P, psfa	(Pi)avg, psfa	Q,psfa	UCPi
0.6	2.8	1,440	1,403	362	0.0157
0.9	2.8	868	831	490	0.0098
1.2	2.8	566	372	572	0.0096

Typical observable trends and repeatability of the online data (Fig. 15) indicate that a $\Delta CP \sim \pm 0.005$ is, in general, representative of the repeatability of the pressure coefficients from this investigation. If this difference in pressure coefficient is considered to be a bias and is present over the instrumented projected area of the nozzle and afterbody ($\Sigma Ai/S = 0.060$ to 0.049) the resultant axial force coefficient $[(\pm\Delta CP) \times (\Sigma Ai/S)]$ would be approximately ±0.0003. Data are shown in Fig. 16 for the cruise nozzle configuration to illustrate the repeatability of integrated pressure data at the three primary test Mach numbers.

4.0 RESULTS AND DISCUSSION

Data presented herein define the effect of support system interference and annular-jet simulation on the surface pressure distribution and pressure-integrated axial force coefficients for the nozzle and afterbody of the 0.2-scale YF-17 model. All results discussed and data presented were obtained at a nominal characteristic Reynolds number of $\sim 30 \times 10^6$, based on model length, and horizontal tail deflection angle of 0 ($\delta_H = 0$) unless otherwise indicated.

4.1 SUPPORT SYSTEM SIMULATION VALIDITY

A comparison of the axial force coefficient (CA) data obtained with the two mutually simulated support systems for the 200- and 300-in.^{2} nozzle configurations at jet off and design nozzle pressure ratio and typical Mach numbers is presented in Fig. 17. The data indicate that at subsonic speeds there is no significant difference between the two support systems with either nozzle configuration tested (Figs. 17a through d and g through j). There are, however, significant differences in the results from the two support system simulations at Mach number 1.2 as seen in Figs. 17e, f, k, and l. The lower axial forces obtained with the sting-mounted model could be caused by differences in the sting attachment simulation which can be seen by comparing installation photographs of the two systems (Figs. 8 and 13). The sting-supported model has more blockage in the region of the support and would alter the shock locations downstream of the model and thus could feed a disturbance through the wake which could affect the annular-jet plume shape. This supposition is somewhat verified by the pressure coefficient data presented in

Figs. 18 and 19. The pressure coefficients on the nozzle surface are more positive (particularly in the jet interaction region, ϕ = 45 and 135) with the sting-support configuration than the wingtip-mounted model indicating more compression on the aft portion of the nozzle.

Except for isolated locations, the agreement of surface pressure coefficient data obtained with the two support systems is good at Mach number 0.6 (Fig. 20). However, the differences in the pressure data increase as Mach number increases. The differences are shown more clearly in the differential pressure coefficient data presented in Fig. 21. The pressure coefficient data obtained with the sting support system are subtracted from the pressure data obtained with the wingtip support system to determine the pressure coefficient difference. The pressure differences are relatively insensitive to both model attitude and jet simulation at Mach numbers less than 0.9.

Thus, within the subsonic flow regime the data obtained with the two support systems are in good agreement indicating that corrective increments could be obtained on one system and applied to data from the other support system. The data at Mach number 1.2, however, indicate differences in the data which are attributed to incomplete support system simulation. Thus, support system interference corrective increments for M = 1.2 should be applied with caution.

4.2 SUPPORT SYSTEM INTERFERENCE

4.2.1 Sting Taper Location

The wingtip-supported model with simulated 3.0-in.-diam stings was used to investigate the effect of sting taper location at two axial positions aft of the nozzle exits at conditions defined in Table 1.

The axial force coefficient and surface pressure data are presented in Figs. 22 and 23 through 25, respectively. Taper location does not influence the data at subsonic speeds except for the apparent change in afterbody (0.8 < X/L < 0.97) axial force coefficient at Mach number 0.6 without jet simulation (Fig. 22a). These data are inconsistent with the other three conditions shown and opposite in trend from the influence one would expect (i.e., moving the support blockage away from the model should reduce the surface pressures on the aft end thus increasing the axial loading). The pressure data (Fig. 23) indicate a uniform shift in the two jet-off data sets which infers a bias error is present in the jet-off data obtained at X_S/DS = 13.8. There is also a smaller, but still apparent, bias error in the jet-on data at Mach numbers 0.6 and 1.2, Figs. 24 and 25.

At supersonic speeds, changes in the afterbody and nozzle axial loads (Fig. 22b) are within the data repeatability of 0.0003. The total aft end axial load (afterbody plus nozzle), however, indicates a decrease as the taper is moved further aft of the nozzle exit. This result is contrary to those of Ref. 4 which implied that, for a single-sting configuration, locating the taper at X_s/DS ratios greater than six from the model base would not influence the test article surface pressures. Thus, the data obtained on the current system should have been insensitive to taper location within the test range.

4.2.2 Sting Diameter

Simulated stings were used with the wingtip-supported model to determine the effect of the sting support system presence on the nozzle and afterbody of the 0.2-scale model. The axial force coefficient and surface pressure coefficient data are presented as a function of simulated sting-to-nozzle exit diameter ratio in Figs. 26 and 27 through 29, respectively. As expected, the jet-off nozzle axial force coefficient decreased with increasing sting diameter. However, at Mach numbers 0.6 and 0.9 the sting effect was not limited to the nozzle area but was also evident on the afterbody (Figs. 26a and b). As the sting diameter increases, it has an effect similar to that of a jet plume formed by increasing nozzle pressure ratios below design. The larger sting alters the aft end flow causing an increase in the model nozzle surface pressure coefficients as shown in Figs. 27 and 28.

The effects of sting diameter are lessened when the jet plume is simulated with an annular jet around the stings as seen in the axial force data presented in Fig. 26 and the pressure data in Fig. 29. This suggests that the annular-jet plume masks the sting interference effects at Mach numbers 0.6, 0.9, and 1.2

4.2.3 Wingtip Support Simulation (LS)

Interference effects from the wingtip support simulators were determined during a portion of the large-sting support test (Phase II). The data obtained, shown in Fig. 30, indicate that there is no significant effect of the wingtip support simulators on the axial force data at subsonic Mach numbers ($\Delta CA < 0.0003$). The simulation of the wingtip supports, however, does not represent the total support system (i.e., horizontal blade support was not included). The data at Mach number 1.2 show a significant increase in afterbody axial force coefficient when the wingtip support simulators are installed, and a small decrease in the nozzle loading. The cause of the increased loading on the afterbody may be from a blockage or "end effect" of the wingtip supports, which accelerates the flow over the afterbody. Effects defined in this section were for the wingtip support simulation only since the horizontal blade simulation was not available.

Surface pressure coefficients presented in Figs. 31 and 32 illustrate the local effects of the wingtip support simulation. It is obvious that there is almost no effect of the wingtip support simulation on the surface pressure at subsonic speeds but a significant effect is evident at the supersonic Mach numbers. At Mach number 1.2, the wingtip support simulation produced a significant decrease in the surface pressure data over the afterbody portion of the model. The lower pressure on the afterbody produces a steeper compression on the nozzle as the local flow adjusts to the base wake.

4.2.4 Wingtip and Horizontal Blade Support Simulation (SS)

The data obtained on these test programs will be eventually compared to the flight data for test technique evaluation. Thus, the support system corrections to be applied to the wingtip-supported data should be based on a configuration as close to the actual flight vehicle as possible. Simulated wingtip missiles and underwing flap actuator fairings were therefore added to the clean-wing model for the 0.2-scale reference configuration. The effects of adding these simulations were obtained so the 0.2-scale model support interference could be compared later to the 0.1-scale data (Ref. 1) which used the clean-wing model as the reference configuration. Adding the missile and fairing simulations did not significantly affect the axial force data (Fig. 33) although some local pressure disturbances (Figs. 34 and 35) were produced on the outboard portion of the model. The interference effects presented herein were determined using the missile and fairing simulation as the reference configuration.

The effects of adding the wingtip and horizontal blade support simulator (see Fig. 13a) to the 0.2-scale sting-supported model are shown in Figs. 36 through 41. The axial force coefficient data for the support system simulation are presented in Fig. 36 for the 200- and 300-in.^{2} nozzle configurations operating at the equivalent design nozzle pressure ratio. The data indicate only a small ($\Delta CA < 0.0003$) sensitivity of the axial force to model attitude within the test range of 0 to 4 deg. In general, the influence of the simulated wingtip support system is within the quoted uncertainty ($\Delta \check{C}A \leqslant 0.0003$) at Mach number 0.6 but increases in magnitude with increasing Mach number. The dependence on Mach number is illustrated by the differential axial force coefficient data shown in Fig. 37 for 0- and 4-deg angle of attack. Comparisons between the data from the wingtip support simulation and the data from the baseline configurations with the 200-in.^{2} nozzle indicate only small changes in the axial force at subsonic speeds. The addition of the horizontal blade in the normal (aft) position increases the interference. The interference is further increased when the horizontal blade simulator is positioned 19 in. closer to the model. In essentially all subsonic cases the interference is manifested as a pressurization of the afterbody and nozzle as shown in the pressure coefficient data presented in Figs. 38 and 39.

The wingtip support system simulation has the opposite effect at supersonic speeds (Figs. 36d and h). The addition of the wingtip support simulators increases the axial loads while addition of the horizontal blade does not significantly change the data. It is also of interest to note that most of the support system influence occurs on the afterbody at supersonic speeds, Fig. 40, with any support interference on the nozzle indicating the same trends observed at the subsonic conditions. The effects on the afterbody at supersonic speeds seem to indicate the interference is wingtip-support-simulator-induced and is probably caused by the simulators producing local accelerations of the flow over the afterbody. The decrease in nozzle axial force would result in a pressurization of the nozzle as the local flow adjusts (recovers) to the base or plume conditions.

The differential pressure coefficient data (Fig. 41), obtained by using the model with wingtip missile and underwing fairing simulators as a reference configuration, again indicate the insensitivity of the model surface pressure to the support system simulation at Mach number 0.6. However, the data at Mach numbers 0.9 and 1.2 show significant local effects of the wingtip support simulation. The placement of the horizontal blade support dominates the interference at Mach number 0.9 but does not change the interference at Mach number 1.2 within the current test envelope. The results show that the support system should be completely simulated to document the total support interference effects for data corrections.

4.3 ANNULAR-JET SIMULATION WITH THE WINGTIP SUPPORT SYSTEM

An important portion of the support interference investigation was to assess the applicability of the annular-jet testing technique to a twin-jet configuration. The annular-jet technique reported in this section simulates a conventional jet exhaust plume by producing an annular-jet plume around simulated sting supports.

Data were obtained with the wingtip-supported model utilizing both conventional jets and annular jets around simulated support stings (see Fig 8). The annular-jet equivalent nozzle pressure ratio (NPRE) which characterizes the maximum plume diameter of a conventional jet was determined by criteria set forth in Ref. 5. However, the axial location of the maximum plume diameter, which is not necessarily correctly simulated, could be a factor which influences the results obtained from the annular-jet simulation technique. The higher annular-jet nozzle pressure ratio, which is generally required to match the conventional plume diameter, causes the location of the maximum plume diameter to move upstream. This could produce increased model surface pressures since the local flow would be more compressed as it adjusts to the simulated plume. The higher model surface pressures would consequently decrease the axial force coefficients on the nozzle and afterbody which could be one cause of the lower annular-jet axial loads shown in Figs. 42a through c for the 200-in.^{2} nozzle. The reduced axial loads with the annular jet, though small (3 or 4 counts), are evident at all Mach numbers and most noticeable on the nozzle at Mach number 1.2. The 300-in.^{2} nozzle configuration with a flatter model-nozzle surface contour is less sensitive to the jet exhaust plume simulation (see Figs. 42d through f).

Surface pressure coefficient data for the 200-in.^{2} and 300-in.^{2} nozzle configurations are presented in Figs. 43 and 44. The small increase in surface pressure coefficient with the annular-jet simulation is apparent. The incremental changes in the surface pressure coefficients between the conventional and annular-jet configurations are presented in Fig. 45. The annular-jet simulation at Mach number 1.2 is shown to affect primarily the nozzle region of the model (Fig. 45c) and be somewhat configuration dependent. At subsonic speeds, however, the annular-jet test technique provides a method of obtaining throttle-dependent effects while masking or at least diminishing the support system interference effects (see Figs. 45a and b). Although the agreement between the conventional and annular-jet integrated pressure data is not exact, the annular-jet simulation differences are small (3 or 4 counts on the larger nozzle) compared to the support system interference (8 to 10 counts, discussed in Section 4.2.4) that would have to be applied to correct the data.

5.0 CONCLUDING REMARKS

The investigation reported herein is part of a broader study to define the adequacy of the currently accepted test techniques used to determine throttle-dependent effects on nozzle/afterbody pressure forces with subscale models. This report documents the results of the investigation on the 0.2-scale YF-17 pressure model conducted with wingtip, large twin-sting, and small twin-sting (annular jet) support systems. The data were obtained at Mach numbers from 0.6 to 1.5 at characteristic Reynolds numbers, based on model length, from 15×10^6 to $\sim 60 \times 10^6$. Results from the support system interference and annular-jet simulation analysis are summarized below.

1. Support system interference was defined for the wingtip support system using the sting-supported model with an annular jet and simulated wingtip and horizontal blade supports. At subsonic speeds the influence of the blade position was the major contributor to support interference, whereas the presence of the wingtip supports caused the interference at supersonic speeds. The influence of the wingtip support system on the axial force coefficient was minimal ($\Delta CA \leqslant 0.0004$) at Mach number 0.6 but increased with Mach number to $\Delta CA = -0.0010$ at Mach number 0.9 and $\Delta CA = 0.0010$ at Mach number 1.2.

2. Simulation of sting supports, while using the wingtip support system, indicated a sensitivity of the aft end surface pressures to the sting system for jet-off conditions. The effects become more significant at the higher Mach numbers but were decreased when the jet was simulated with high-pressure air indicating a masking of the support interference of the stings with a properly simulated annular jet.

3. Simulation of the conventional jet exhaust plume with an annular jet is a valid technique for obtaining design nozzle pressure ratio performance data with minimum interference from the stings. Additional definition of the off-design simulation and configuration dependency is needed to refine the technique.

REFERENCES

1. Lucas, Ernest J. "Wind Tunnel Results from a Nozzle Afterbody Test of a 0.1-Scale Fighter Aircraft in the Mach Number Range of 0.6 to 1.6." AEDC-TR-78-25, June 1978.

2. Test Facilities Handbook (Tenth Edition). "Propulsion Wind Tunnel Facility, Vol. 4." Arnold Engineering Development Center, May 1974.

3. Abernethy, R. B. and Thompson, J. W., Jr. "Handbook – Uncertainty in Gas Turbine Measurements." AEDC-TR-73-5 (AD755356), February 1973.

4. Reichenau, David E. A. "Sting and Strut Support Interference Effects on a Cylindrical Model with an Ogive Nose at Mach Numbers from 0.7 to 1.4." AEDC-TR-72-175 (AD905771L), November 1972.

5. Price, Earl A., Jr. "A Parametric Investigation of the Annular Jet Concept for Obtaining Afterbody Drag Data at Transonic Mach Numbers." AEDC-TR-77-104 (ADA050891), February 1978.

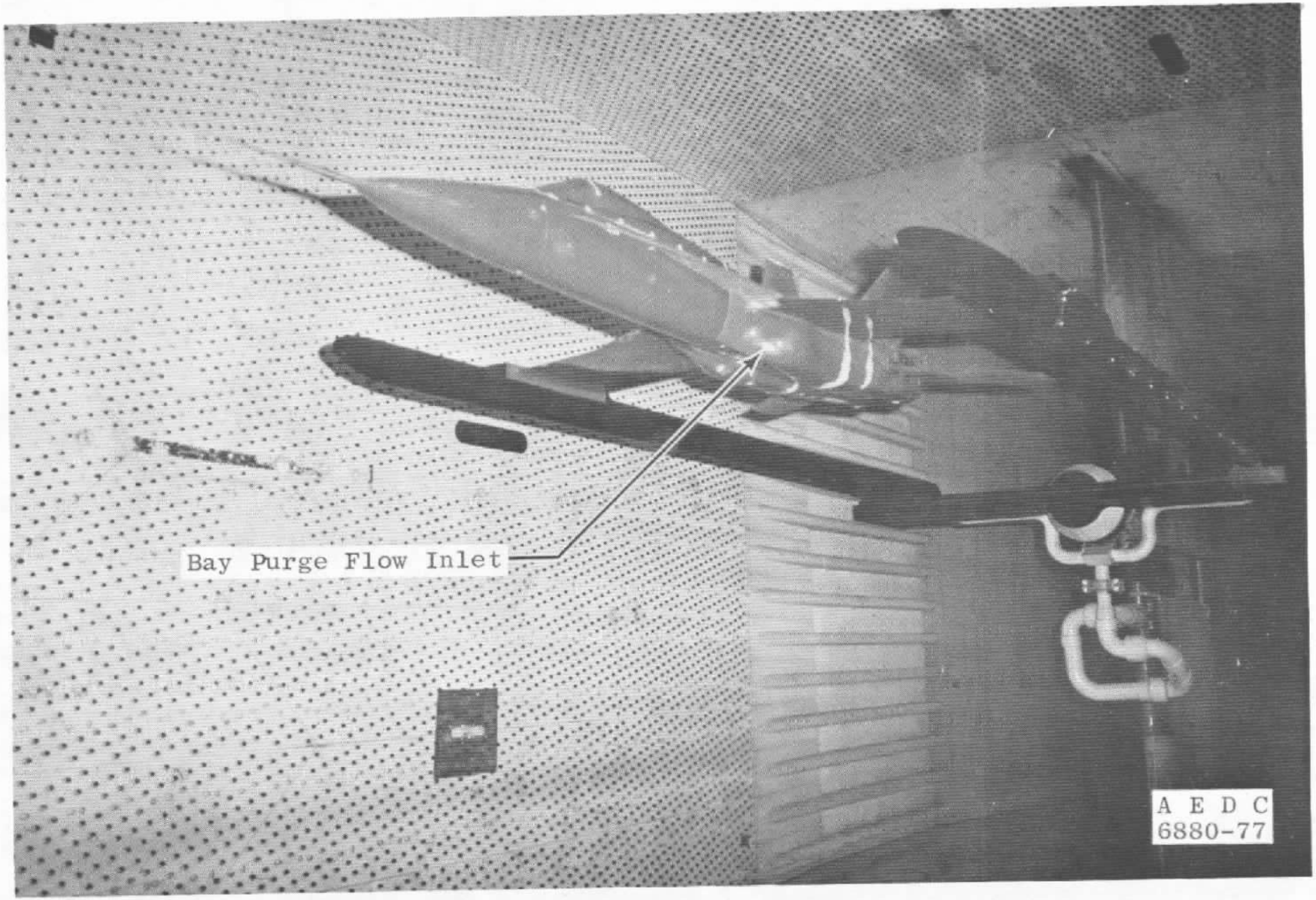

Figure 1. Wingtip-supported model installation.

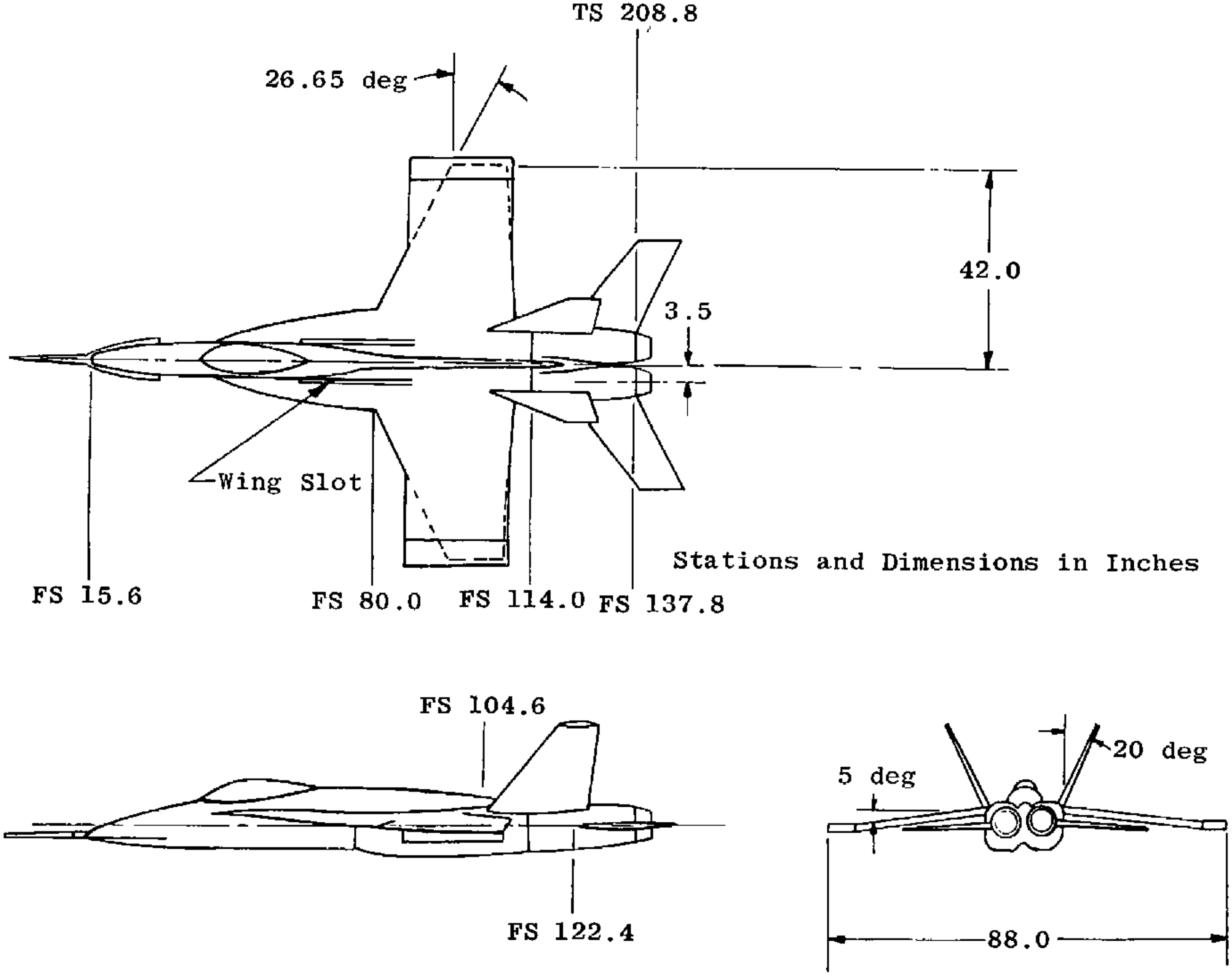

a. Dimensional layout
Figure 2. YF-17 model.

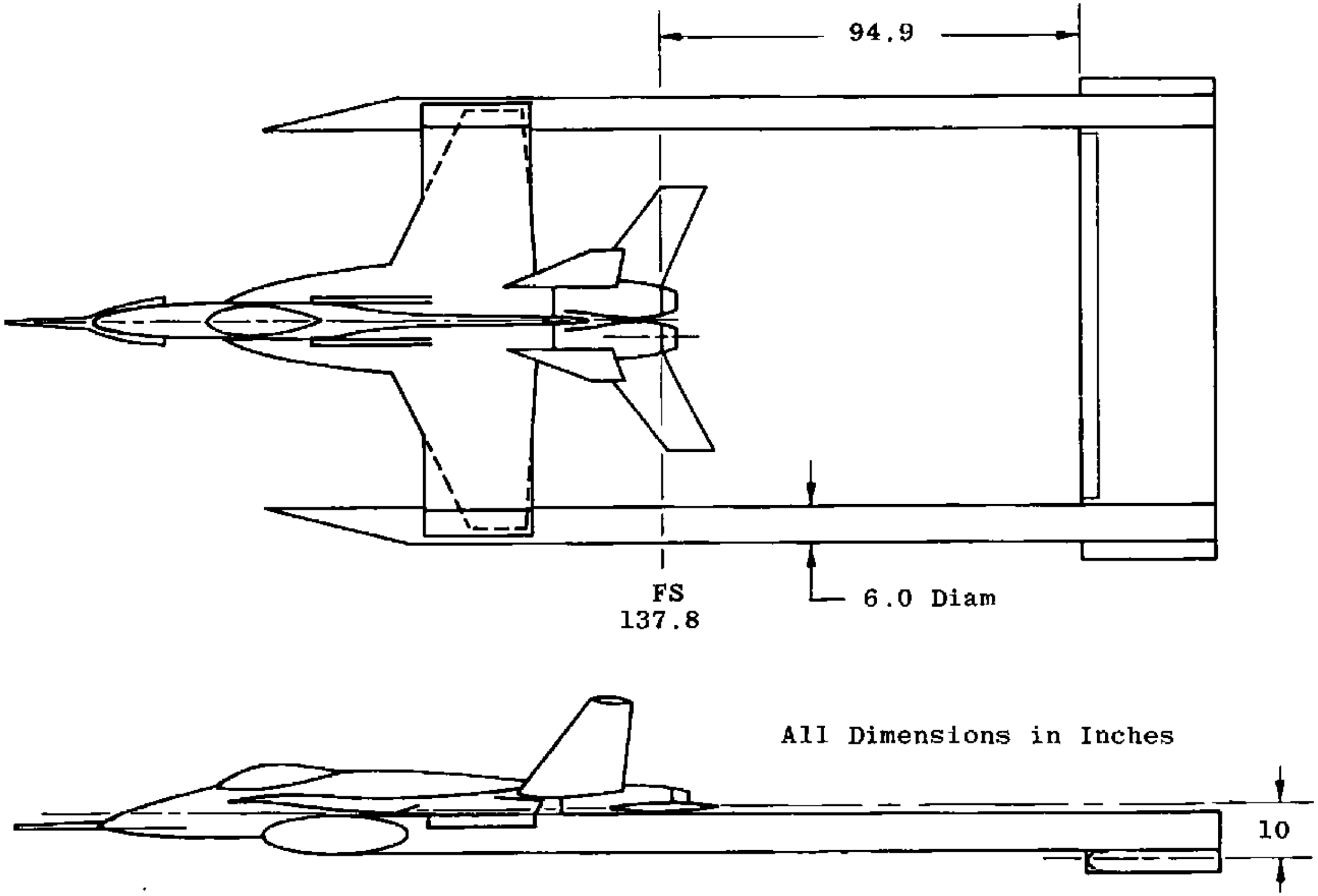

b. Support system location
Figure 2. Concluded.

Figure 3. Rear 3/4 view of wingtip-supported model.

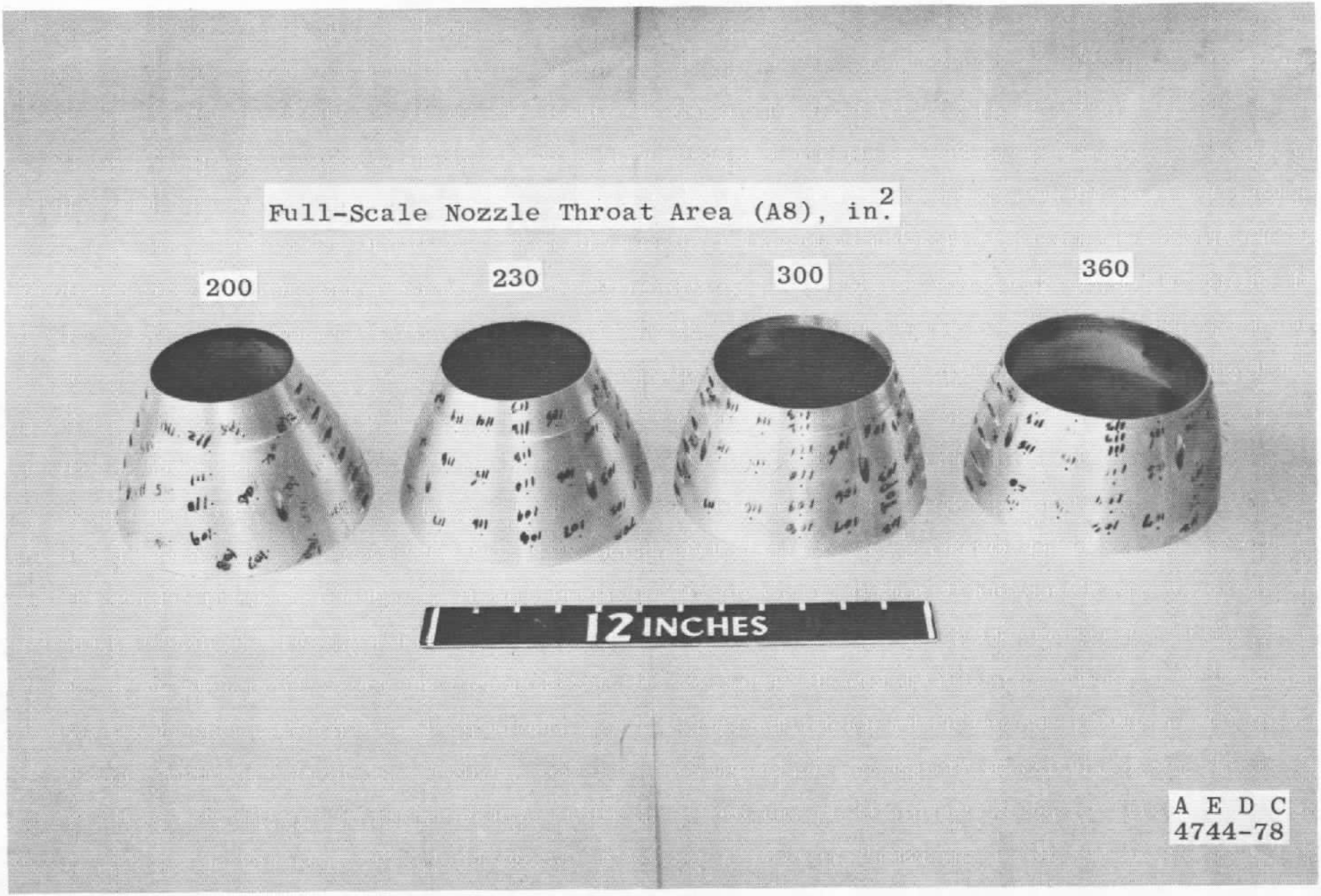

a. Nozzle comparison
Figure 4. Nozzle closure simulators.

X_n, in.	r, in.
0	2.415
0.152	2.415
0.352	2.332
0.552	2.234
0.752	2.122
0.952	1.990
1.152	1.866
1.352	1.766
1.552	1.690
1.752	1.632
1.952	1.602
2.027	1.600
2.152	1.604
2.352	1.614
2.552	1.624
2.752	1.636
2.952	1.646
3.152	1.656
3.352	1.666
3.552	1.676
3.752	1.688
3.952	1.698
4.152	1.708
4.286	1.716

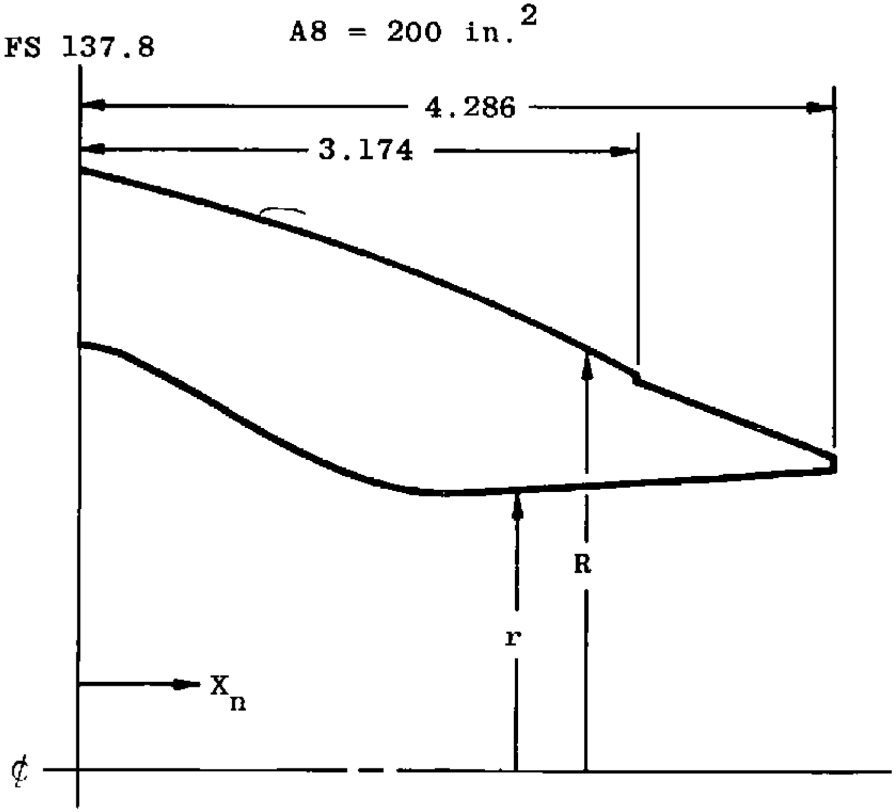

All Dimensions in Inches

X_n, in.	R, in.
0	3.380
0.152	3.350
0.352	3.304
0.552	3.258
0.752	3.204
0.952	3.146
1.152	3.086
1.352	3.024
1.552	2.956
1.752	2.880
1.952	2.804
2.152	2.722
2.352	2.636
2.552	2.544
2.752	2.448
2.952	2.344
3.152	2.240
3.174	2.228
3.174	2.202
4.286	1.776

b. 200-in.^{2} nozzle contours (cruise)
Figure 4. Continued.

X_n, in.	r, in.
0	2.415
0.162	2.415
0.362	2.327
0.562	2.224
0.762	2.104
0.794	2.083
0.962	1.982
1.162	1.885
1.362	1.808
1.562	1.752
1.598	1.744
1.762	1.719
1.856	1.715
1.952	1.719
1.962	1.720
2.162	1.736
2.362	1.752
2.562	1.768
2.762	1.784
2.962	1.800
3.162	1.816
3.362	1.832
3.562	1.848
3.762	1.864
3.962	1.880
4.145	1.895

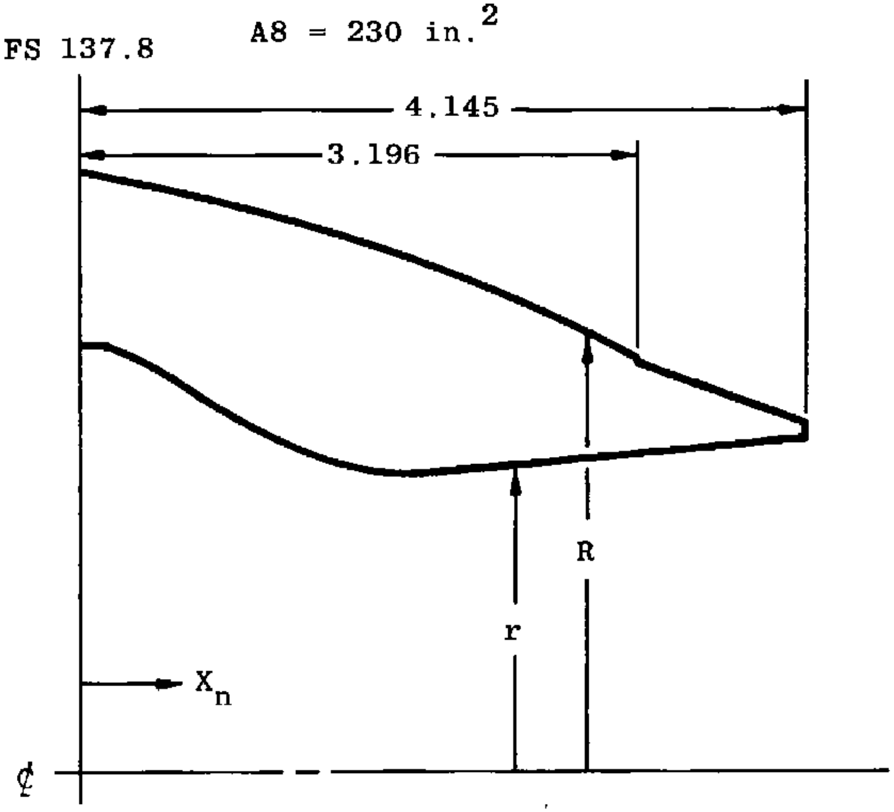

All Dimensions in Inches

X_n, in.	R, in.
0	3.380
0.162	3.352
0.362	3.312
0.562	3.270
0.762	3.224
0.962	3.174
1.162	3.118
1.362	3.060
1.562	2.998
1.762	2.930
1.962	2.860
2.162	2.784
2.362	2.704
2.562	2.620
2.762	2.530
2.962	2.436
3.162	2.336
3.196	2.320
3.196	2.294
3.362	2.234
3.562	2.164
3.762	2.092
3.962	2.020
4.145	1.955

c. 230-in.^{2} nozzle contours (intermediate)
Figure 4. Continued.

X_n, in.	r, in.
0	2.415
0.174	2.415
0.374	2.314
0.574	2.204
0.774	2.114
0.974	2.044
1.174	1.994
1.287	1.972
1.373	1.962
1.475	1.958
1.574	1.962
1.641	1.970
1.774	1.988
1.974	2.016
2.174	2.044
2.374	2.072
2.574	2.100
2.774	2.128
2.974	2.156
3.174	2.184
3.374	2.210
3.574	2.240
3.774	2.268
3.820	2.274

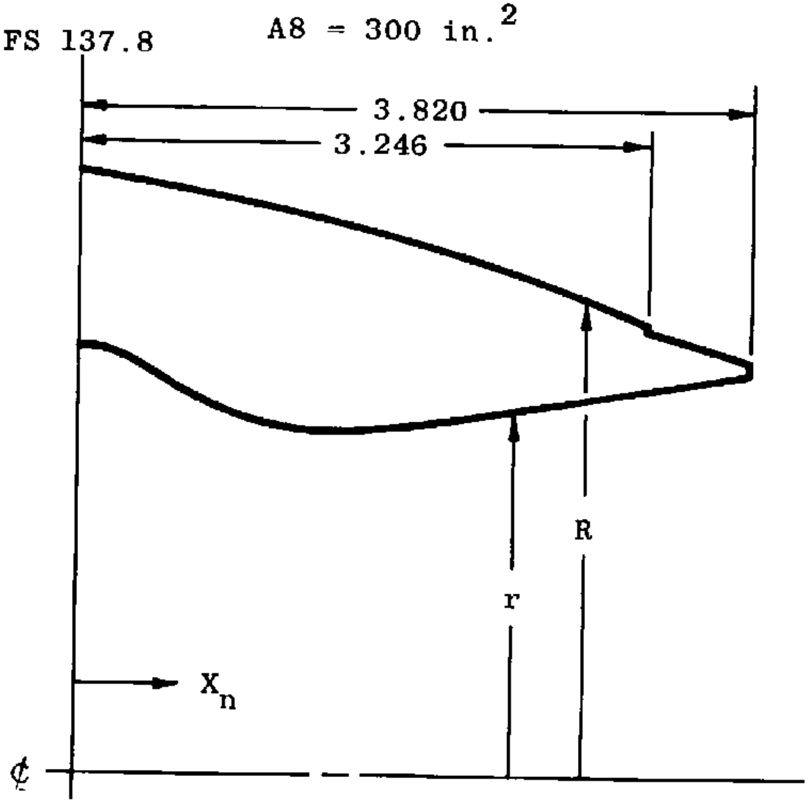

All Dimensions in Inches

X_n, in.	R, in.
0	3.380
0.174	3.360
0.374	3.332
0.574	3.302
0.774	3.268
0.974	3.232
1.174	3.192
1.374	3.144
1.574	3.096
1.774	3.044
1.974	2.988
2.174	2.928
2.374	2.862
2.574	2.792
2.774	2.720
2.974	2.640
3.174	2.556
3.246	2.528
3.246	2.502
3.374	2.464
3.574	2.404
3.774	2.348
3.820	2.334

d. 300-in.^{2} nozzle contours (reheat)
Figure 4. Continued.

X_n, in.	r, in.
0	2.415
0.170	2.415
0.196	2.402
0.370	2.320
0.570	2.246
0.770	2.191
0.970	2.154
1.031	2.146
1.167	2.139
1.170	2.139
1.370	2.156
1.385	2.159
1.570	2.193
1.770	2.230
1.970	2.267
2.170	2.304
2.370	2.341
2.570	2.378
2.770	2.415
2.970	2.452
3.170	2.489
3.370	2.526
3.549	2.559

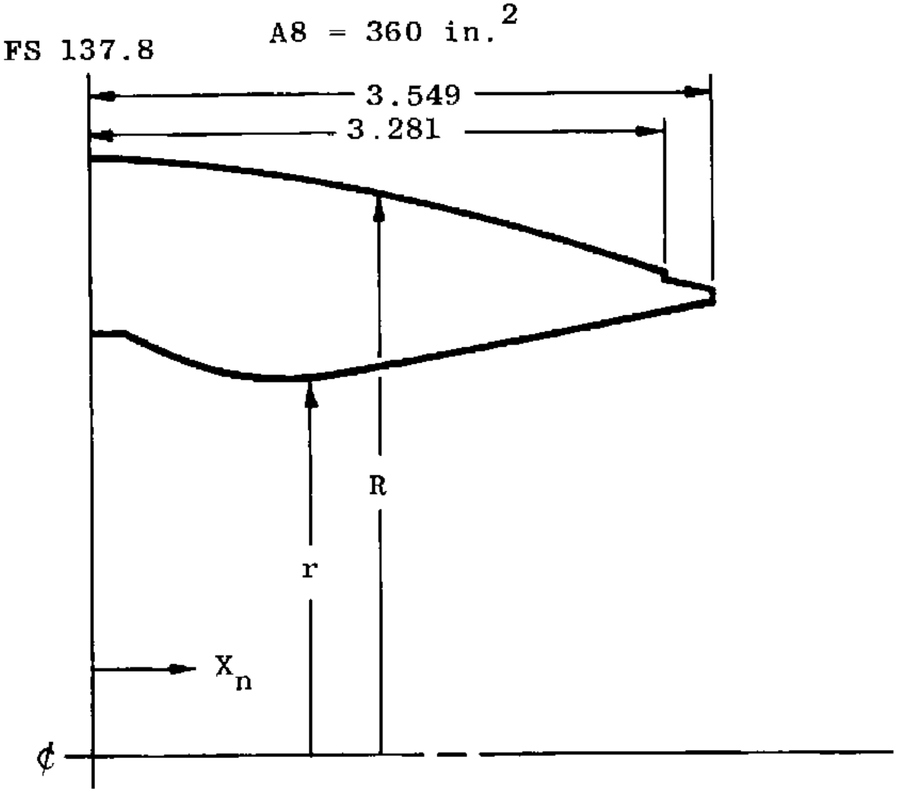

All Dimensions in Inches

X_n, in.	R, in.
0	3.380
0.170	3.371
0.370	3.356
0.570	3.338
0.770	3.316
0.970	3.290
1.170	3.261
1.370	3.227
1.570	3.190
1.770	3.150
1.970	3.105
2.170	3.056
2.370	3.004
2.570	2.947
2.770	2.886
2.970	2.821
3.170	2.752
3.281	2.712
3.281	2.686
3.370	2.663
3.549	2.619

e. 360-in.^{2} nozzle contours (intermediate A/B)
Figure 4. Concluded.

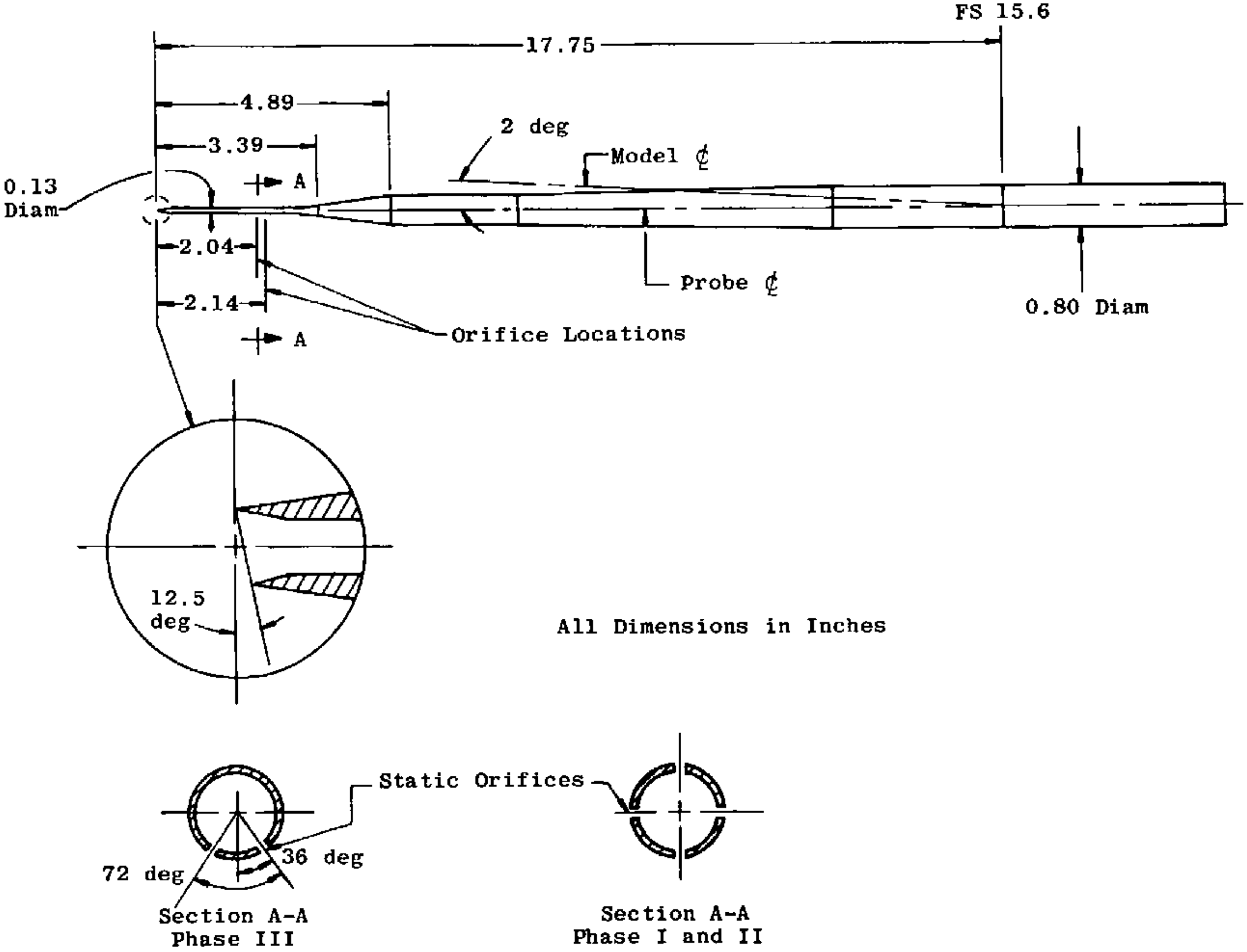

Figure 5. Pitot boom simulation details.

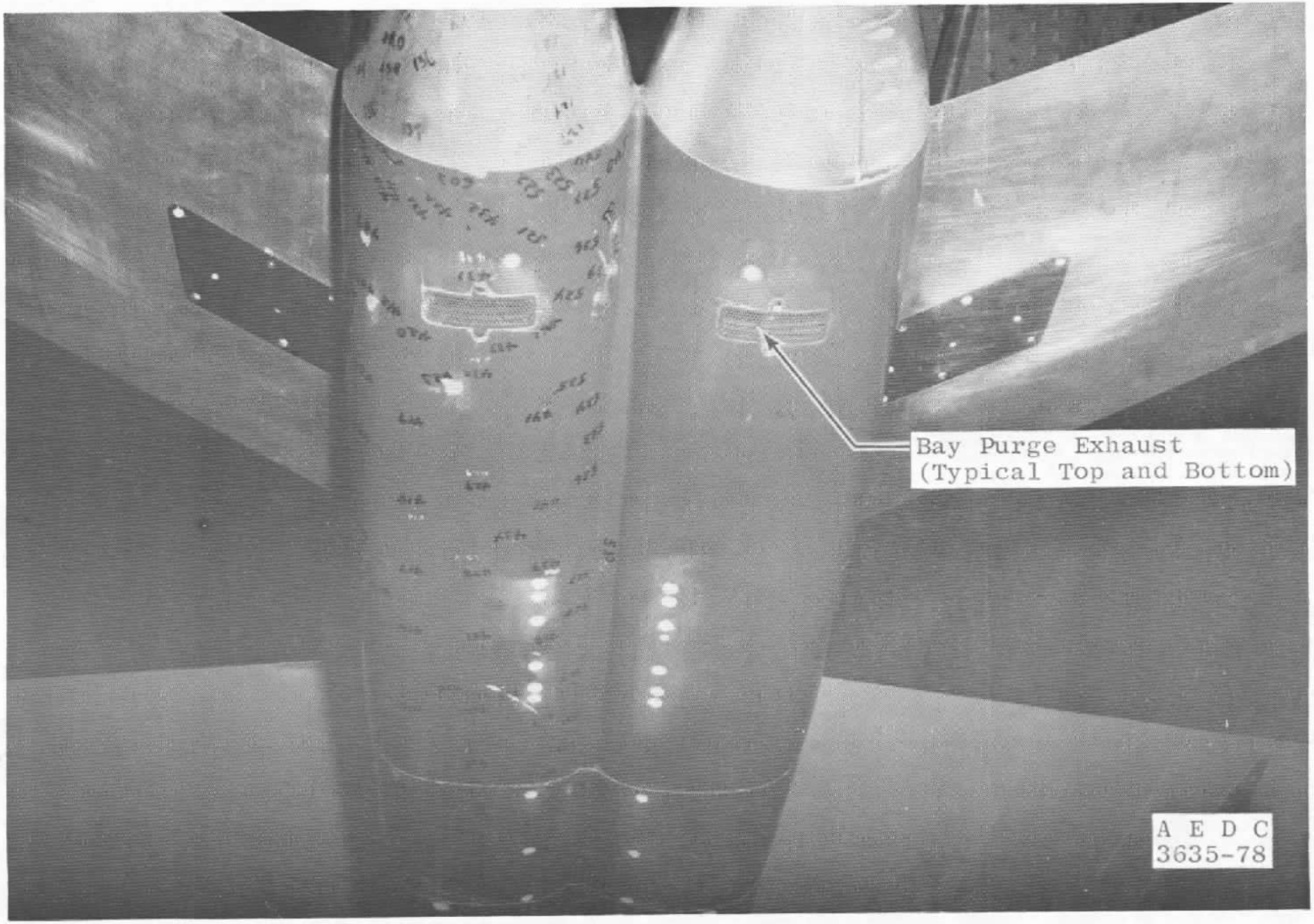

Figure 6. Bay purge exhaust.

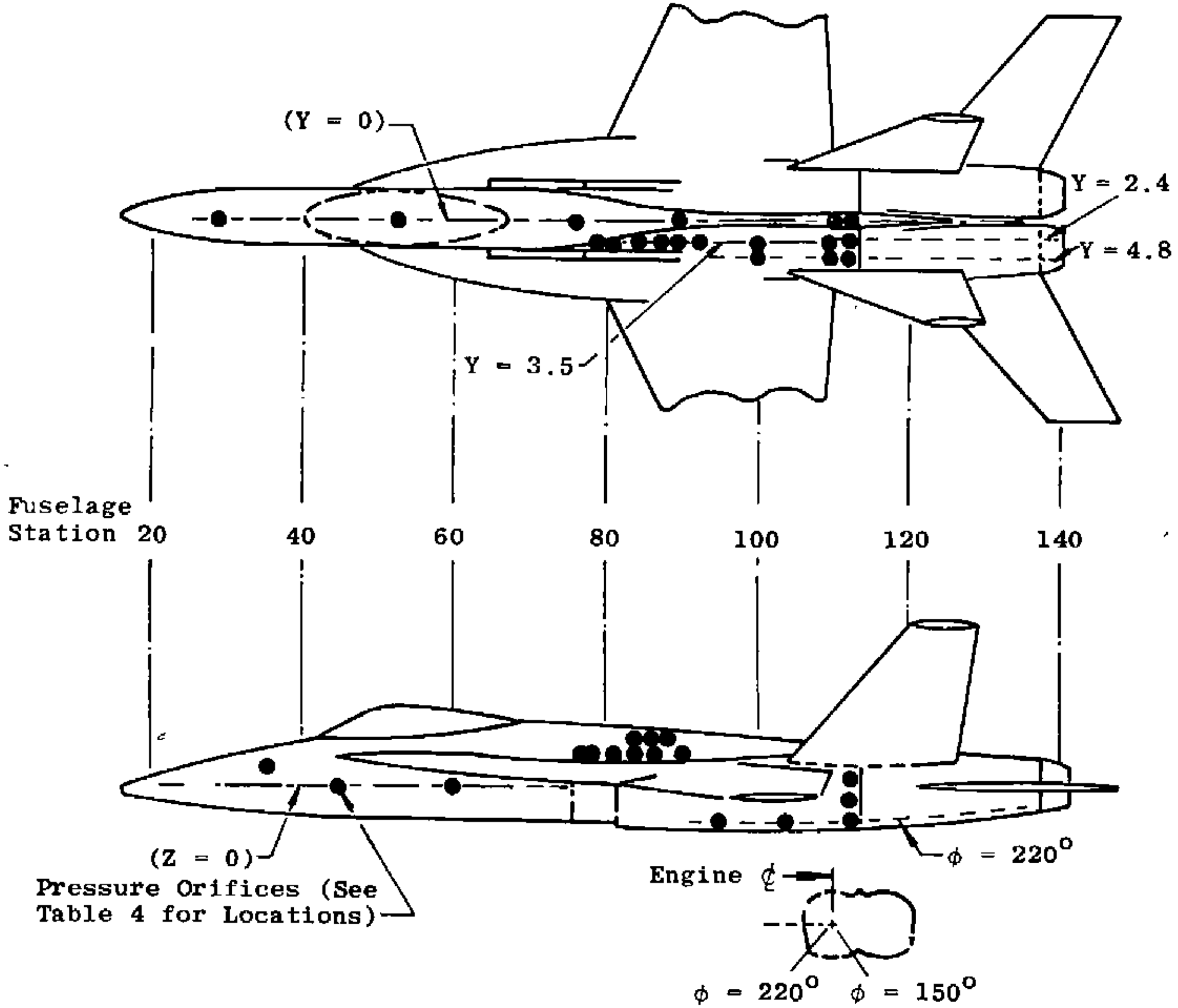

a. Forebody

Figure 7. Surface pressure instrumentation location.

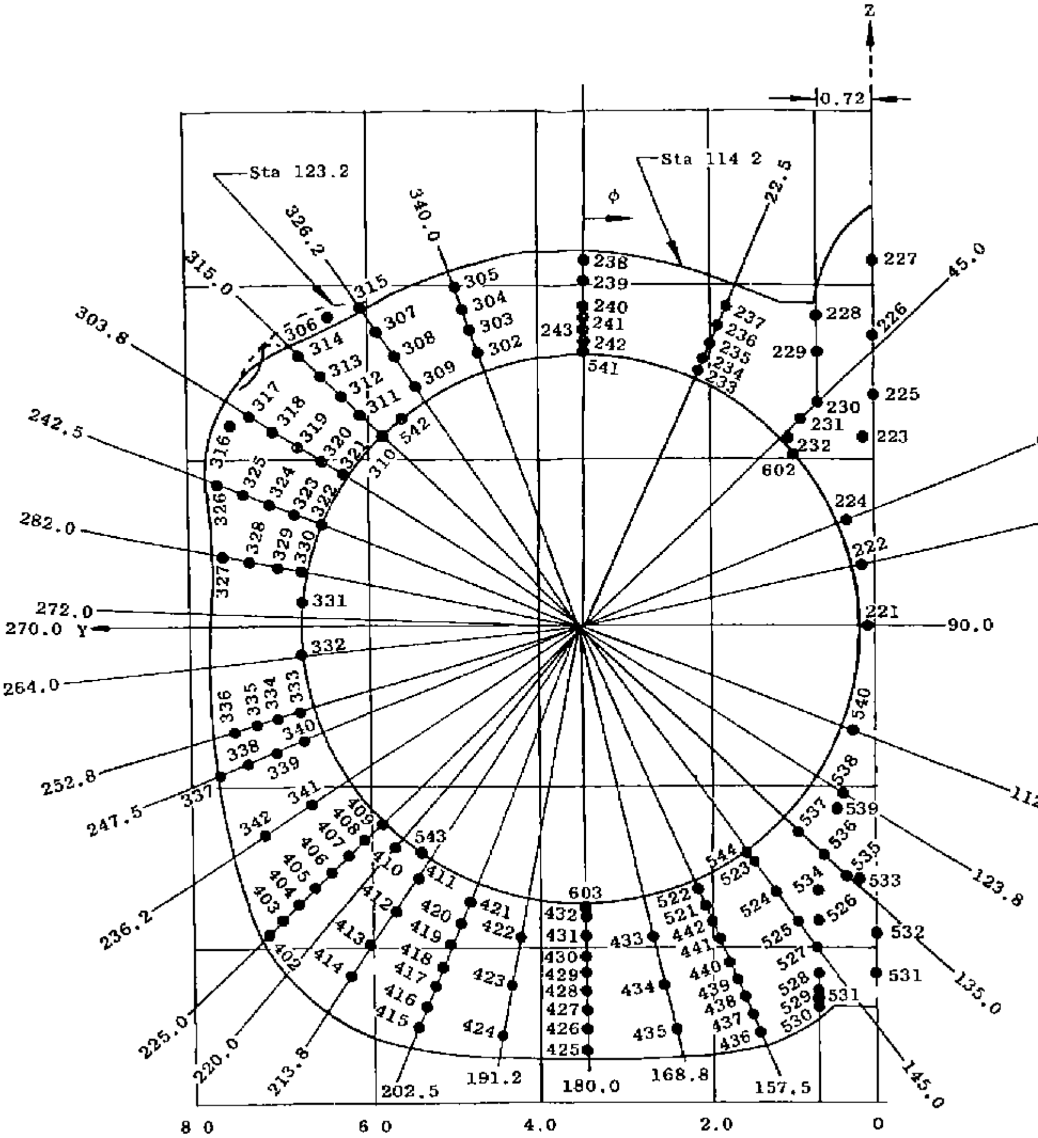

b. Afterbody

Figure 7. Continued.

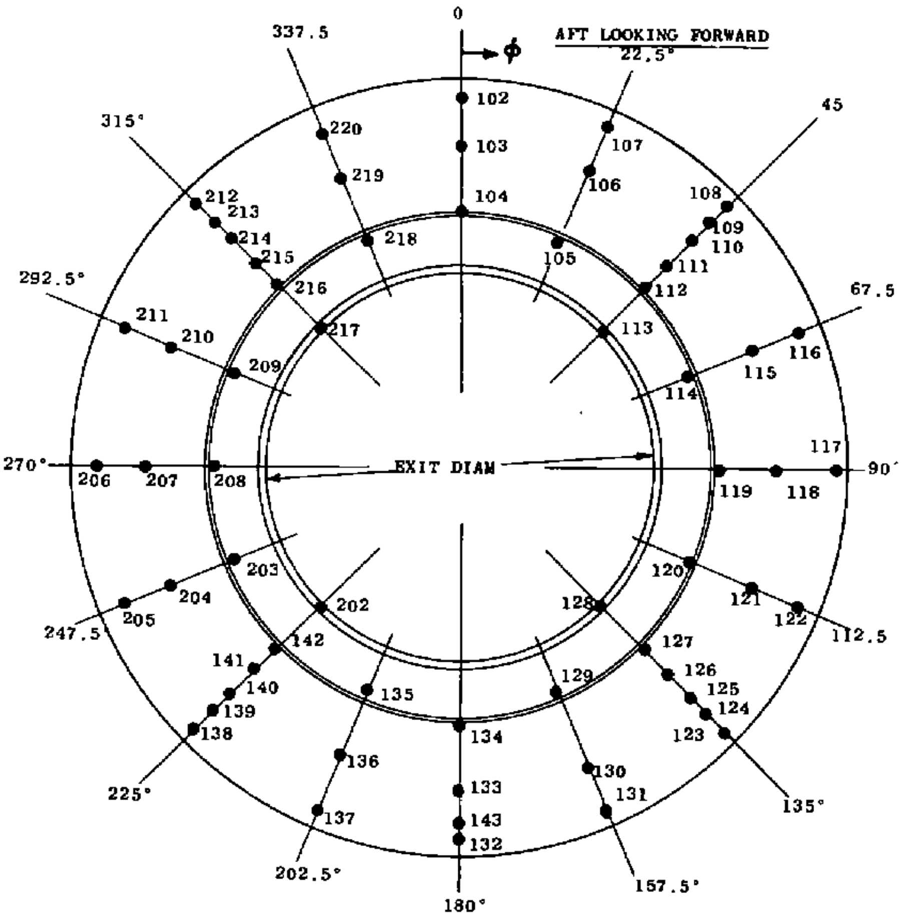

c. Typical nozzle
Figure 7. Concluded.

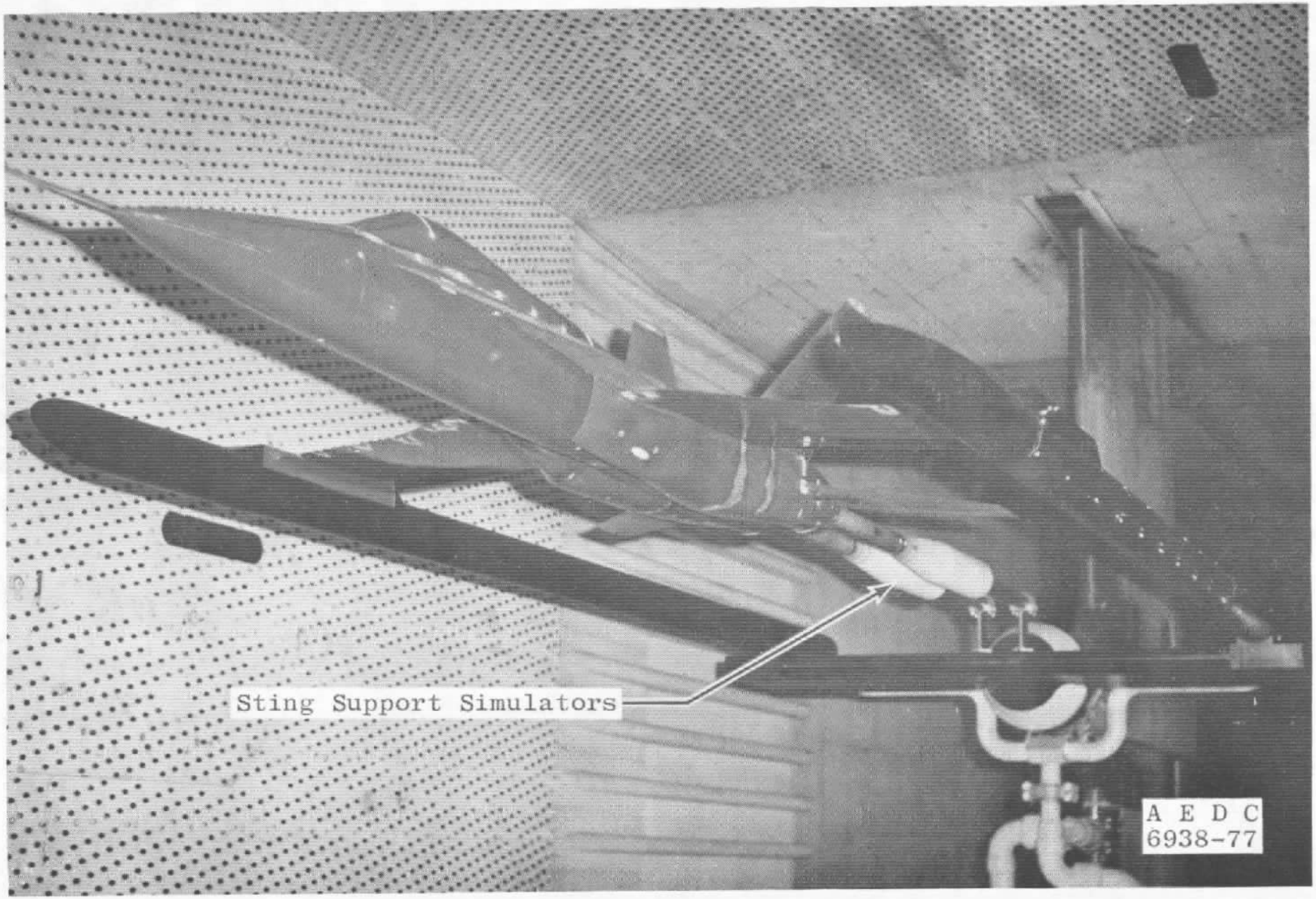

Figure 8. Simulation of sting support system.

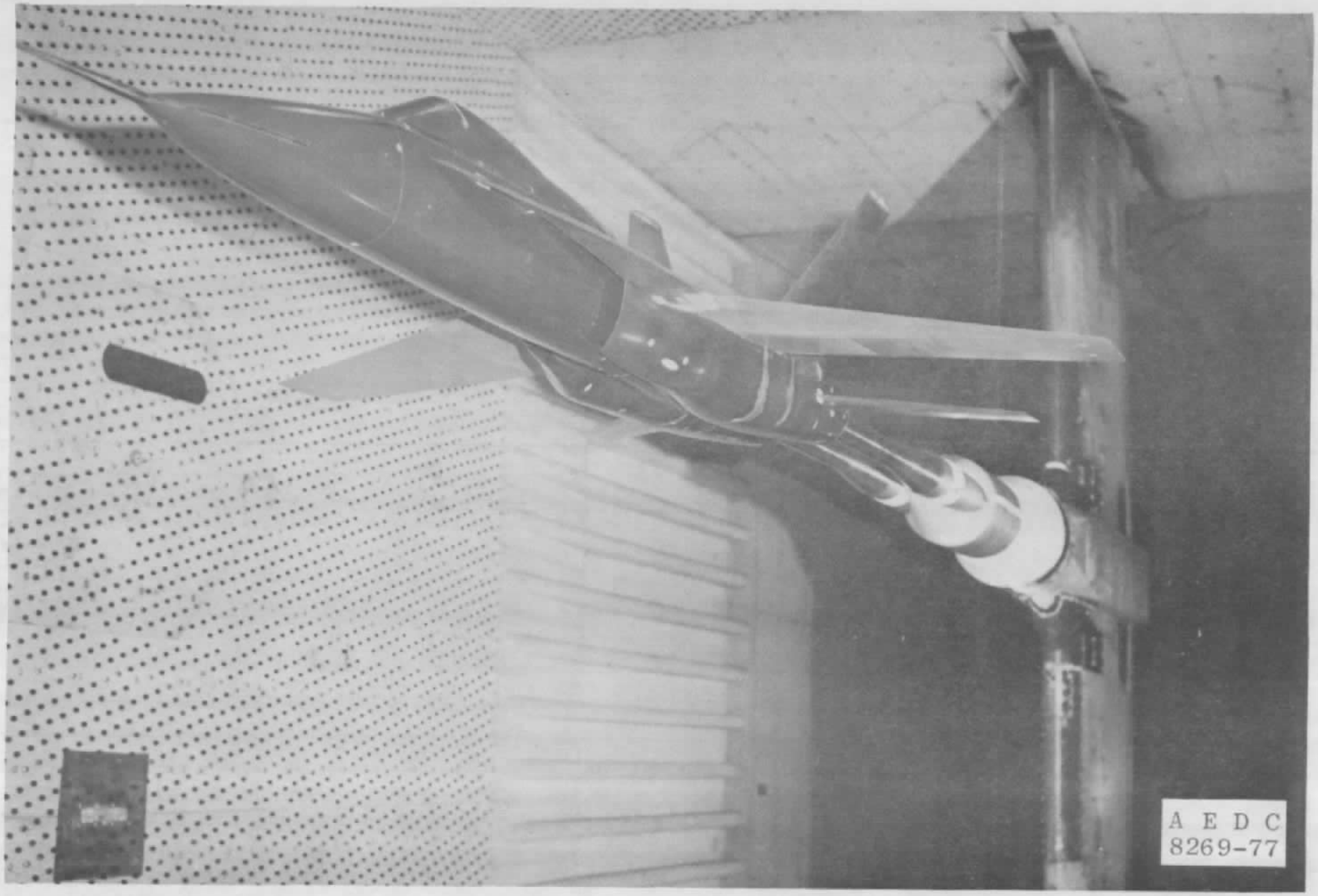

a. Front 3/4 view
Figure 9. Large-sting-supported model.

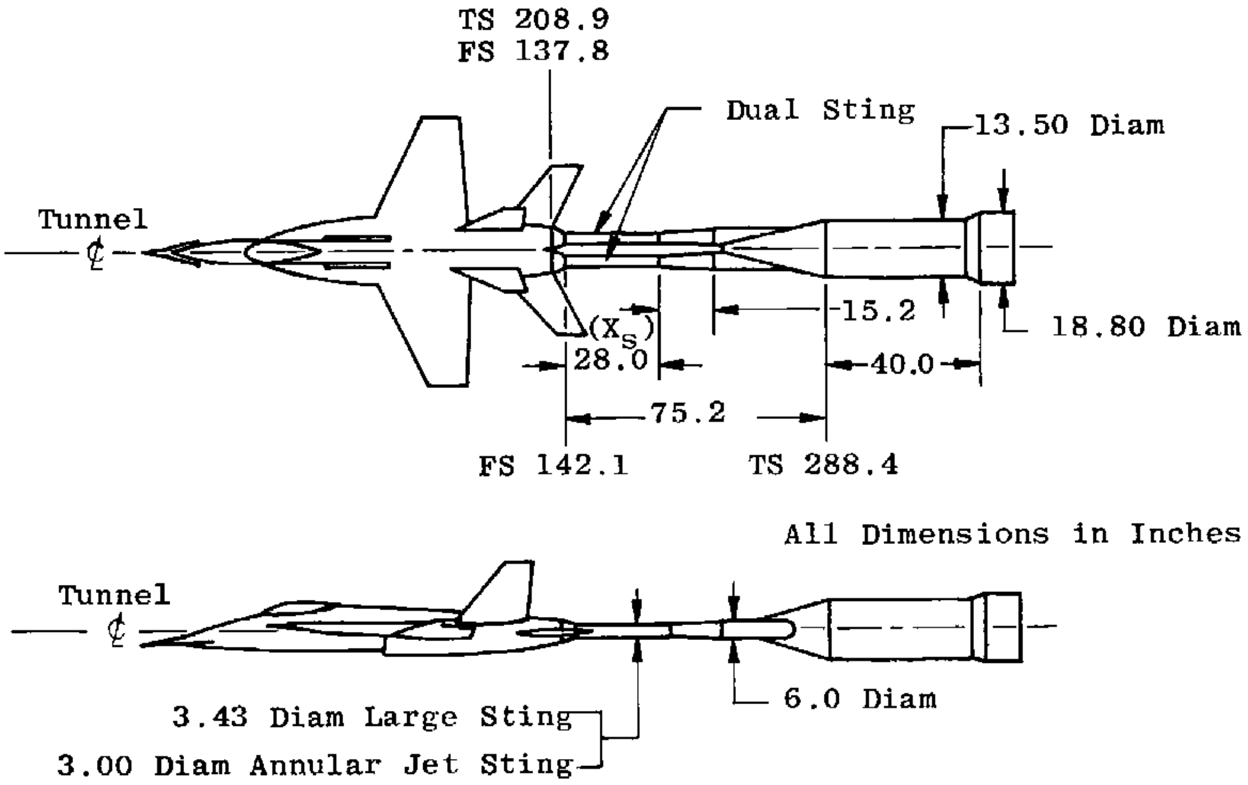

b. Support system dimensions
Figure 9. Continued.

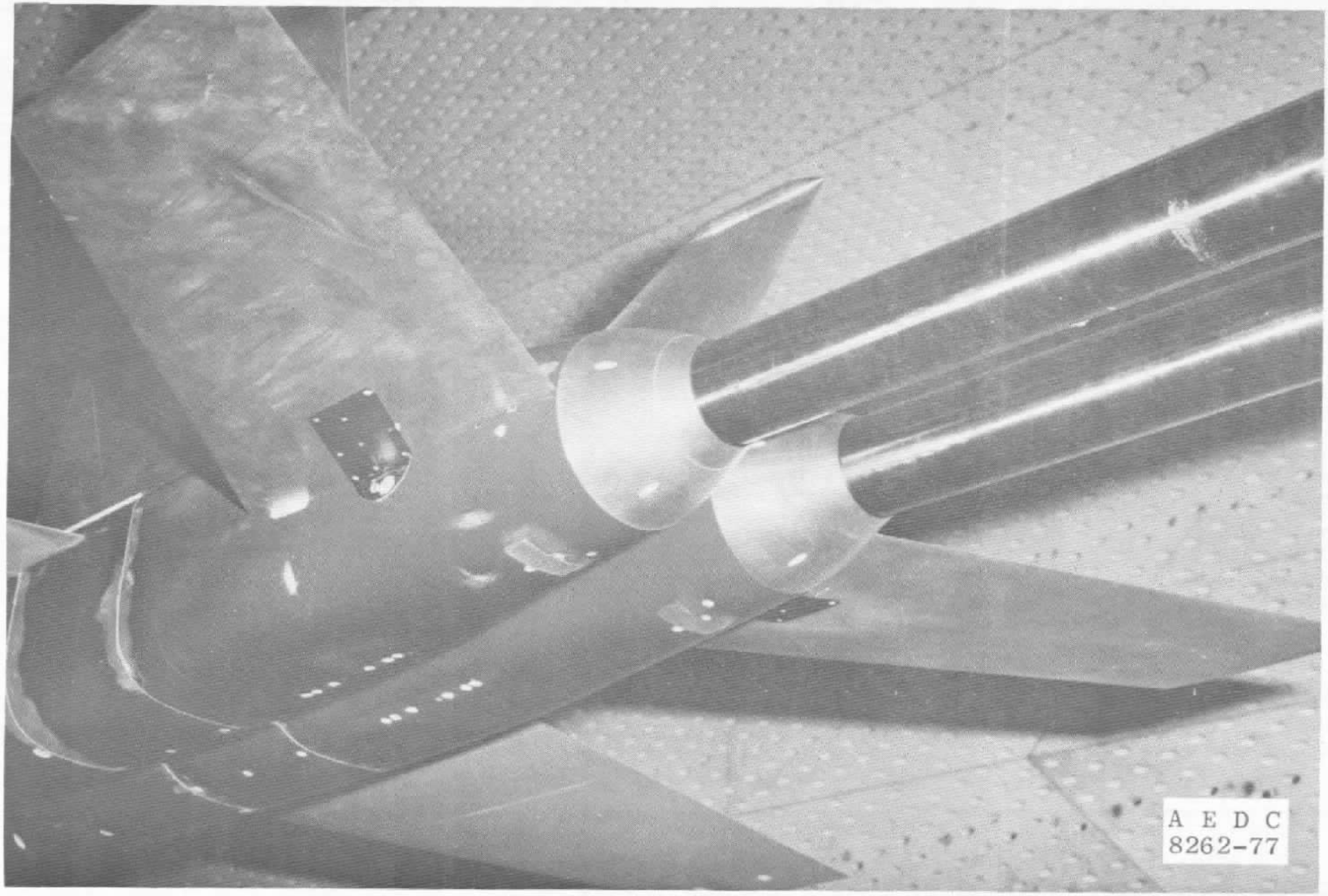

c. Rear 3-4 view
Figure 9. Concluded.

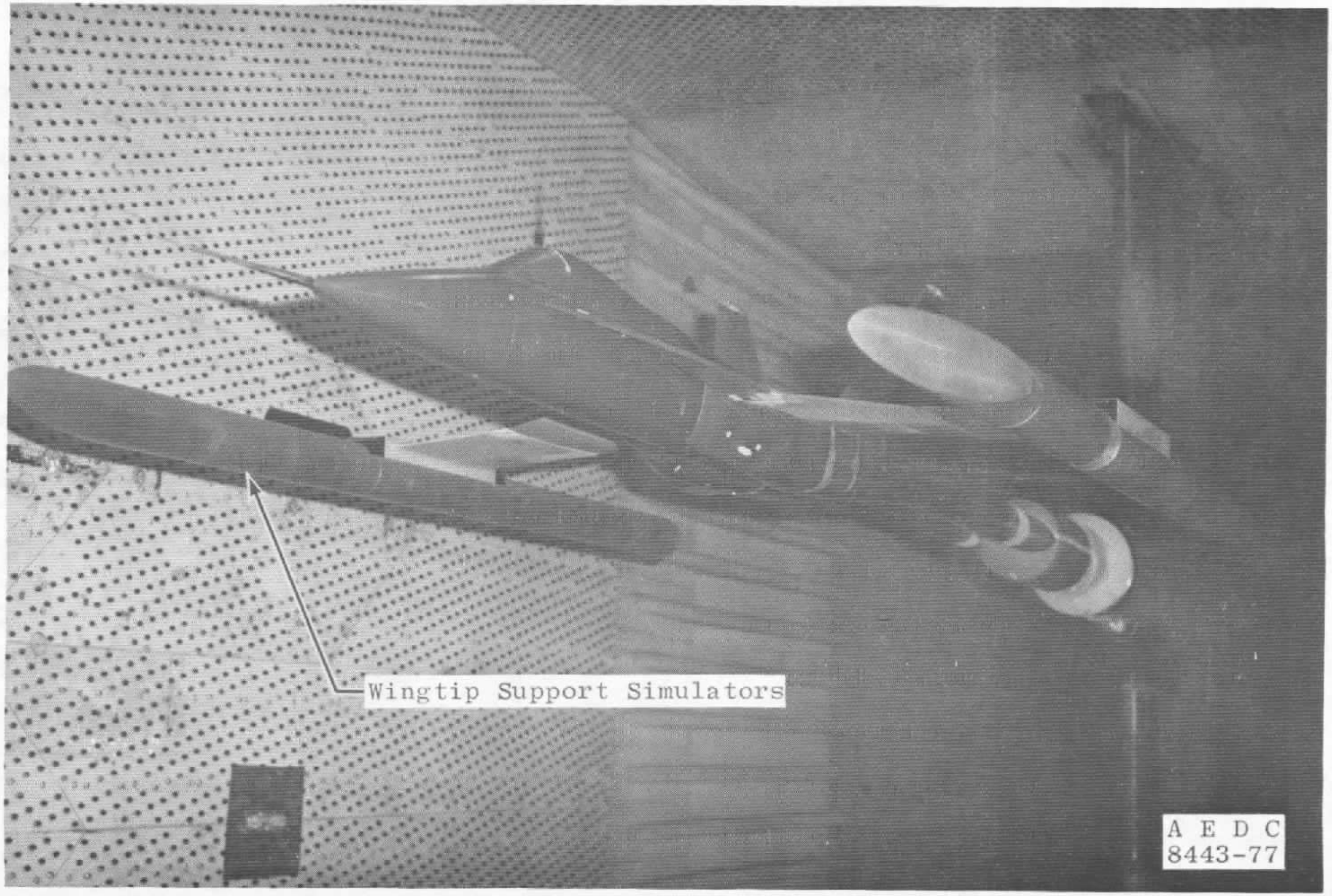

a. Phase I wingtip supports
Figure 10. Wingtip support simulation.

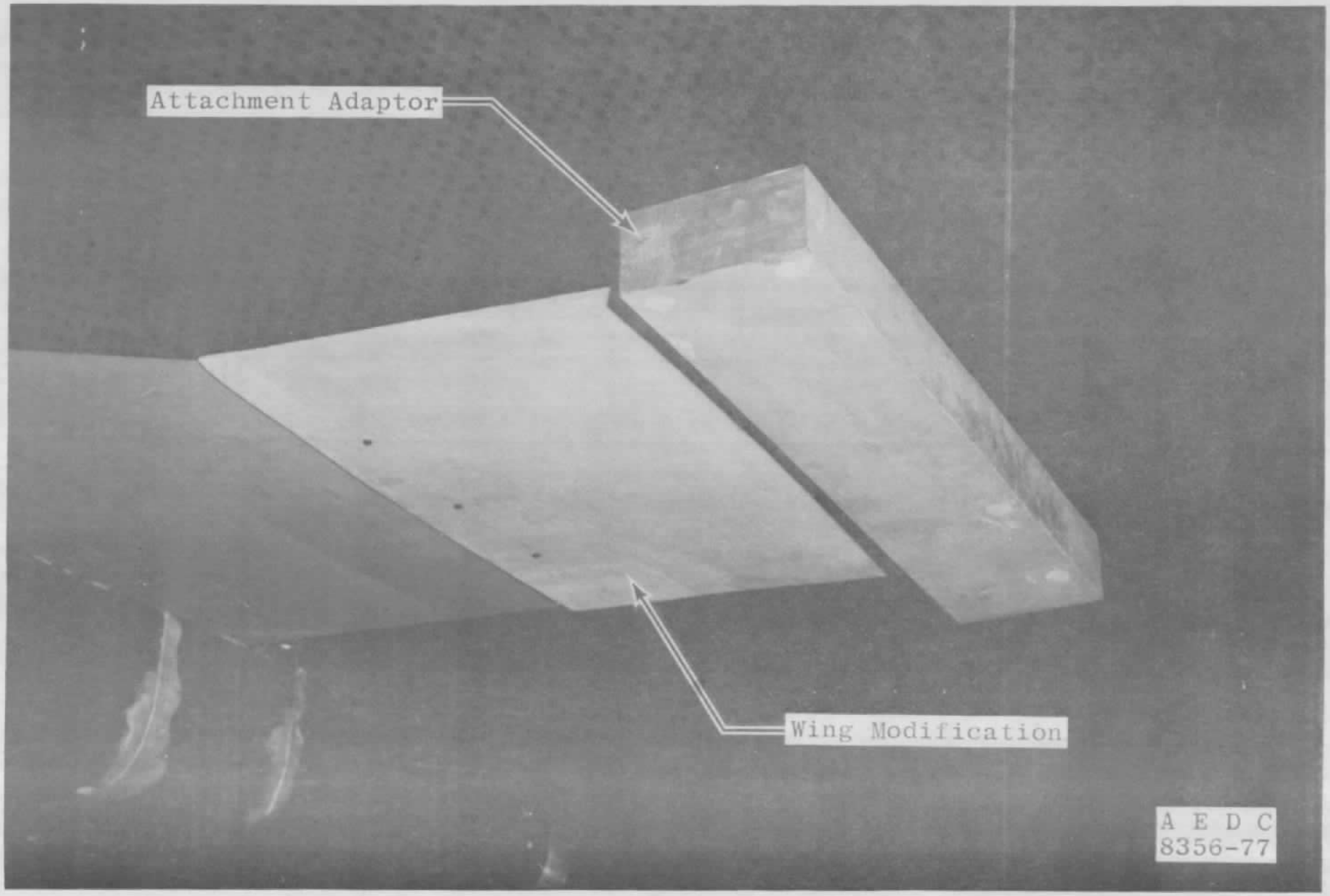

b. Wing support attachment
Figure 10. Concluded.

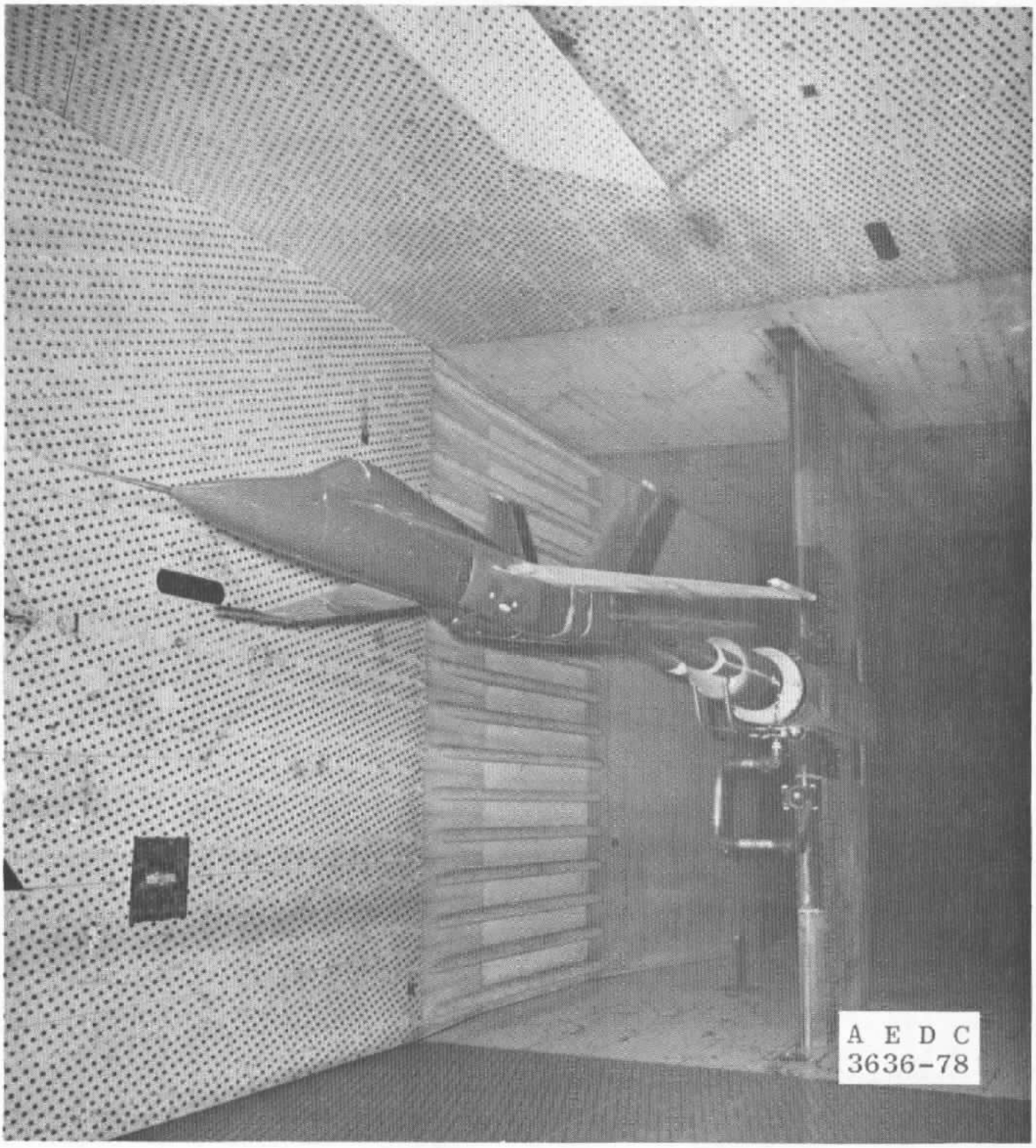

a. Model installation
Figure 11. Small-sting-supported model.

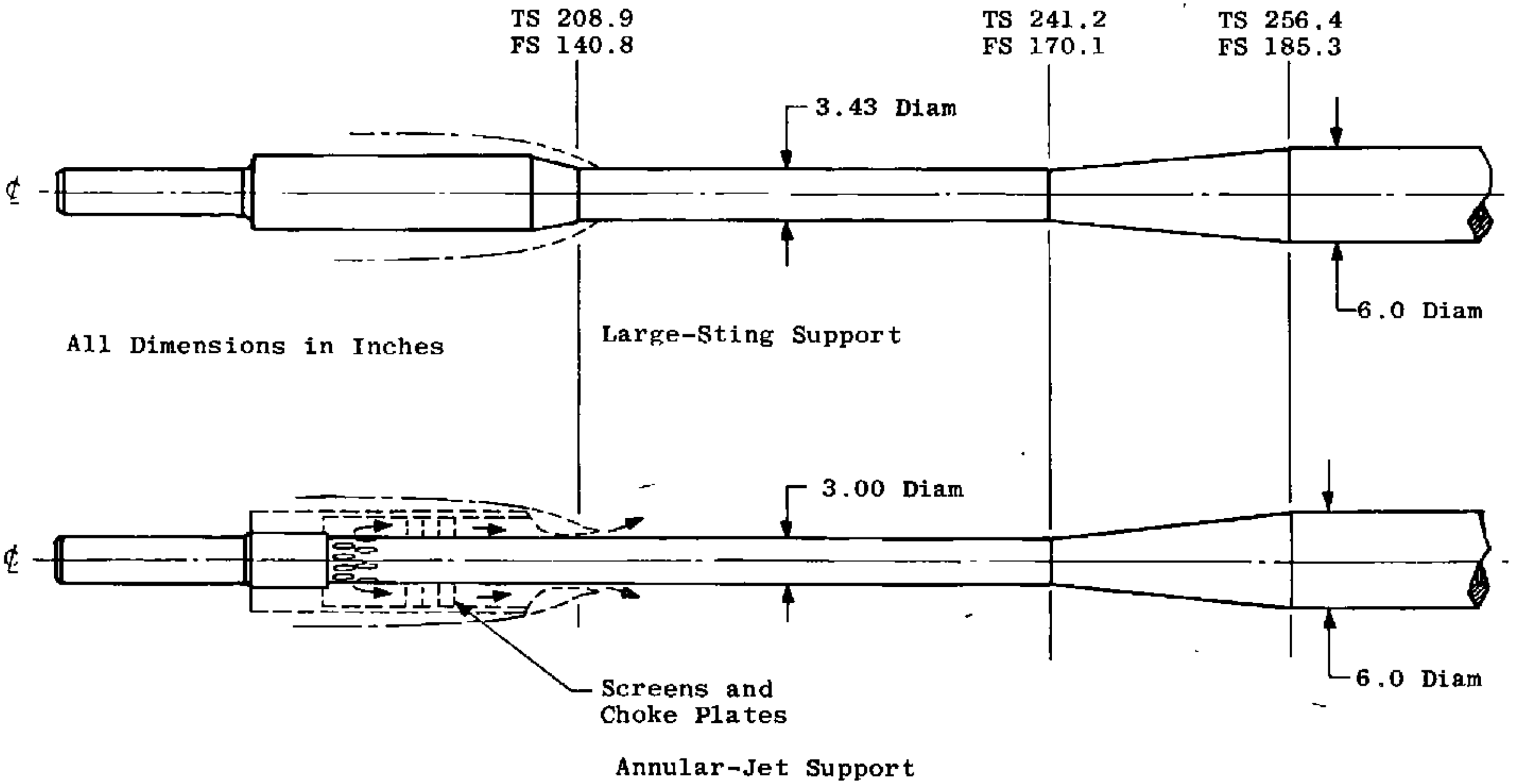

b. Sting supports
Figure 11. Continued.

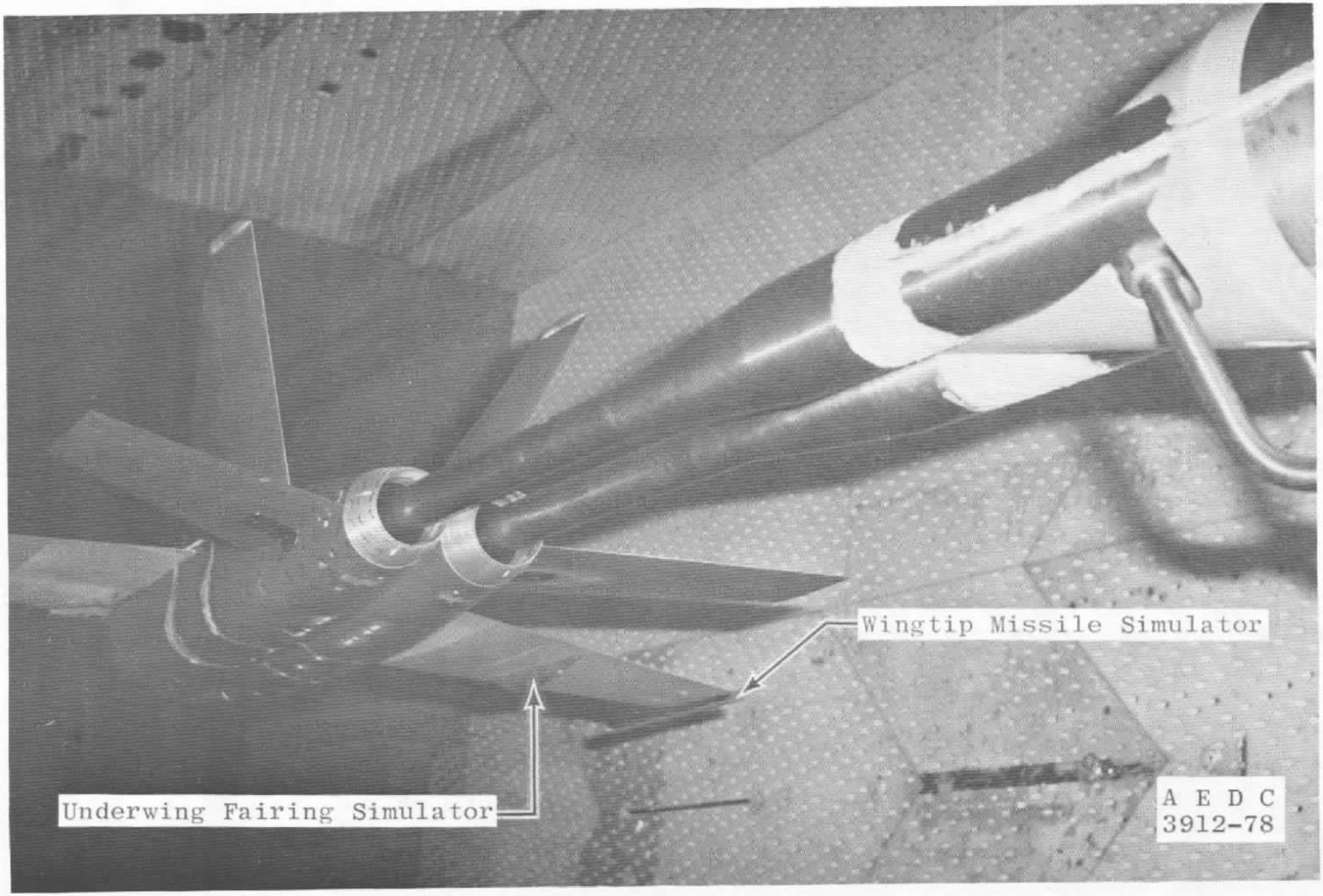

c. Rear 3/4 view
Figure 11. Continued.

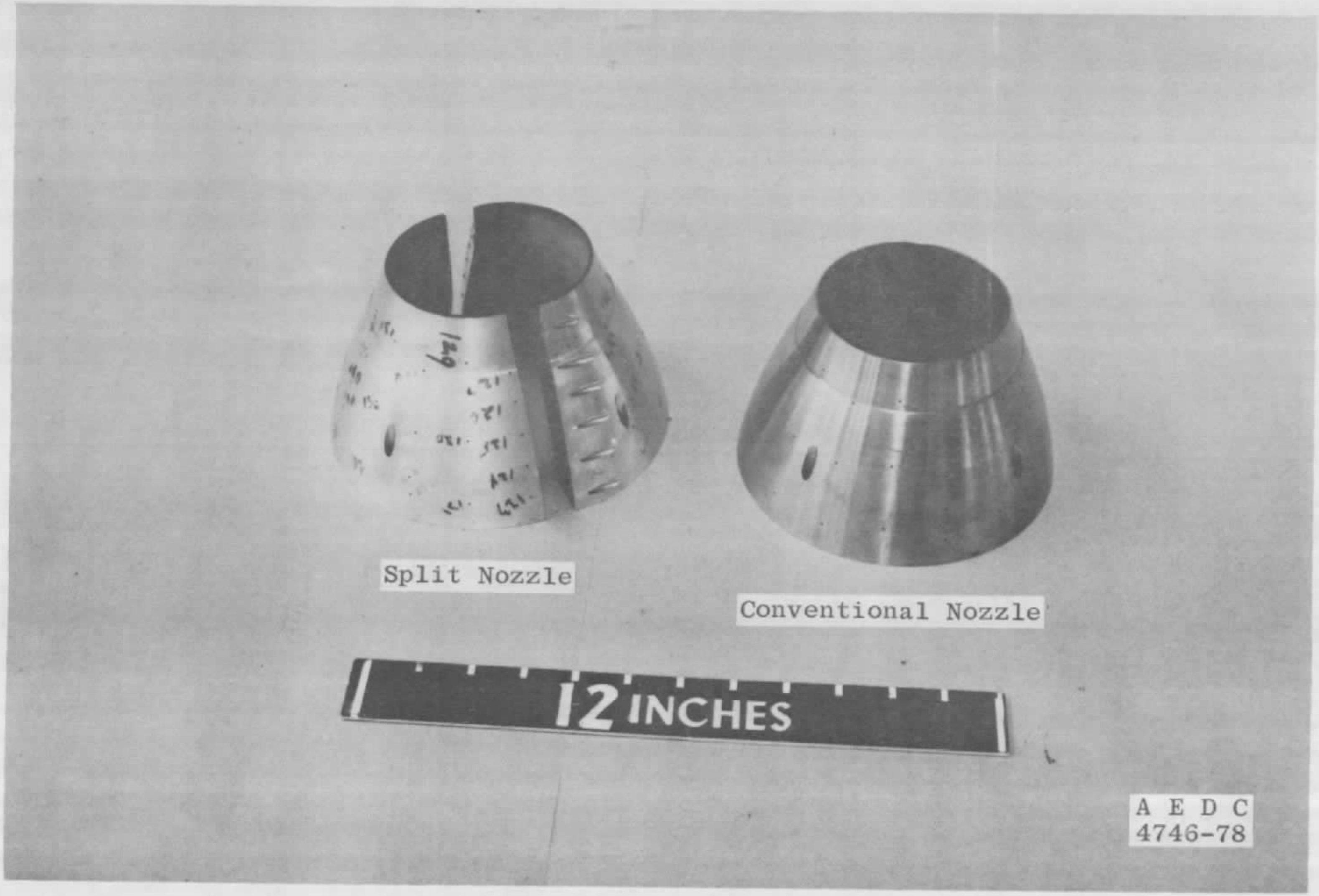

d. Conventional and split annular-jet nozzles
Figure 11. Concluded.

X_n, in.	r, in.
0	2.414
0.185	2.405
0.385	2.372
0.585	2.323
0.785	2.262
0.985	2.192
1.185	2.113
1.385	2.025
1.585	1.938
1.785	1.854
1.985	1.786
2.185	1.733
2.385	1.701
2.585	1.679
2.785	1.667
2.985	1.662
3.185	1.661
3.385	1.663
3.585	1.671
3.785	1.685
3.985	1.694
4.185	1.708
4.275	1.714

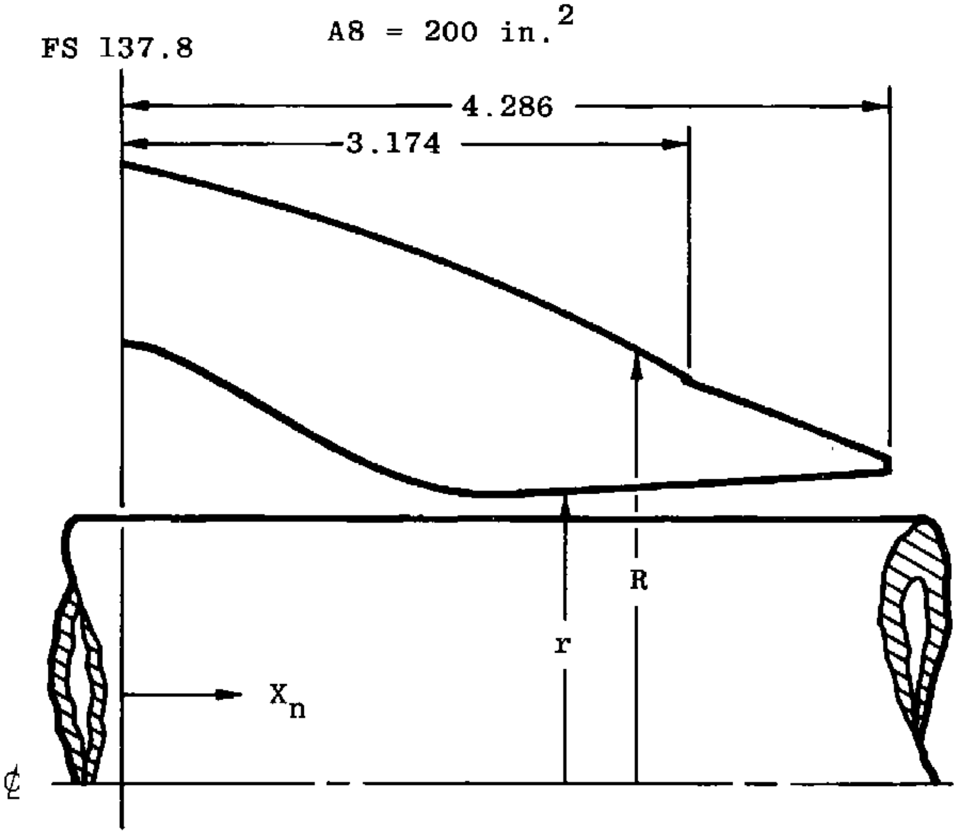

All Dimensions in Inches

X_n, in.	R, in.
0	3.380
0.152	3.350
0.352	3.304
0.552	3.258
0.752	3.204
0.952	3.146
1.152	3.086
1.352	3.024
1.552	2.956
1.752	2.880
1.952	2.804
2.152	2.722
2.352	2.636
2.552	2.544
2.752	2.448
2.952	2.344
3.152	2.240
3.174	2.228
3.174	2.202
4.286	1.776

a. 200-in.^{2} nozzle contours (cruise)
Figure 12. Annular-jet nozzle internal coordinates.

X_n, in.	r, in.
0	2.414
0.200	2.408
0.400	2.402
0.600	2.378
0.800	2.342
1.000	2.311
1.200	2.277
1.400	2.237
1.600	2.190
1.800	2.140
2.000	2.086
2.200	2.031
2.400	1.977
2.600	1.926
2.800	1.880
3.000	1.847
3.200	1.828
3.250	1.827
3.300	1.828
3.400	1.834
3.562	1.846
3.962	1.878
4.135	1.892

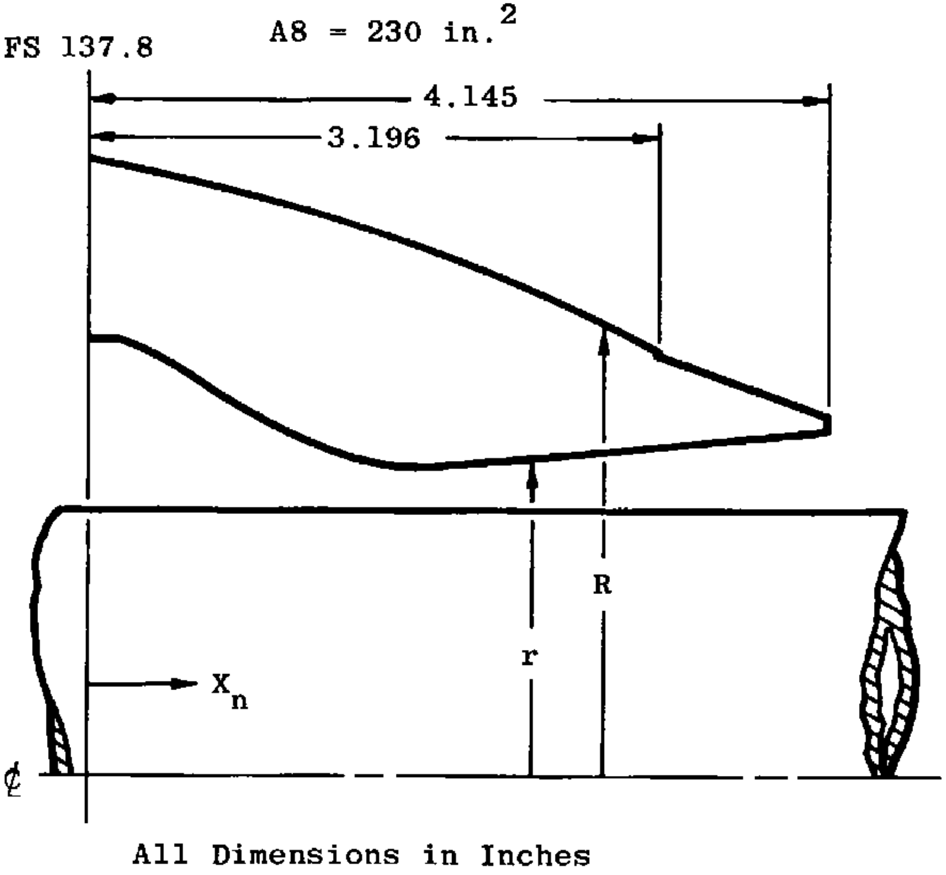

X_n, in.	R, in.
0	3.380
0.162	3.352
0.362	3.312
0.562	3.270
0.762	3.224
0.962	3.174
1.162	3.118
1.362	3.060
1.562	2.998
1.762	2.930
1.962	2.860
2.162	2.784
2.362	2.704
2.562	2.620
2.762	2.530
2.962	2.436
3.162	2.336
3.196	2.320
3.196	2.294
3.362	2.234
3.562	2.164
3.762	2.092
3.962	2.020
4.145	1.955

b. 230-in.^{2} nozzle contours (intermediate)

Figure 12. Continued.

X_n, in.	r, in.
0	2.422
0.219	2.414
0.419	2.396
0.619	2.374
0.819	2.351
1.019	2.327
1.219	2.304
1.419	2.280
1.619	2.253
1.819	2.223
2.019	2.190
2.219	2.154
2.419	2.115
2.519	2.103
2.619	2.101
2.719	2.111
2.919	2.141
3.119	2.170
3.319	2.198
3.519	2.228
3.719	2.258
3.815	2.272

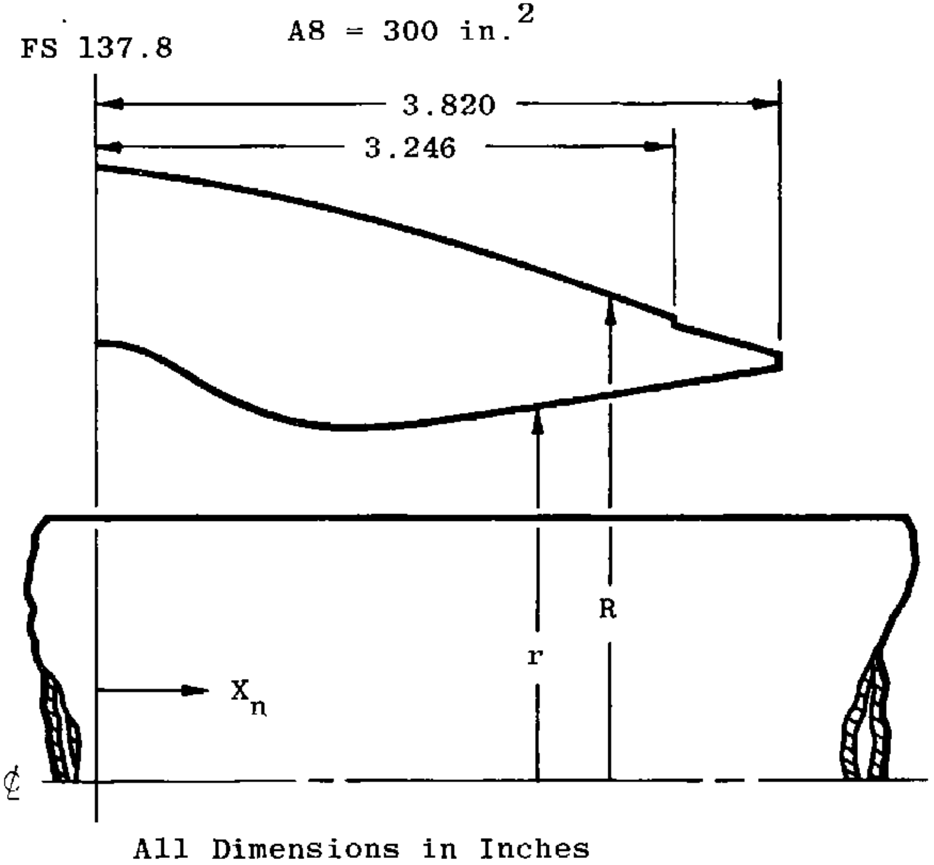

X_n, in.	R, in.
0	3.380
0.174	3.360
0.374	3.332
0.574	3.302
0.774	3.268
0.974	3.232
1.174	3.192
1.374	3.144
1.574	3.096
1.774	3.044
1.974	2.988
2.174	2.928
2.374	2.862
2.574	2.792
2.774	2.720
2.974	2.640
3.174	2.556
3.246	2.528
3.246	2.502
3.374	2.464
3.574	2.404
3.774	2.348
3.820	2.334

c. 300-in.^{2} nozzle contours (reheat)
Figure 12. Continued.

X_n, in.	r, in.
0	2.412
0.200	2.412
0.400	2.408
0.600	2.401
0.800	2.395
1.000	2.388
1.200	2.379
1.400	2.367
1.600	2.348
1.800	2.316
2.000	2.293
2.050	2.292
2.100	2.296
2.200	2.310
2.370	2.339
2.770	2.413
3.170	2.487
3.370	2.528
3.549	2.562

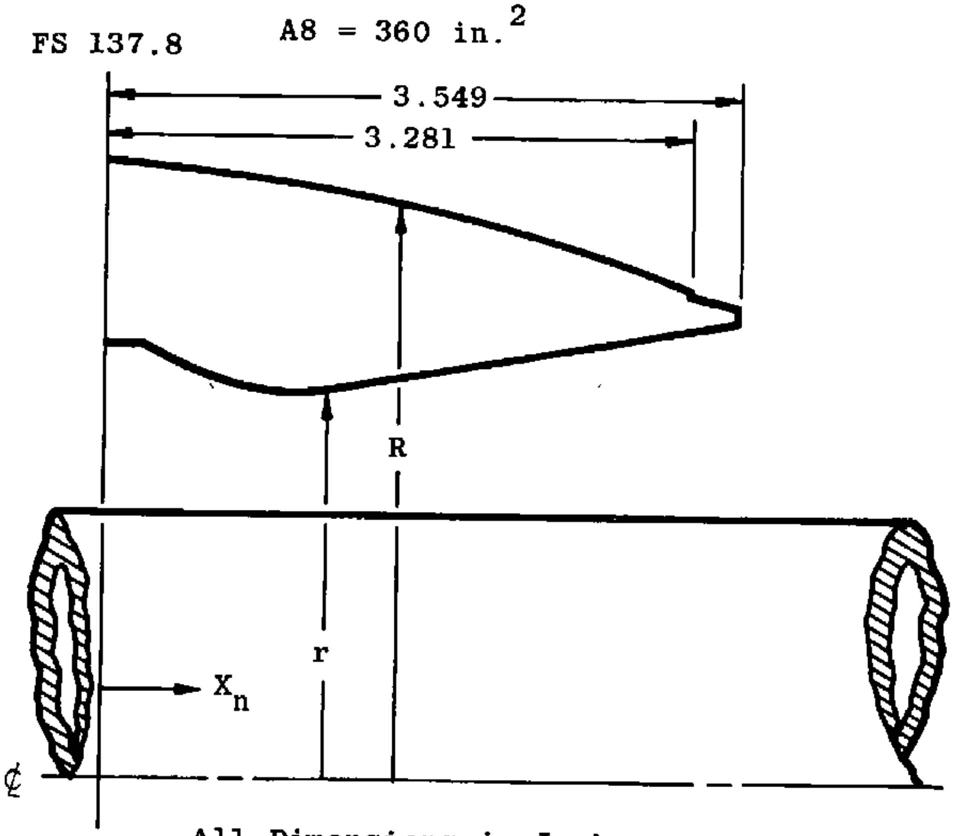

All Dimensions in Inches

X_n, in.	R, in.
0	3.380
0.170	3.371
0.370	3.356
0.570	3.338
0.770	3.316
0.970	3.290
1.170	3.261
1.370	3.227
1.570	3.190
1.770	3.150
1.970	3.105
2.170	3.056
2.370	3.004
2.570	2.947
2.770	2.886
2.970	2.821
3.170	2.752
3.281	2.712
3.281	2.686
3.370	2.663
3.549	2.619

d. 360-in.^{2} nozzle contours (intermediate A/B)
Figure 12. Concluded.

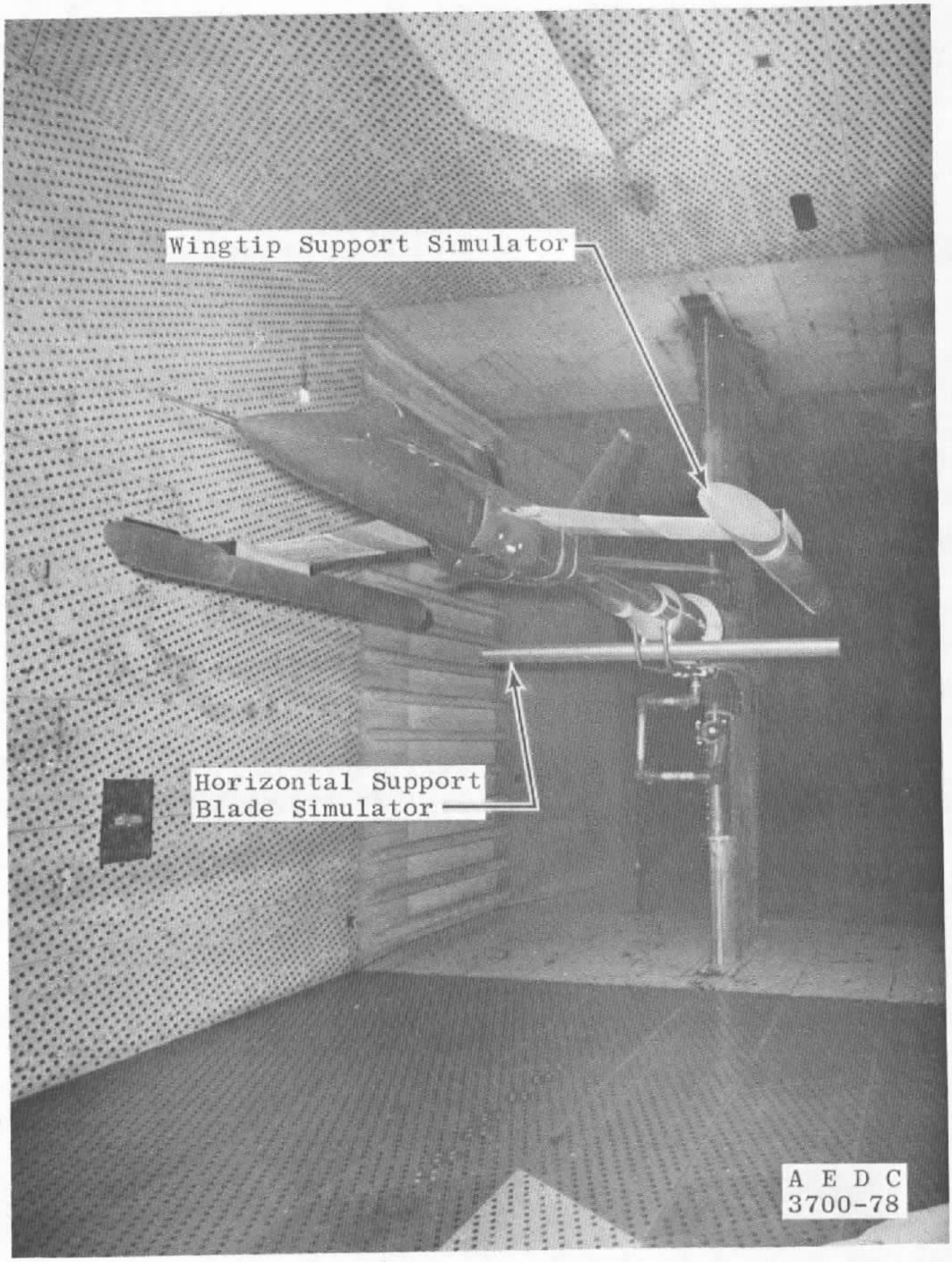

a. Installation
Figure 13. Simulation of wingtip support system.

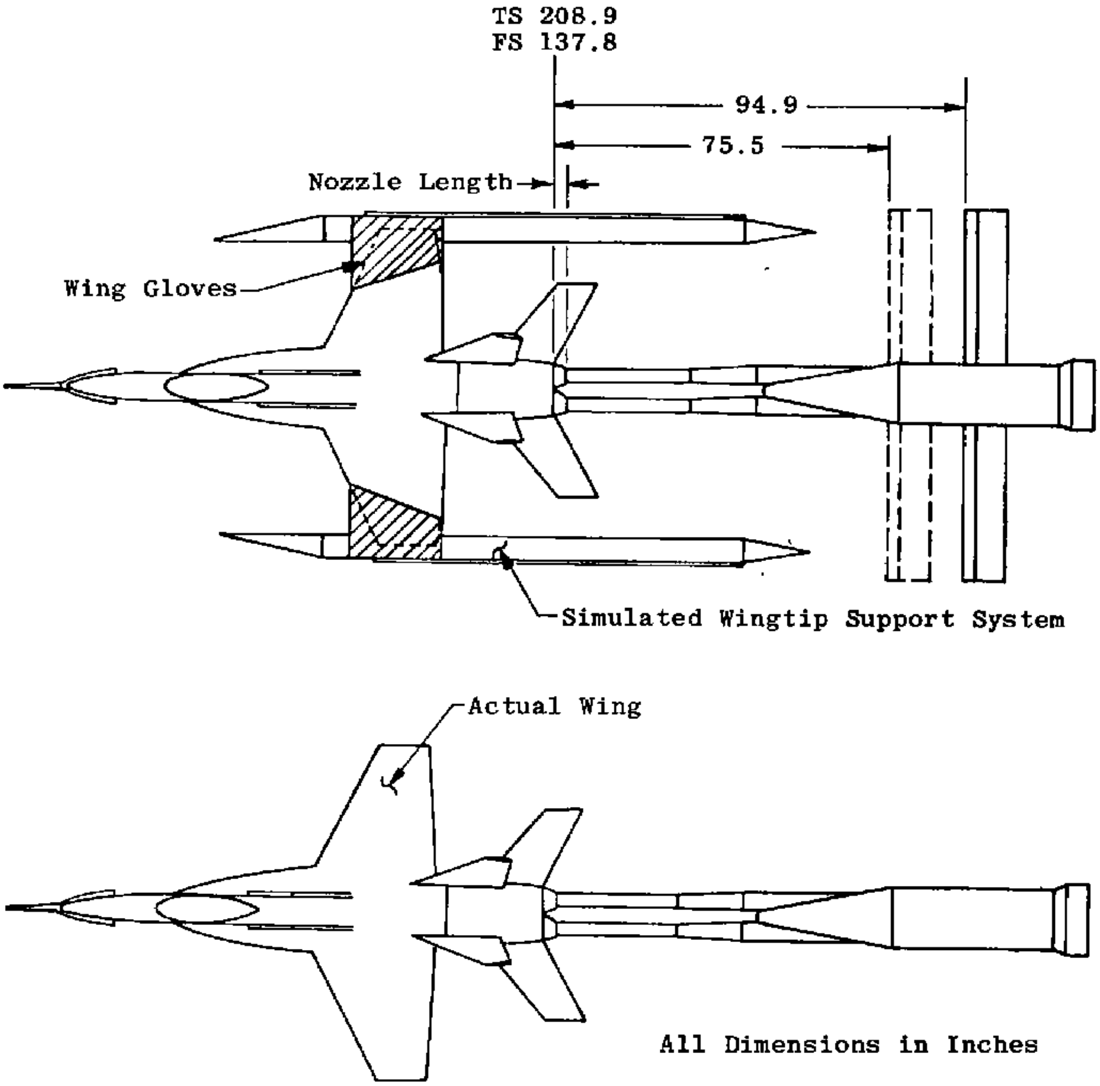

b. Phase I support system simulator locations
Figure 13. Concluded.

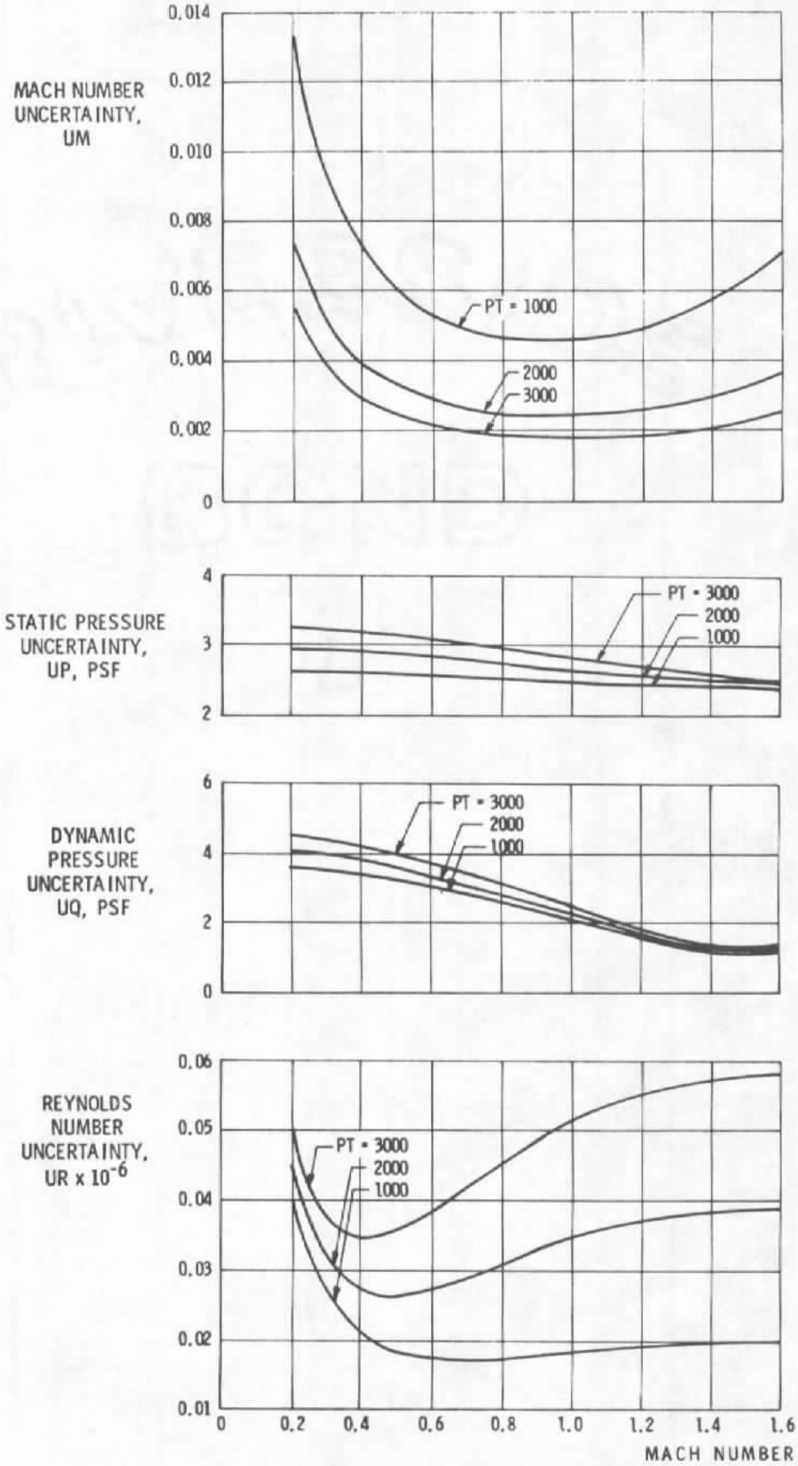

Figure 14. Estimated uncertainties in wind tunnel parameters.

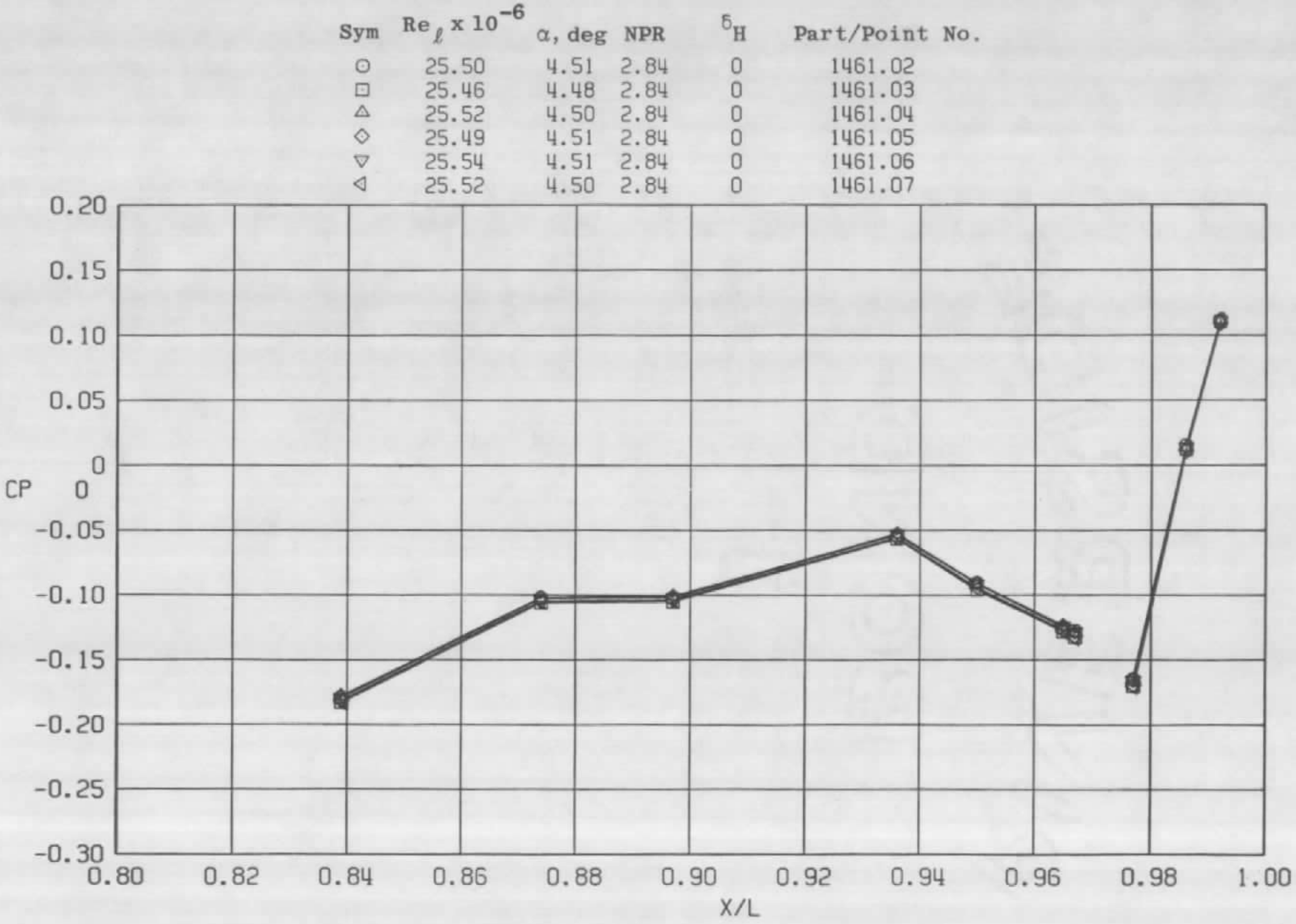

a. M = 0.6

Figure 15. Typical surface pressure coefficient repeatability.

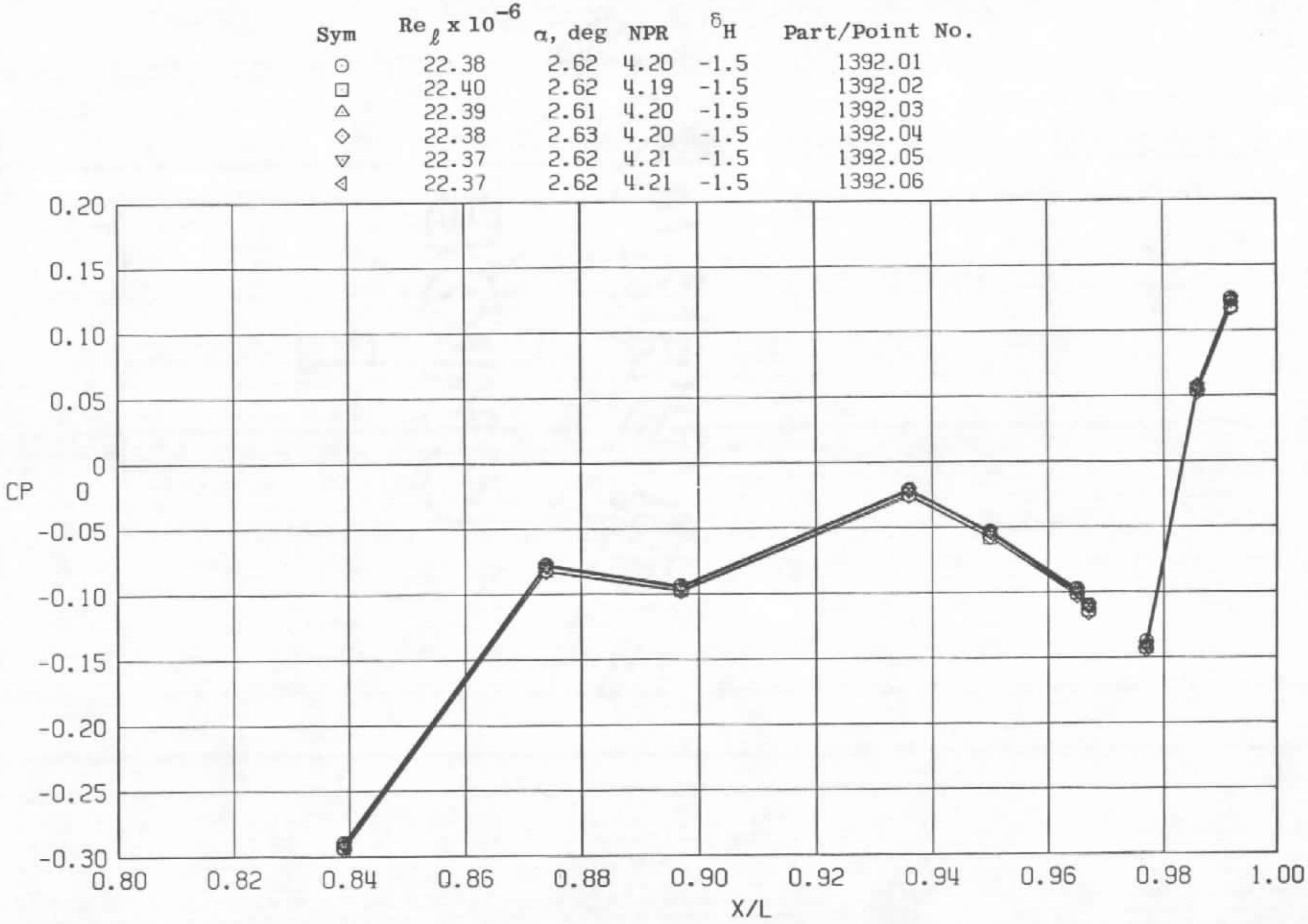

b. M = 0.9
Figure 15. Continued.

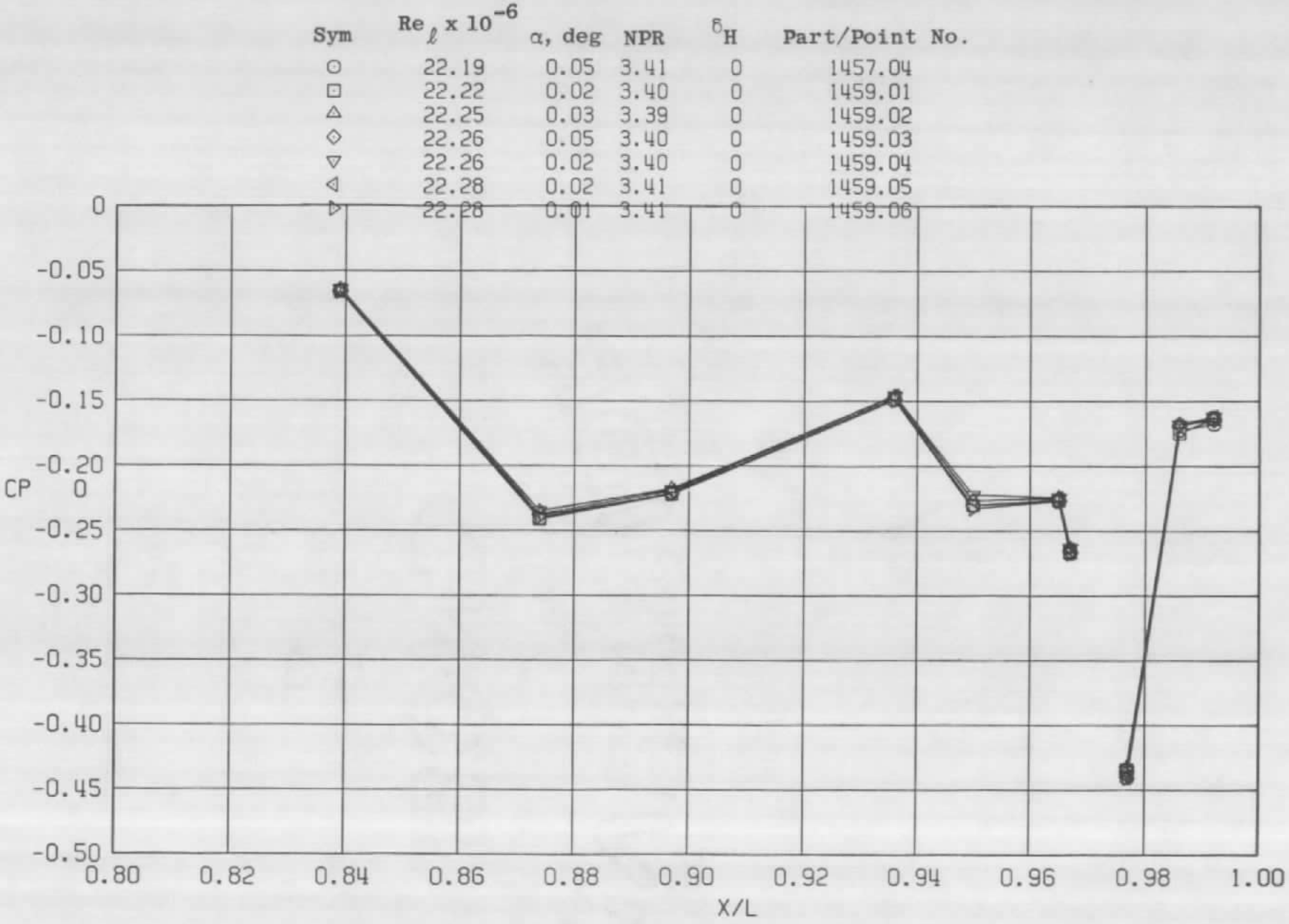

c. M = 1.2

Figure 15. Continued.

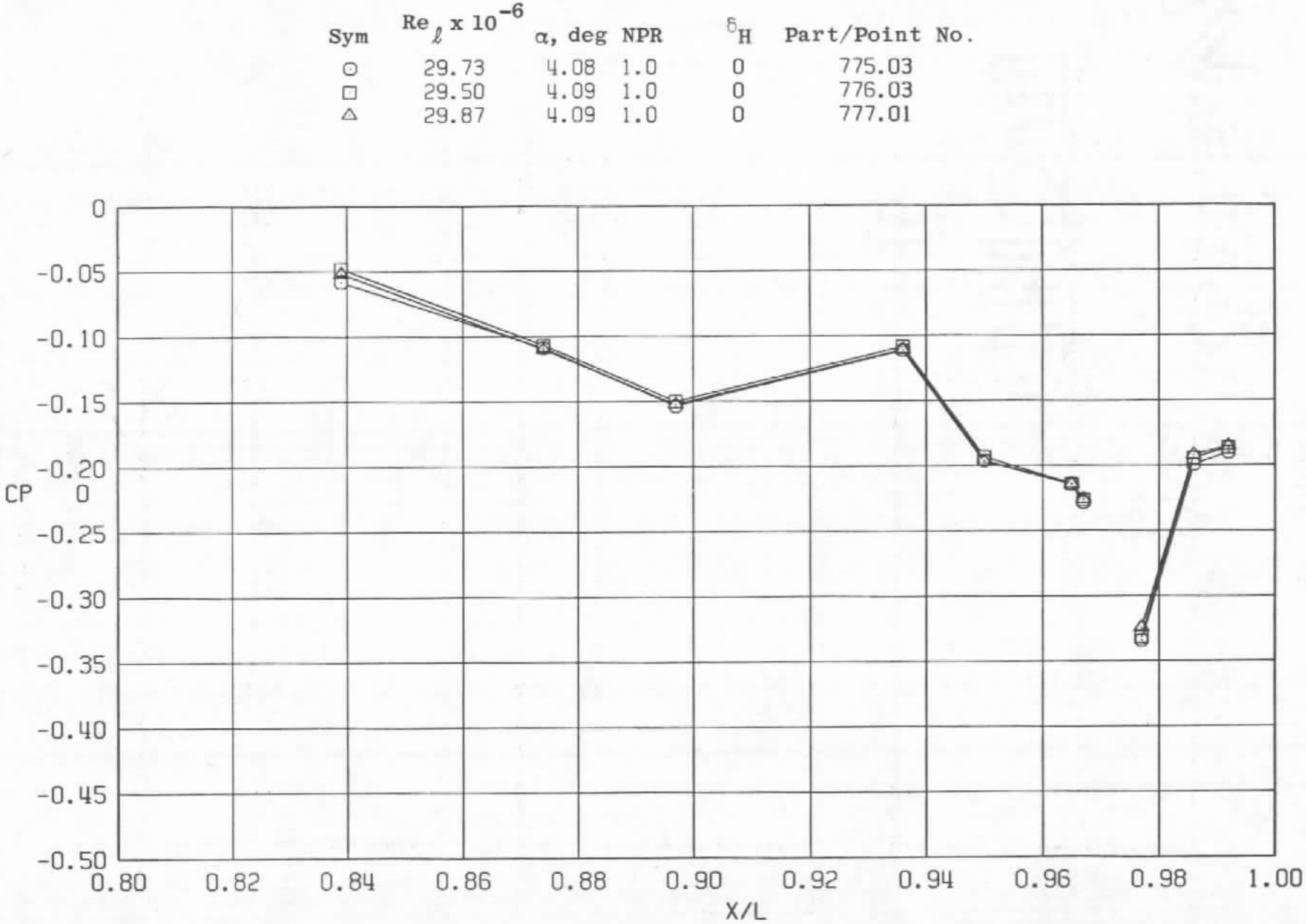

d. M = 1.5
Figure 15. Concluded.

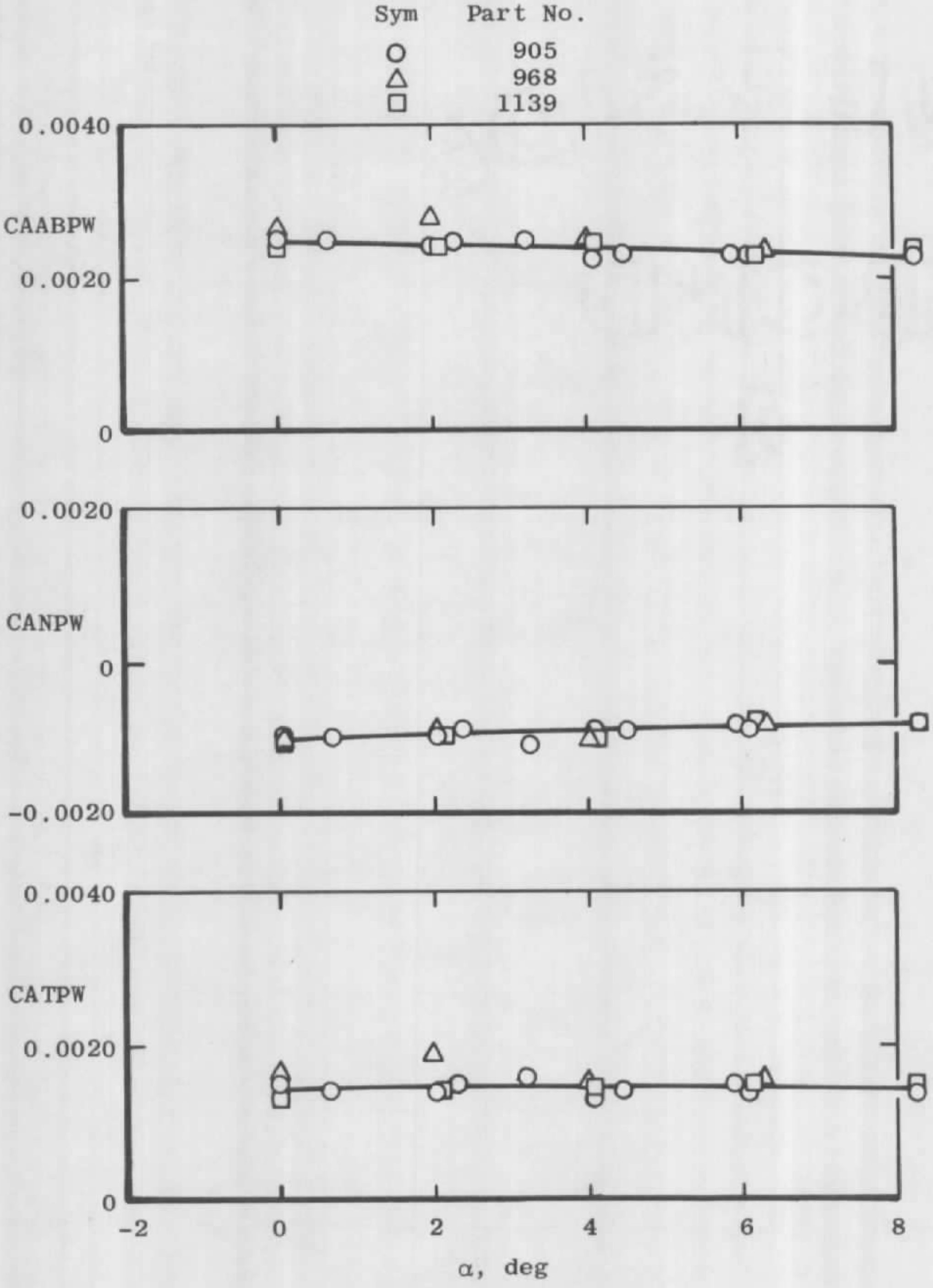

a. A8 = 200 in.², M = 0.6

Figure 16. Repeatability of integrated pressure data.

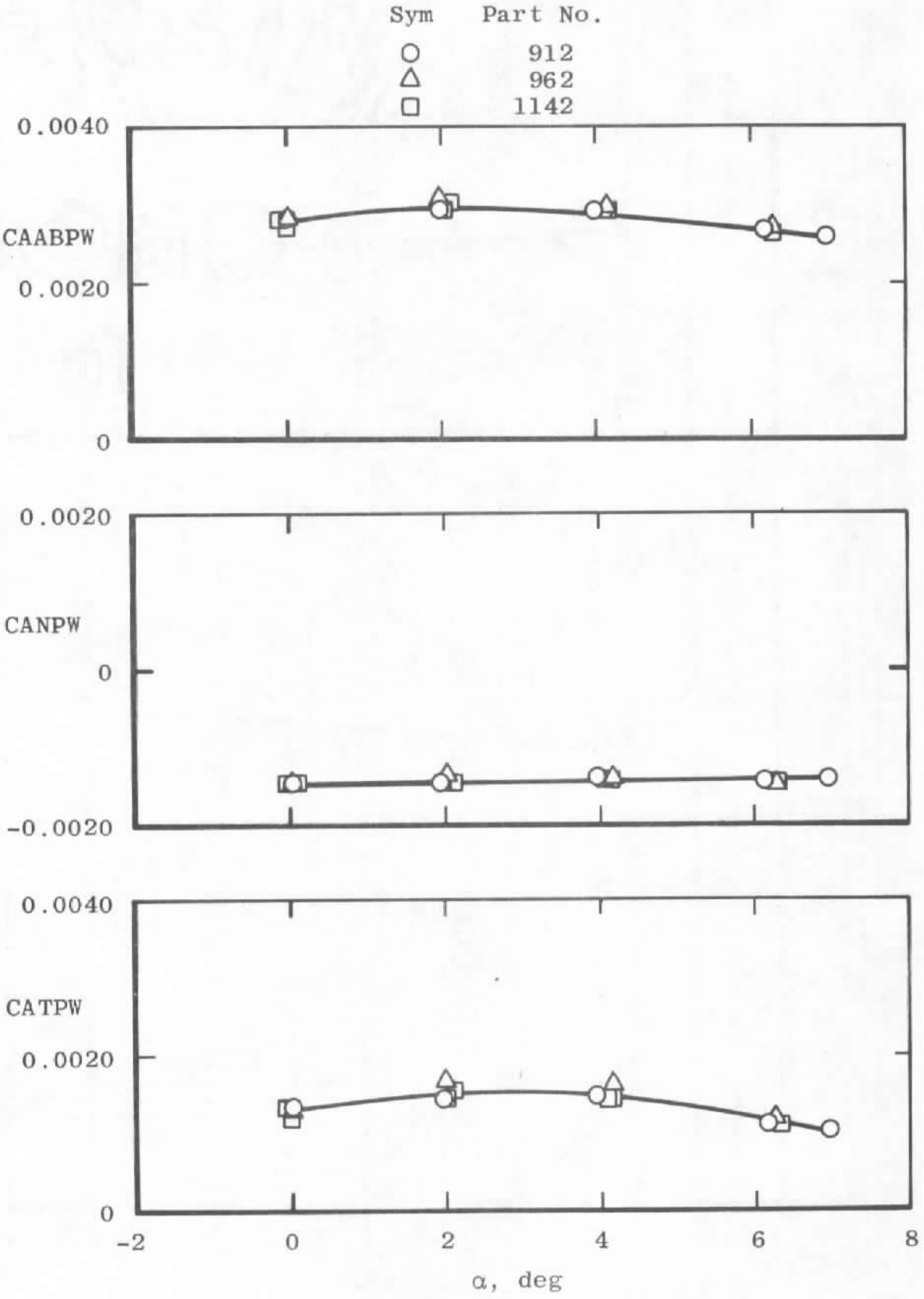

b. A8 = 200 in.^{2}, M = 0.9
Figure 16. Continued.

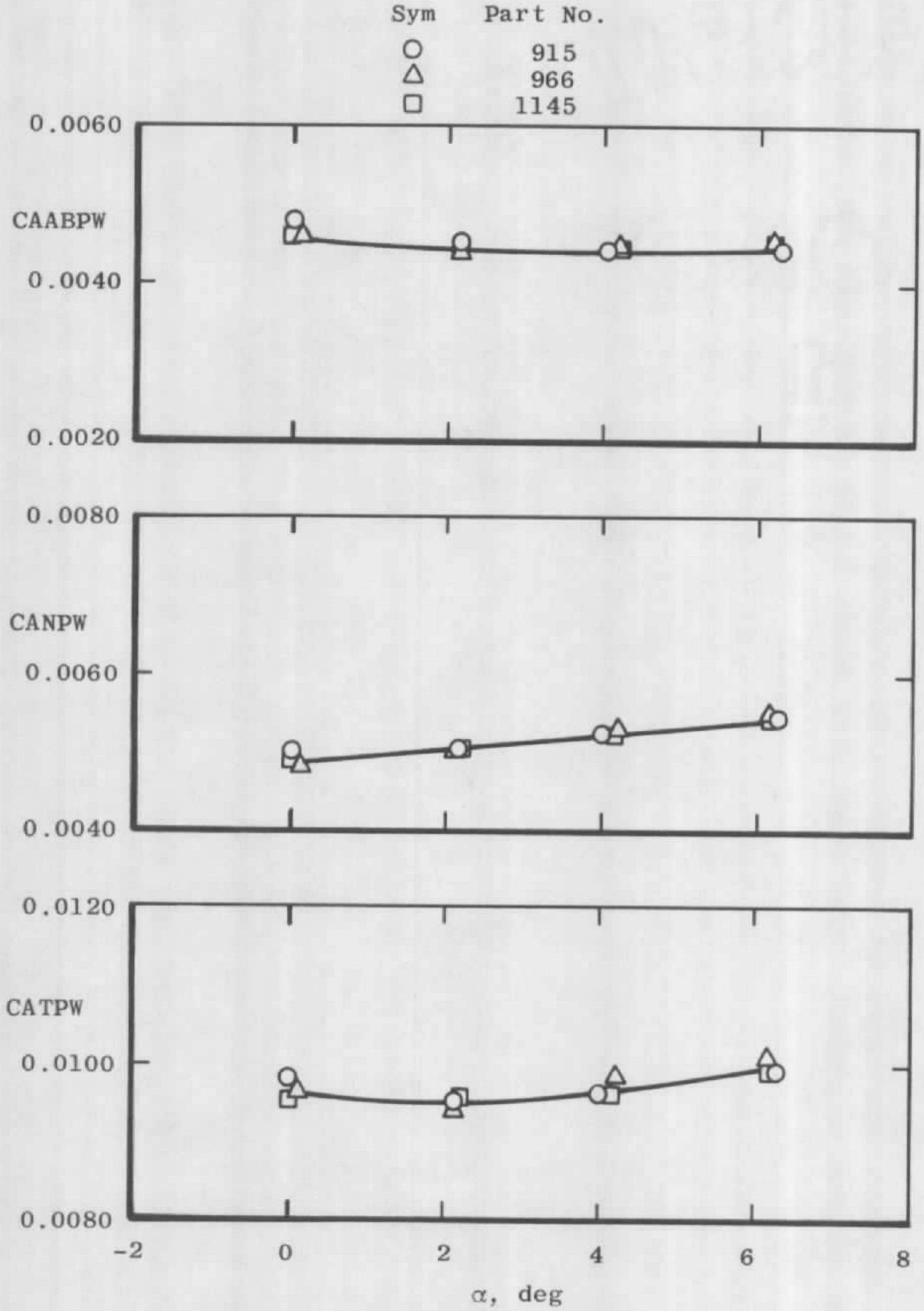

c. A8 = 200 in.², M = 1.2
Figure 16. Continued.

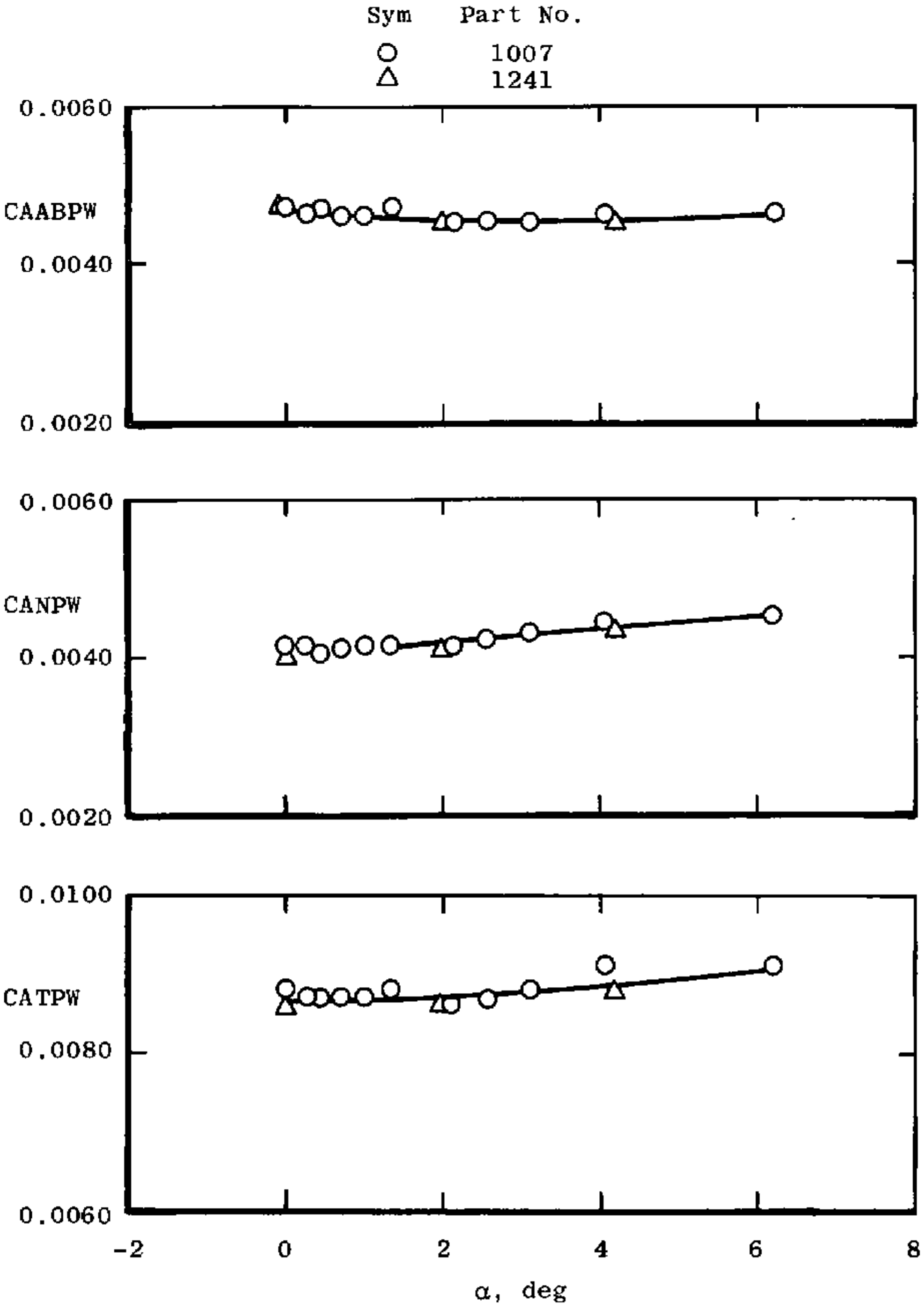

d. A8 = 300 in.², M = 1.2
Figure 16. Continued.

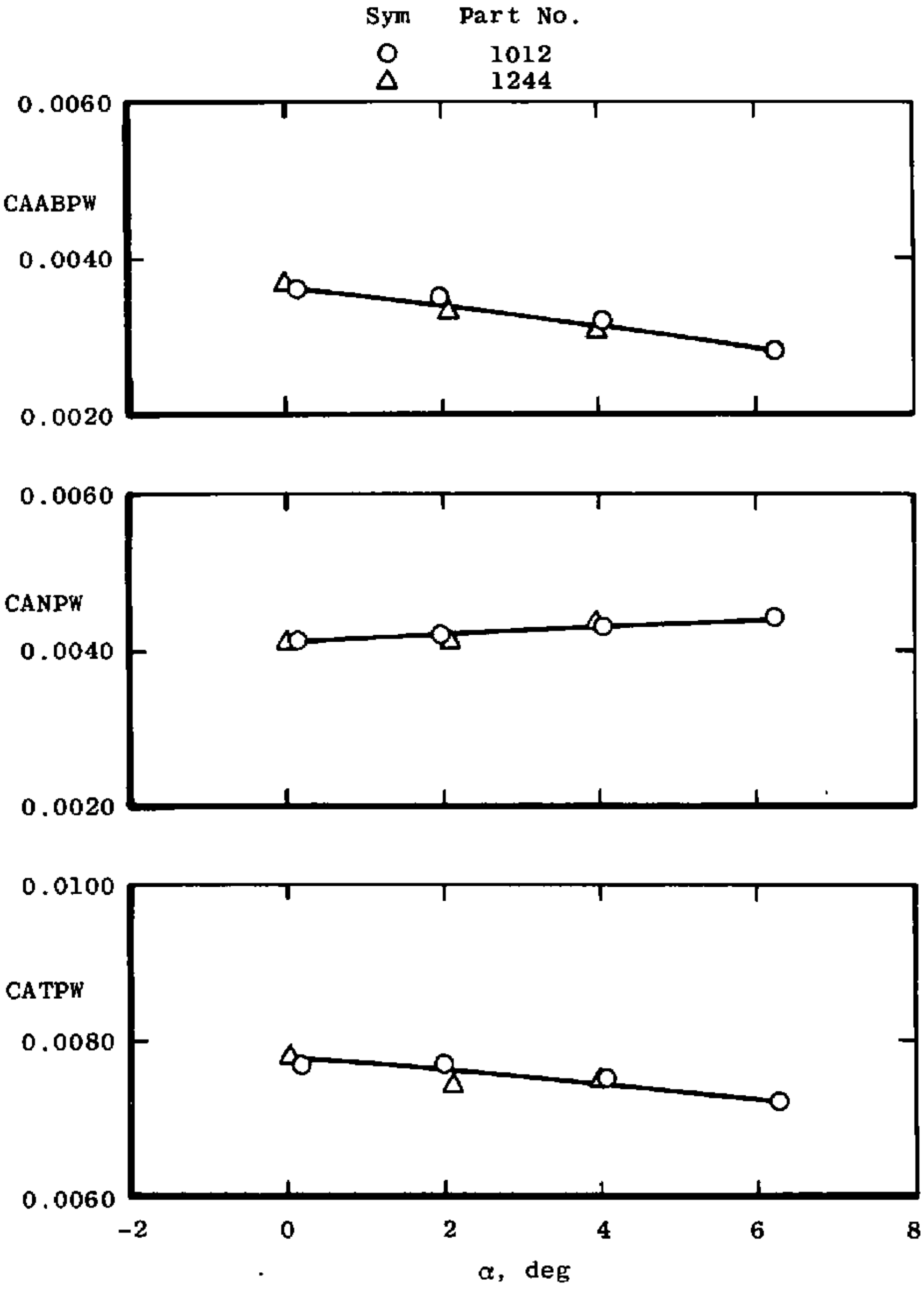

e. A8 = 300 in.^{2}, M = 1.5
Figure 16. Concluded.

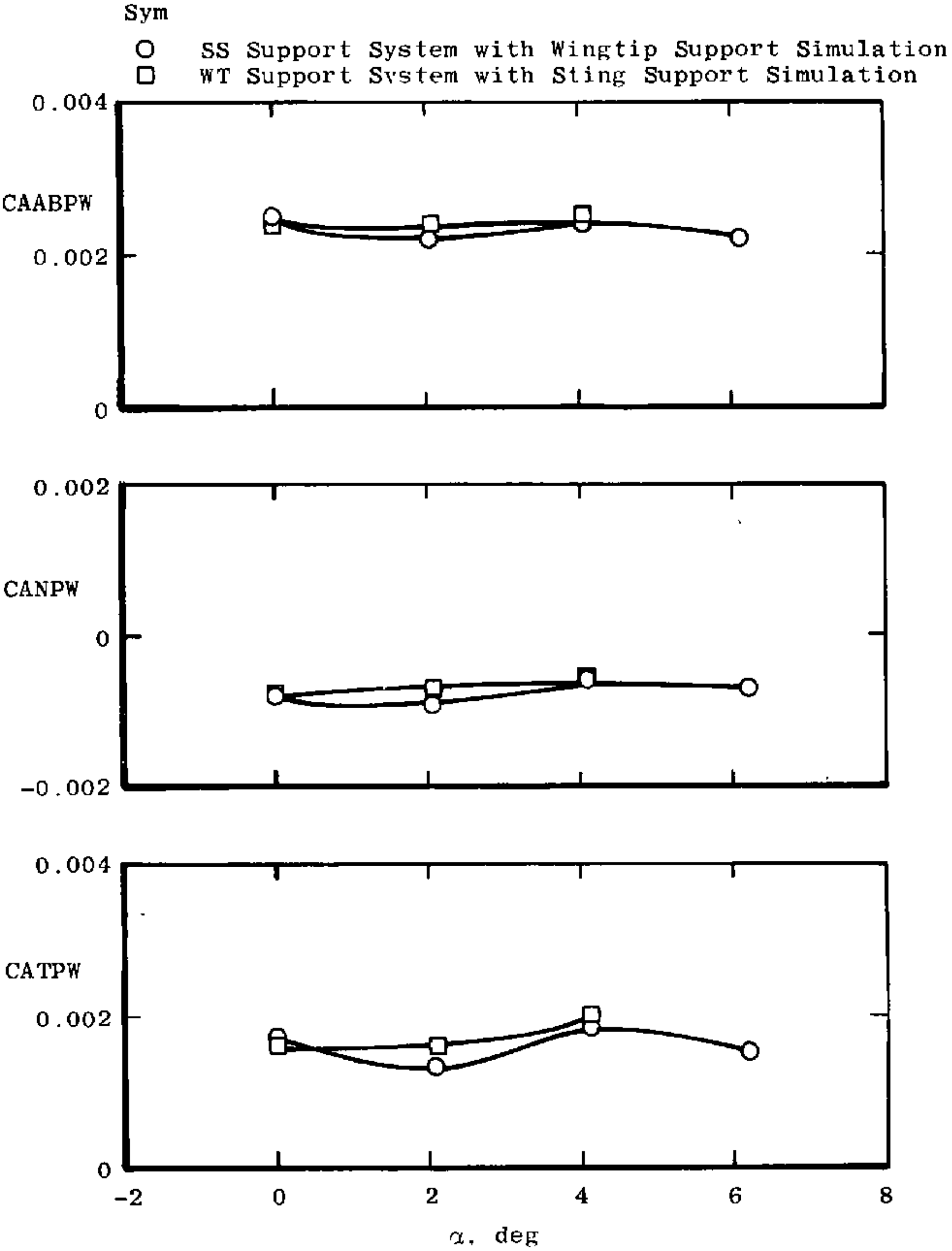

a. M = 0.6, NPRE = 1.0, A8 = 200 in.^{2}

Figure 17. Effect of support system simulation on axial force coefficients.

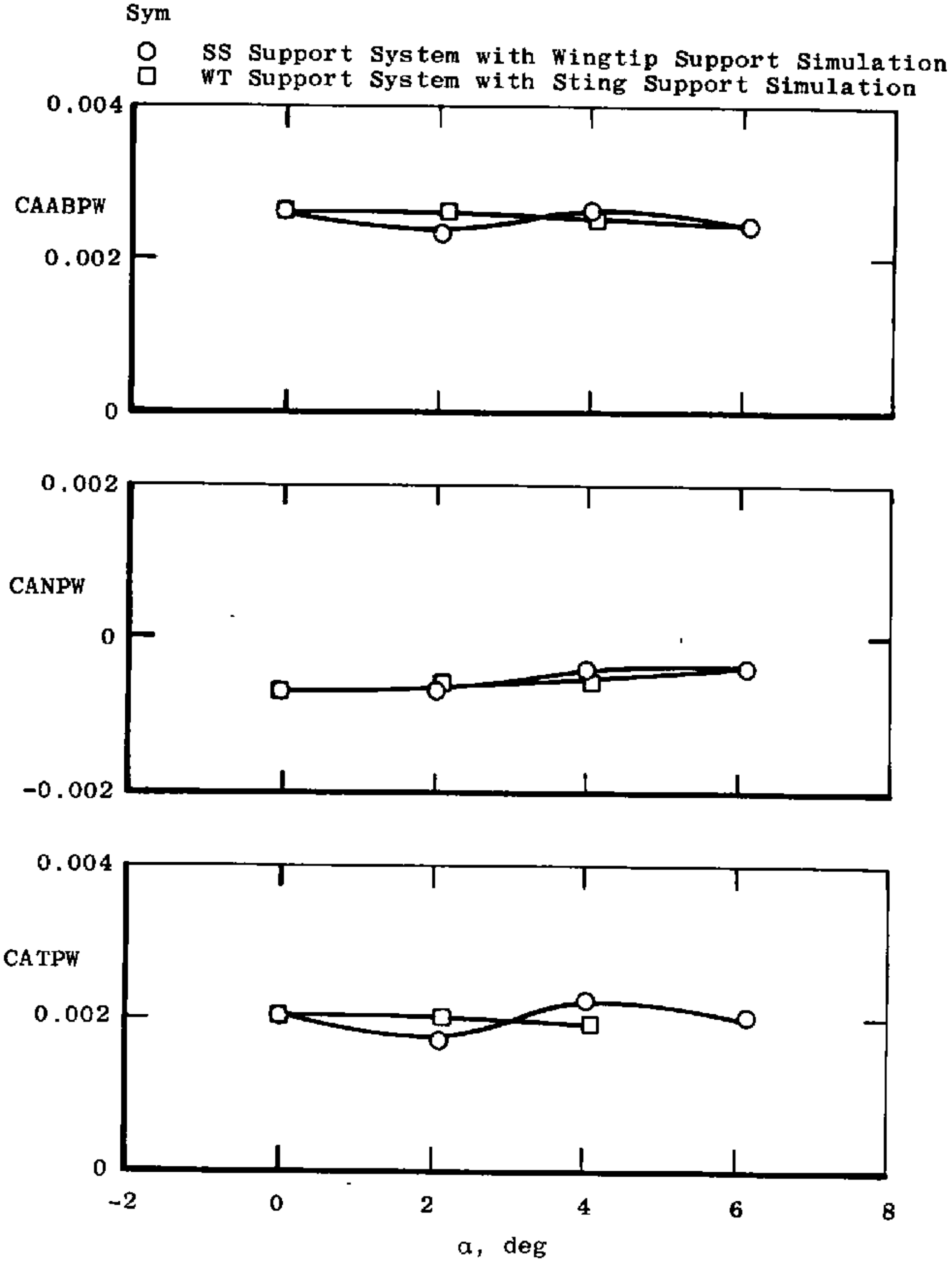

b. M = 0.6, NPRE = 3.4, A8 = 200 in.^{2}
Figure 17. Continued.

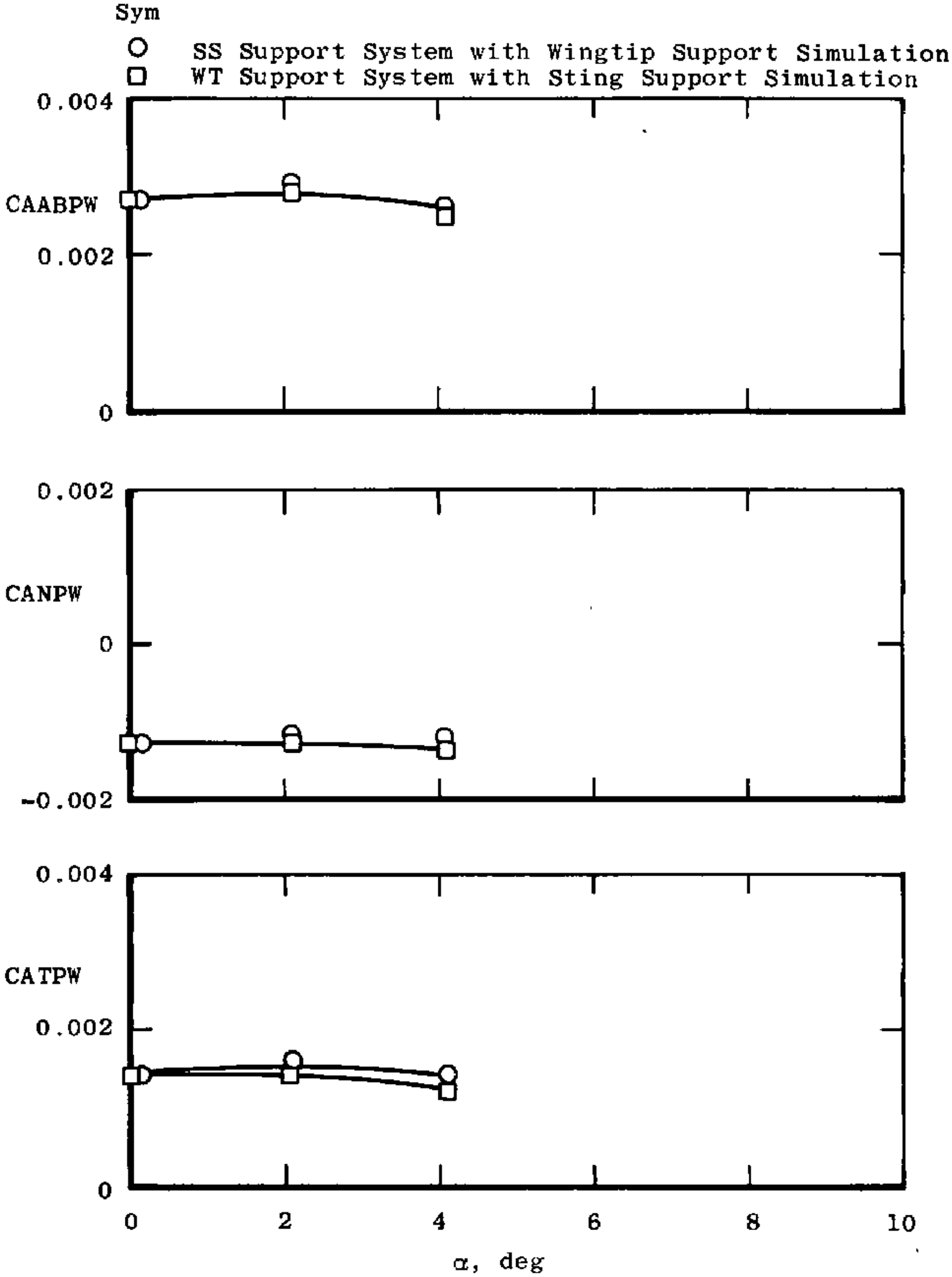

c. M = 0.9, NPRE = 1.0, A8 = 200 in.^{2}
Figure 17. Continued.

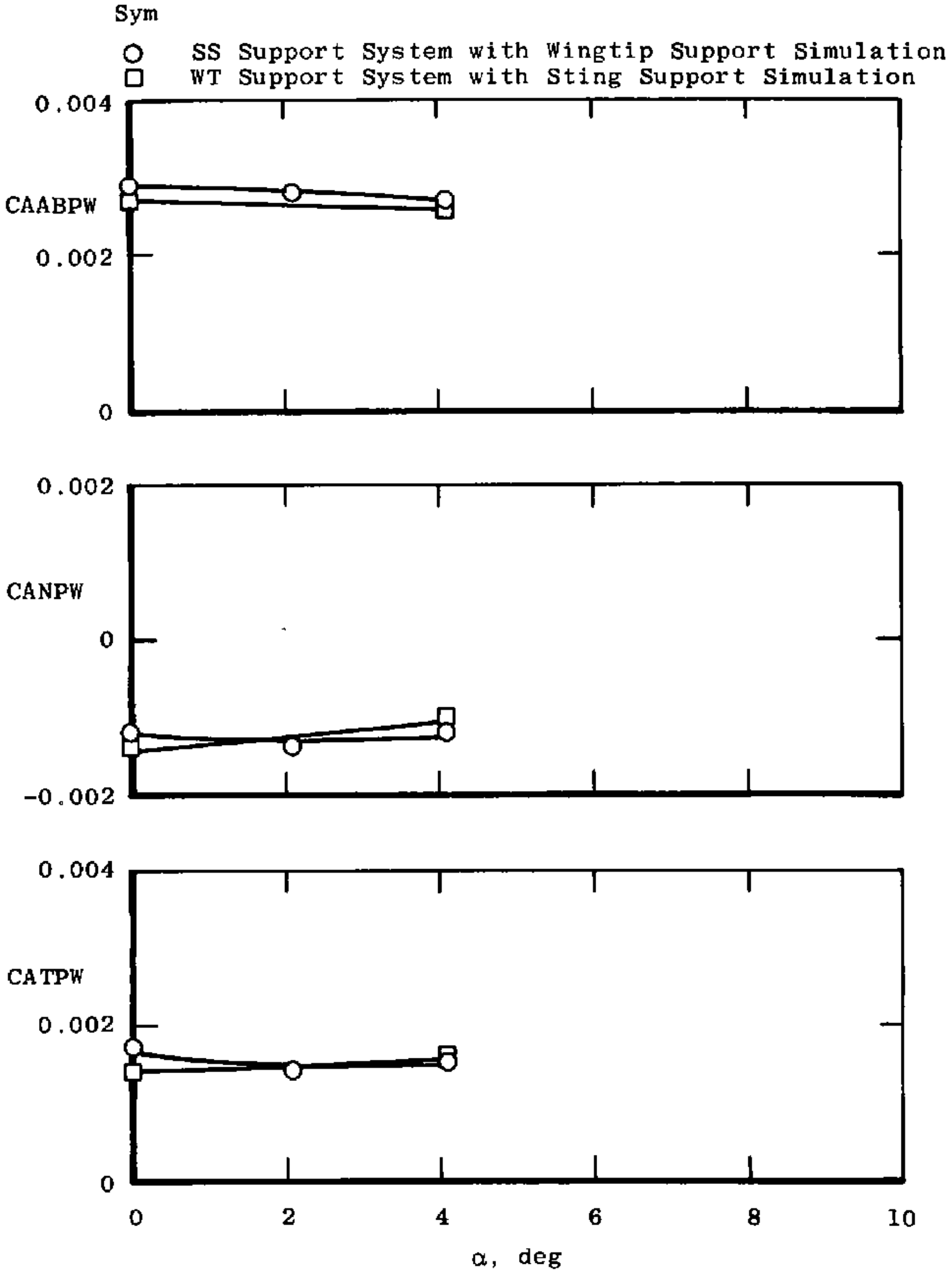

d. M = 0.9, NPRE = 3.4, A8 = 200 in.^{2}
Figure 17. Continued.

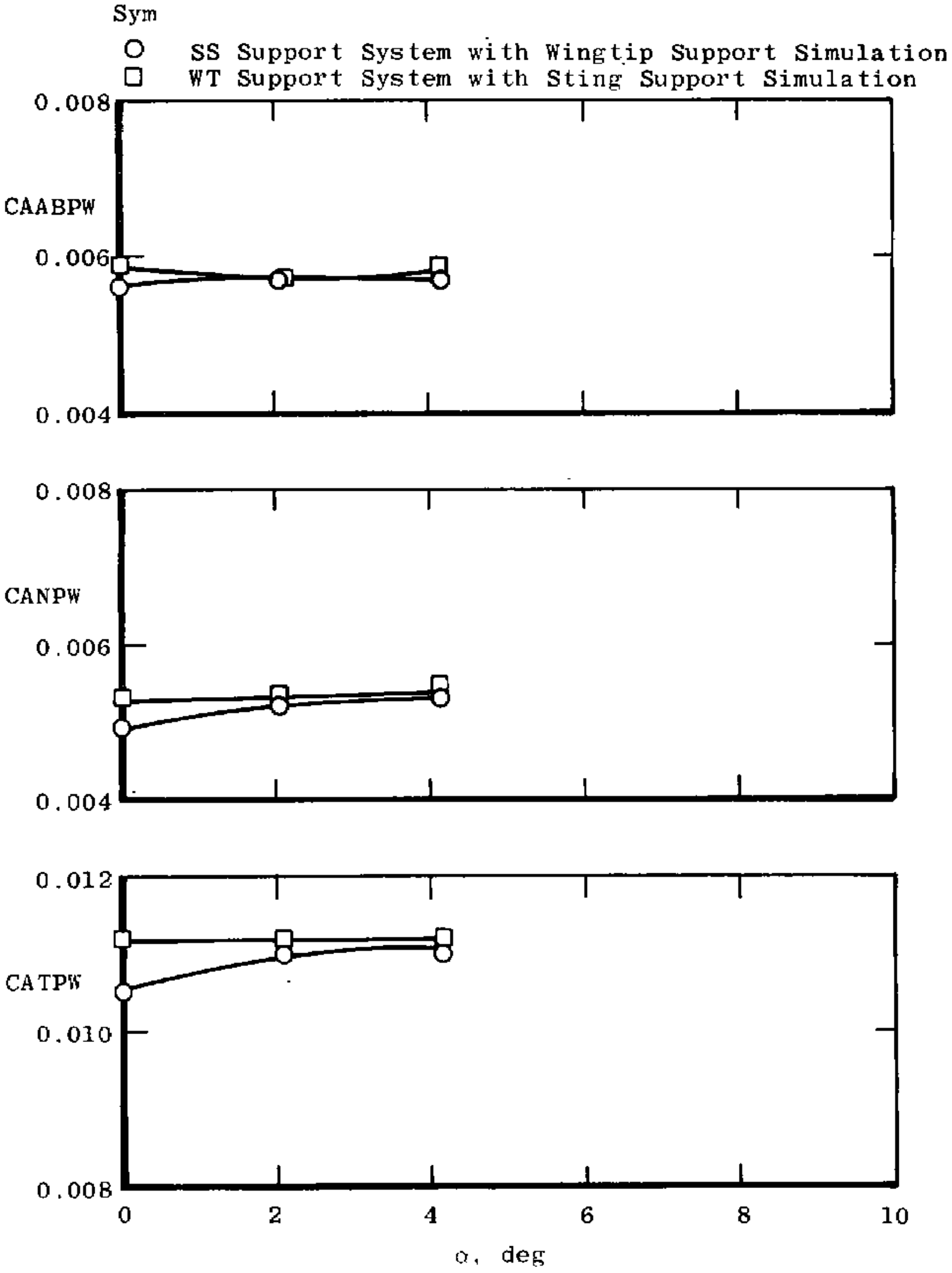

e. M = 1.2, NPRE = 1.0, A8 = 200 in.^{2}
Figure 17. Continued.

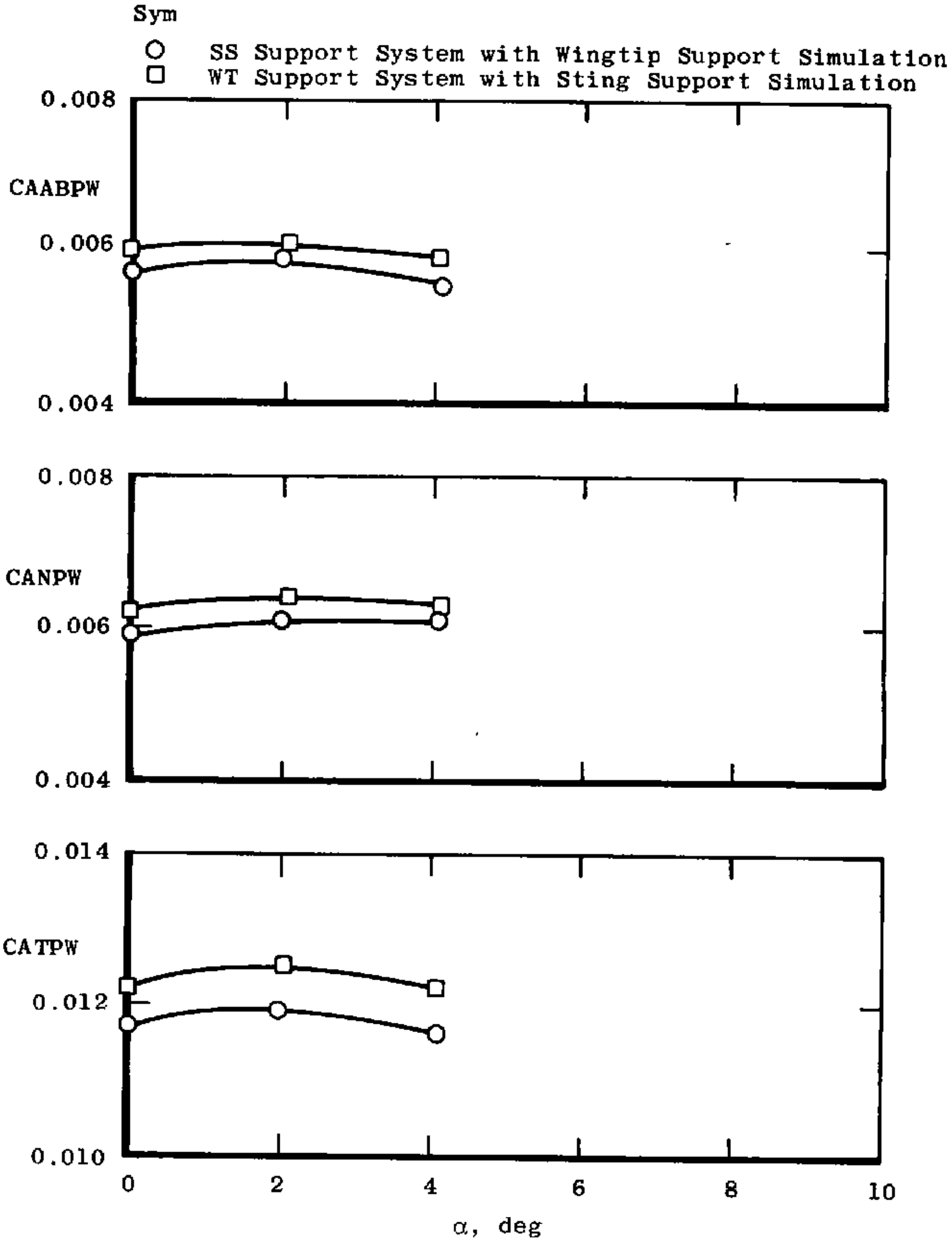

f. M = 1.2, NPRE = 3.4, A8 = 200 in.^{2}
Figure 17. Continued.

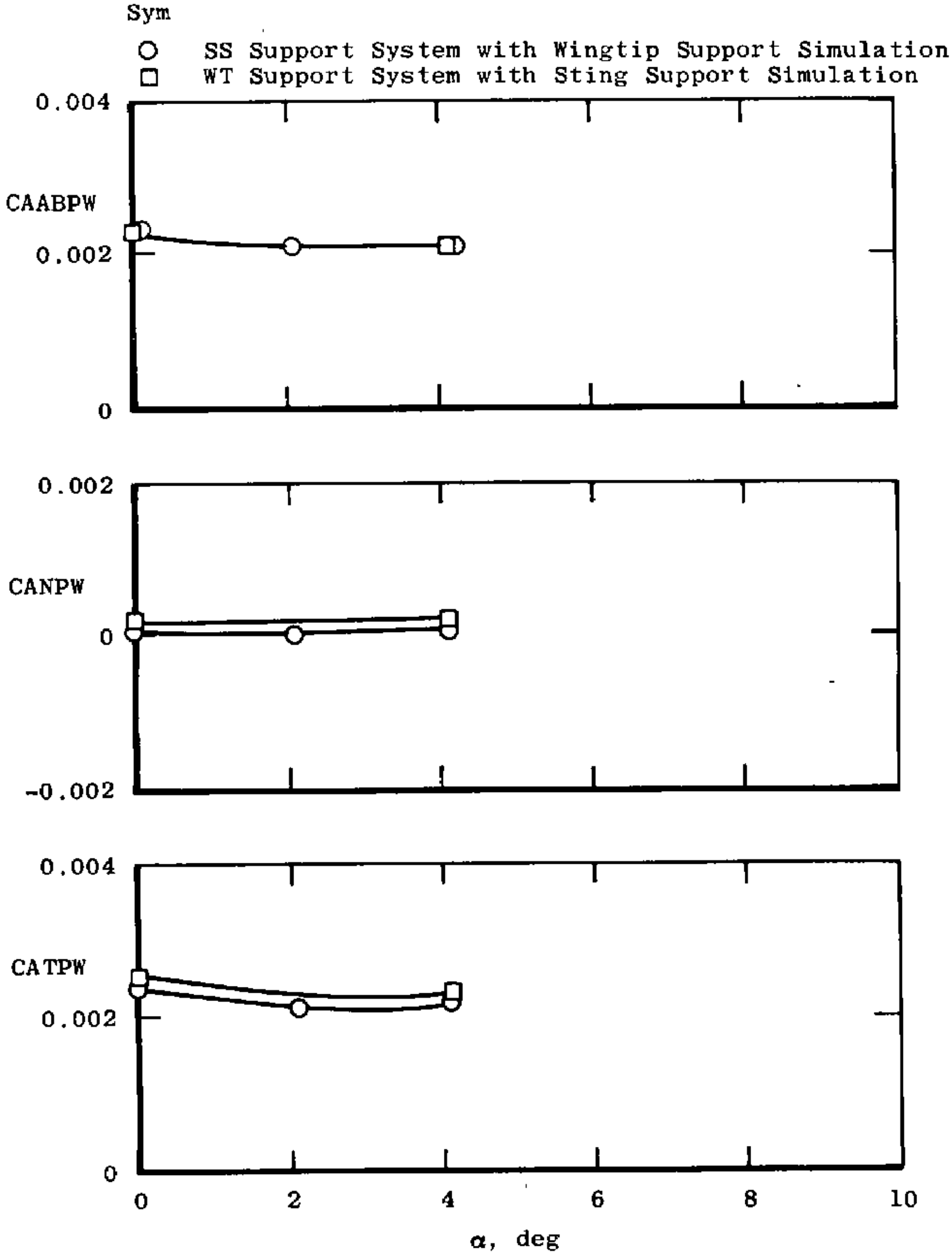

g. M = 0.6, NPRE = 1.0, A8 = 300 in.^{2}
Figure 17. Continued.

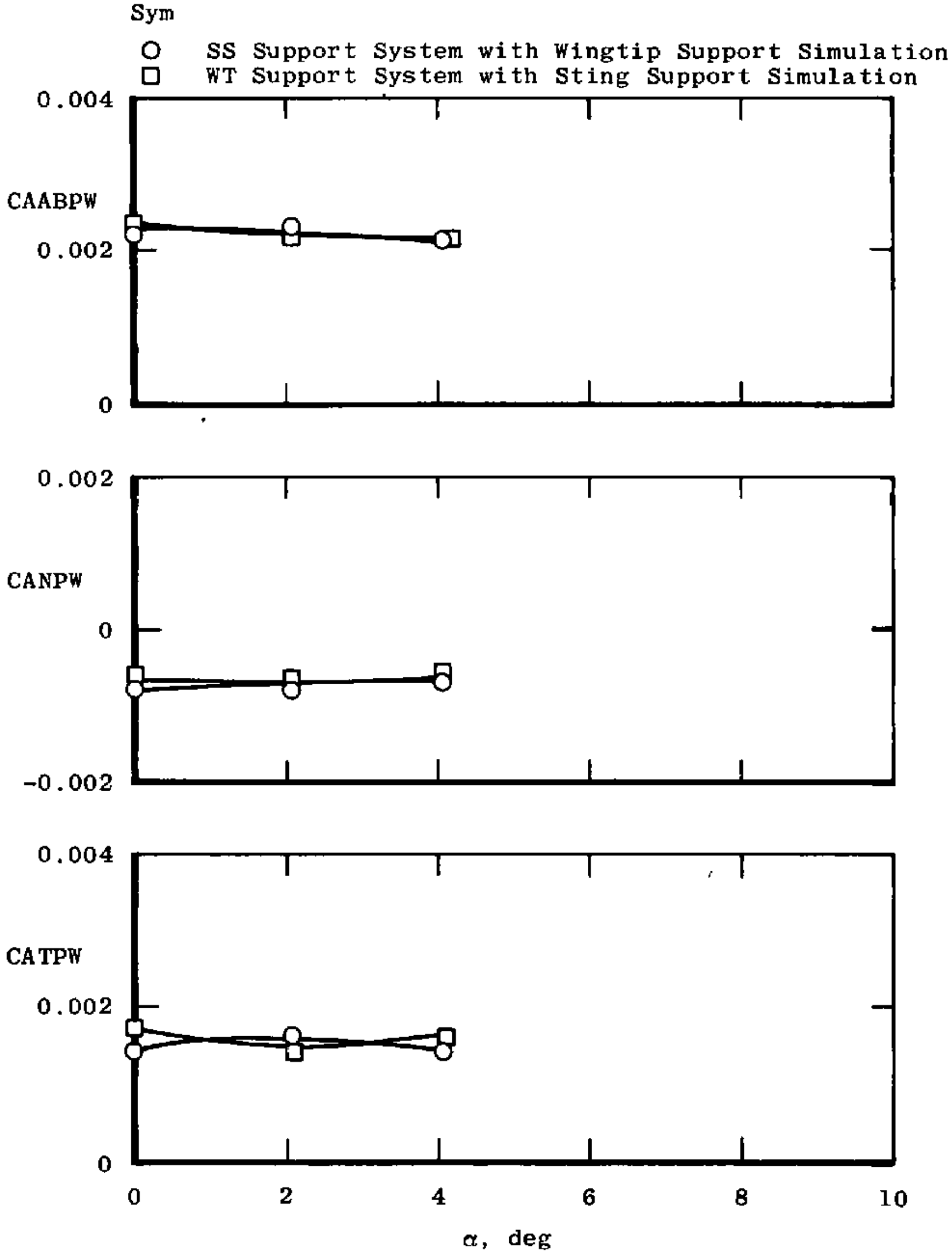

h. M = 0.6, NPRE = 3.4, A8 = 300 in.²
Figure 17. Continued.

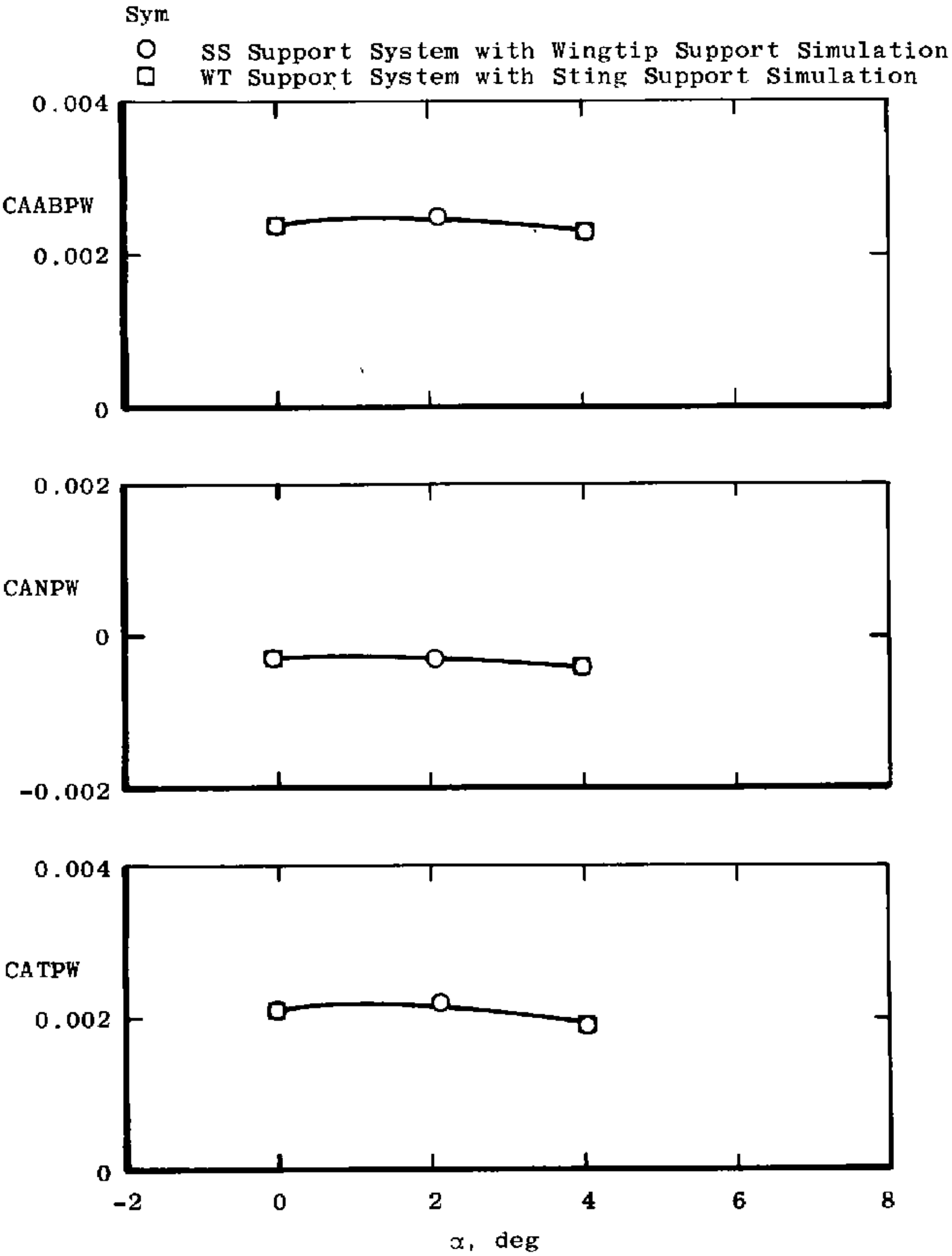

i. M = 0.9, NPRE = 1.0, A8 = 300 in.²
Figure 17. Continued.

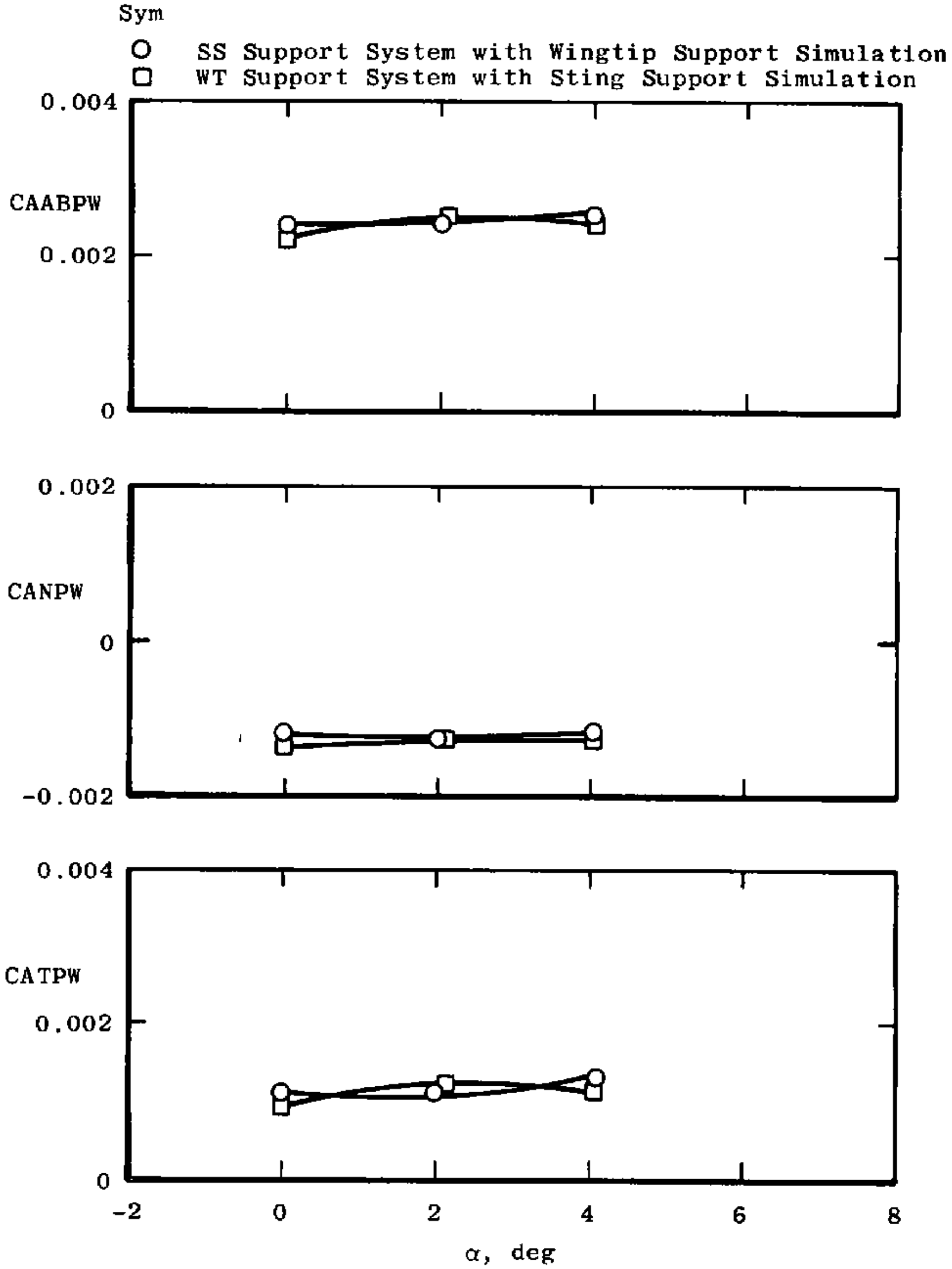

j. M = 0.9, NPRE = 5.0, A8 = 300 in.^{2}
Figure 17. Continued.

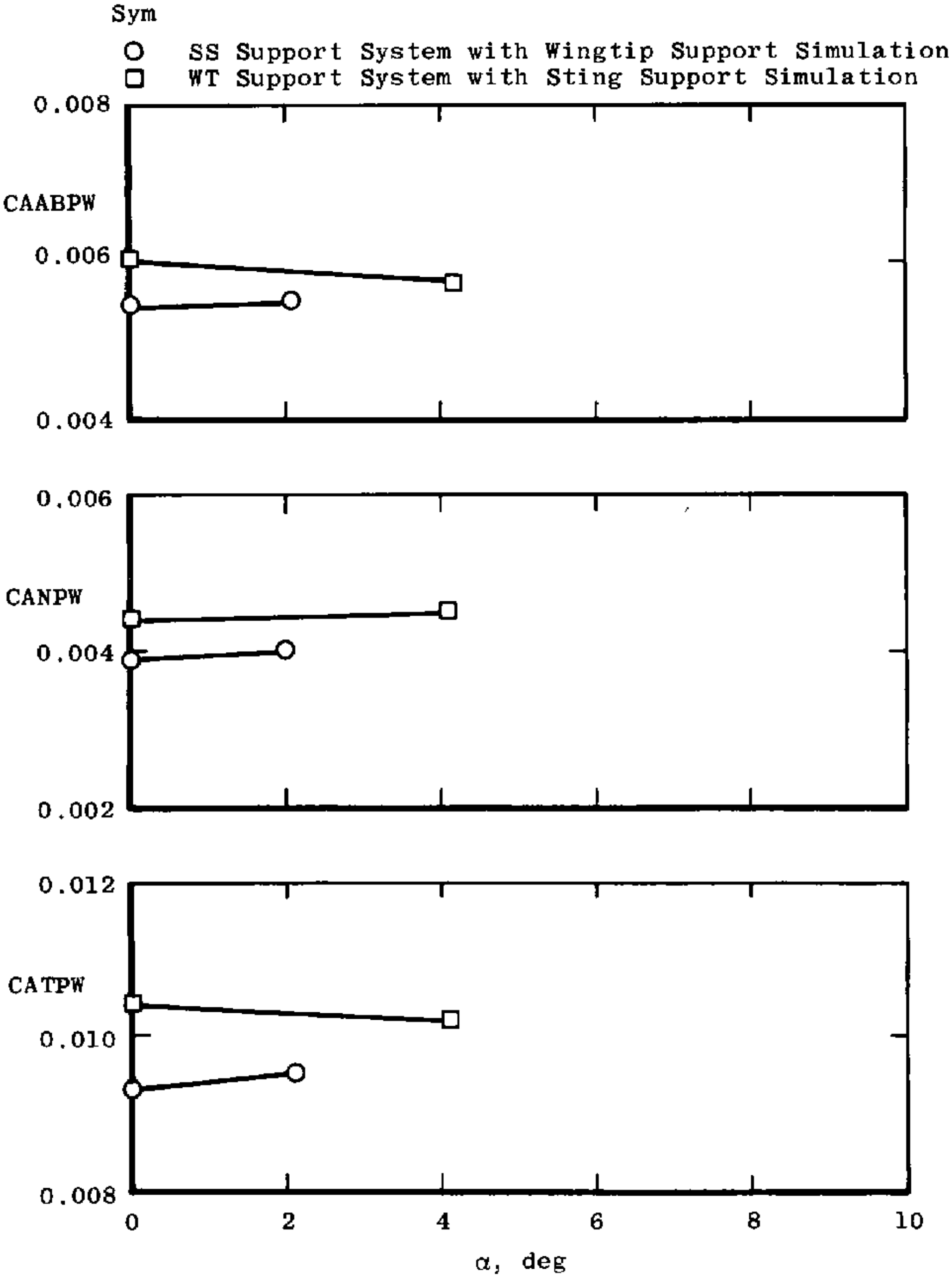

k. M = 1.2, NPRE = 1.0, A8 = 300 in.^{2}
Figure 17. Continued.

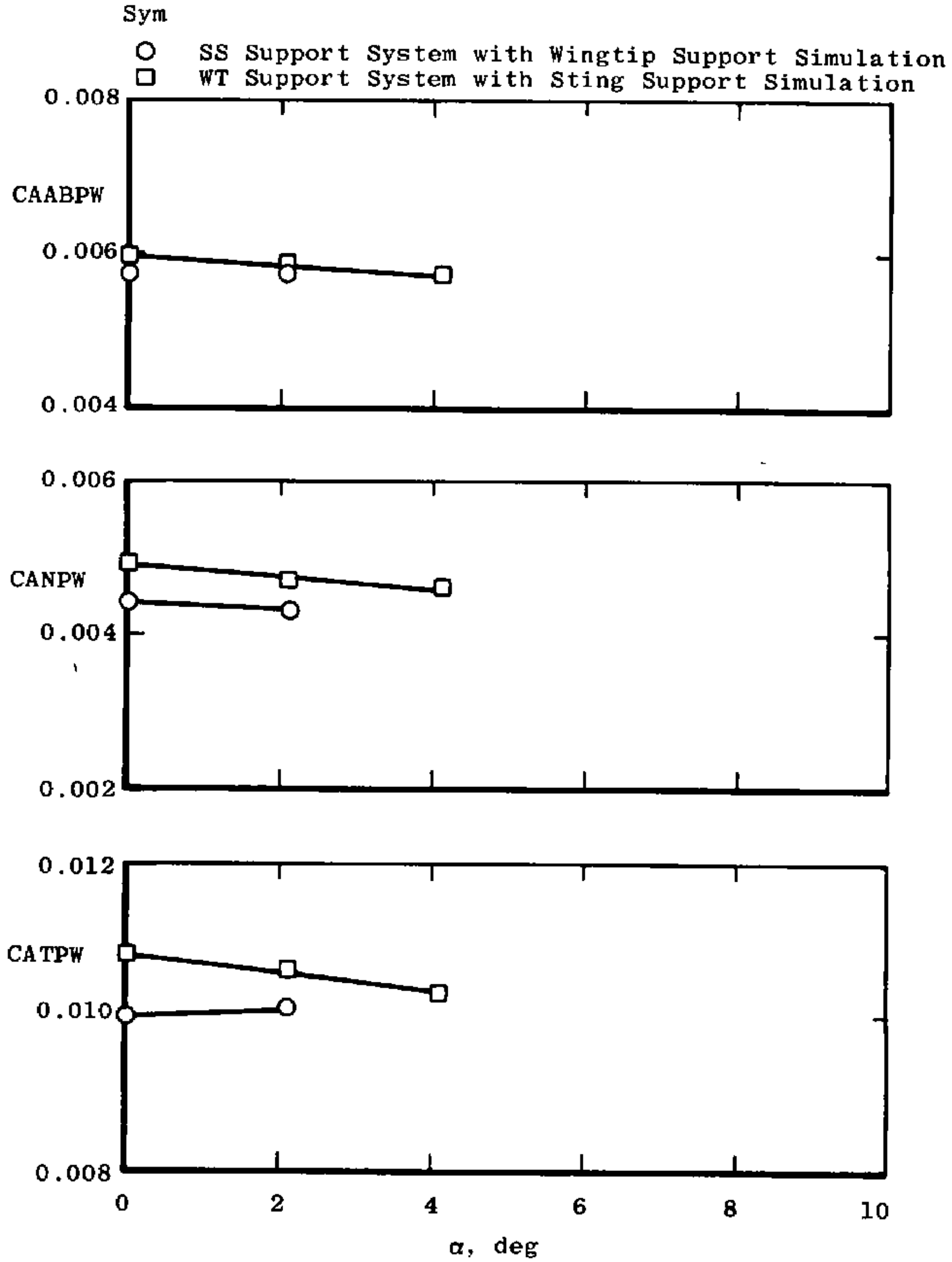

l. M = 1.2, NPRE = 5.0, A8 = 300 in.^{2}
Figure 17. Concluded.

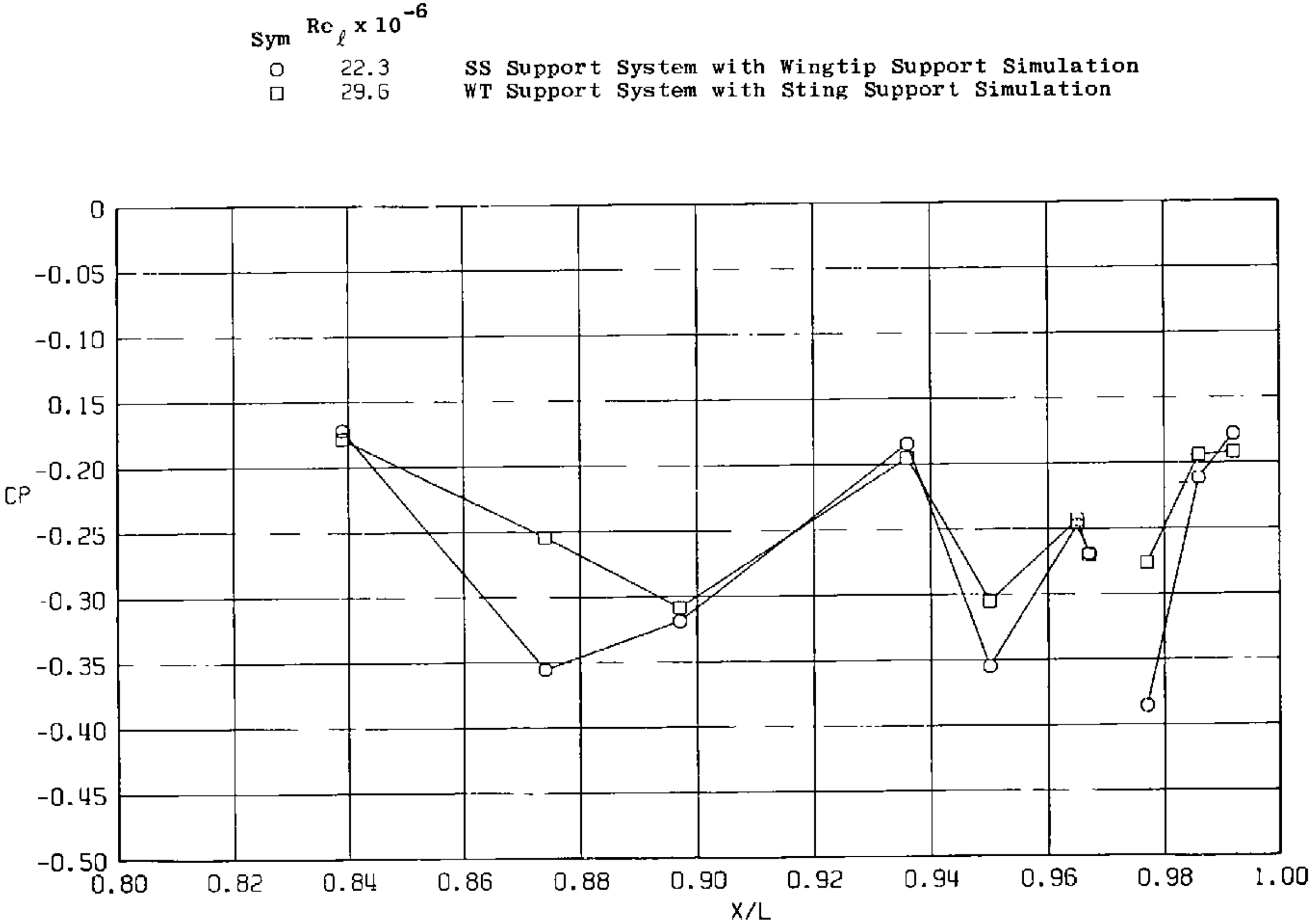

a. $\phi = 0$

Figure 18. Effect of support system simulation on surface pressure coefficients, A8 = 200 in.^{2}, M = 1.2, α = 4.1 deg, NPRE = 3.4.

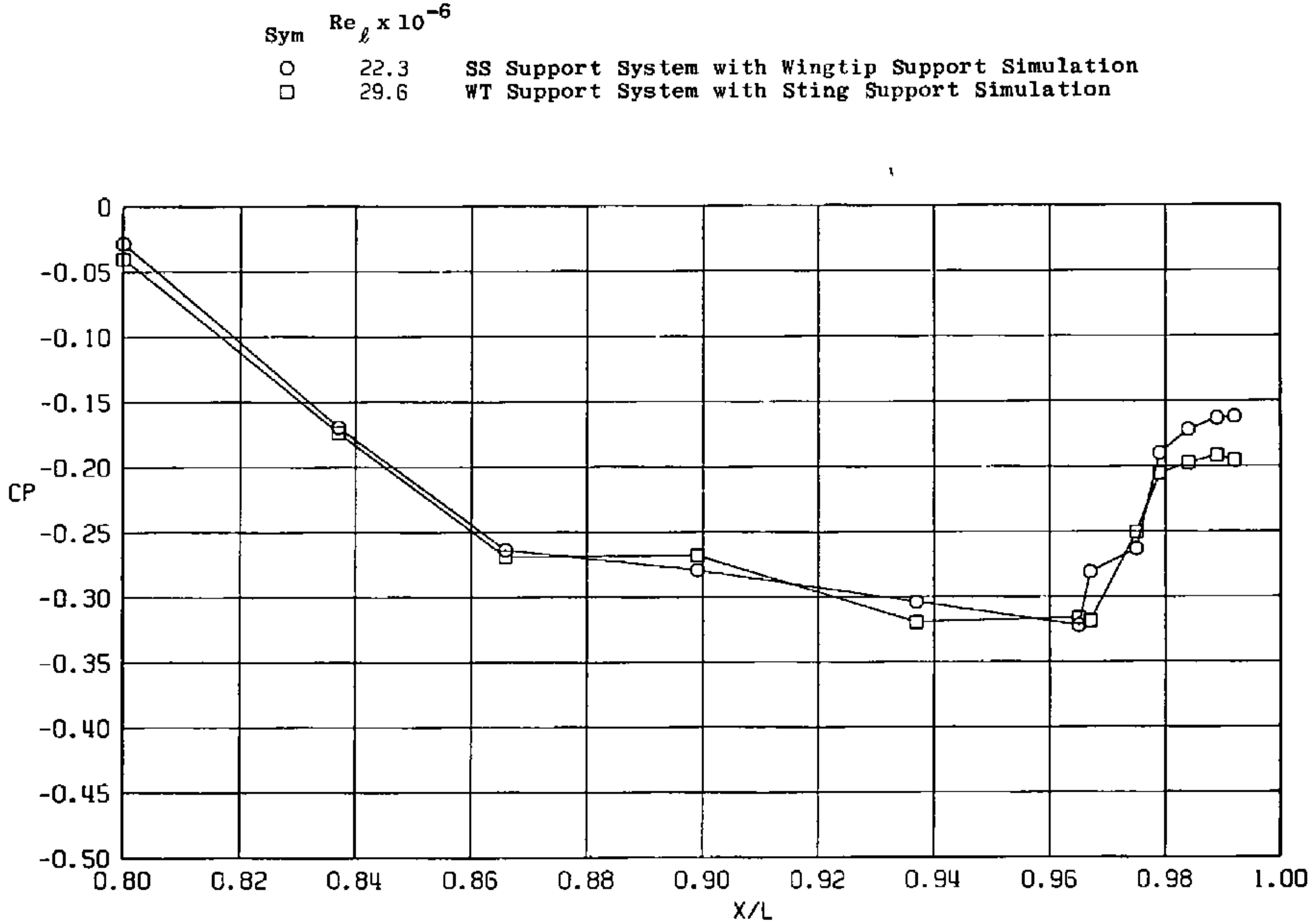

b. ϕ = 45 deg

Figure 18. Continued.

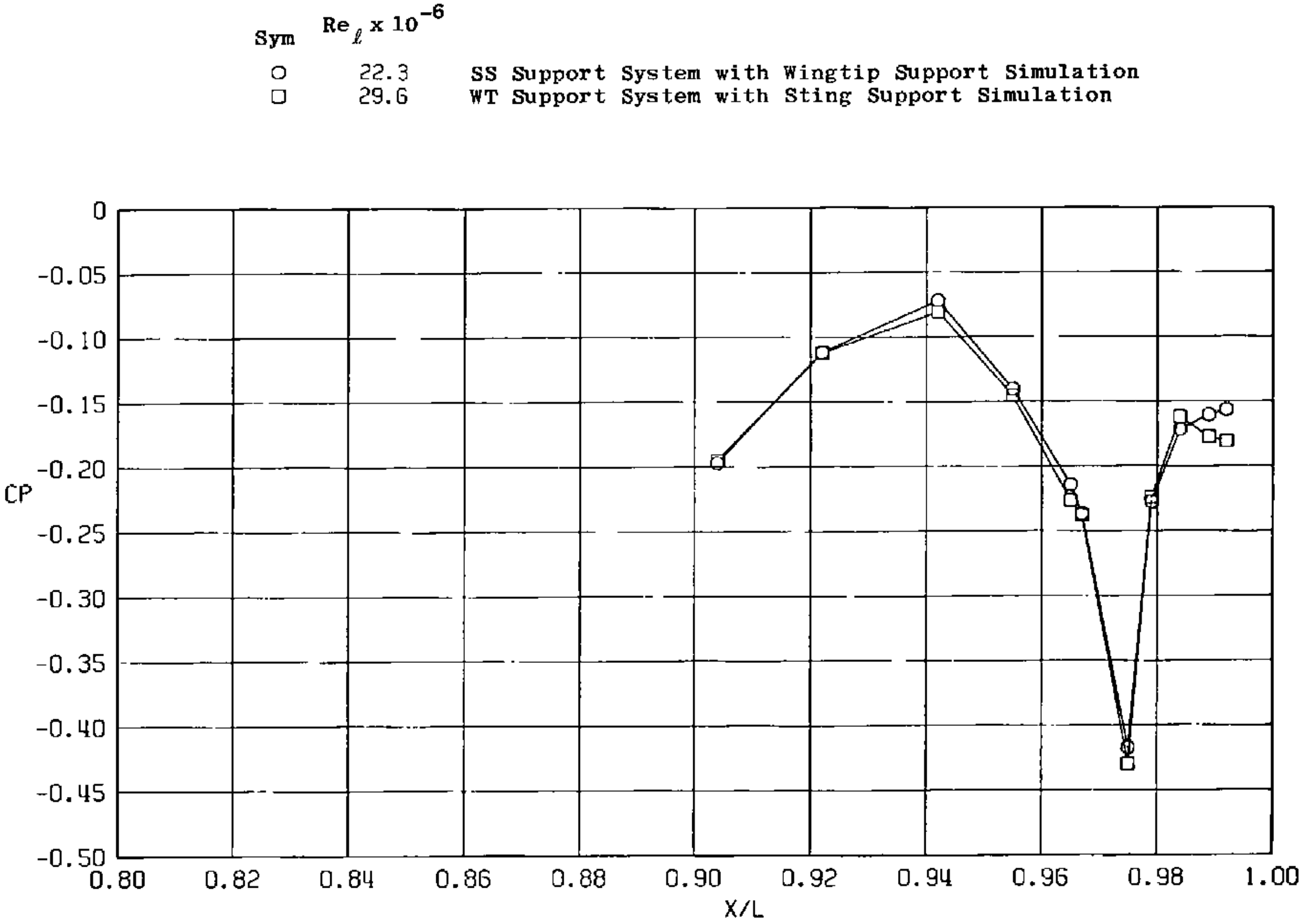

c. ϕ = 135 deg
Figure 18. Continued.

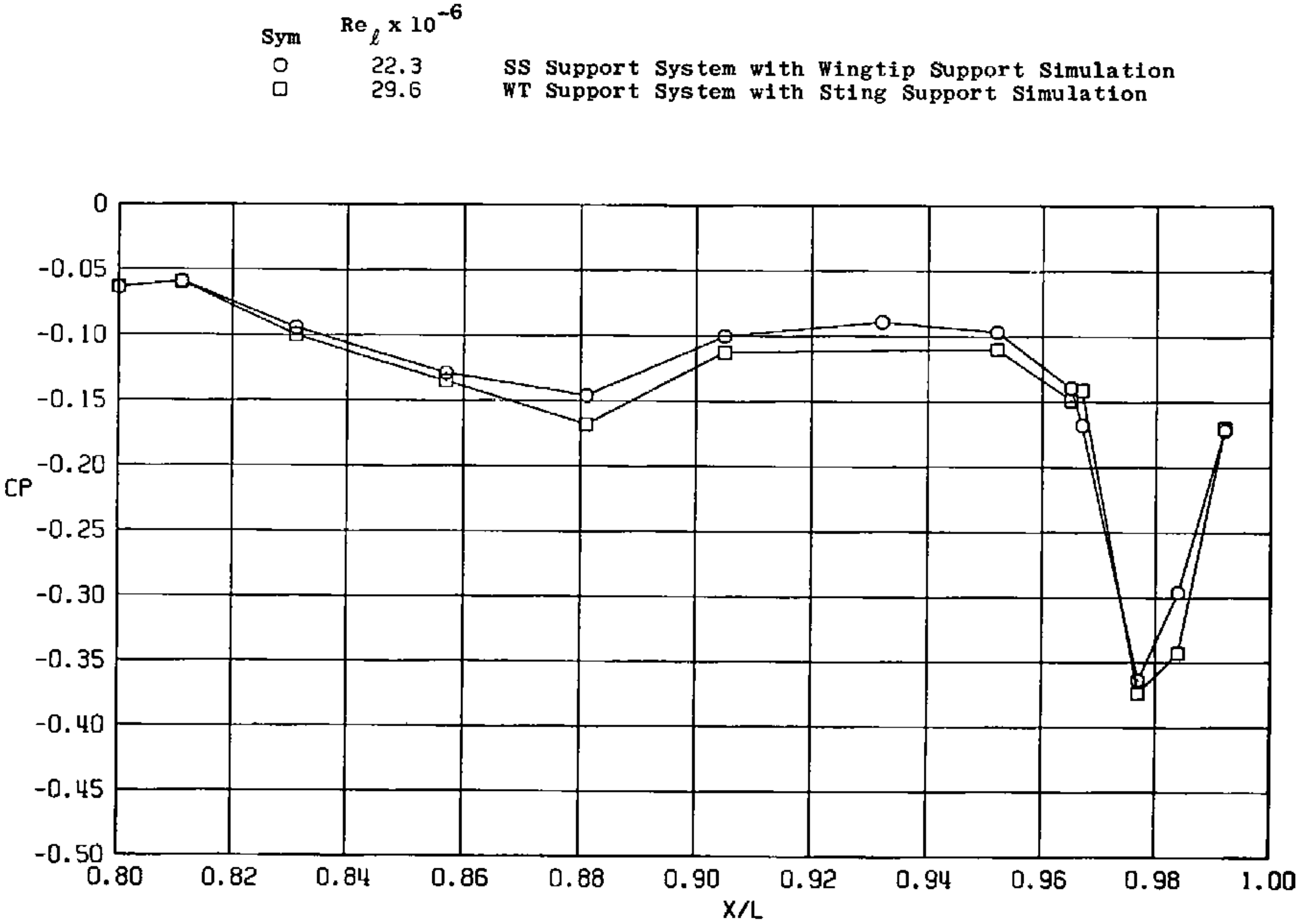

d. ϕ = 180 deg
Figure 18. Continued.

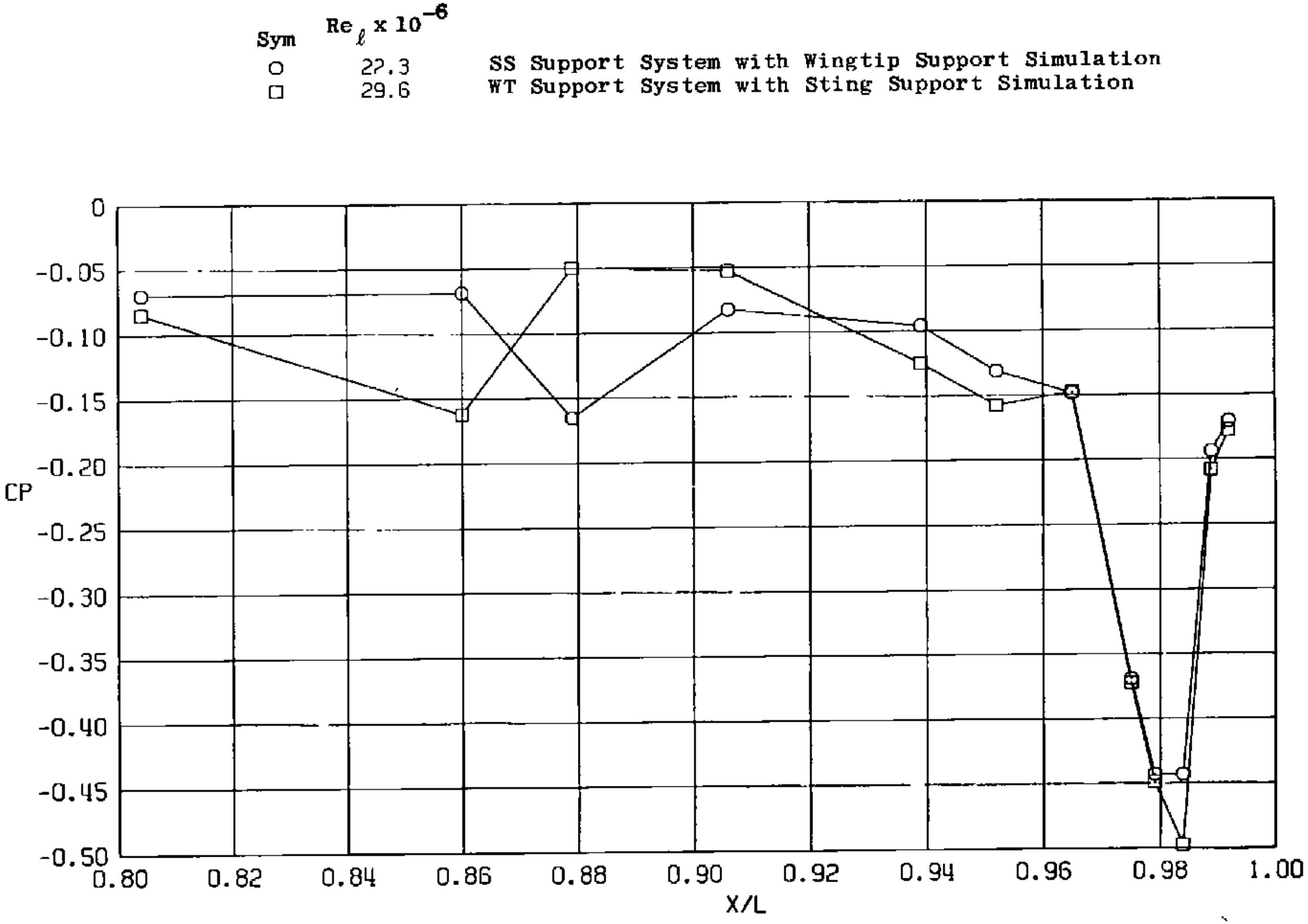

e. ϕ = 225 deg

Figure 18. Continued.

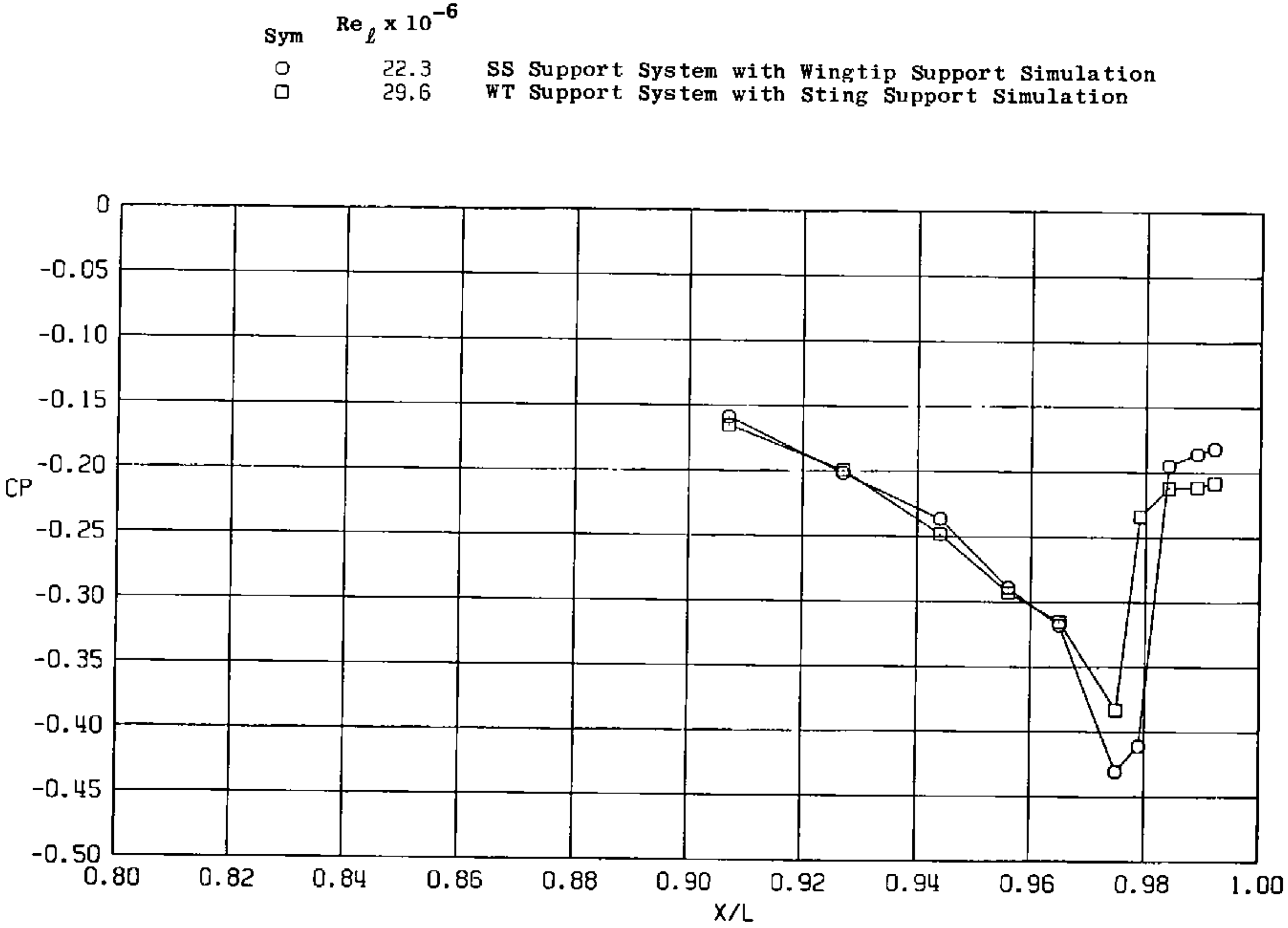

f. ϕ = 315 deg

Figure 18. Concluded.

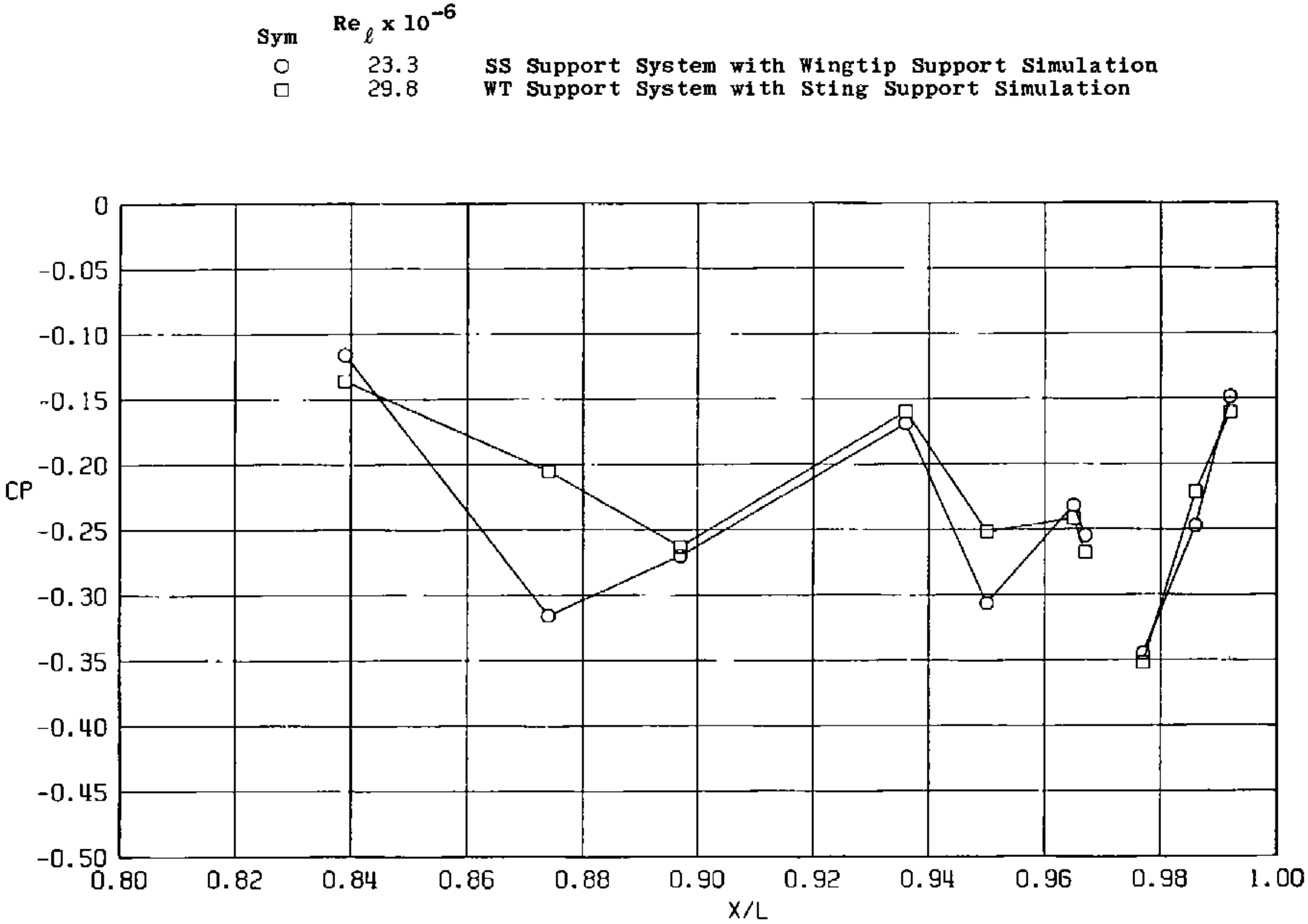

a. $\phi = 0$

Figure 19. Effect of support system simulation on surface pressure coefficients, A8 = 300 in.^{2}, M = 1.2, α = 4.1 deg, NPRE = 5.0.

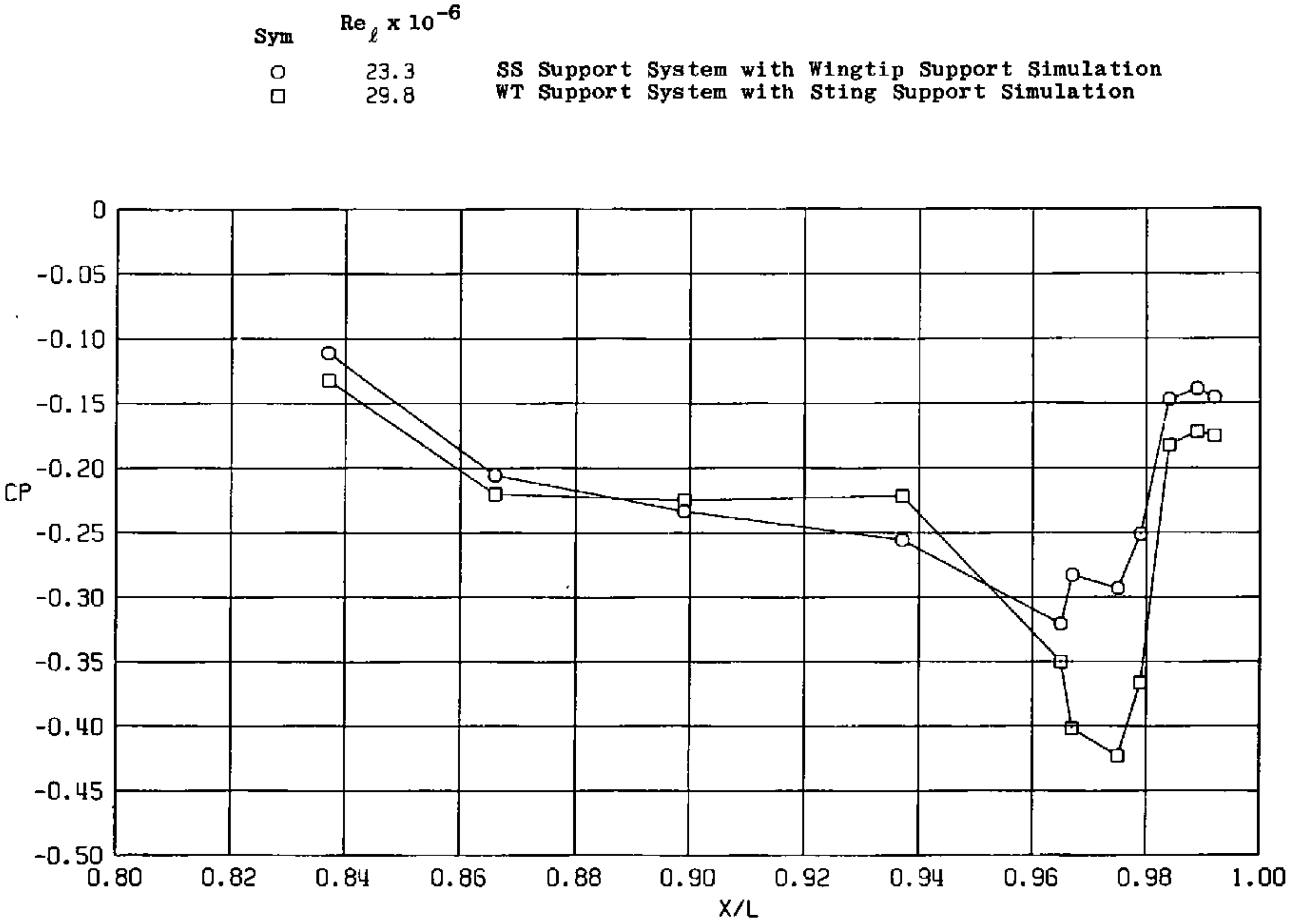

b. ϕ = 45 deg

Figure 19. Continued.

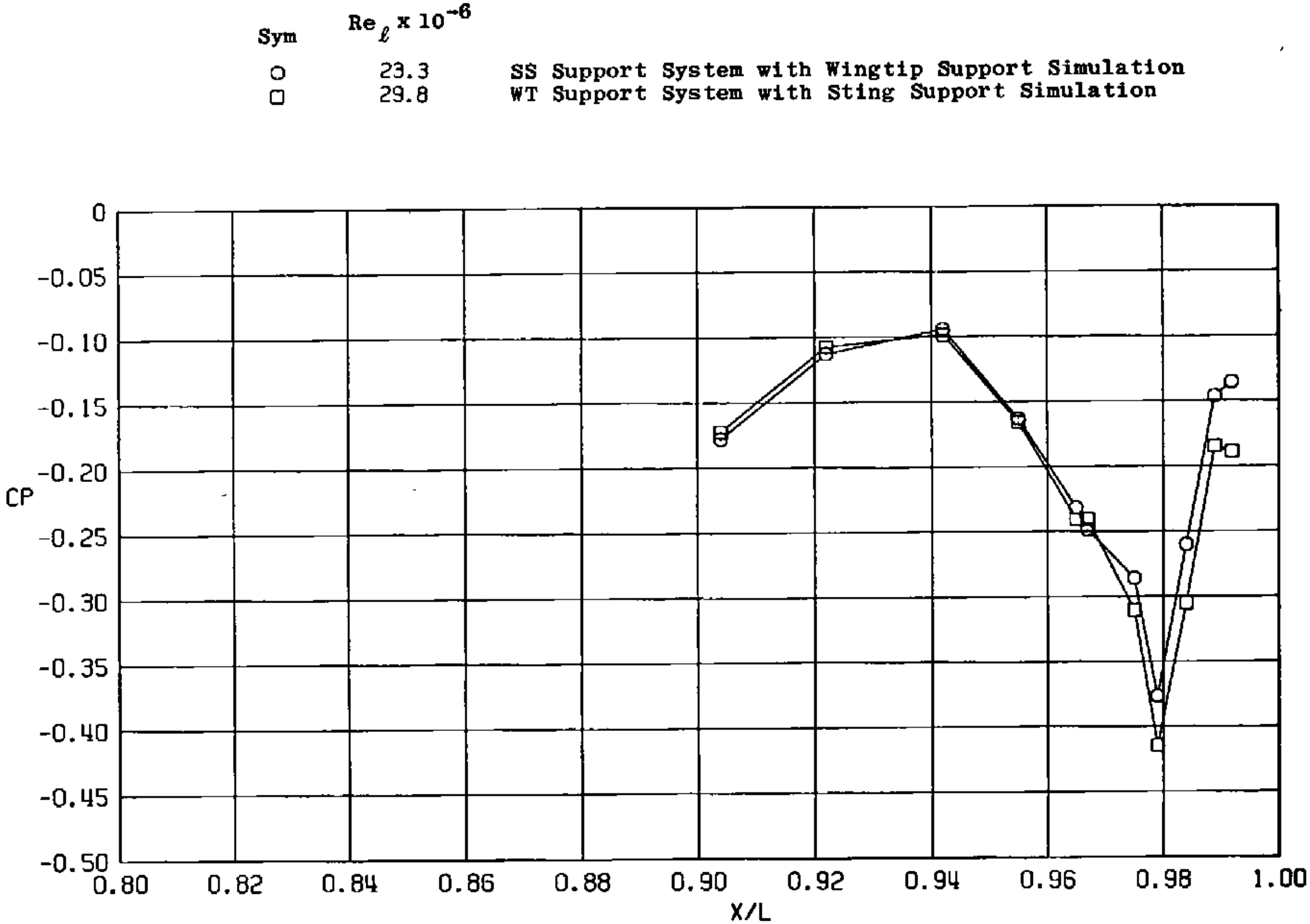

c. ϕ = 135 deg
Figure 19. Continued.

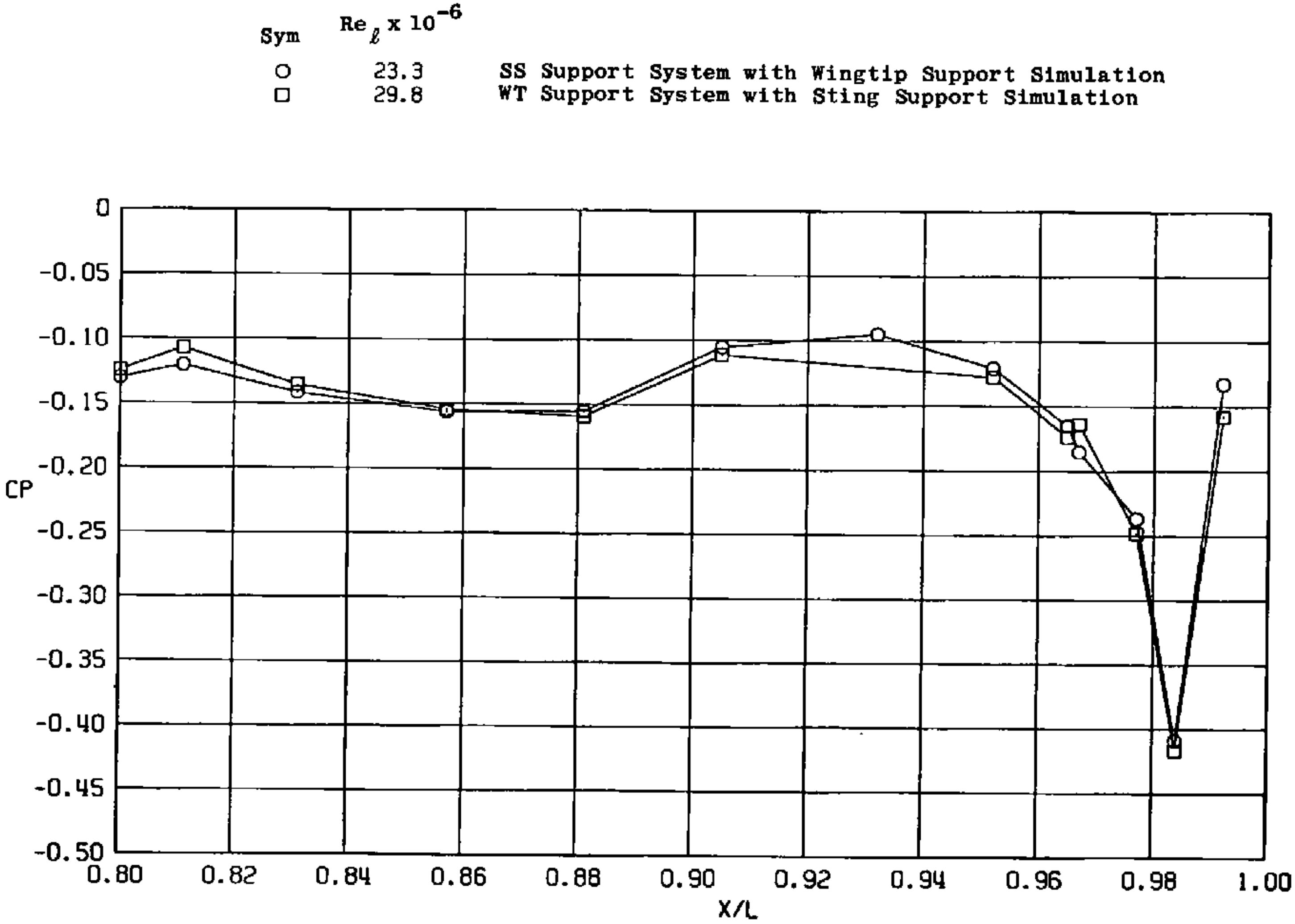

d. ϕ = 180 deg

Figure 19. Continued.

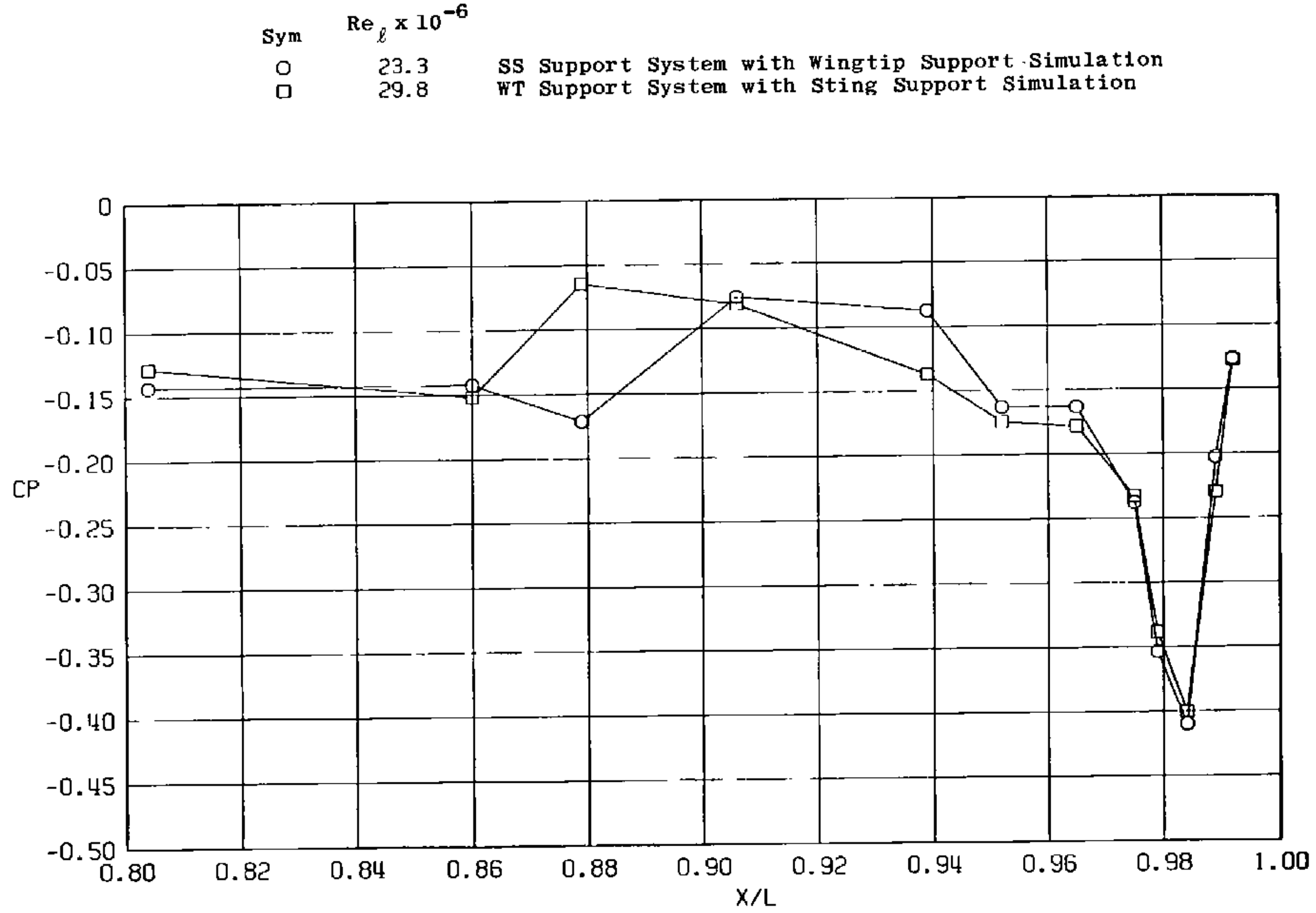

e. ϕ = 225 deg
Figure 19. Continued.

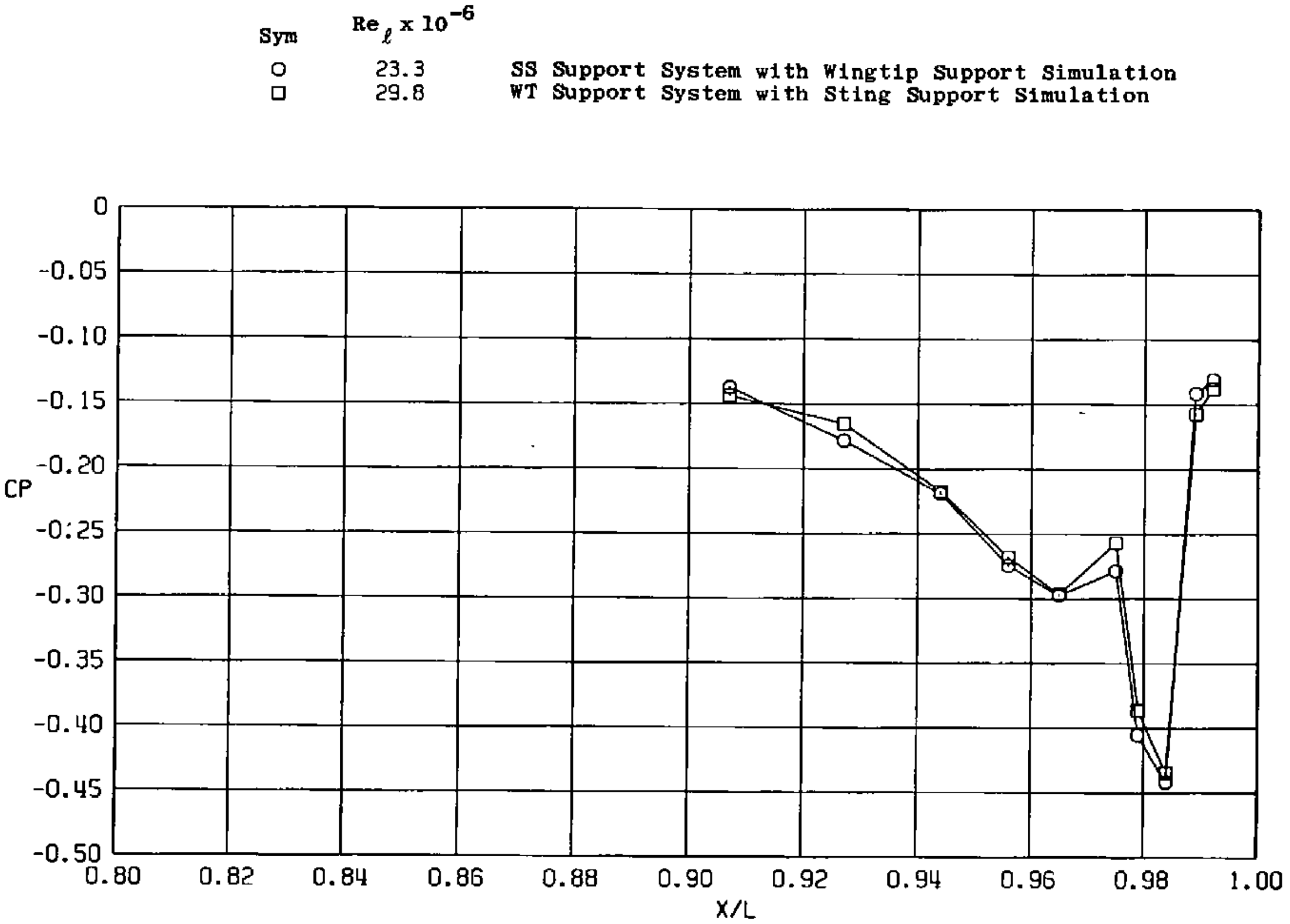

f. ϕ = 315 deg

Figure 19. Concluded.

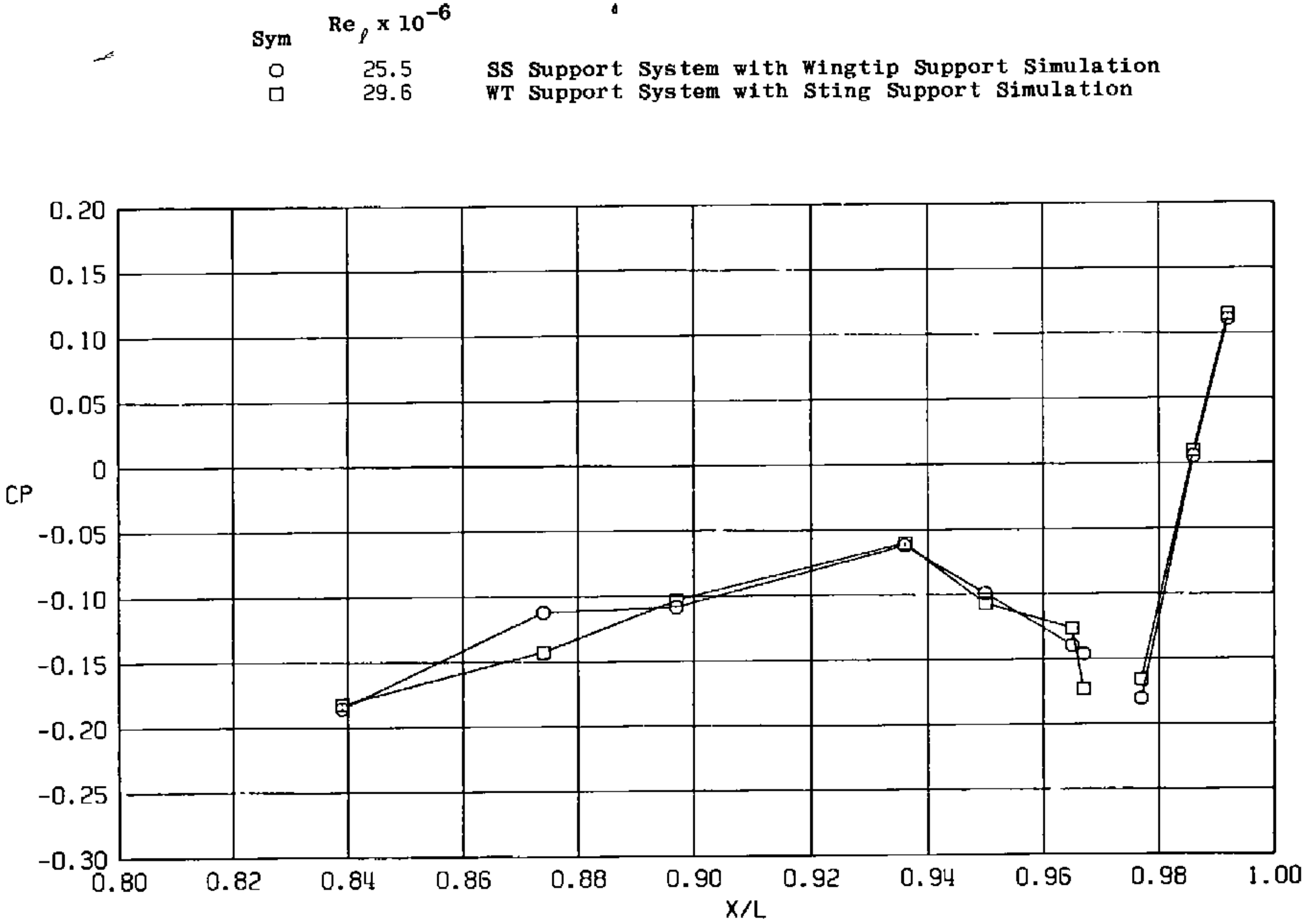

a. $\phi = 0$

Figure 20. Effect of support system simulation on surface pressure coefficients, A8 = 200 in.^{2}, M = 0.6, α = 4.1 deg, NPRE = 3.4.

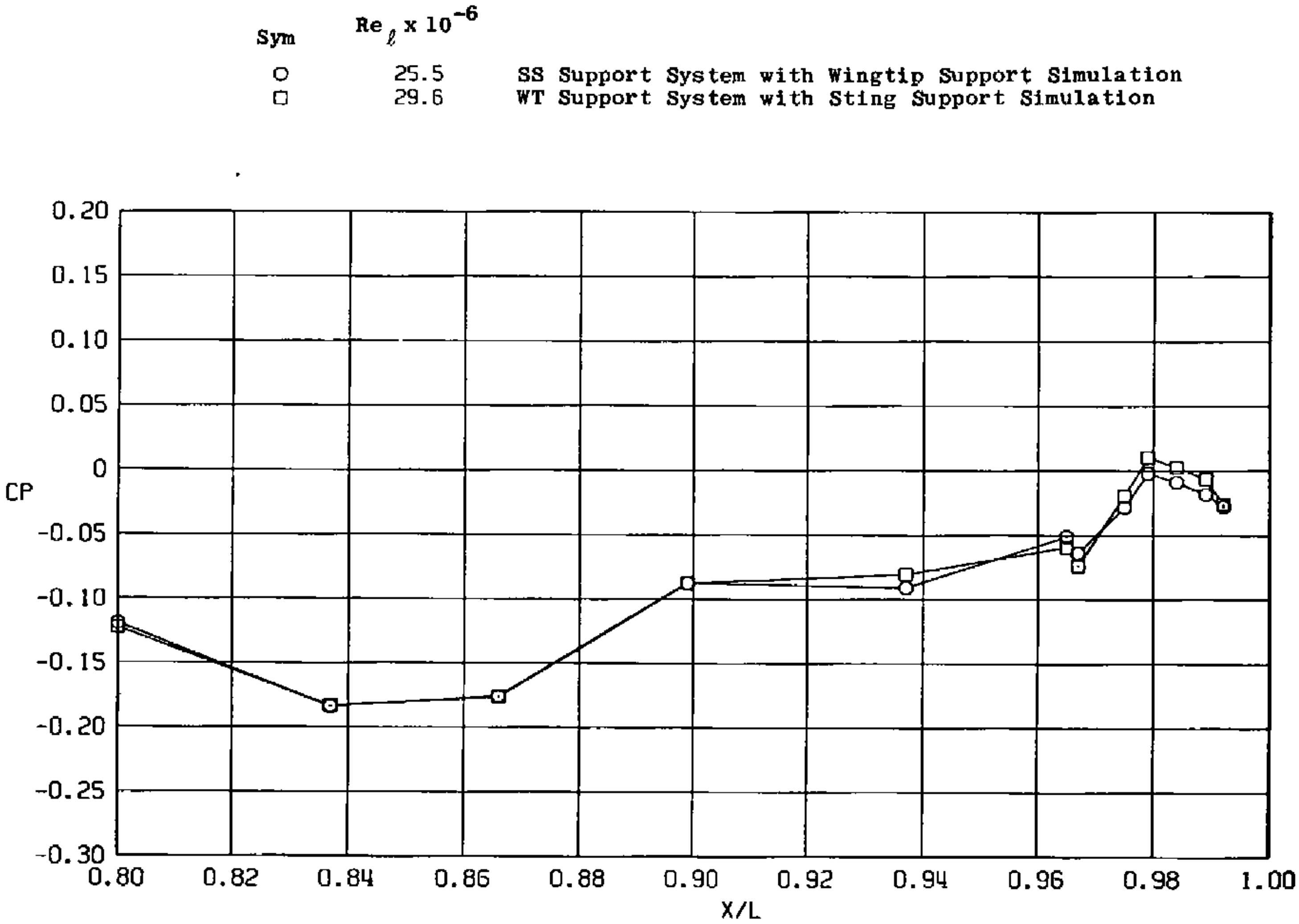

b. ϕ = 45 deg

Figure 20. Continued.

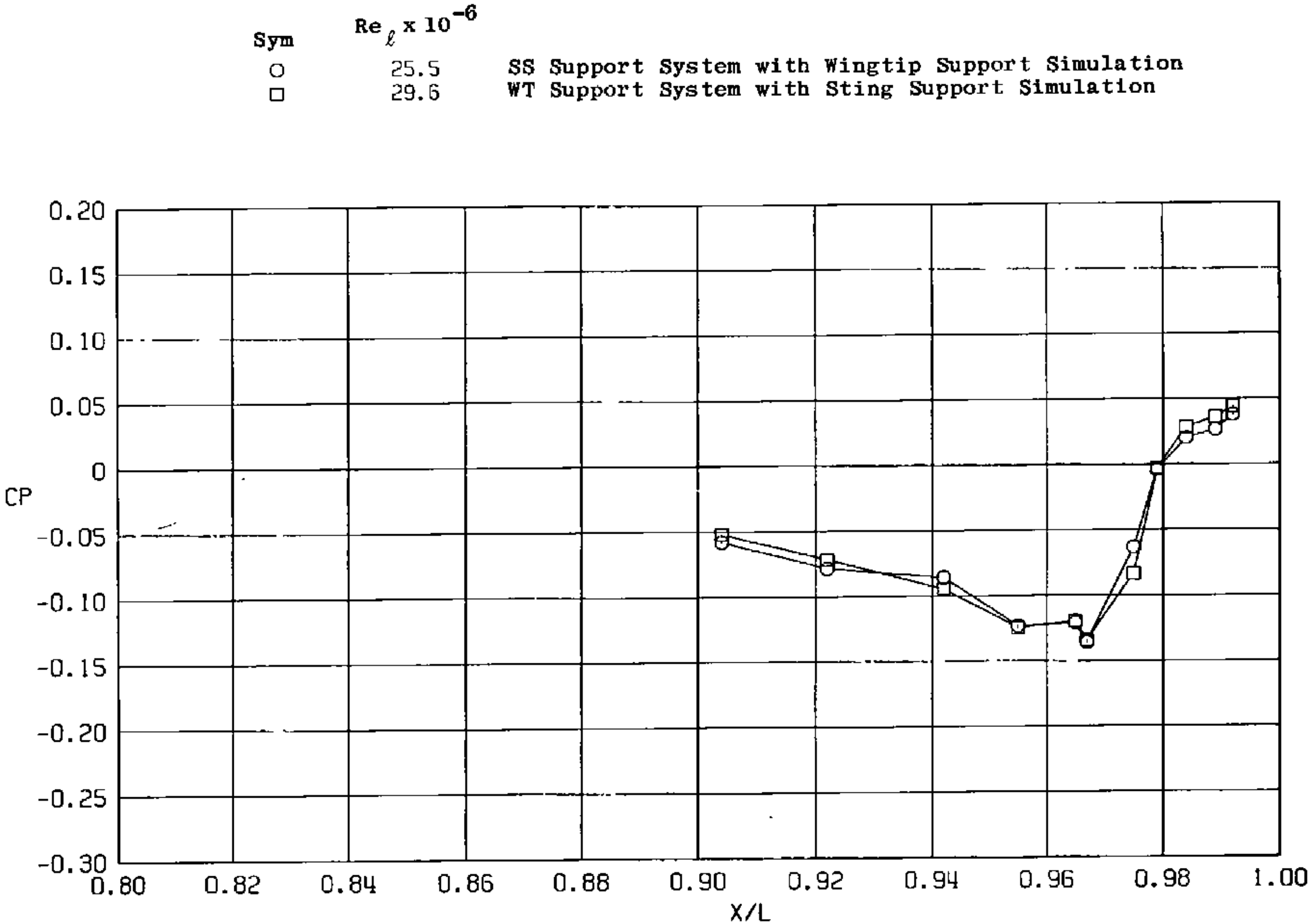

c. ϕ = 135 deg
Figure 20. Continued.

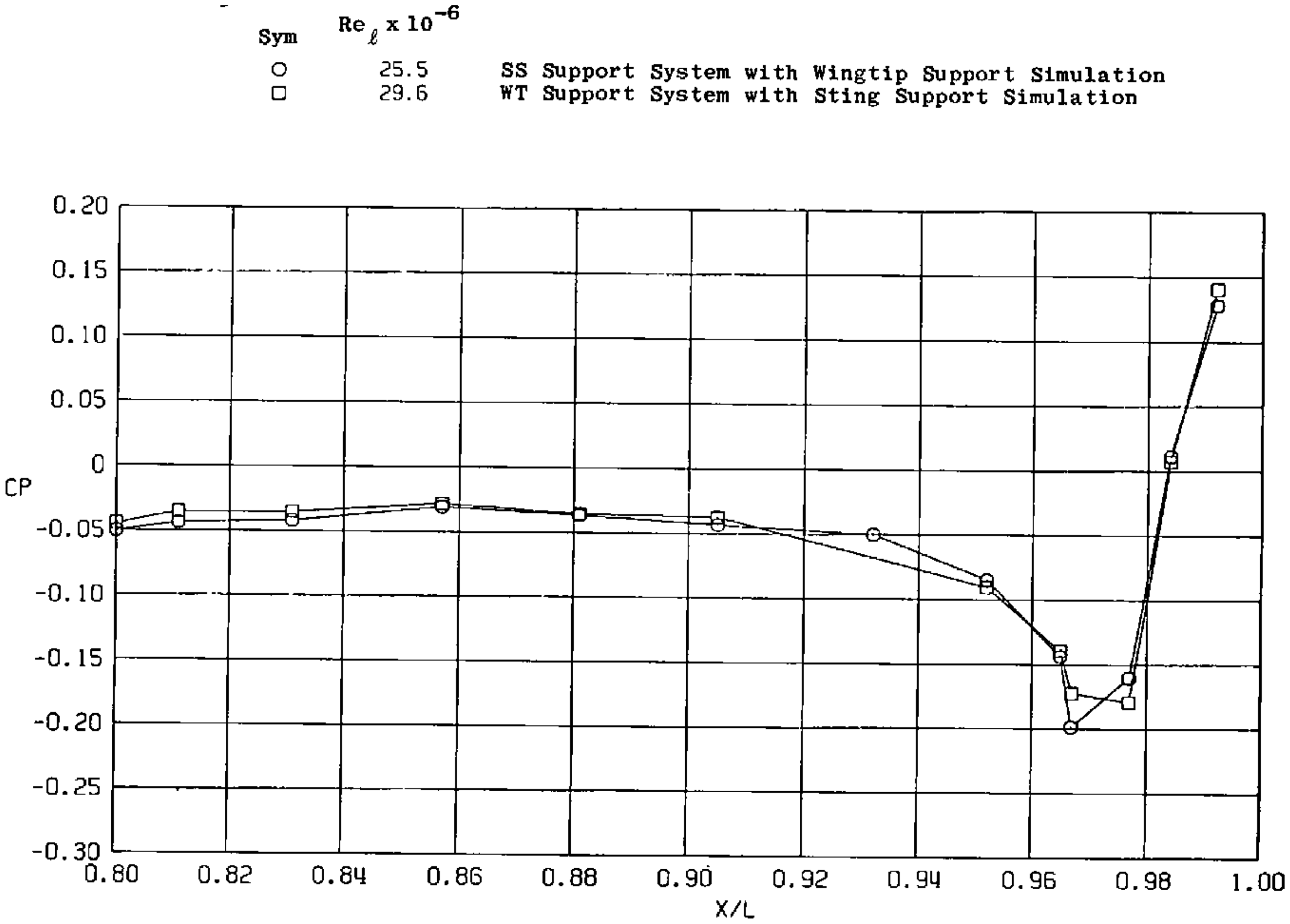

d. ϕ = 180 deg

Figure 20. Continued.

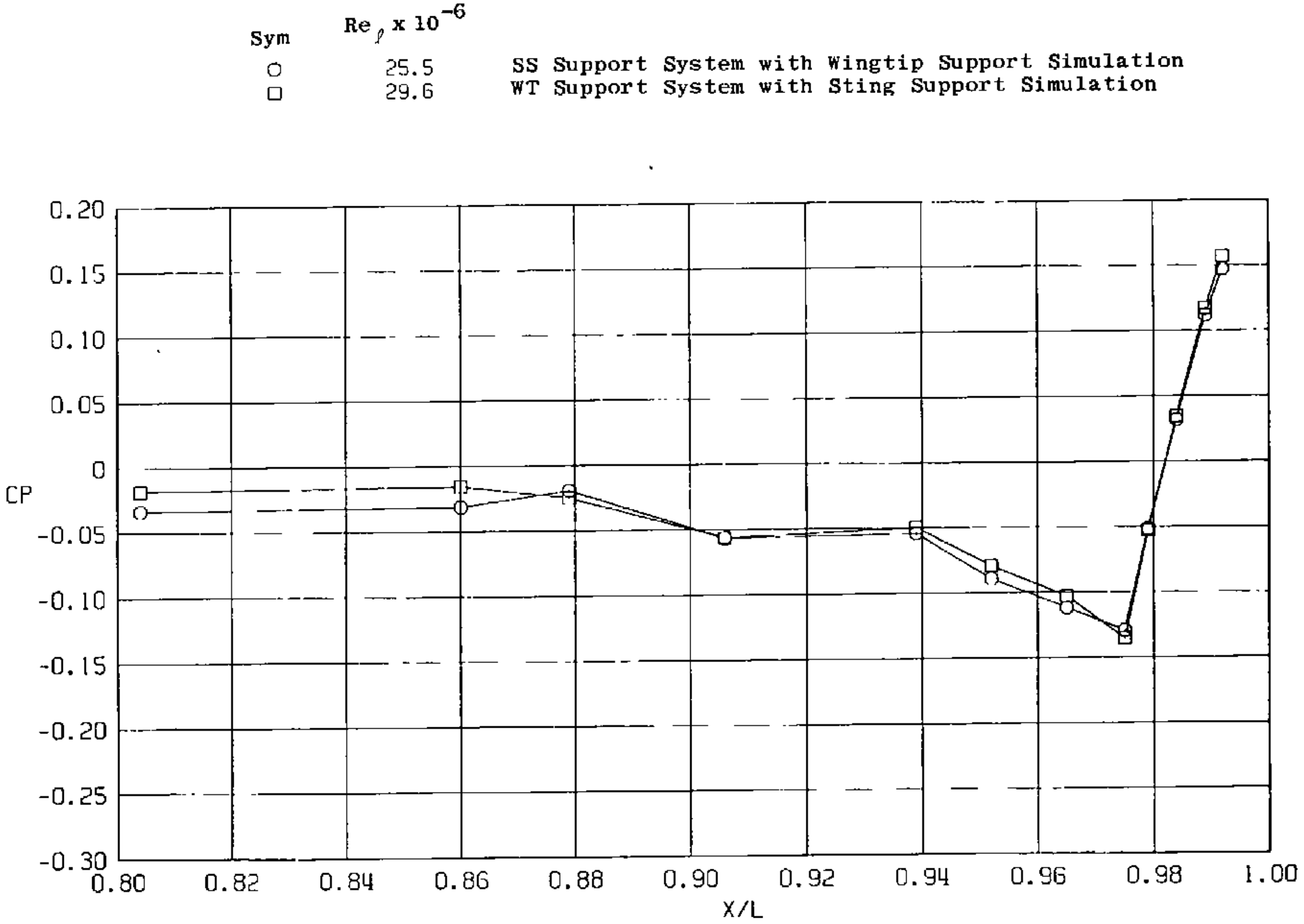

e. ϕ = 225 deg

Figure 20. Continued.

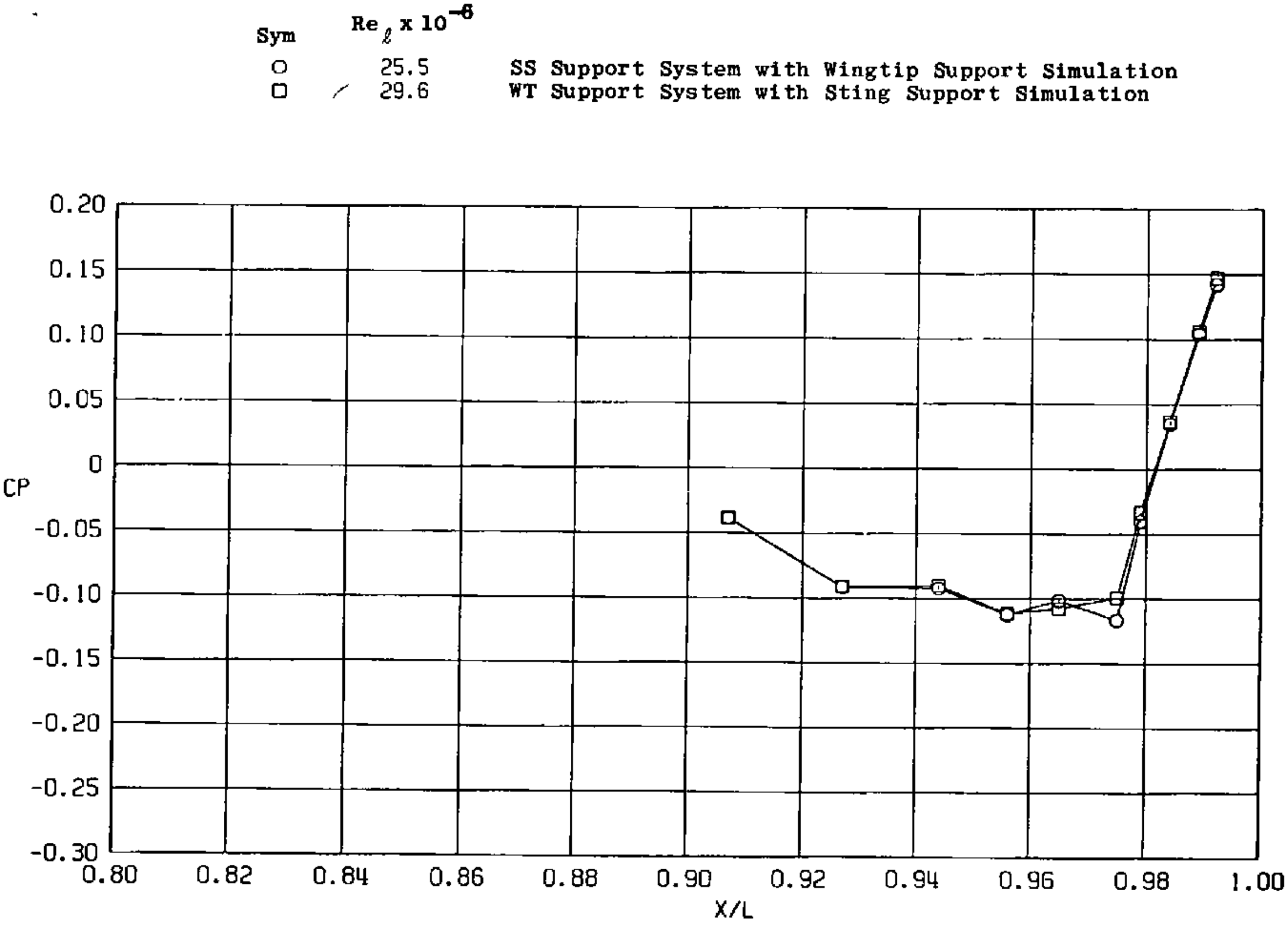

f. ϕ = 315 deg
Figure 20. Concluded.

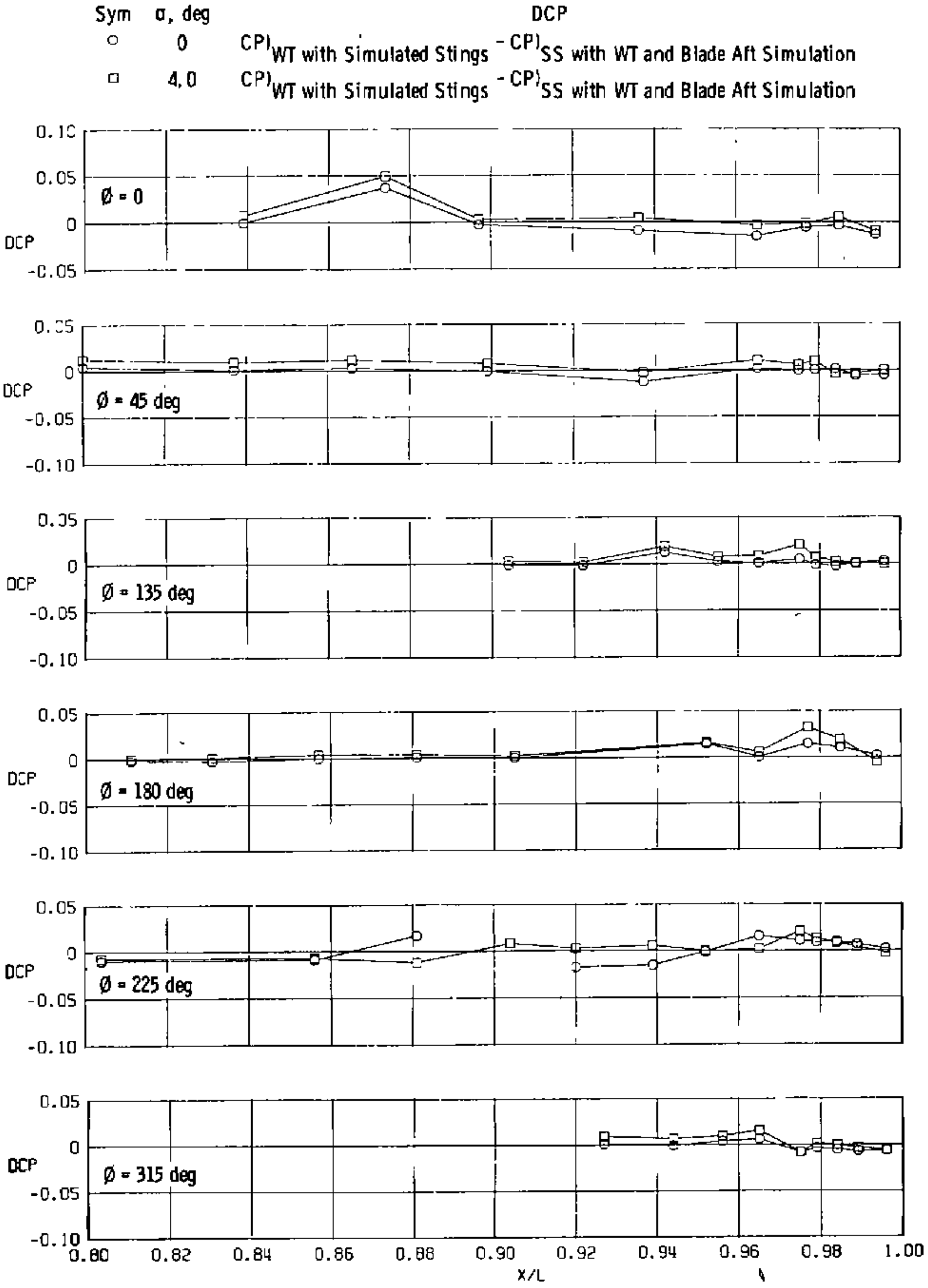

a. A8 = 200 in.², M = 0.6, NPR = 1.0

Figure 21. Incremental effects of support system simulation on surface pressure distributions.

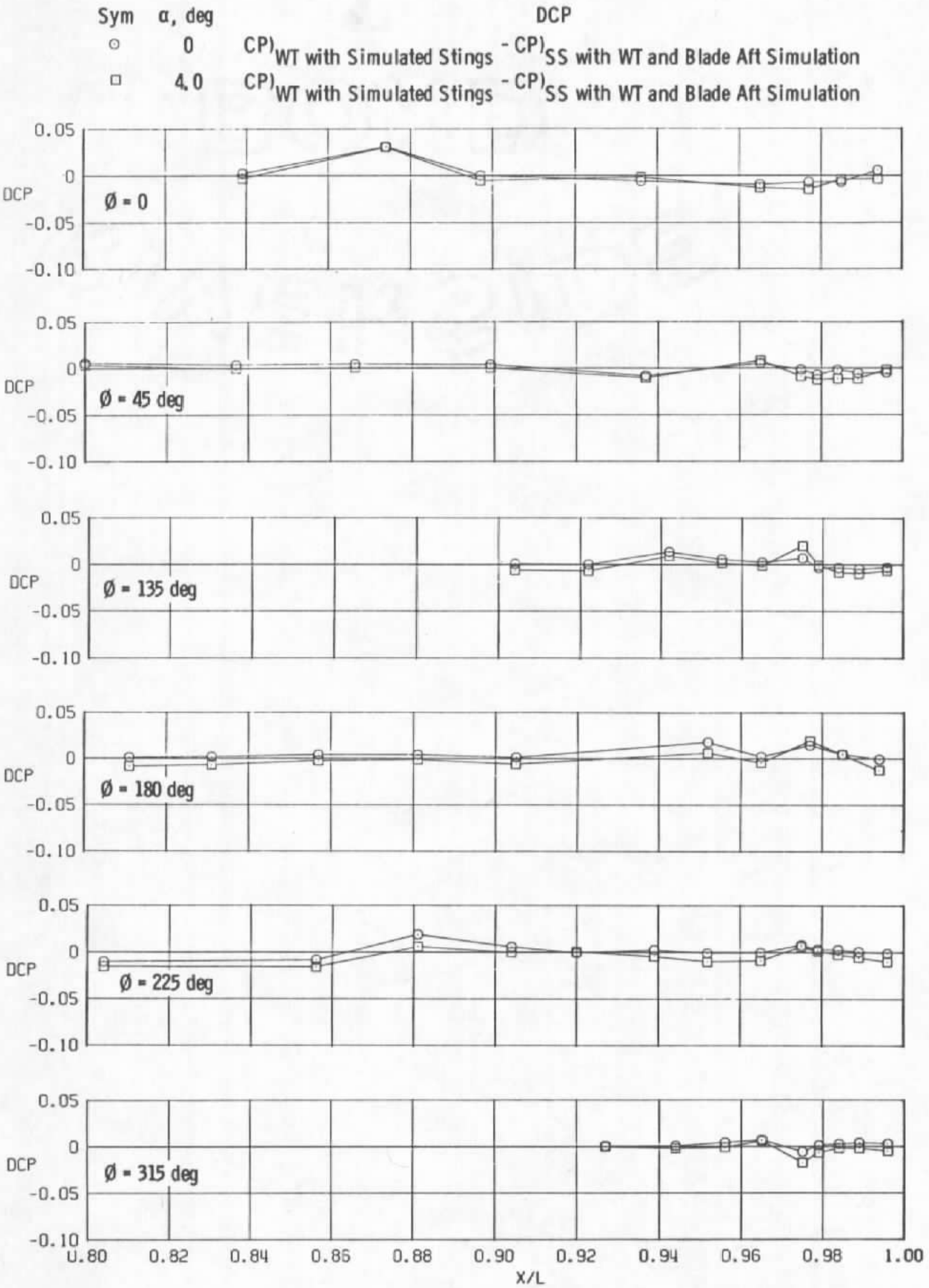

b. A8 = 200 in.^{2}, M = 0.6, NPRE = 3.4
Figure 21. Continued.

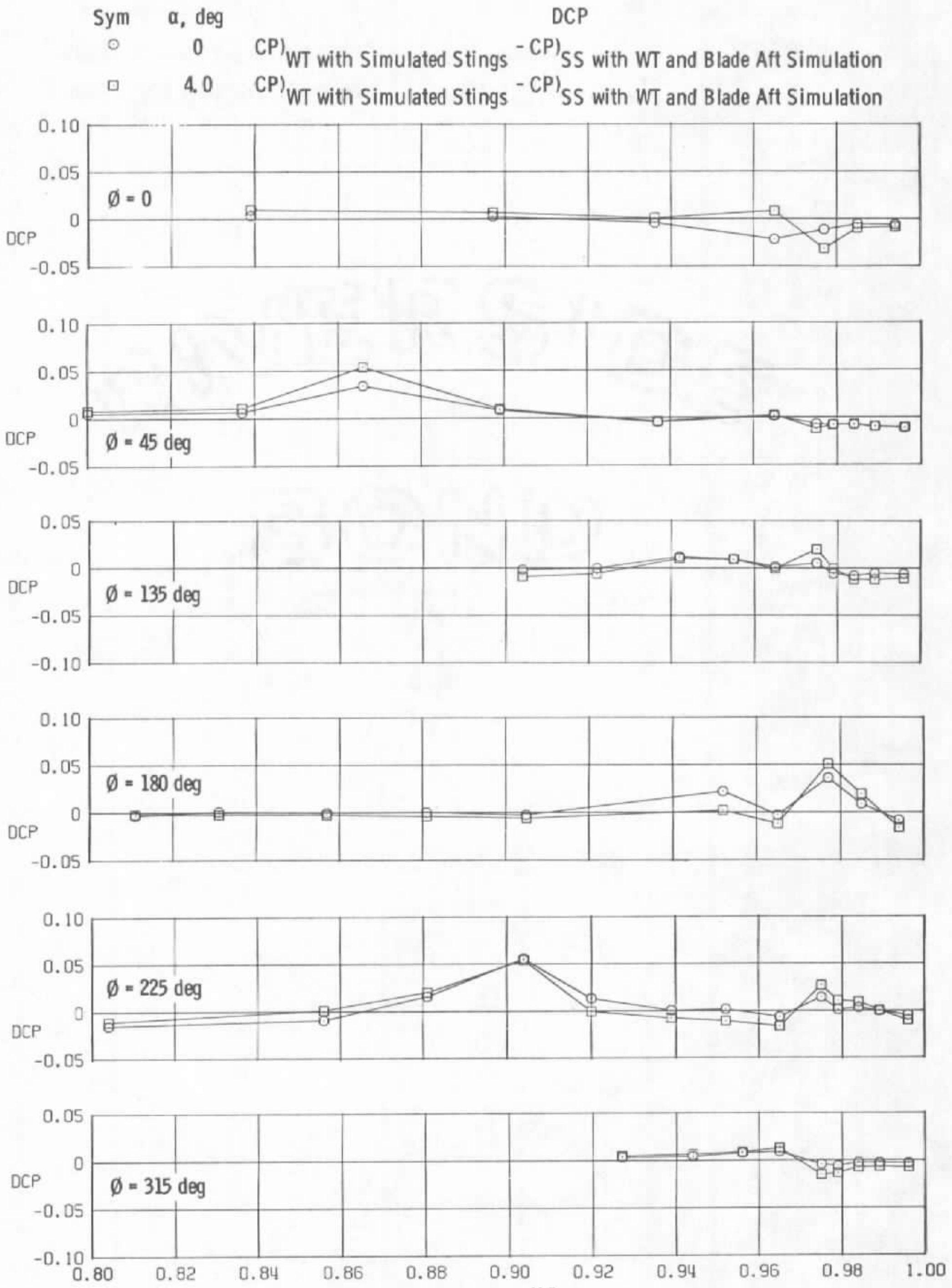

c. A8 = 300 in.², M = 0.9, NPR = 1.0
Figure 21. Continued.

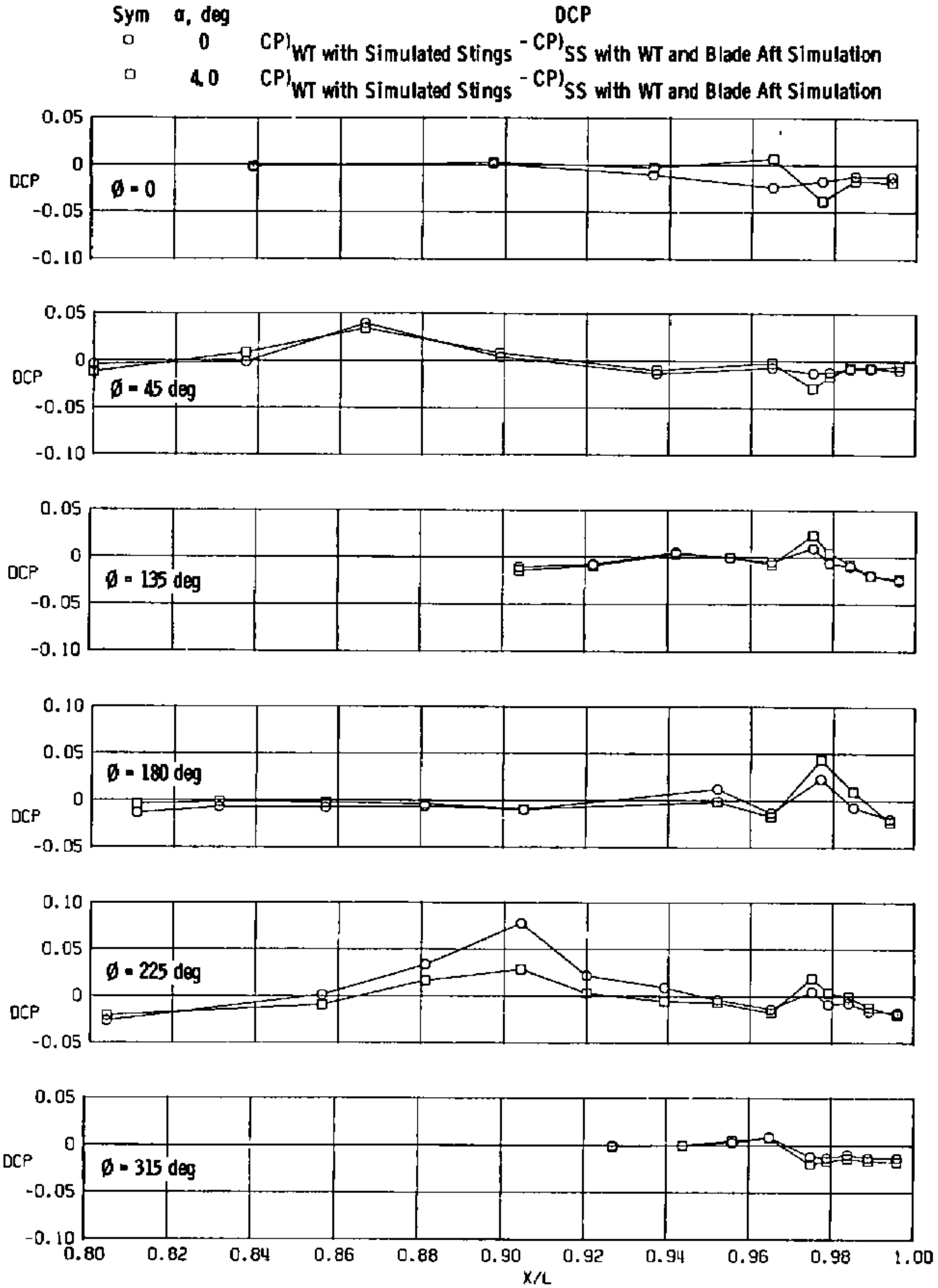

d. A8 = 300 in.², M = 0.9, NPRE = 5.0

Figure 21. Continued.

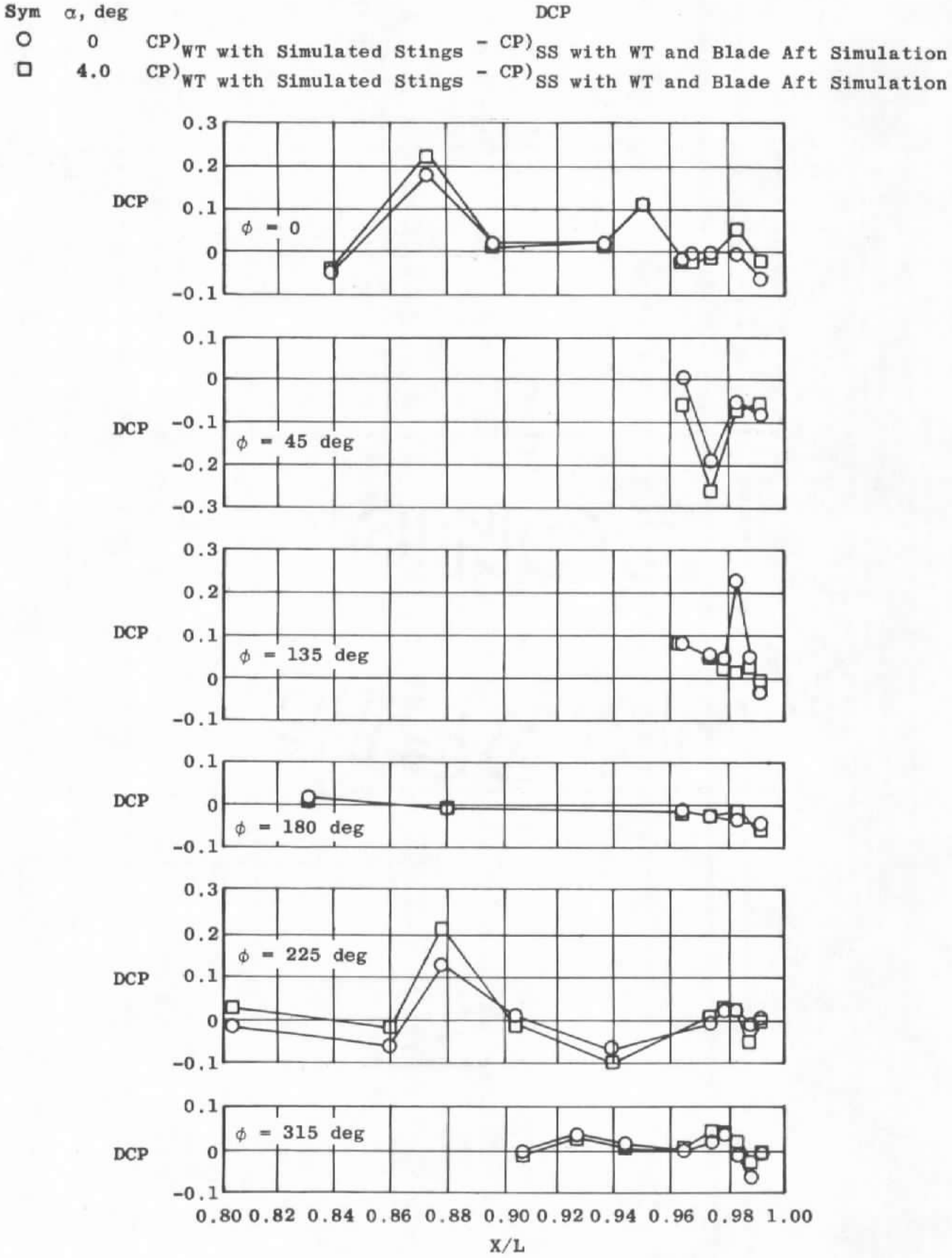

e. A8 = 300 in.^{2}, M = 1.2, NPR = 5.2
Figure 21. Concluded.

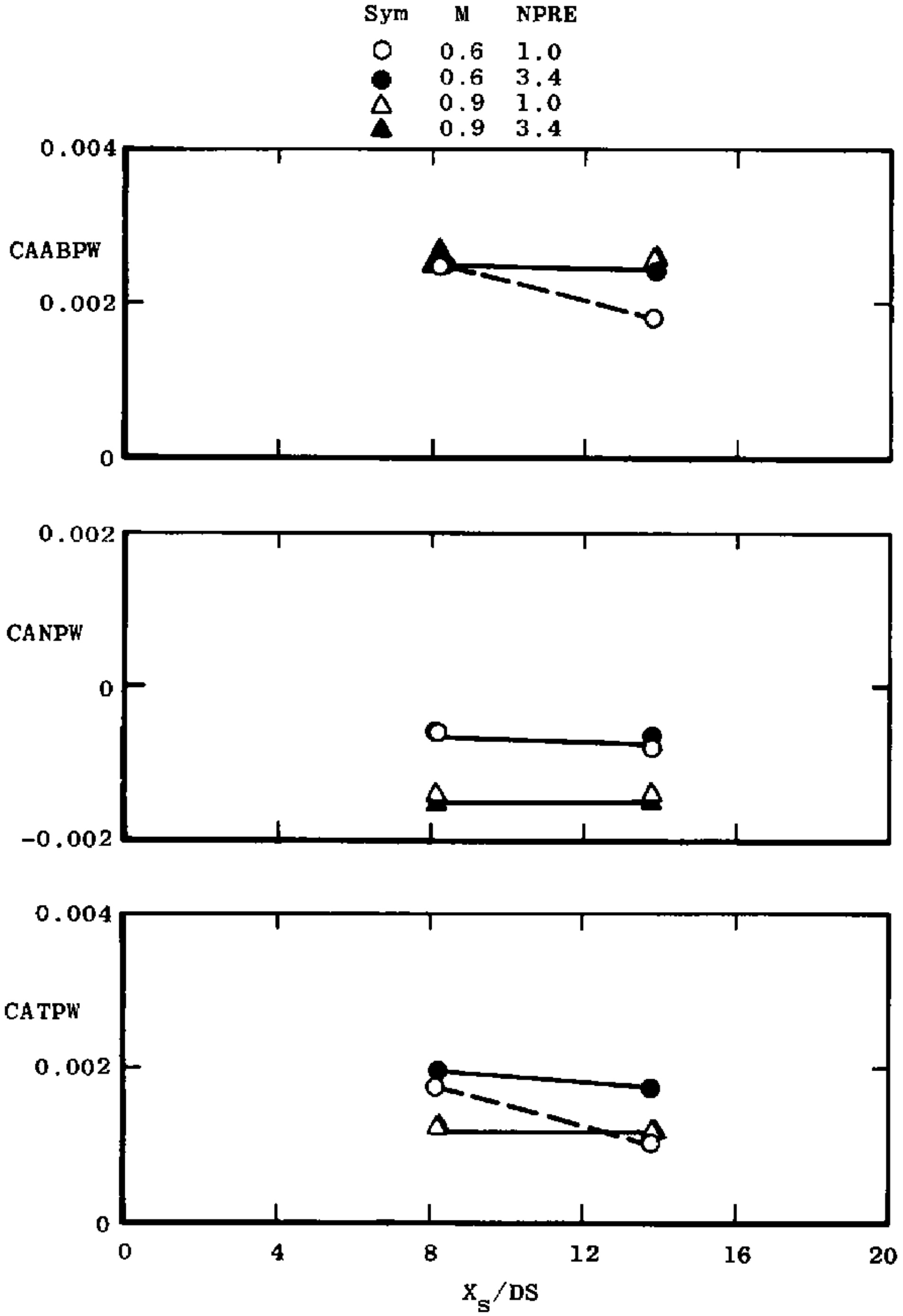

a. Subsonic Mach numbers

Figure 22. Effect of sting taper location on axial force coefficients, A8 = 200 in.^{2}, α = 4.1 deg (WT).

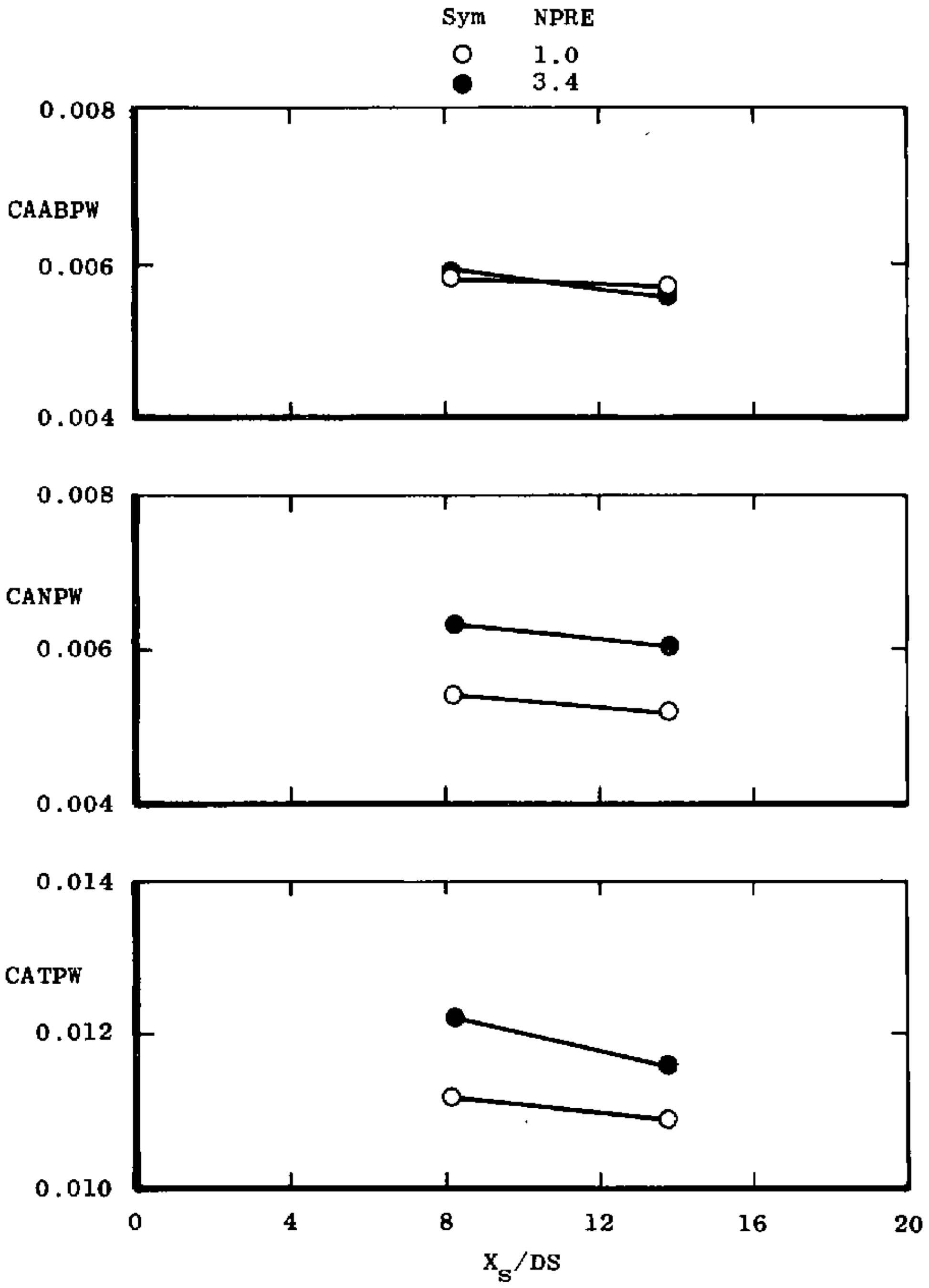

b. M = 1.2
Figure 22. Concluded.

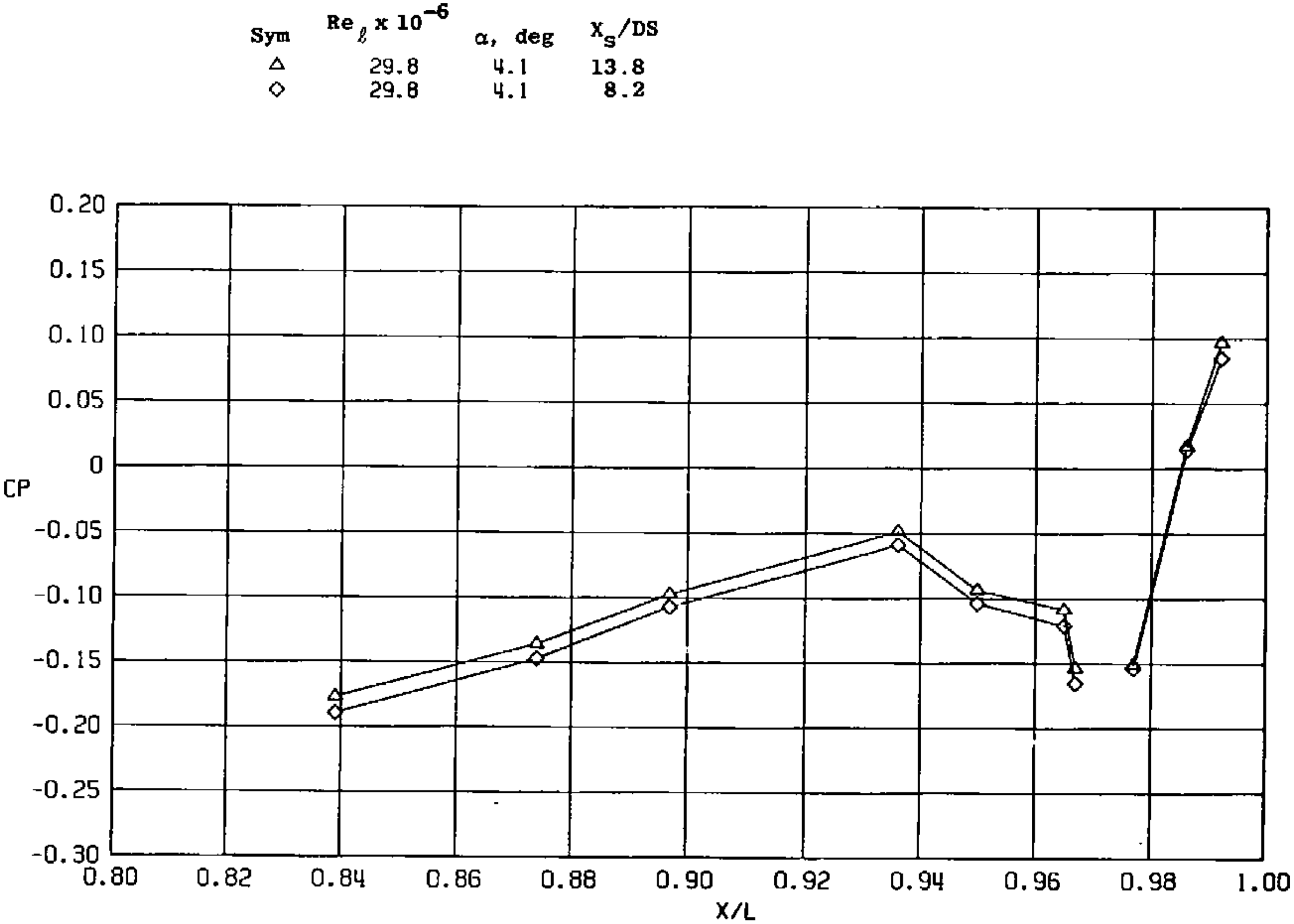

a. $\phi = 0$

Figure 23. Effect of sting taper location on surface pressure coefficients, A8 = 200 in.^{2}, M = 0.6 (WT), NPR = 1.0.

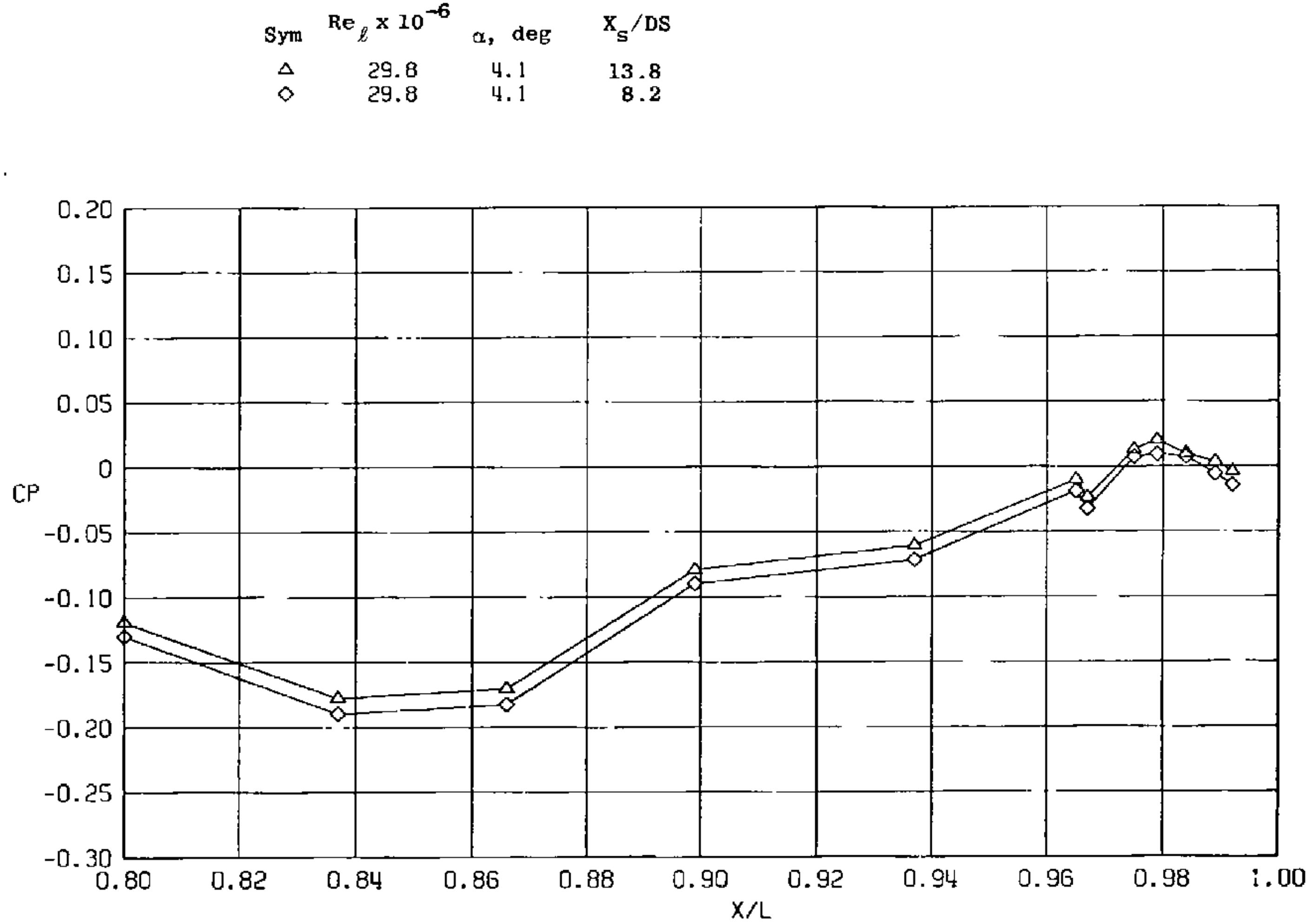

b. ϕ = 45 deg
Figure 23. Continued.

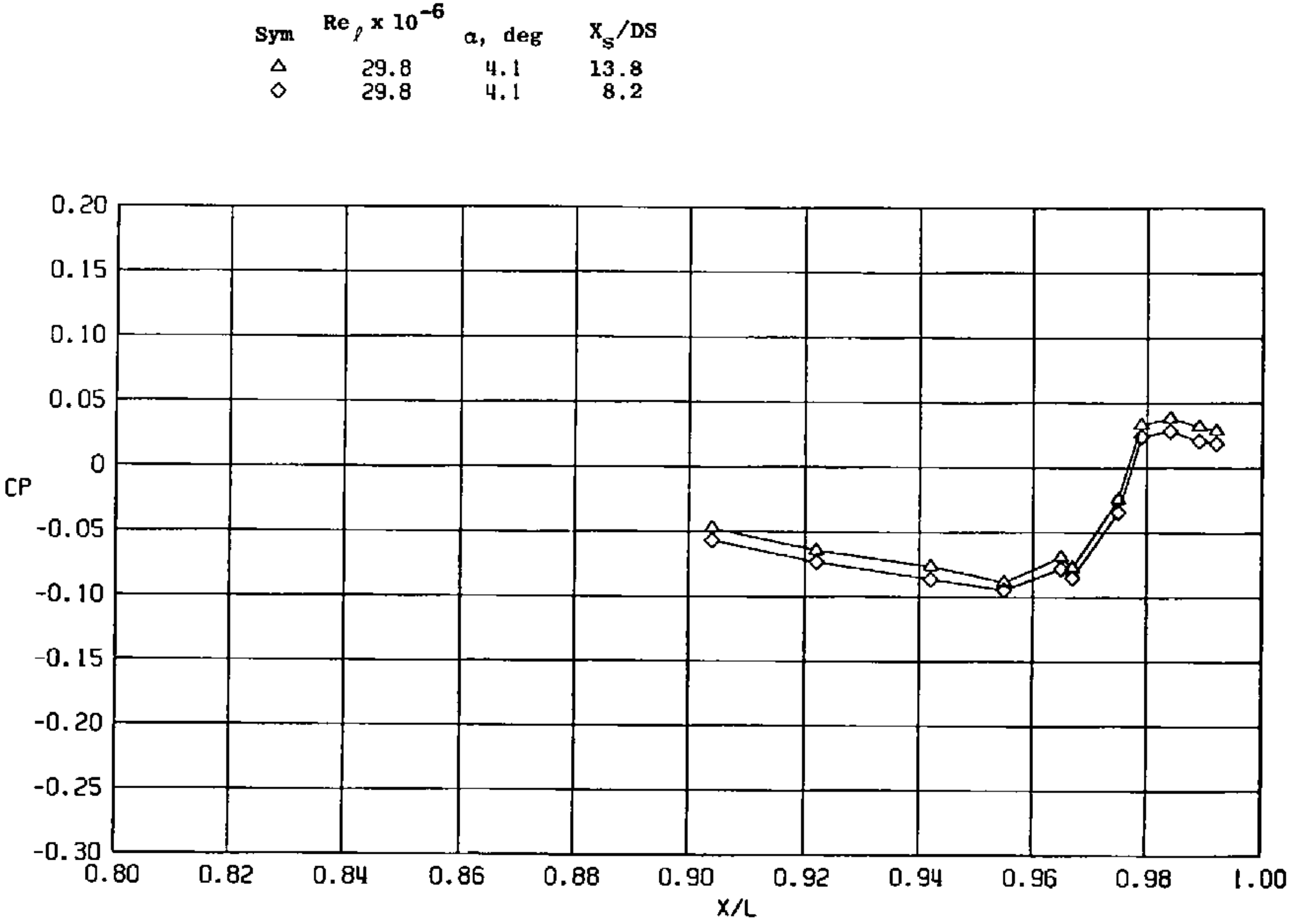

c. ϕ = 135 deg
Figure 23. Continued.

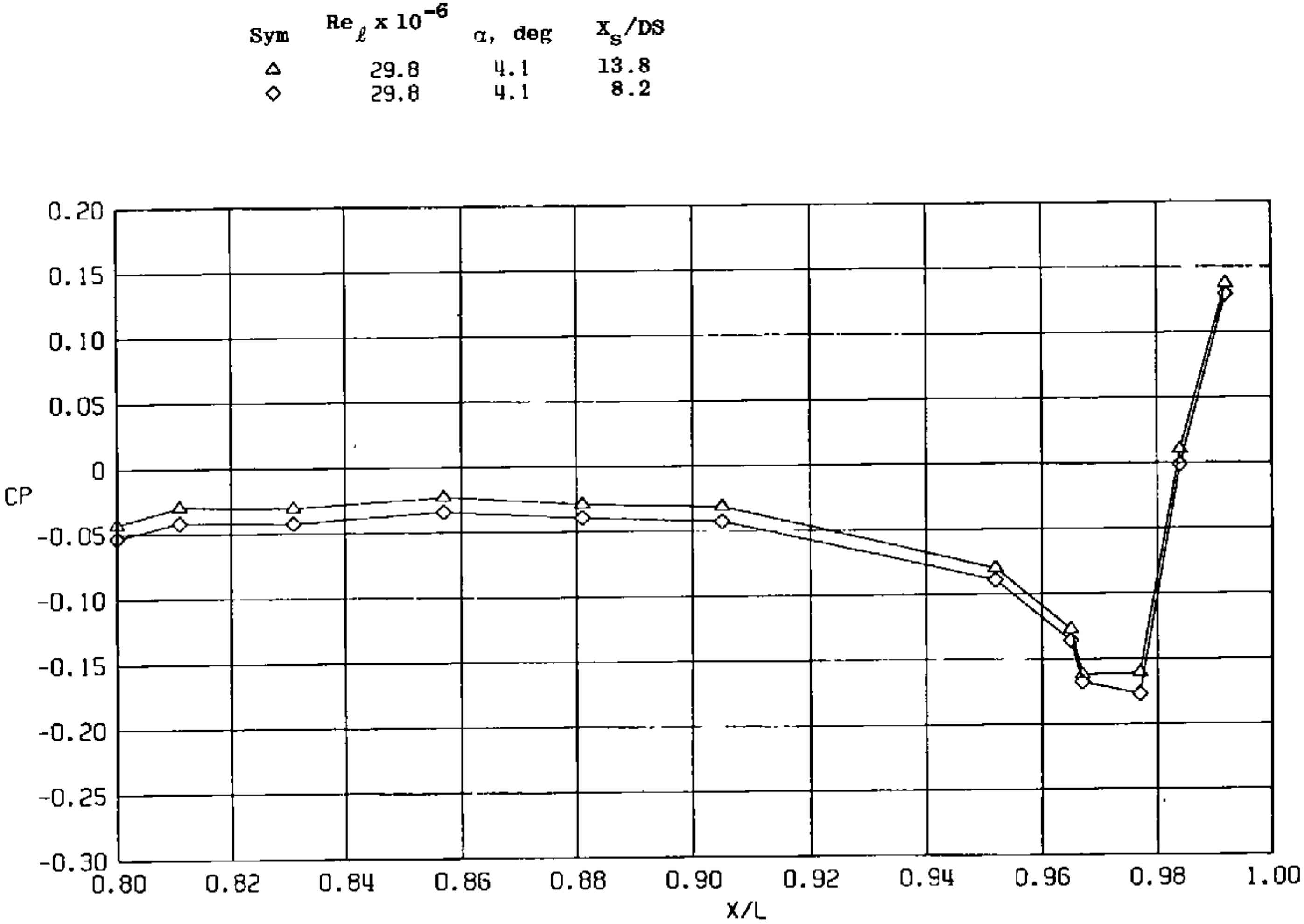

d. ϕ = 180 deg
Figure 23. Continued.

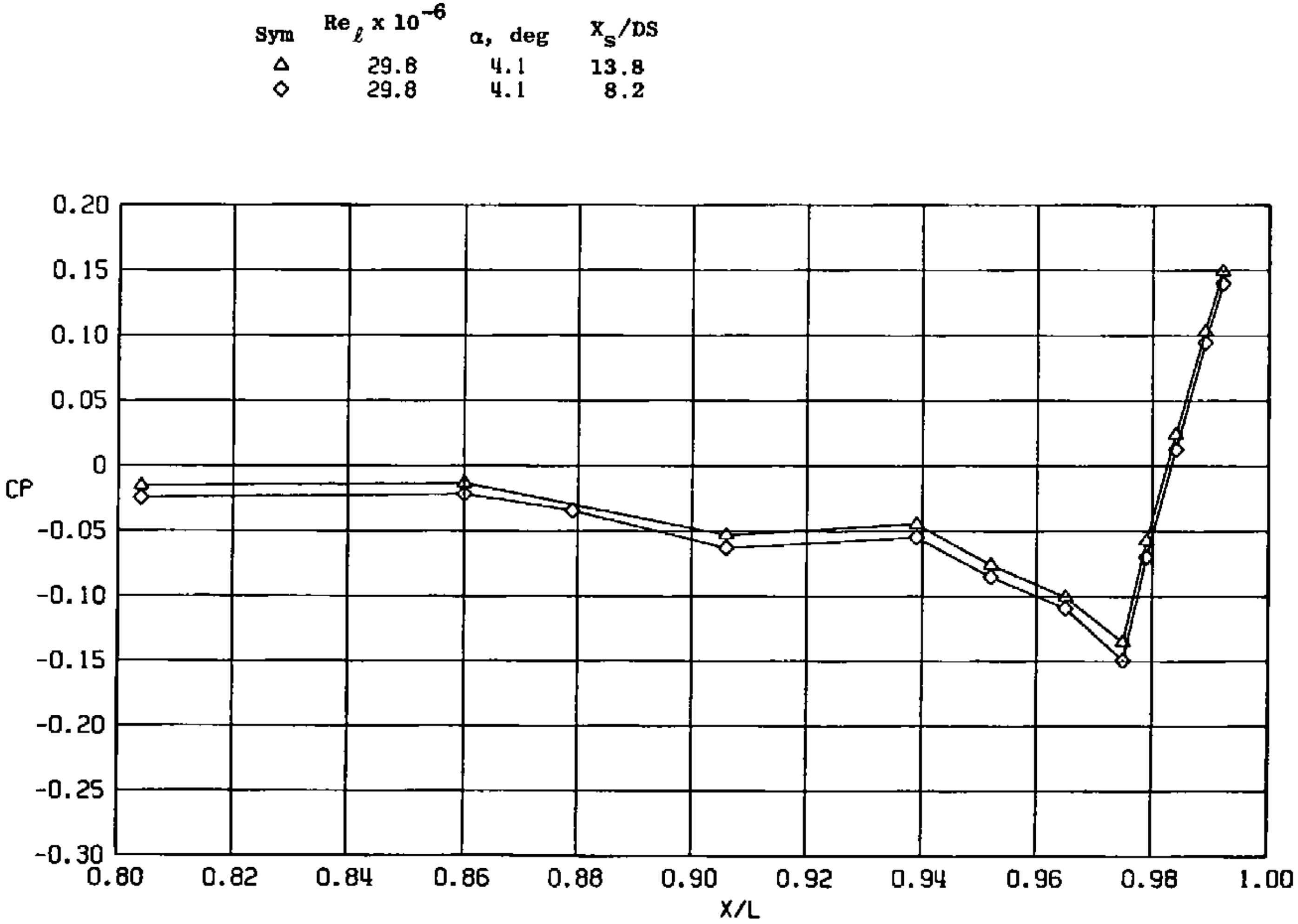

e. ϕ = 225 deg

Figure 23. Continued.

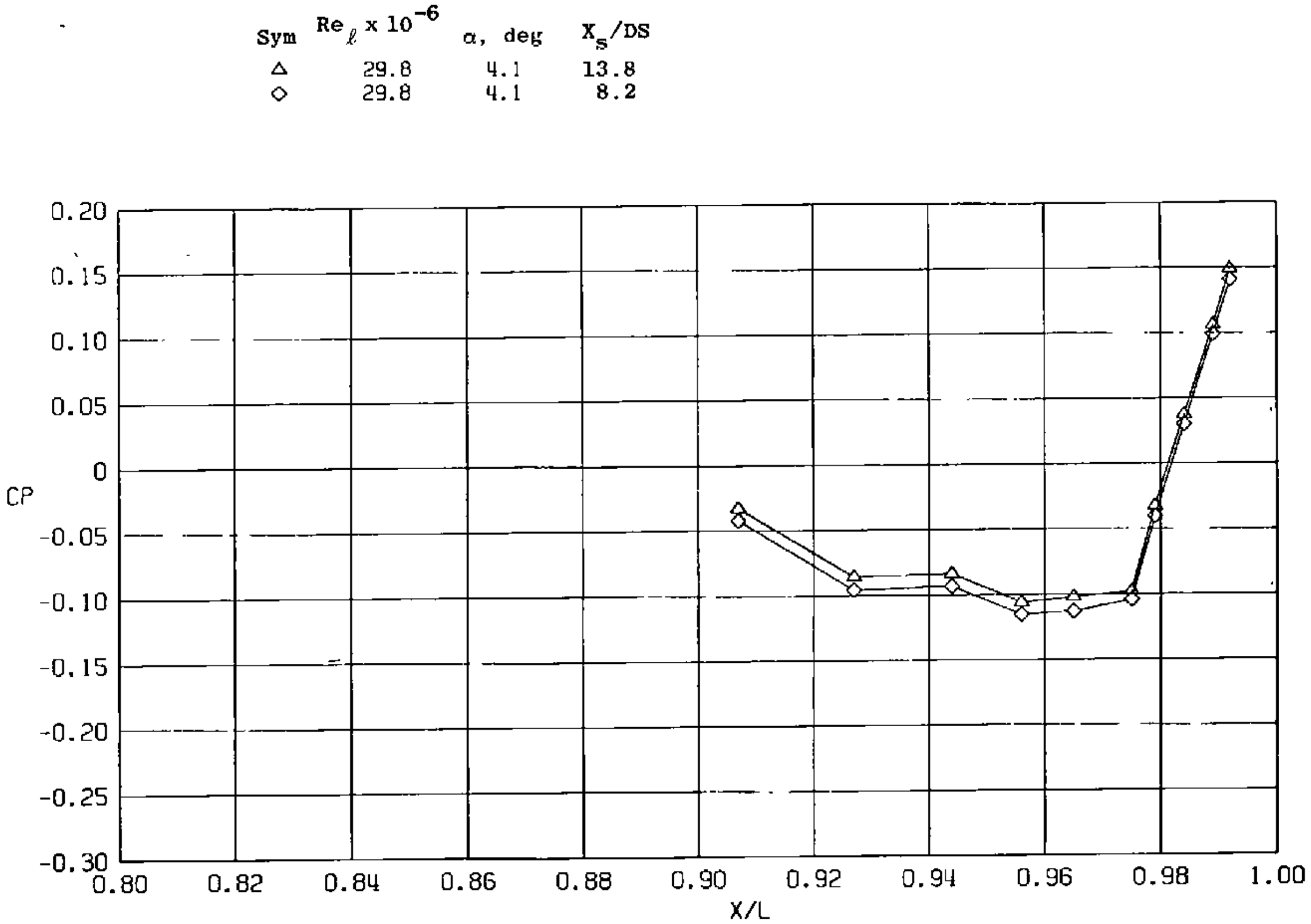

f. ϕ = 315 deg
Figure 23. Concluded.

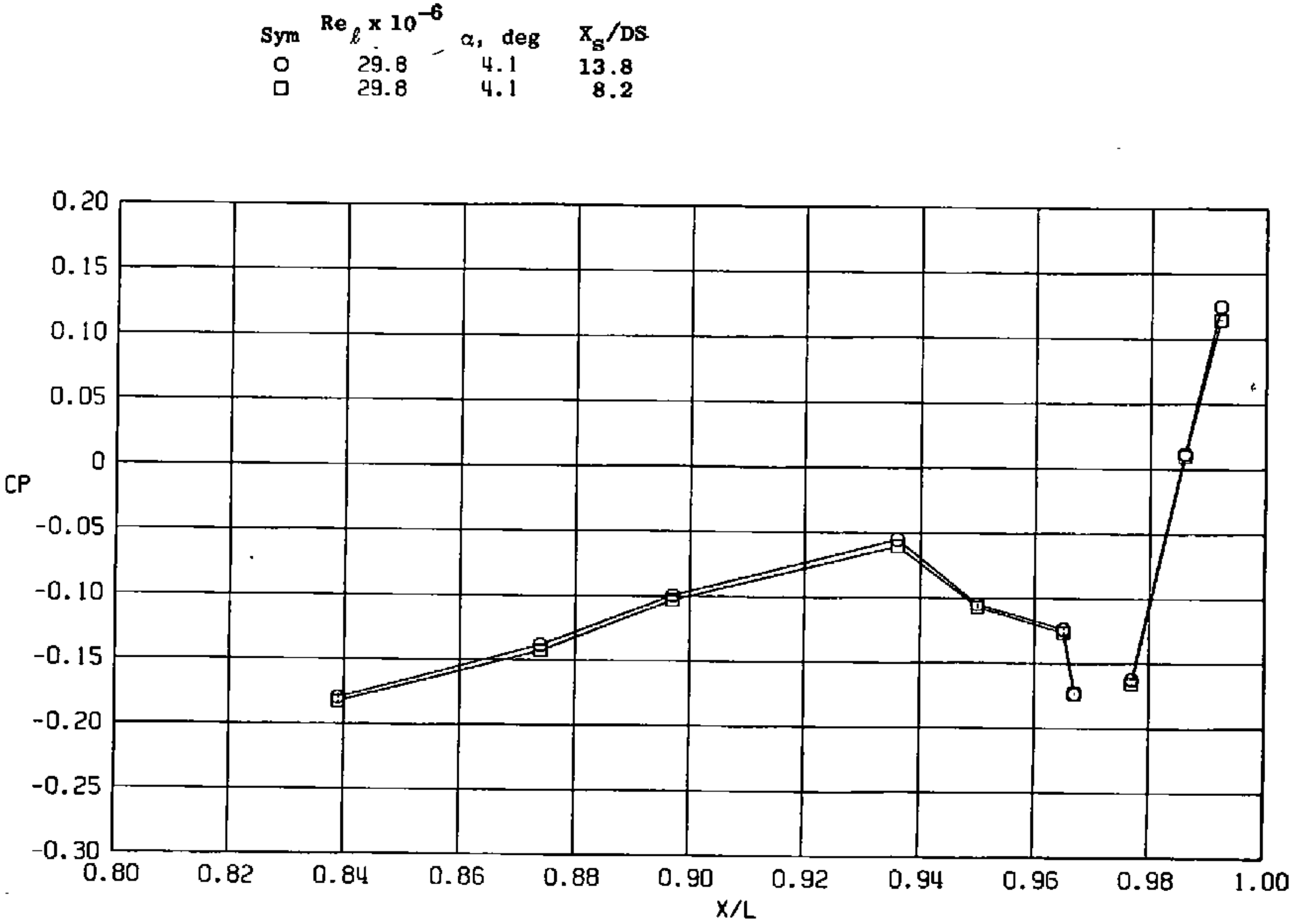

a. $\phi = 0$

Figure 24. Effect of sting taper location on surface pressure coefficients, A8 = 200 in.^{2}, M = 0.6 (WT), NPRE = 3.4.

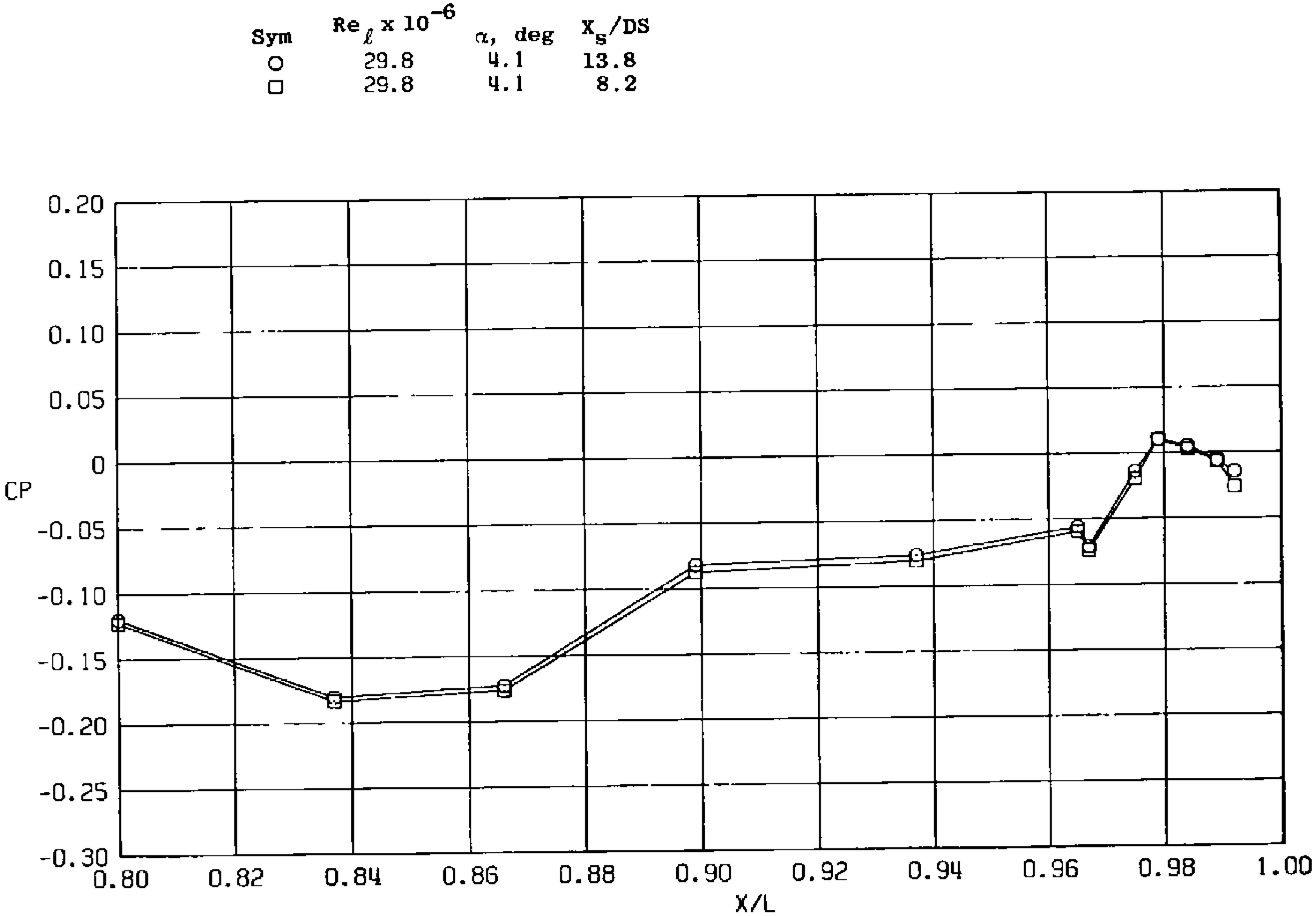

b. ϕ = 45 deg
Figure 24. Continued.

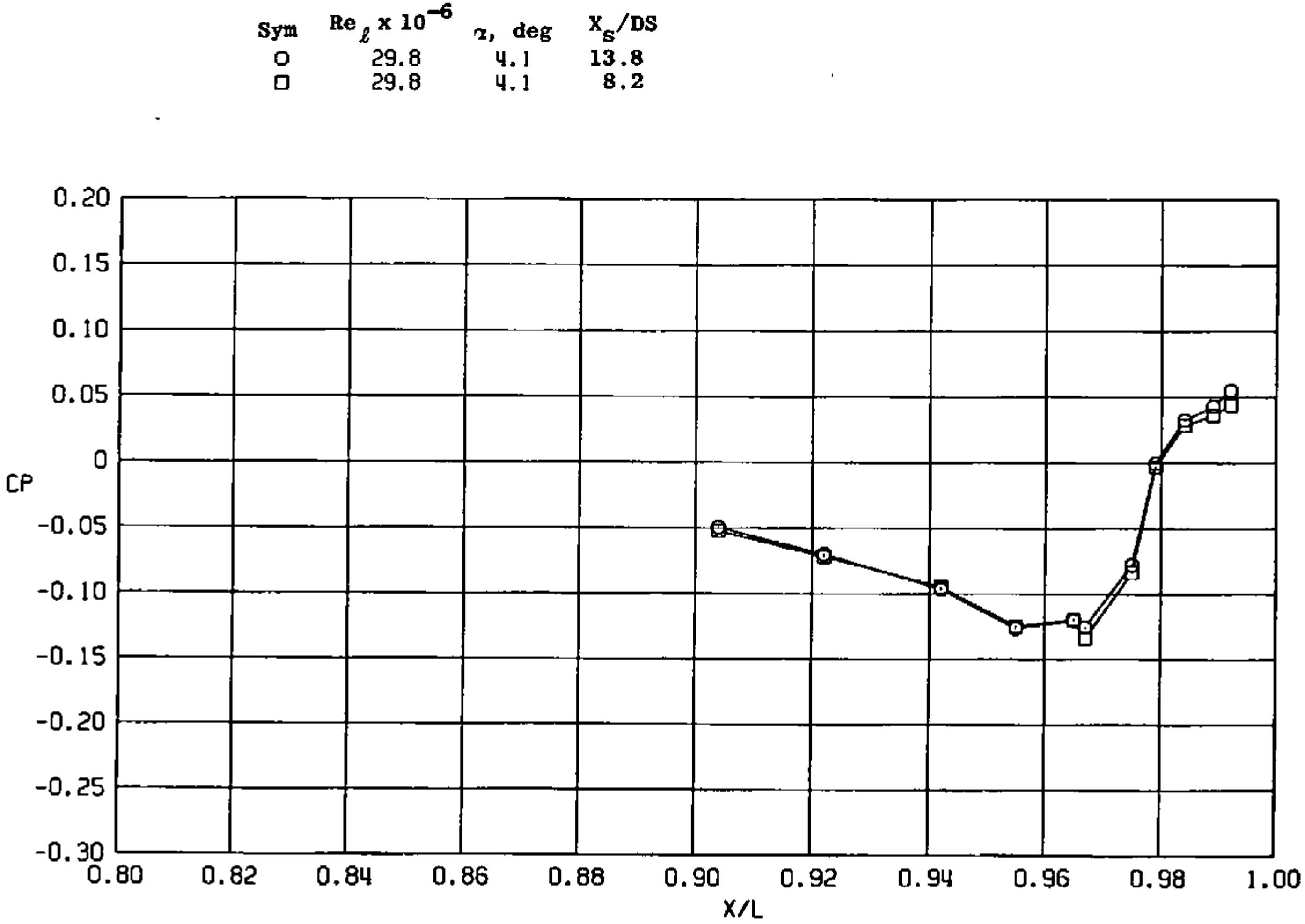

c. ϕ = 135 deg
Figure 24. Continued.

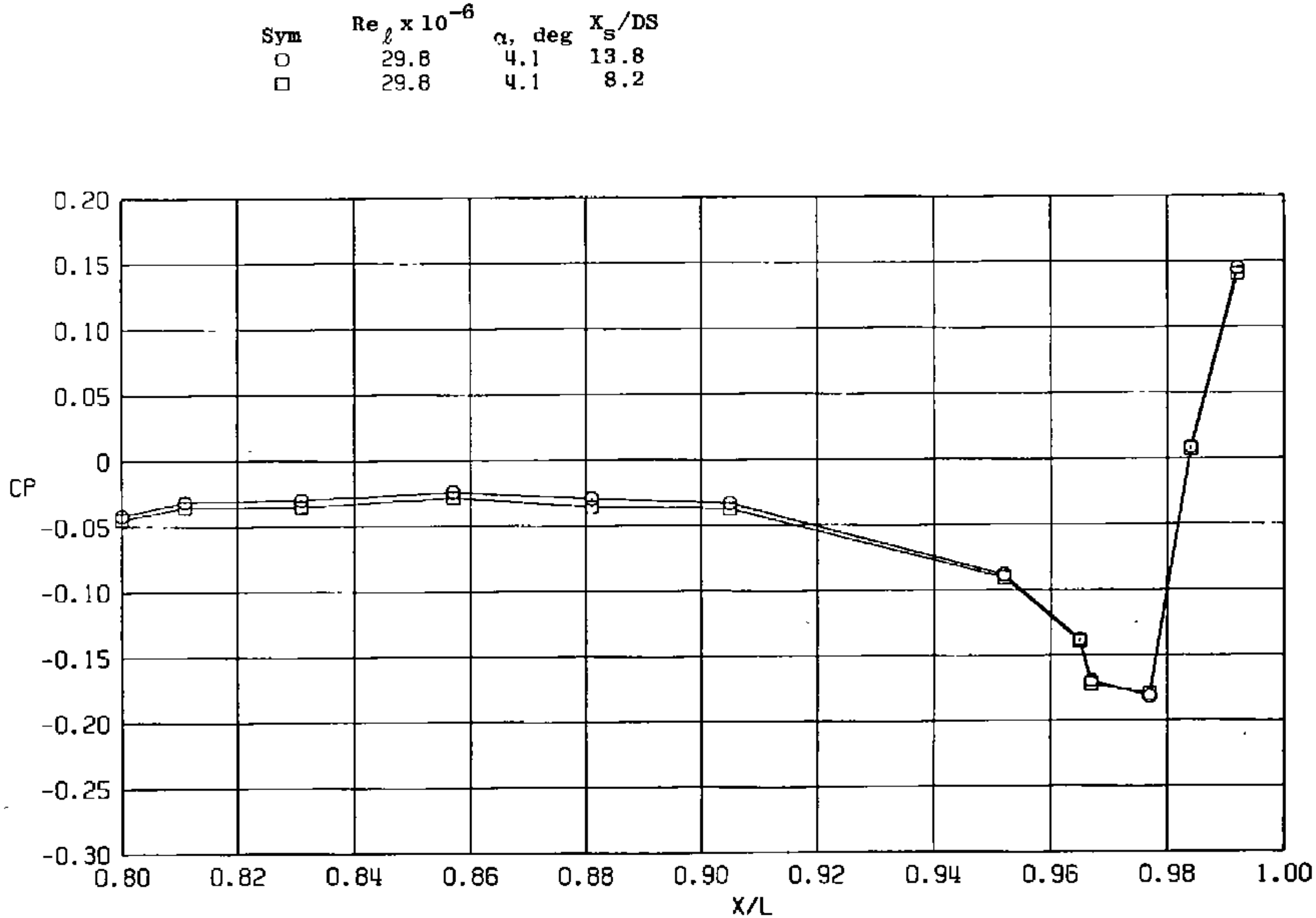

d. ϕ = 180 deg
Figure 24. Continued.

Sym	$Re_{\ell} \times 10^{-6}$	α, deg	X_s/DS
○	29.8	4.1	13.8
□	29.8	4.1	8.2

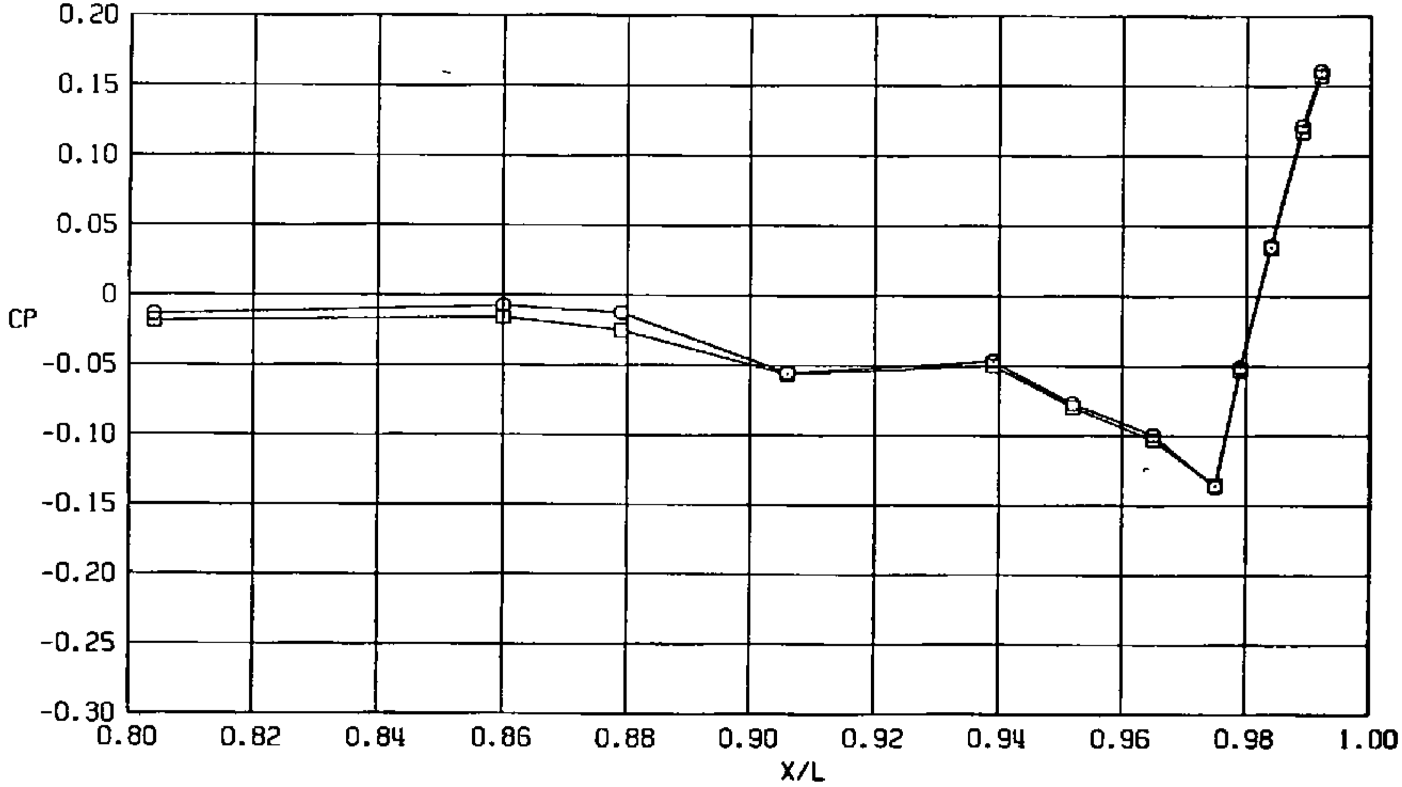

e. ϕ = 225 deg
Figure 24. Continued.

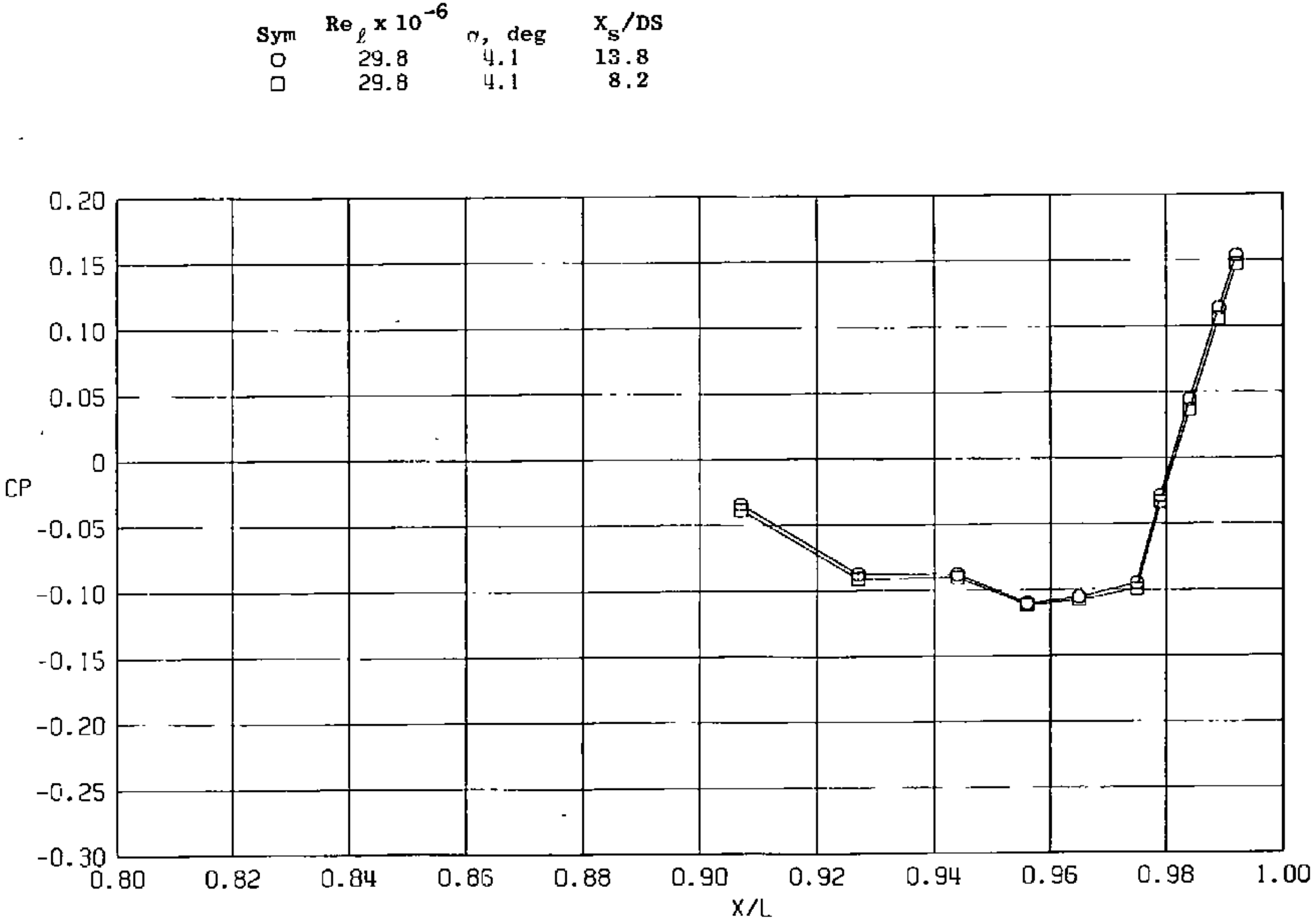

f. ϕ = 315 deg
Figure 24. Concluded.

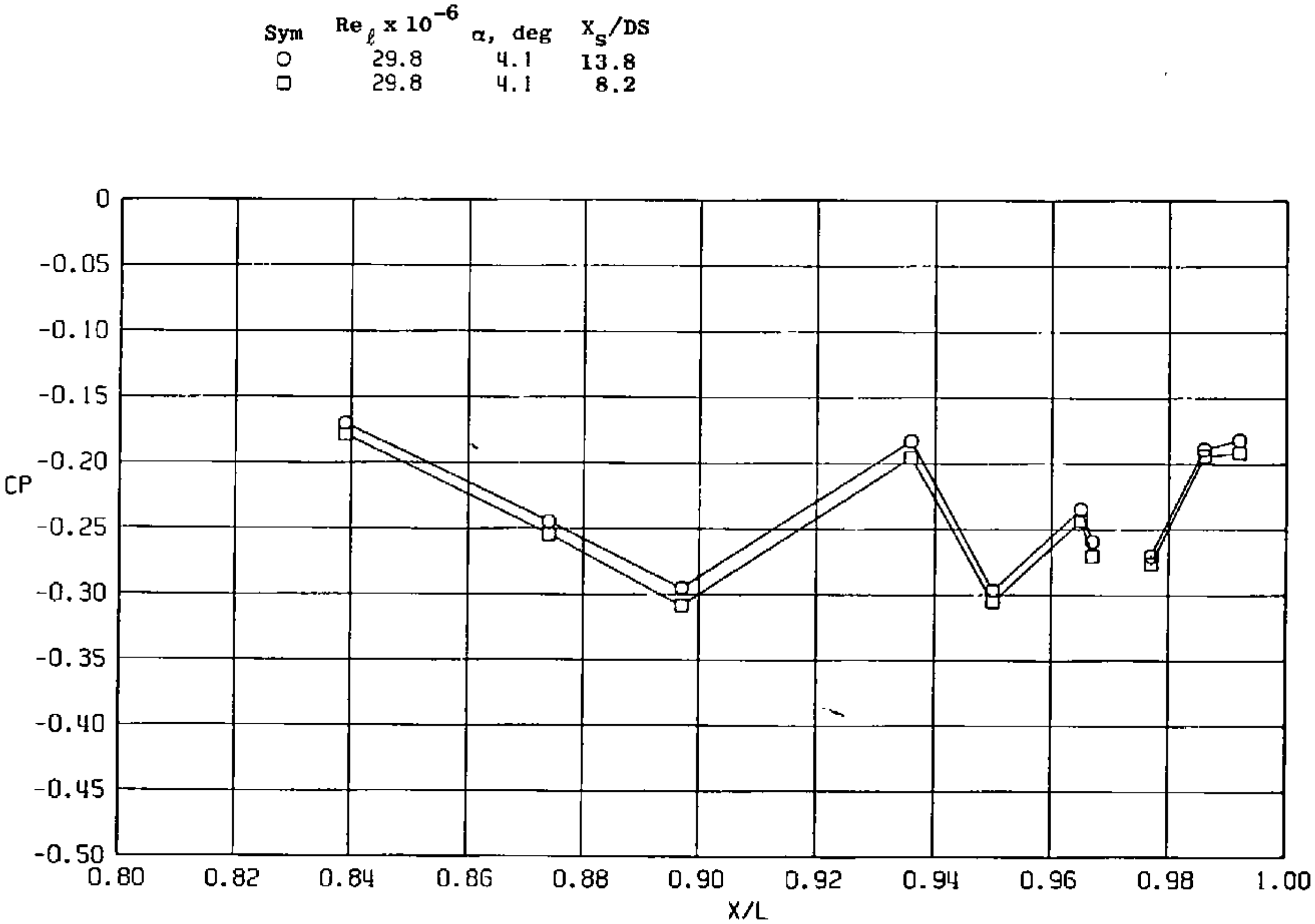

a. $\phi = 0$

Figure 25. Effect of sting taper location on surface pressure coefficients, A8 = 200 in.^{2}, M = 1.2 (WT), NPRE = 3.4.

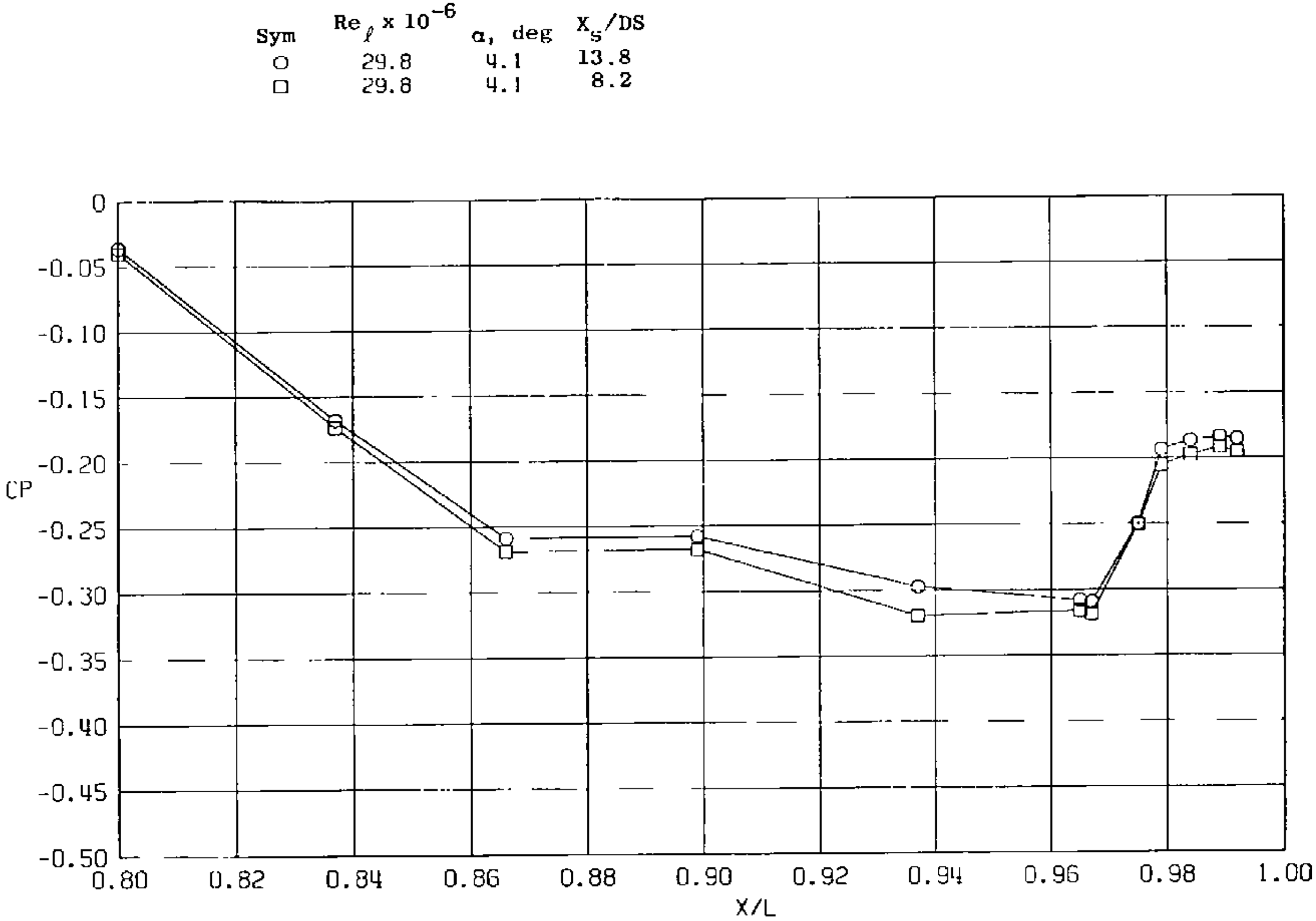

b. ϕ = 45 deg

Figure 25. Continued.

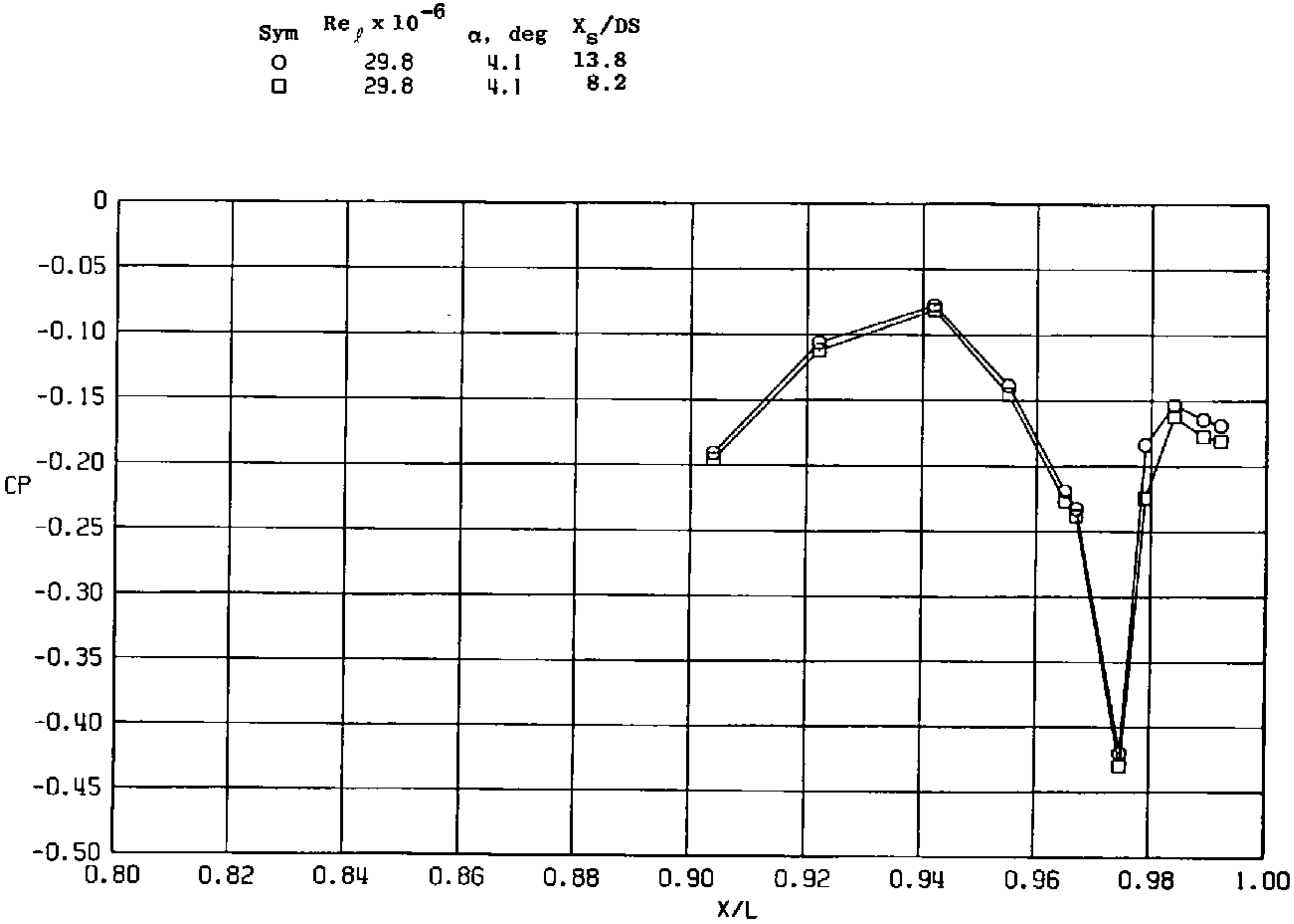

c. ϕ = 135 deg
Figure 25. Continued.

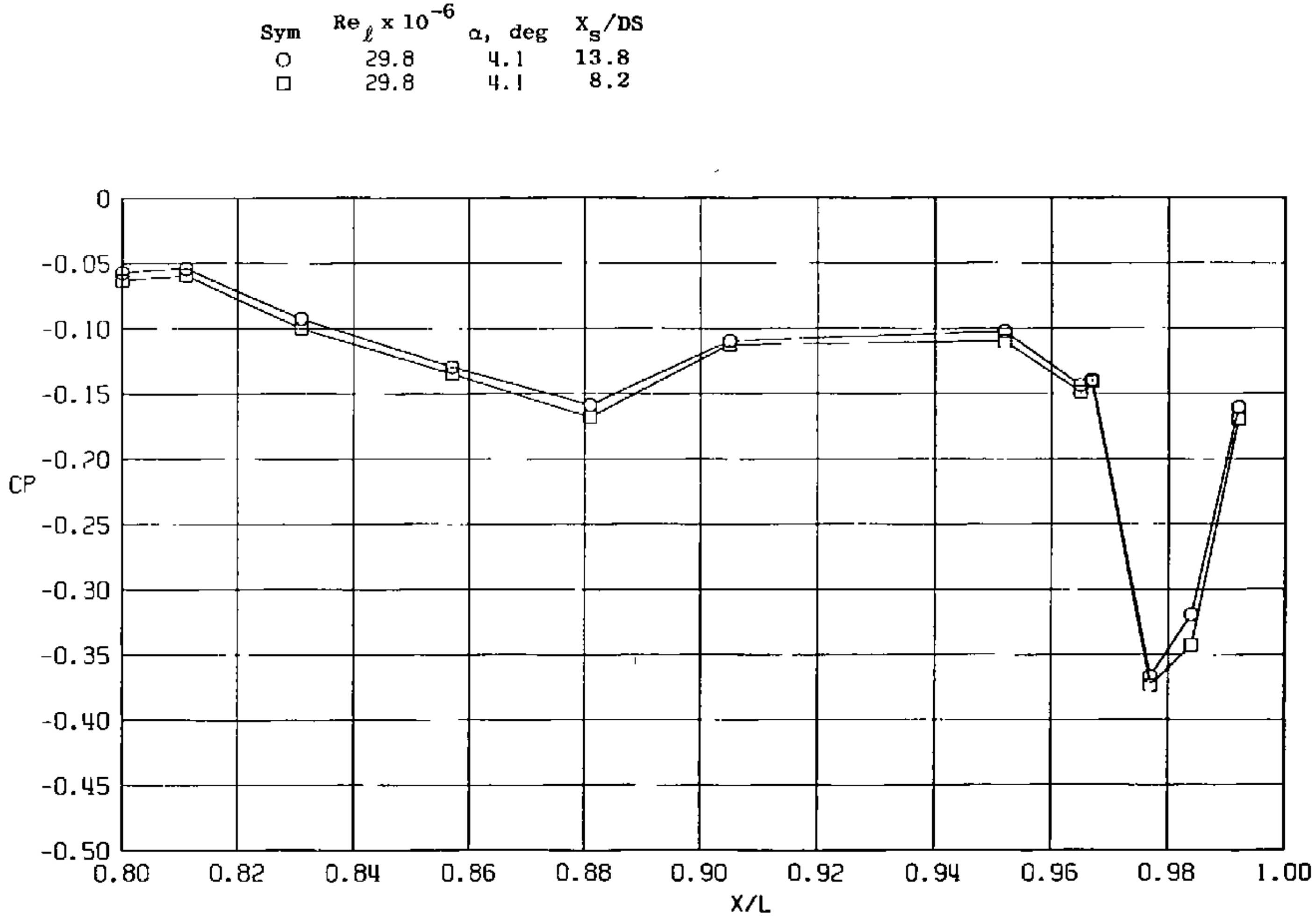

d. ϕ = 180 deg

Figure 25. Continued.

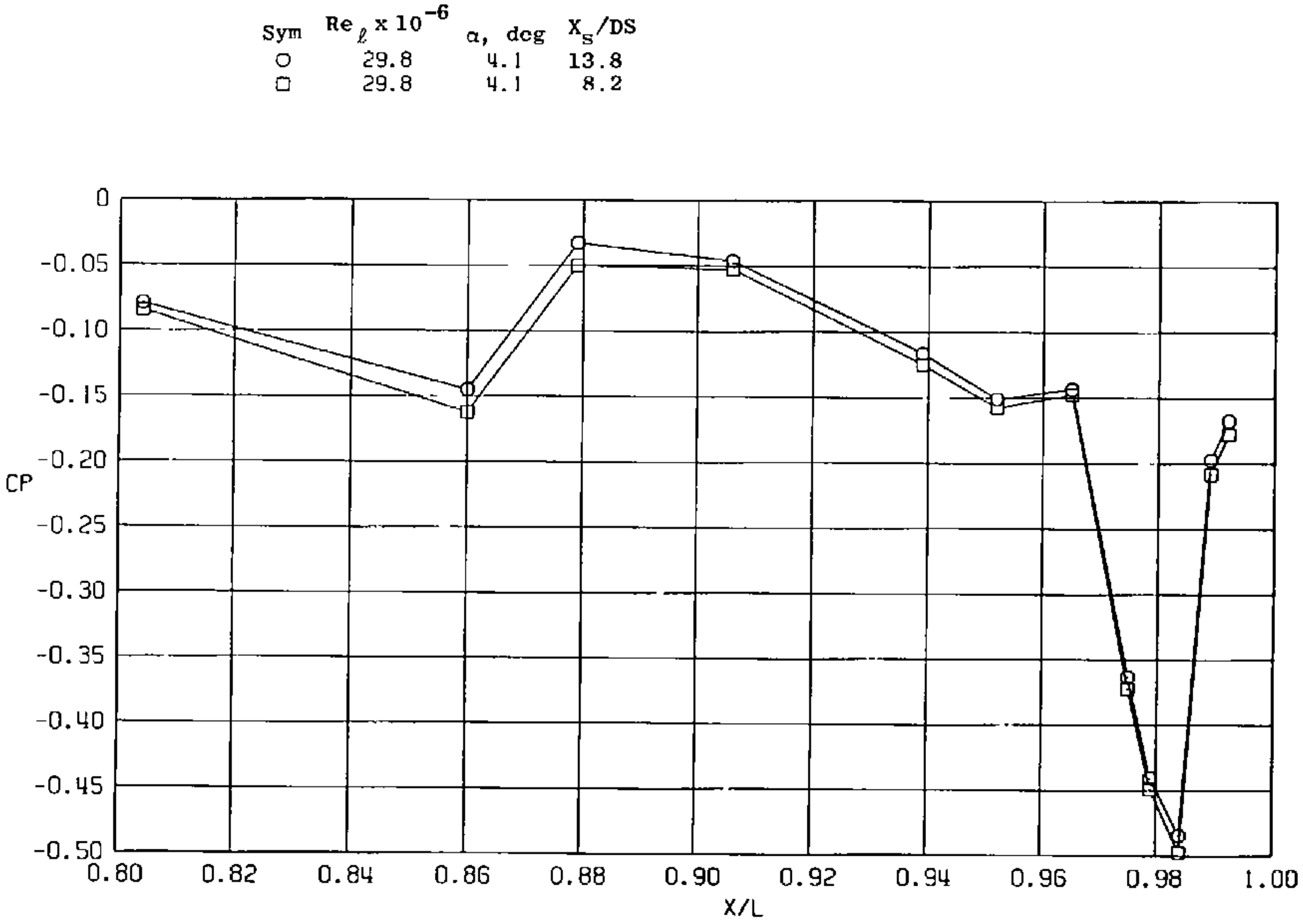

e. ϕ = 225 deg
Figure 25. Continued.

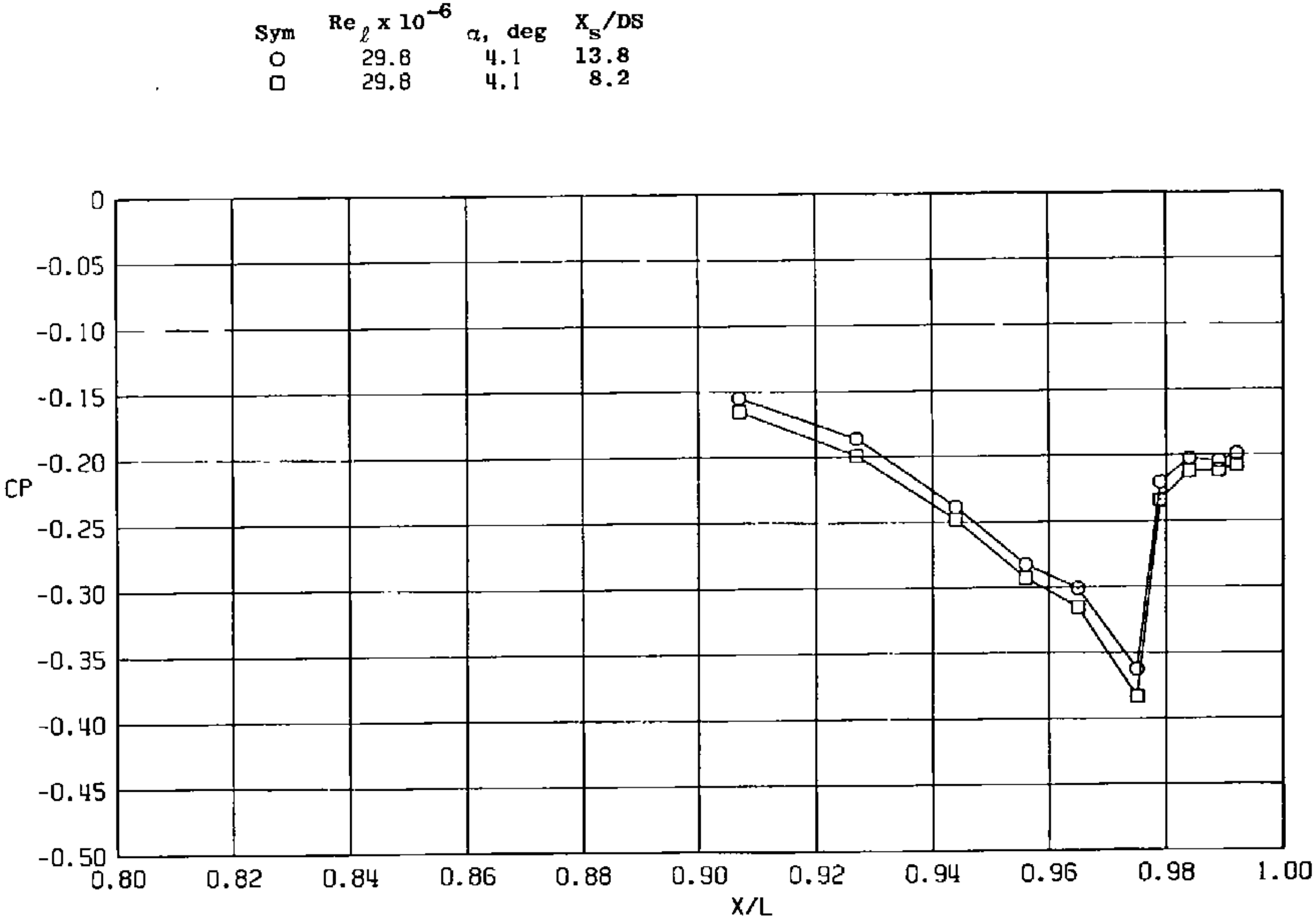

f. ϕ = 315 deg
Figure 25. Concluded.

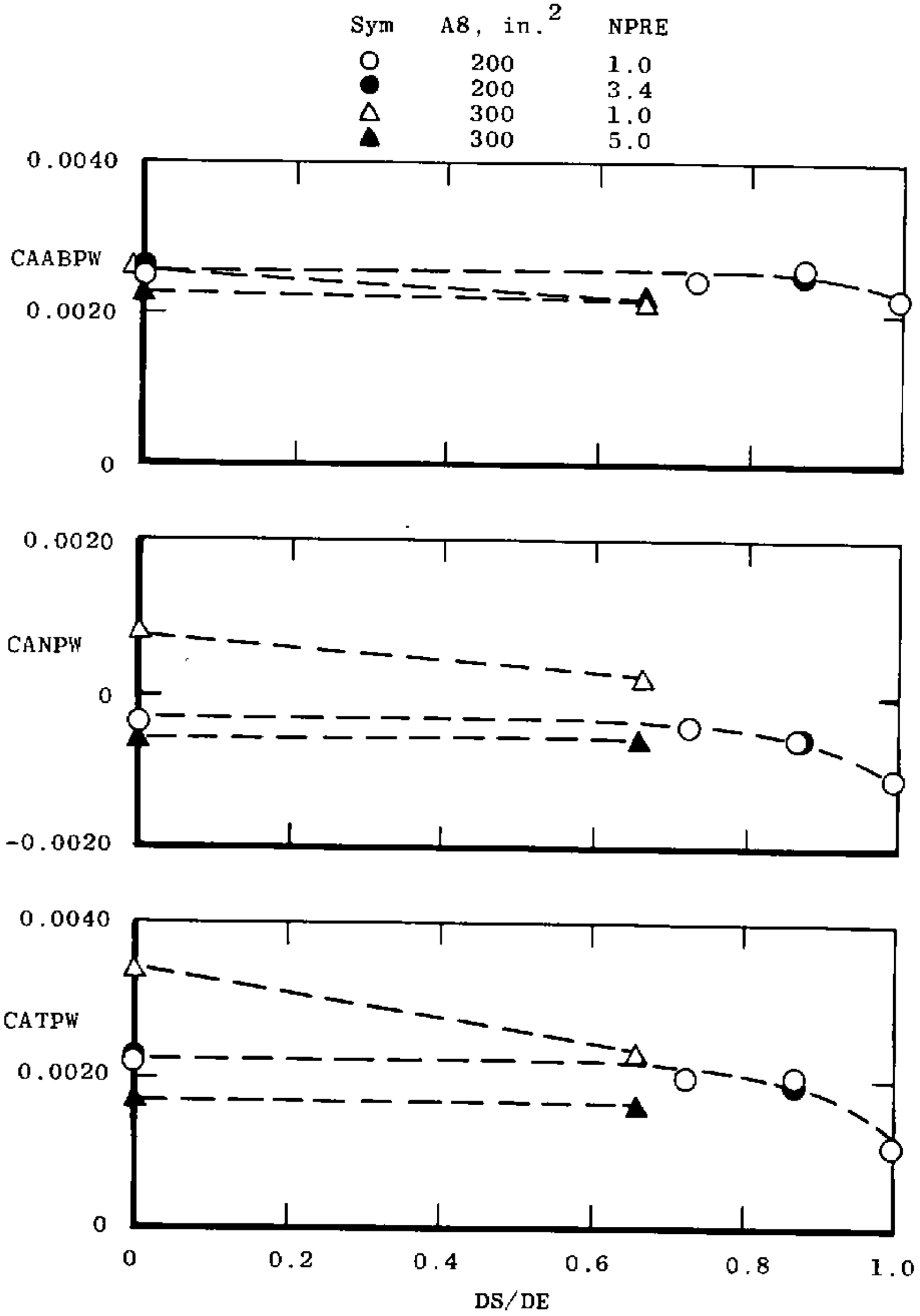

a. M = 0.6

Figure 26. Effect of sting diameter on axial force coefficient (WT).

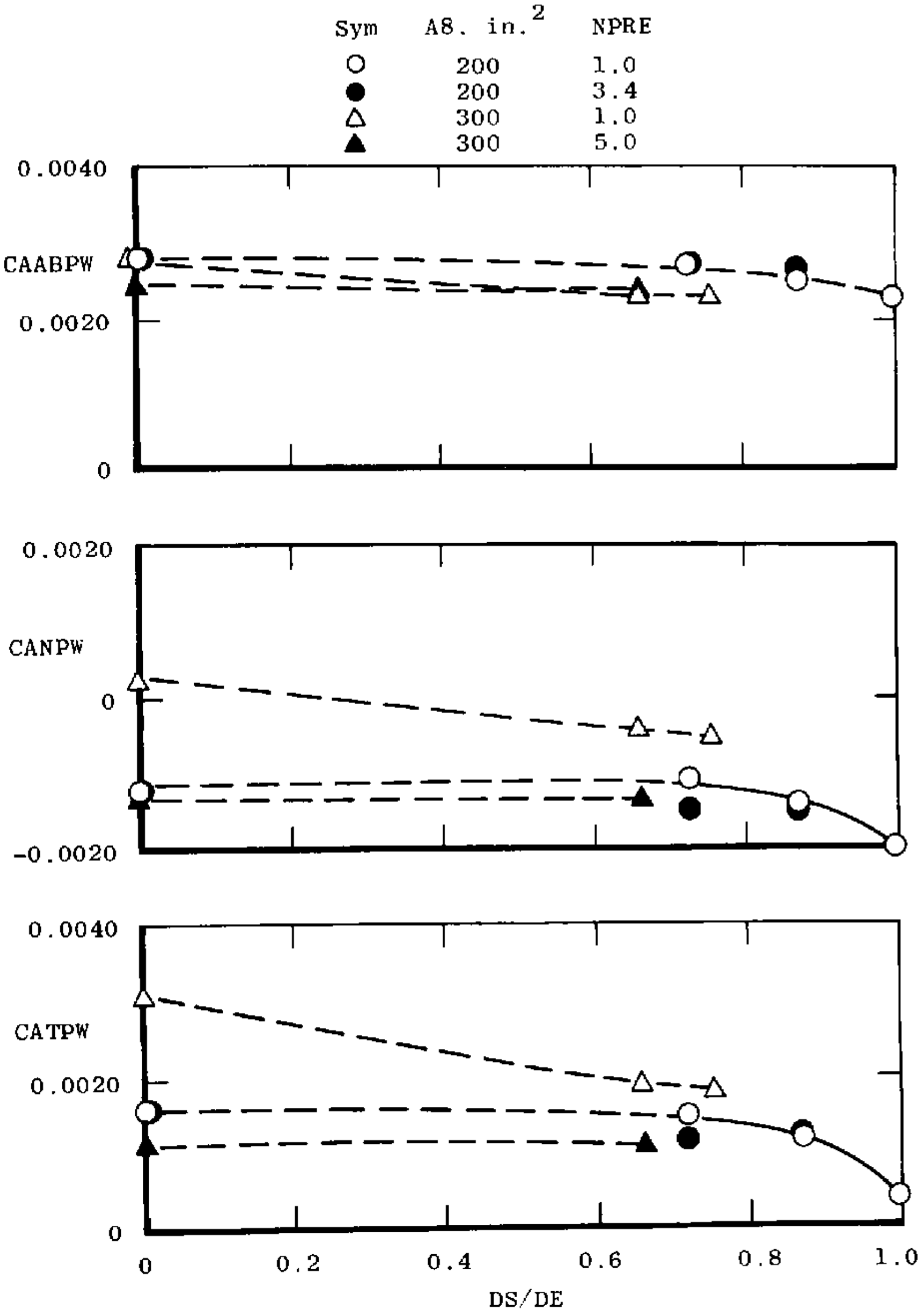

b. M = 0.9

Figure 26. Continued.

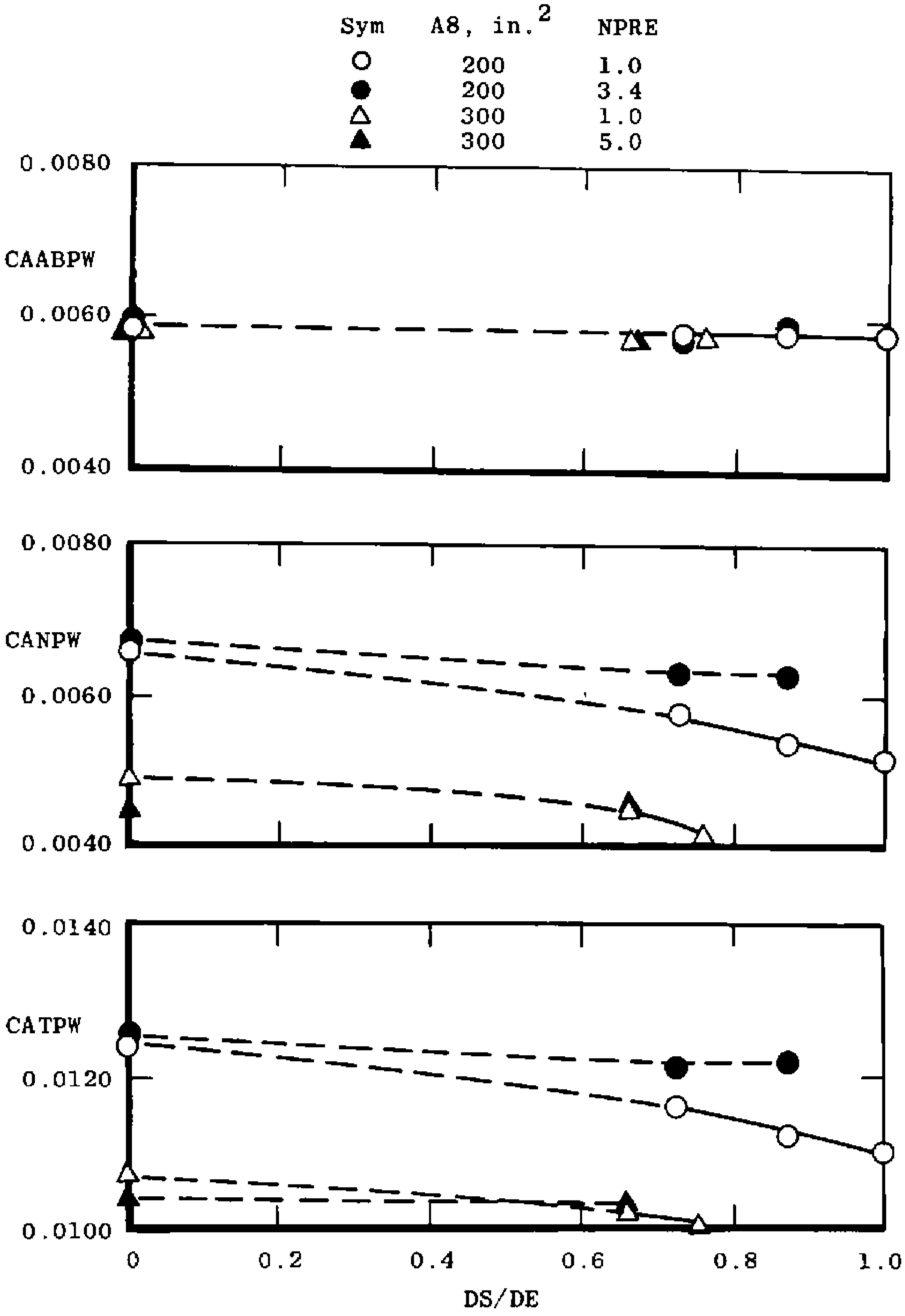

c. M = 1.2
Figure 26. Concluded.

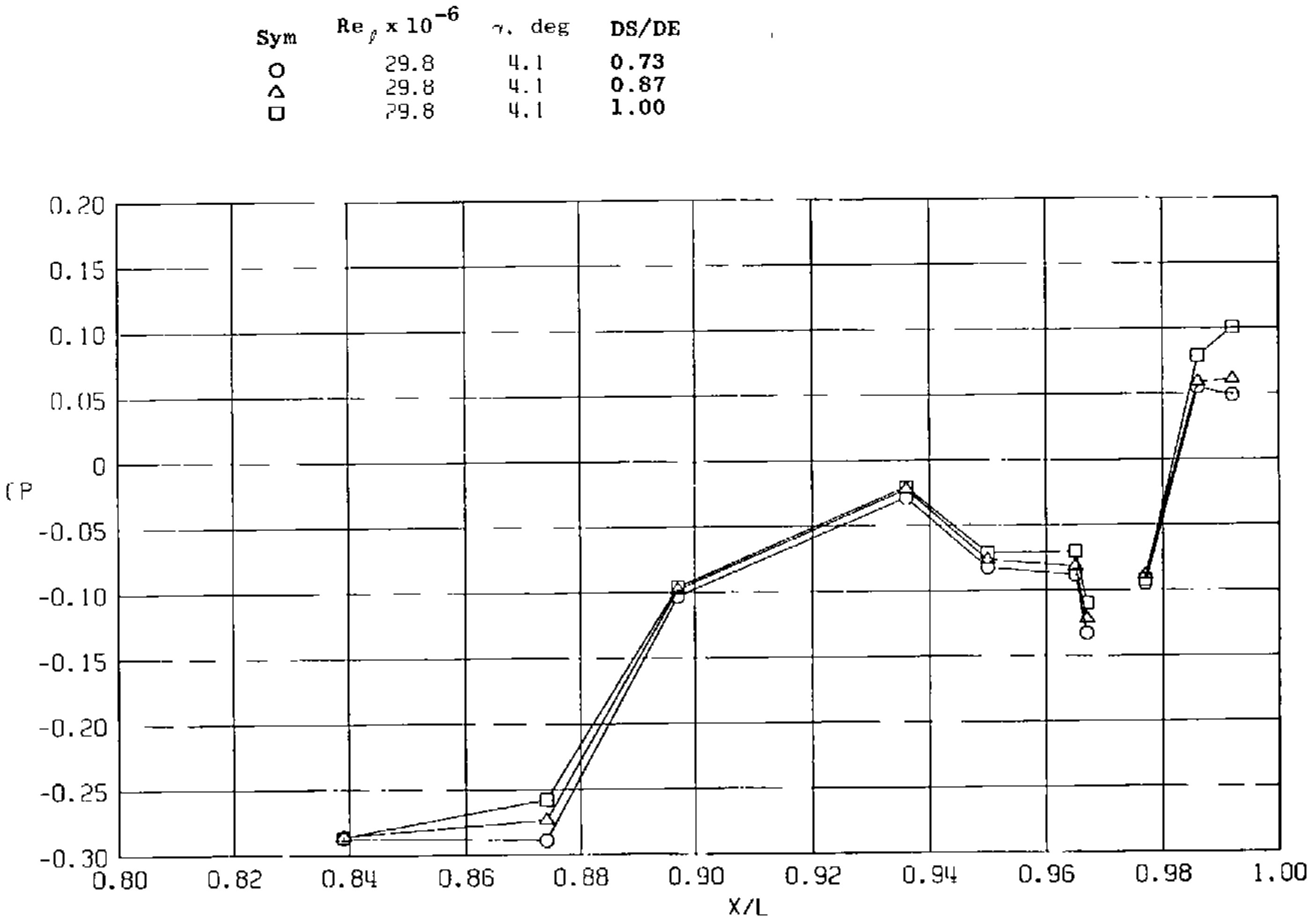

a. $\phi = 0$

Figure 27. Effect of sting diameter on surface pressure coefficients, A8 = 200 in.^{2}, M = 0.9 (WT), NPR = 1.0.

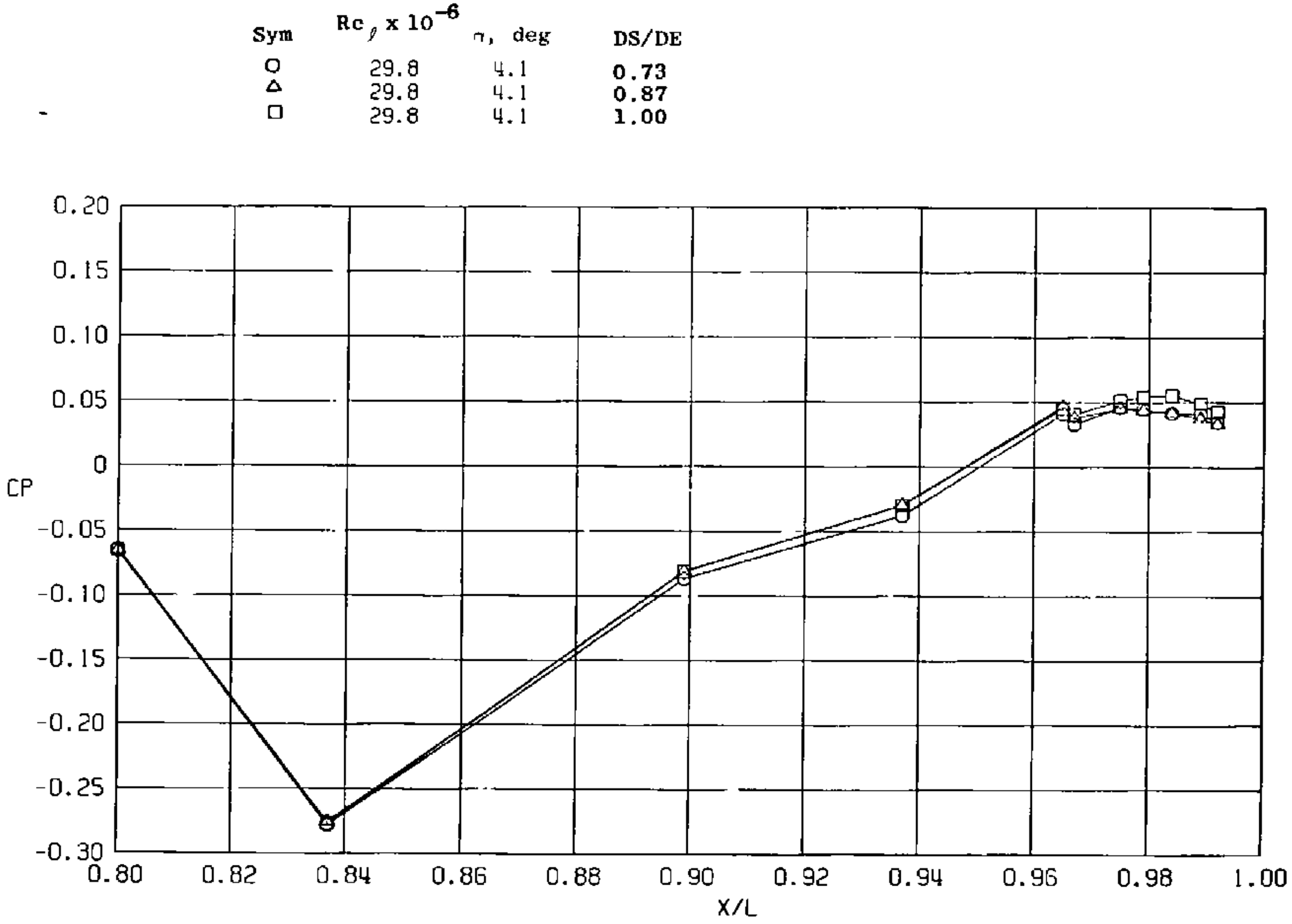

b. ϕ = 45 deg
Figure 27. Continued.

Sym	$Re_{\ell} \times 10^{-6}$	α, deg	DS/DE
○	29.8	4.1	0.73
△	29.8	4.1	0.87
□	29.8	4.1	1.00

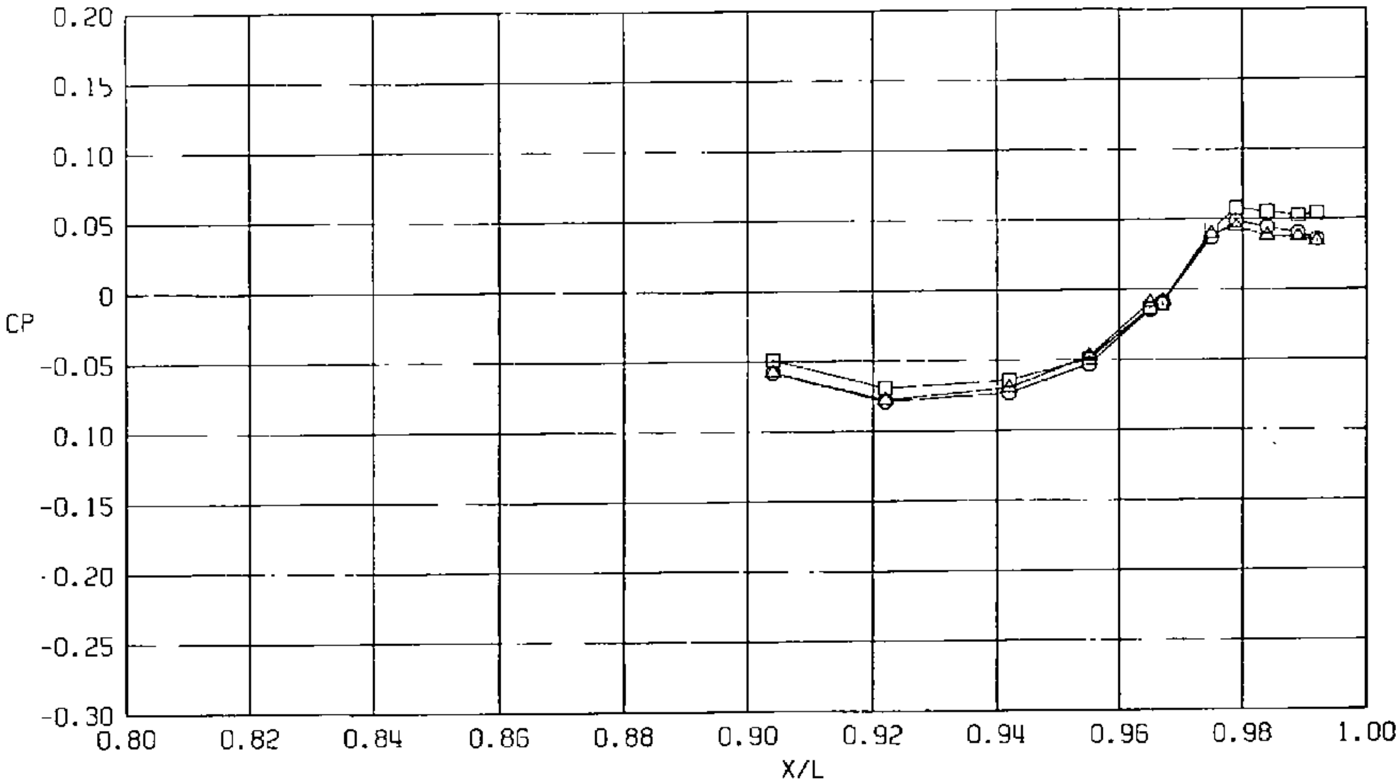

c. ϕ = 135 deg

Figure 27. Continued.

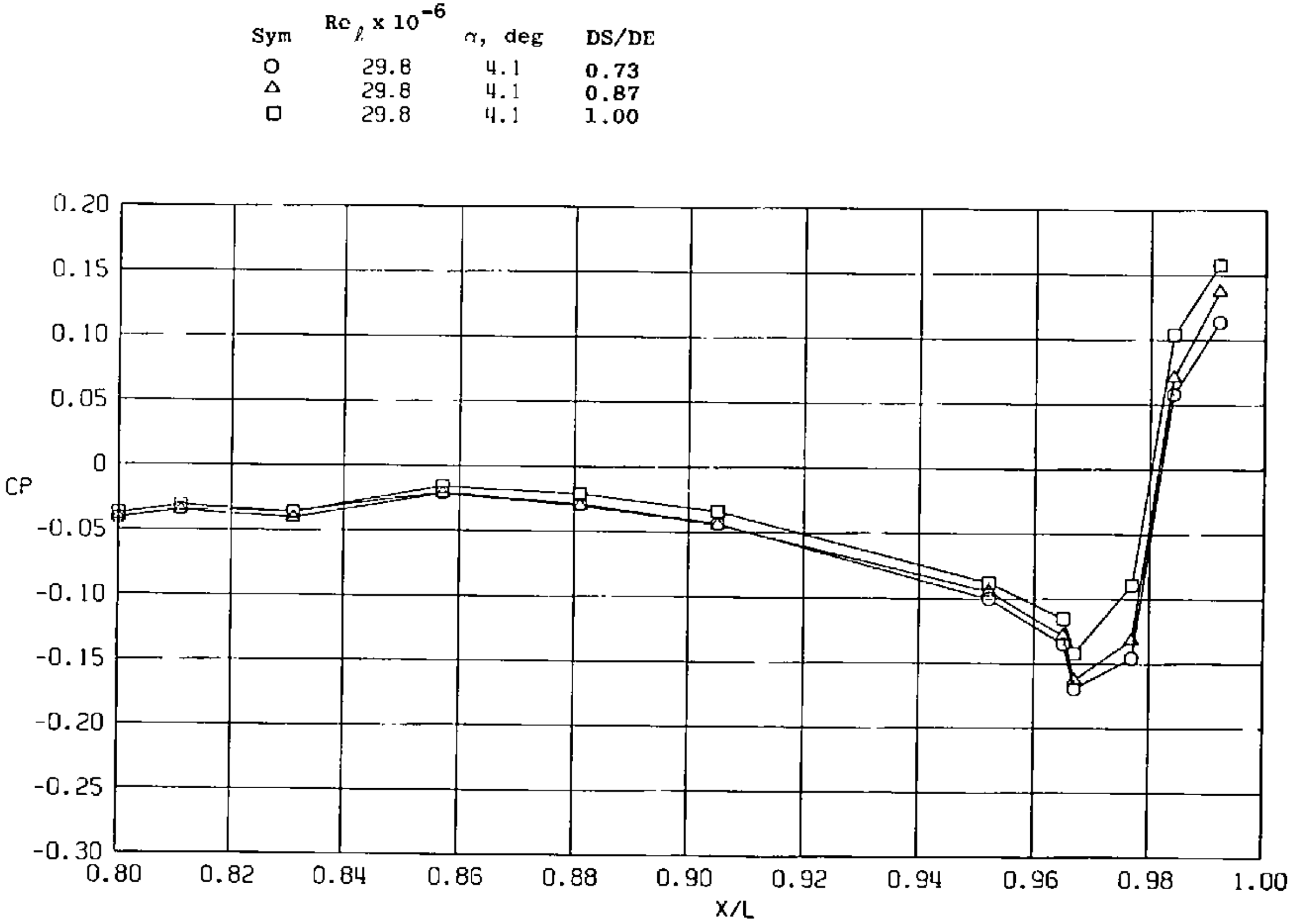

d. ϕ = 180 deg
Figure 27. Continued.

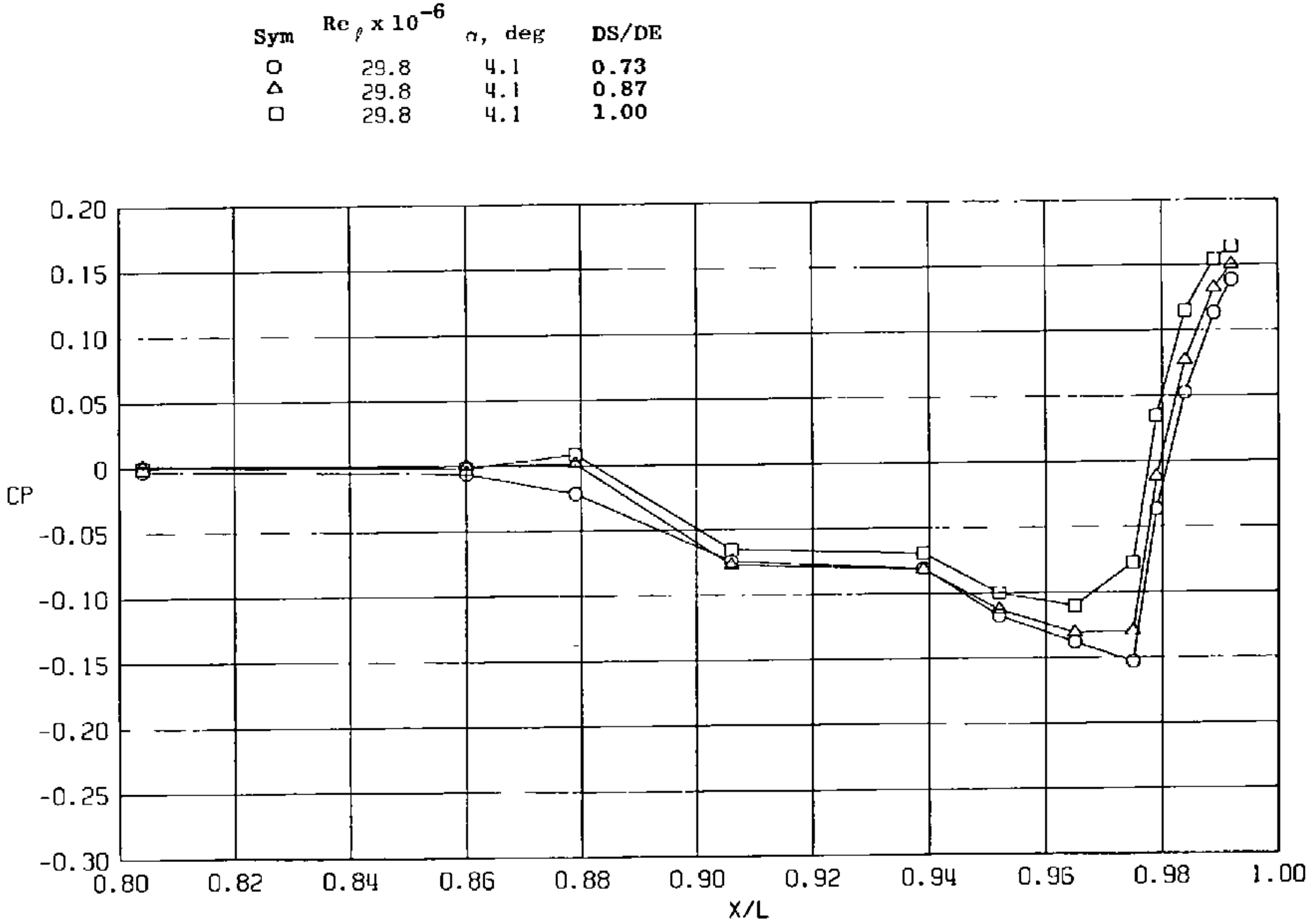

e. ϕ = 225 deg
Figure 27. Continued.

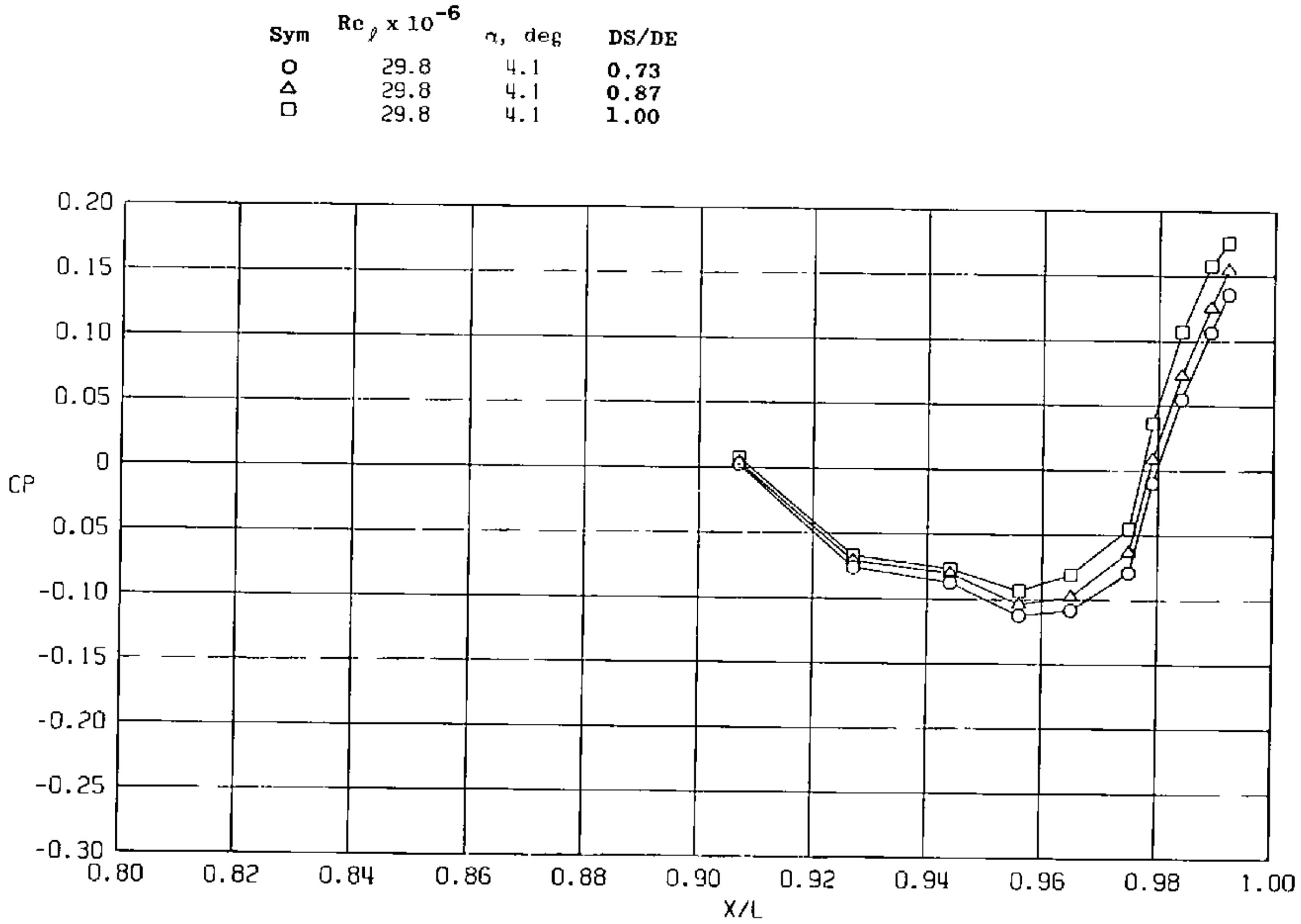

f. ϕ = 315 deg
Figure 27. Concluded.

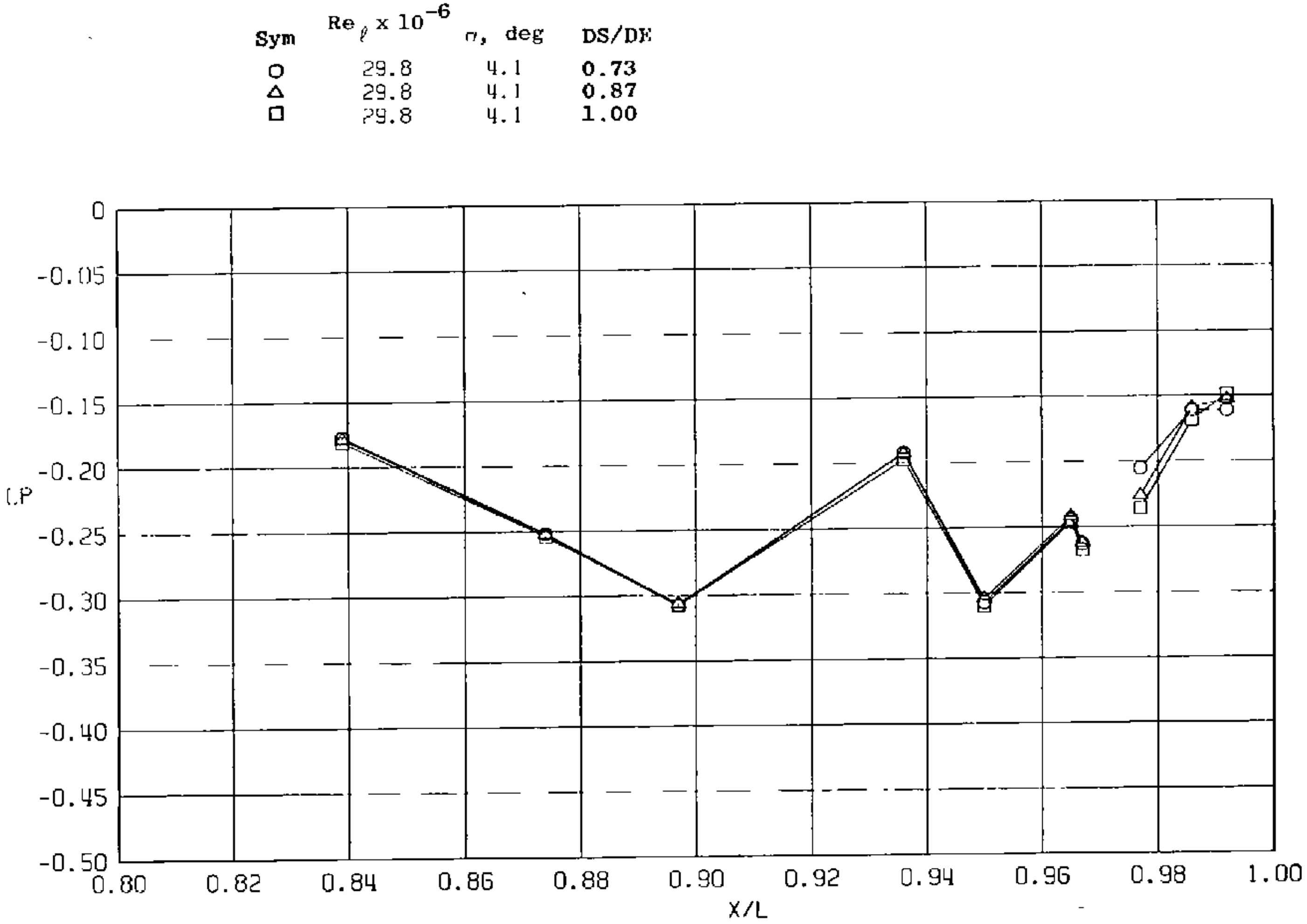

a. ϕ = 0

Figure 28. Effect of sting diameter on surface pressure coefficients, A8 = 200 in.^{2}, M = 1.2 (WT), NPR = 1.0.

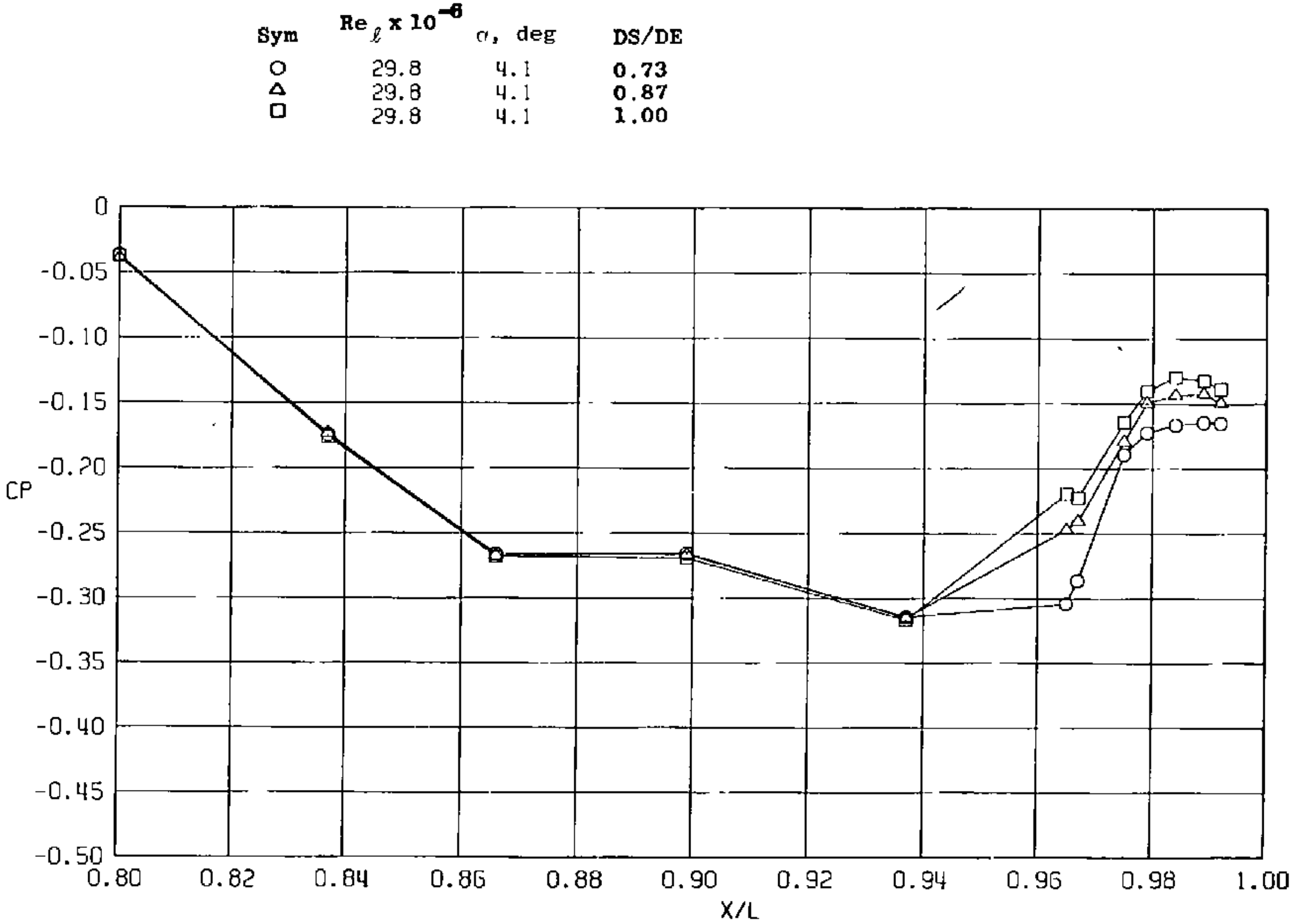

b. ϕ = 45 deg
Figure 28. Continued.

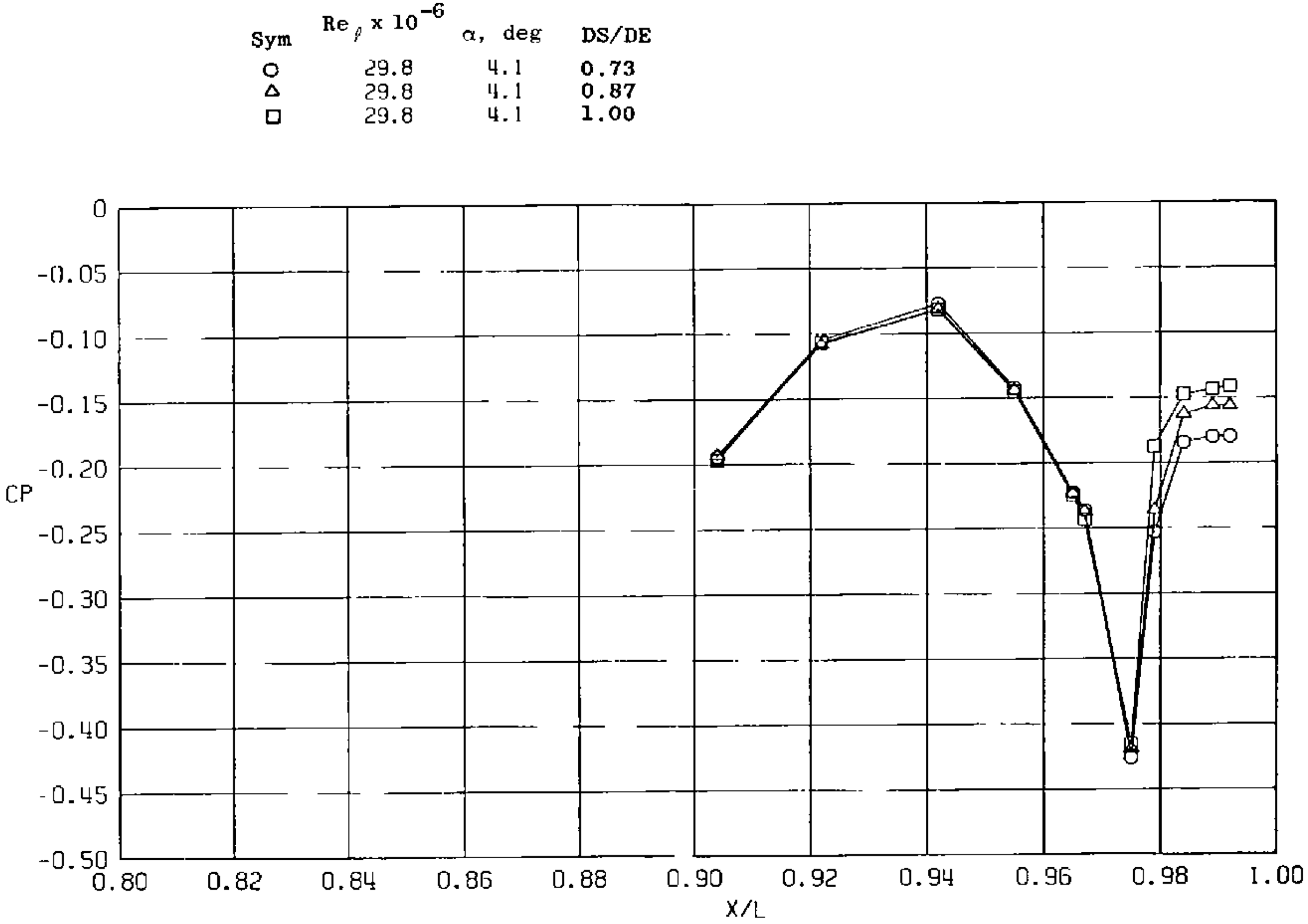

c. ϕ = 135 deg
Figure 28. Continued.

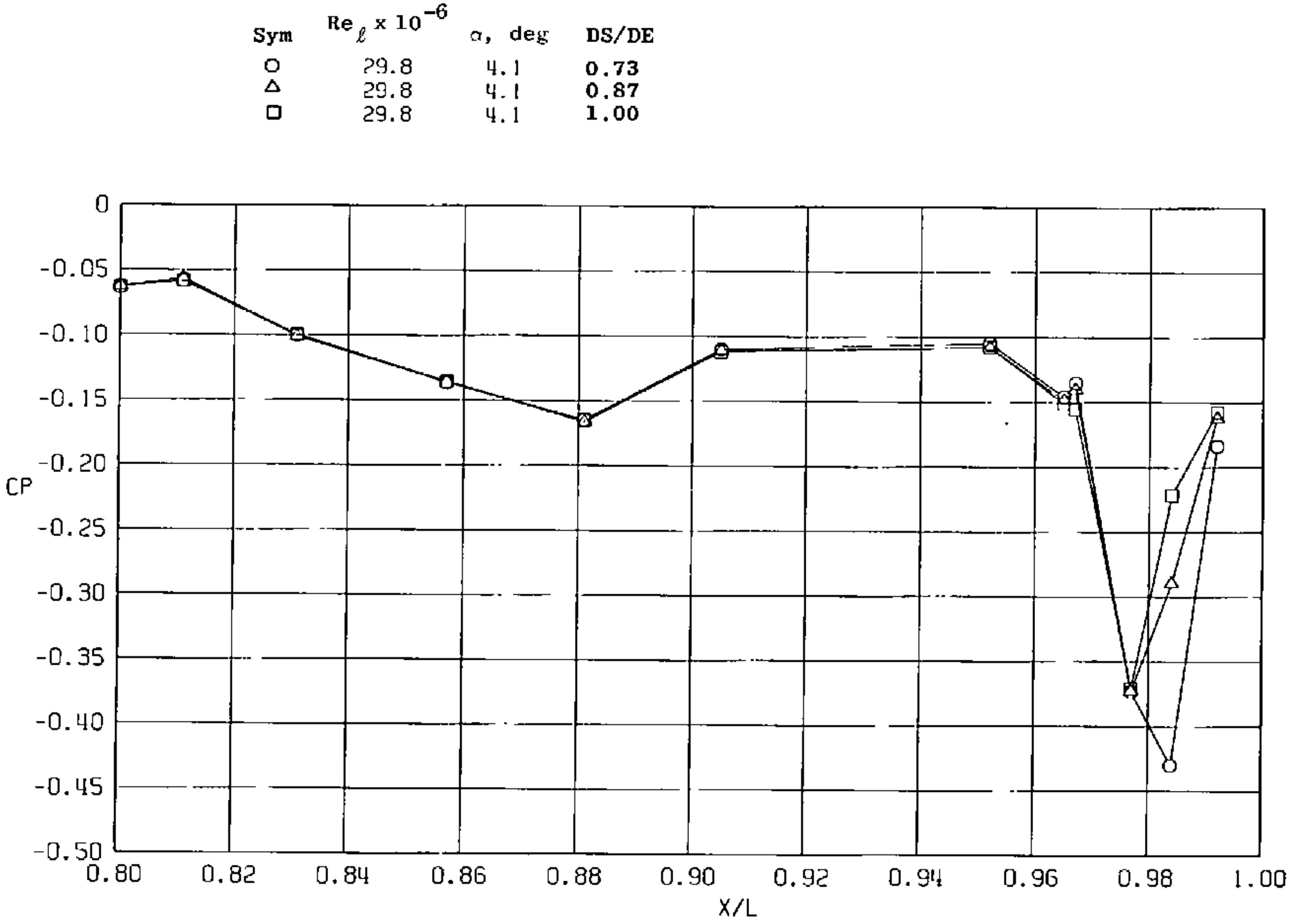

d. ϕ = 180 deg
Figure 28. Continued.

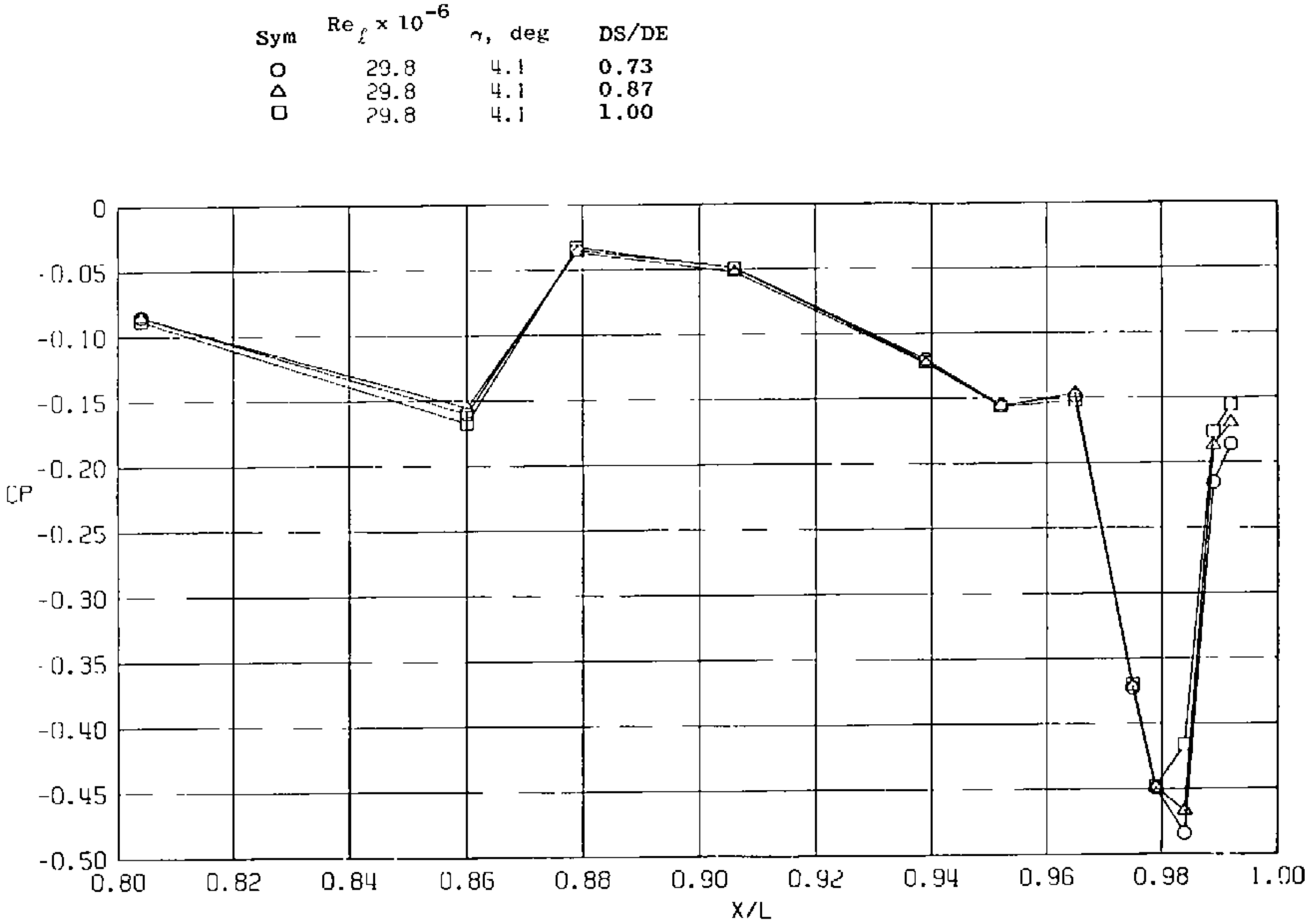

e. ϕ = 225 deg
Figure 28. Continued.

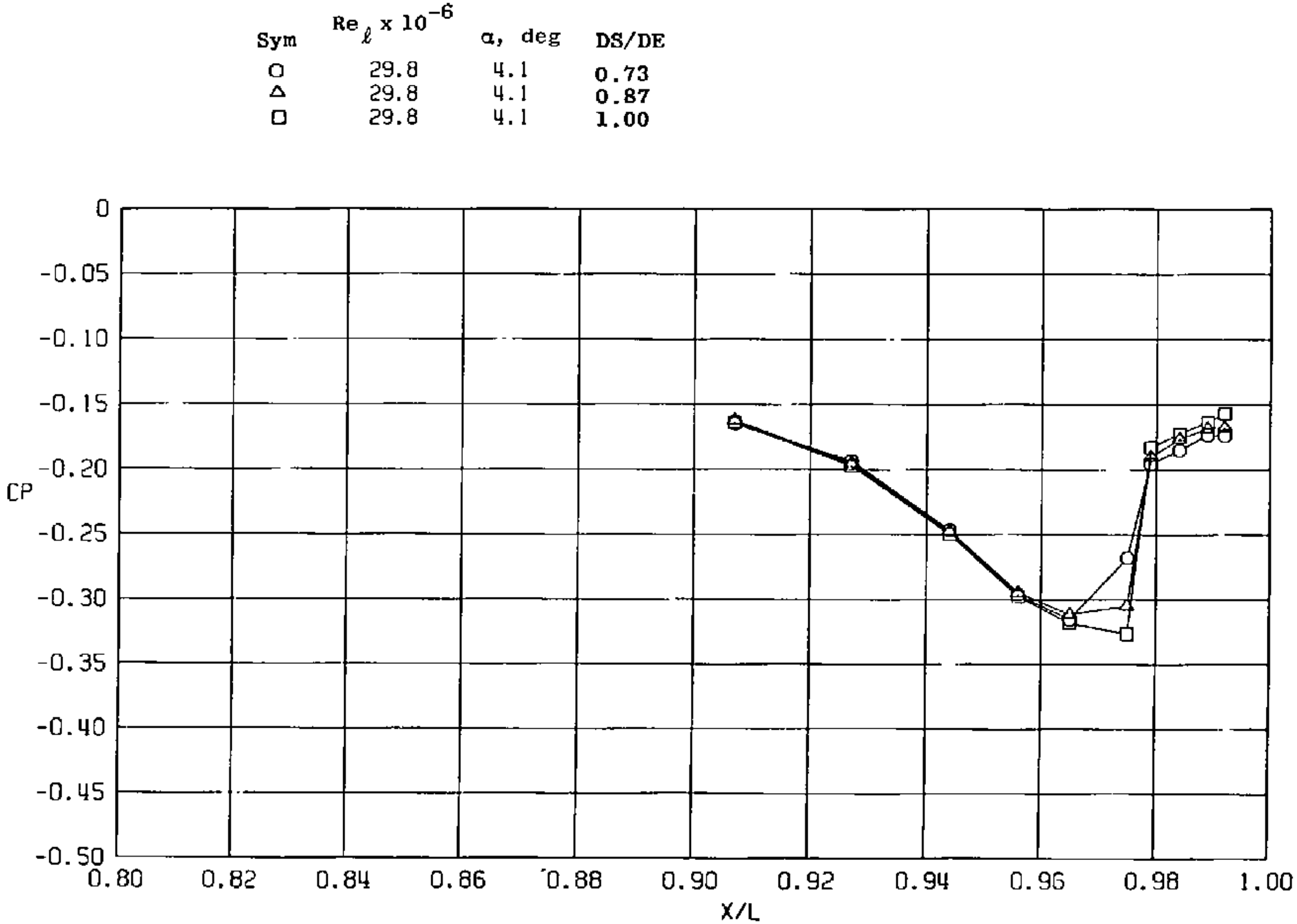

f. ϕ = 315 deg
Figure 28. Concluded.

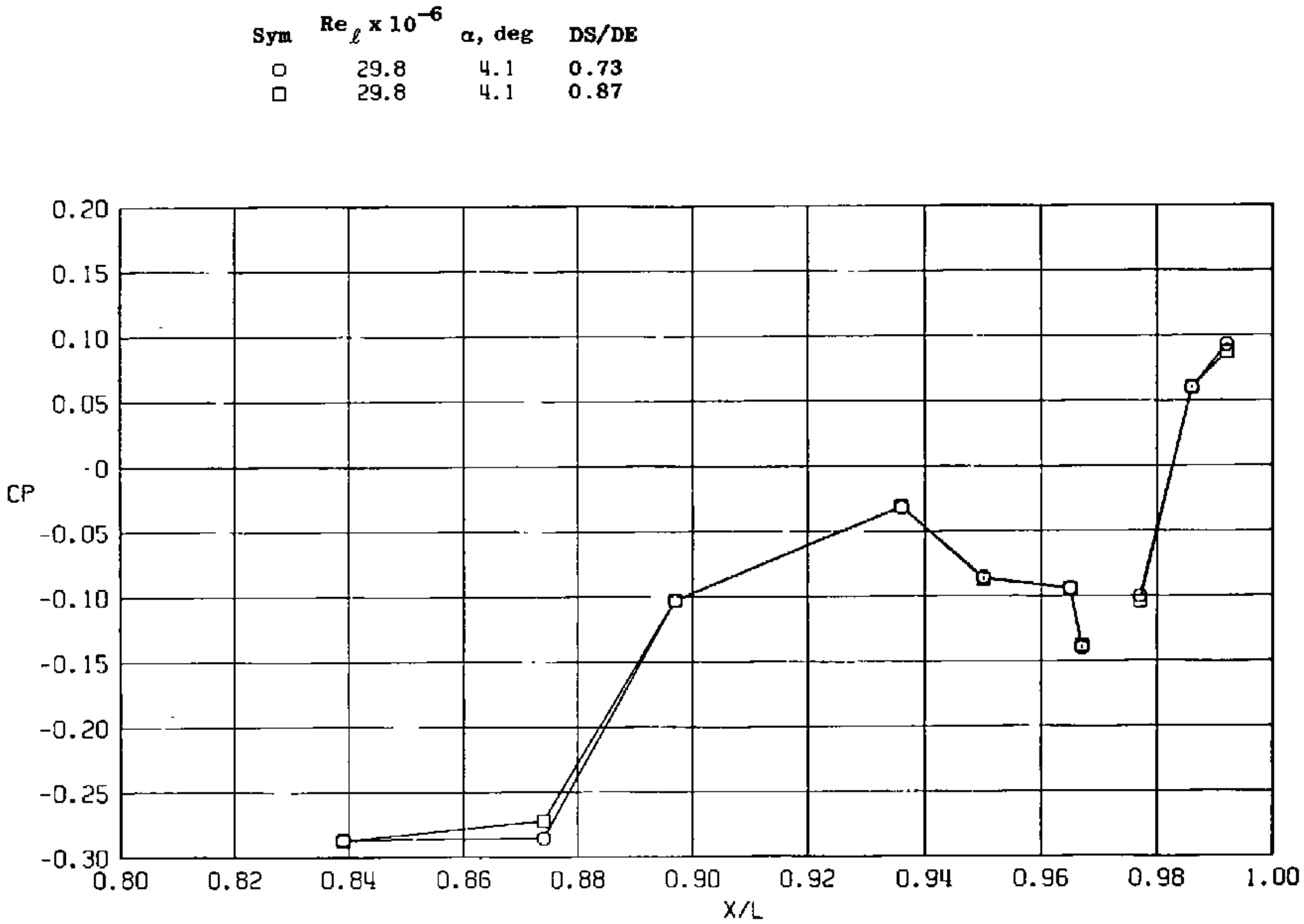

a. $\phi = 0$

Figure 29. Effect of sting diameter on surface pressure coefficients, A8 = 200 in.^{2}, M = 0.9 (WT), NPRE = 3.4.

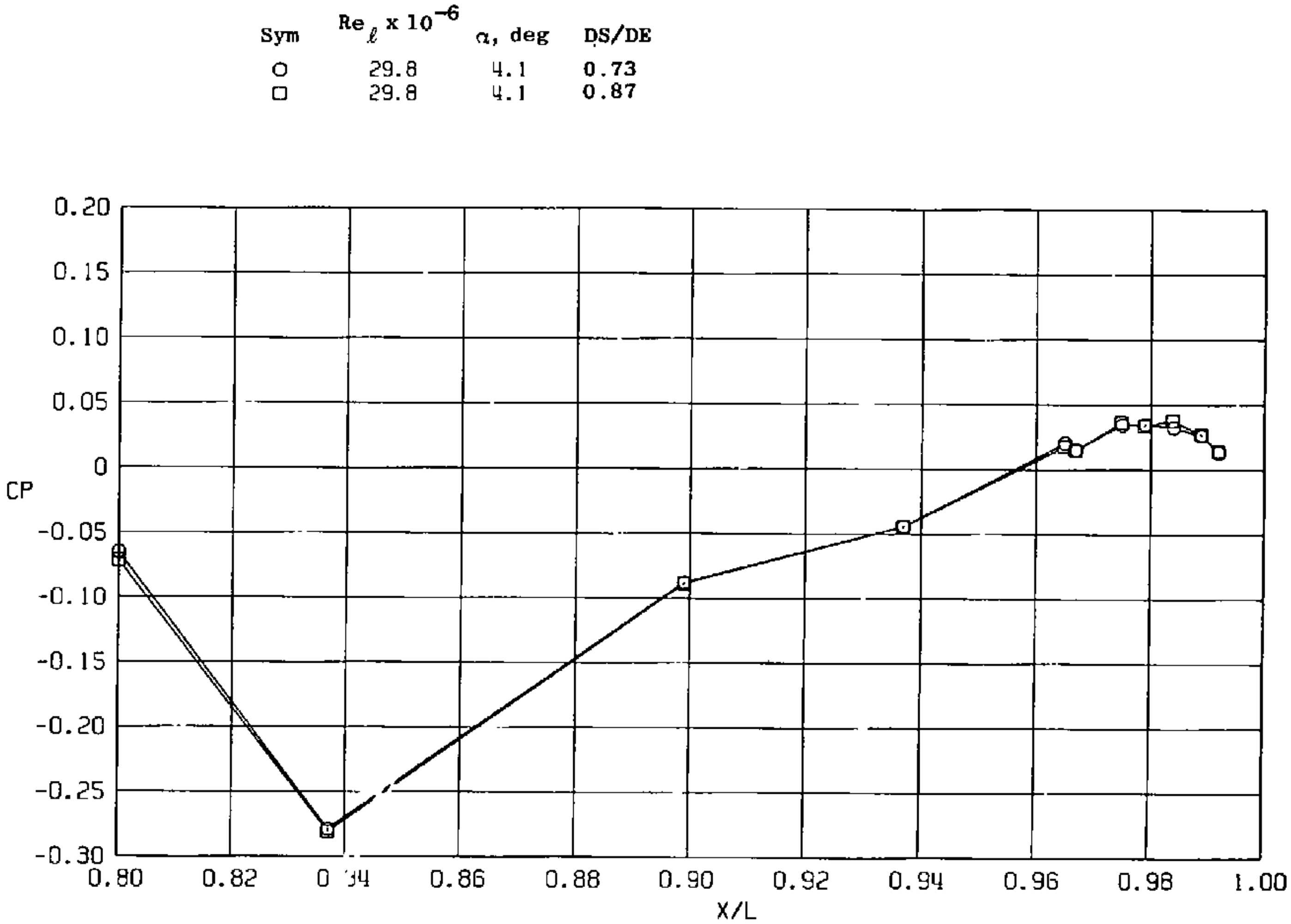

b. ϕ = 45 deg
Figure 29. Continued.

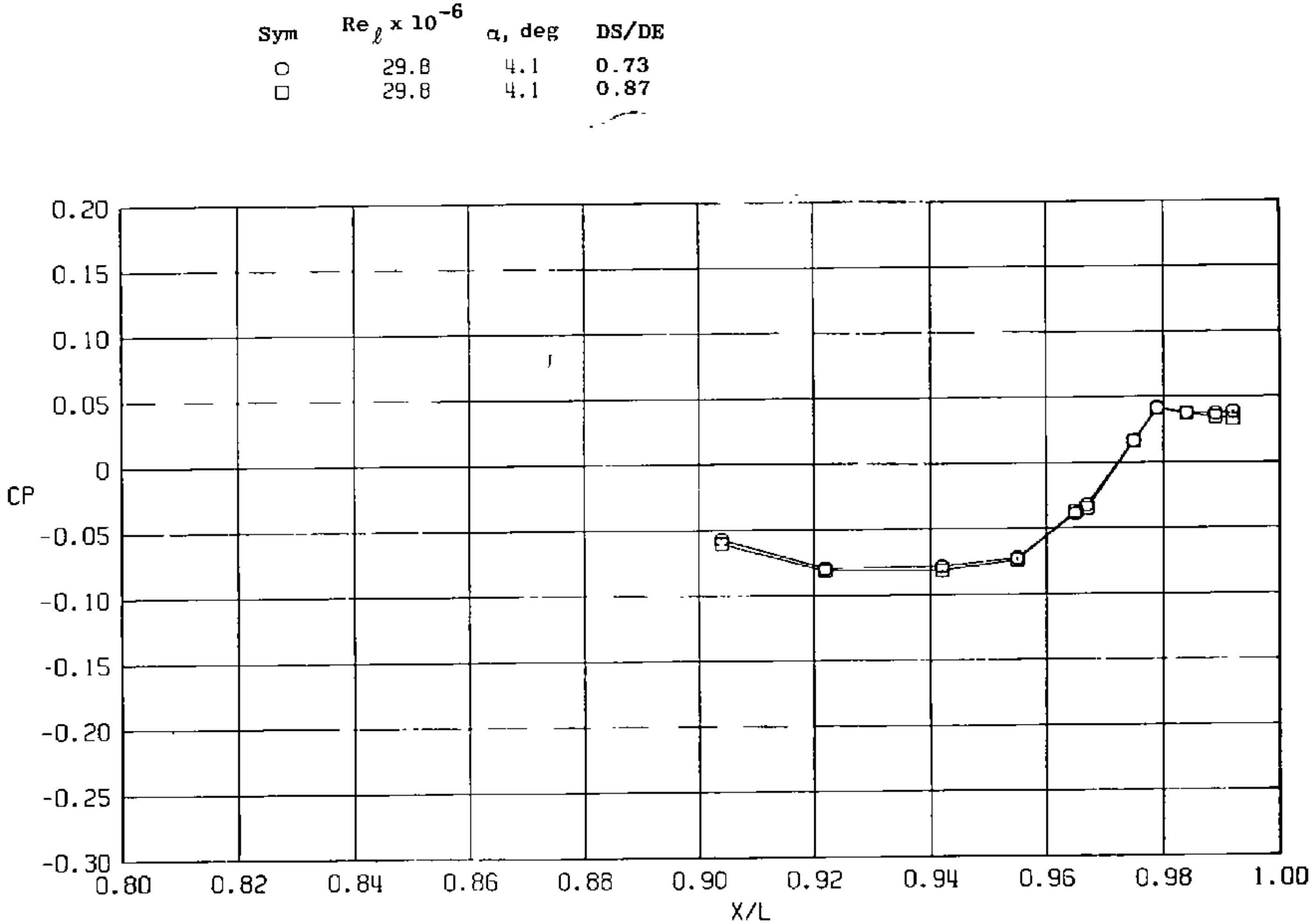

c. ϕ = 135 deg

Figure 29. Continued.

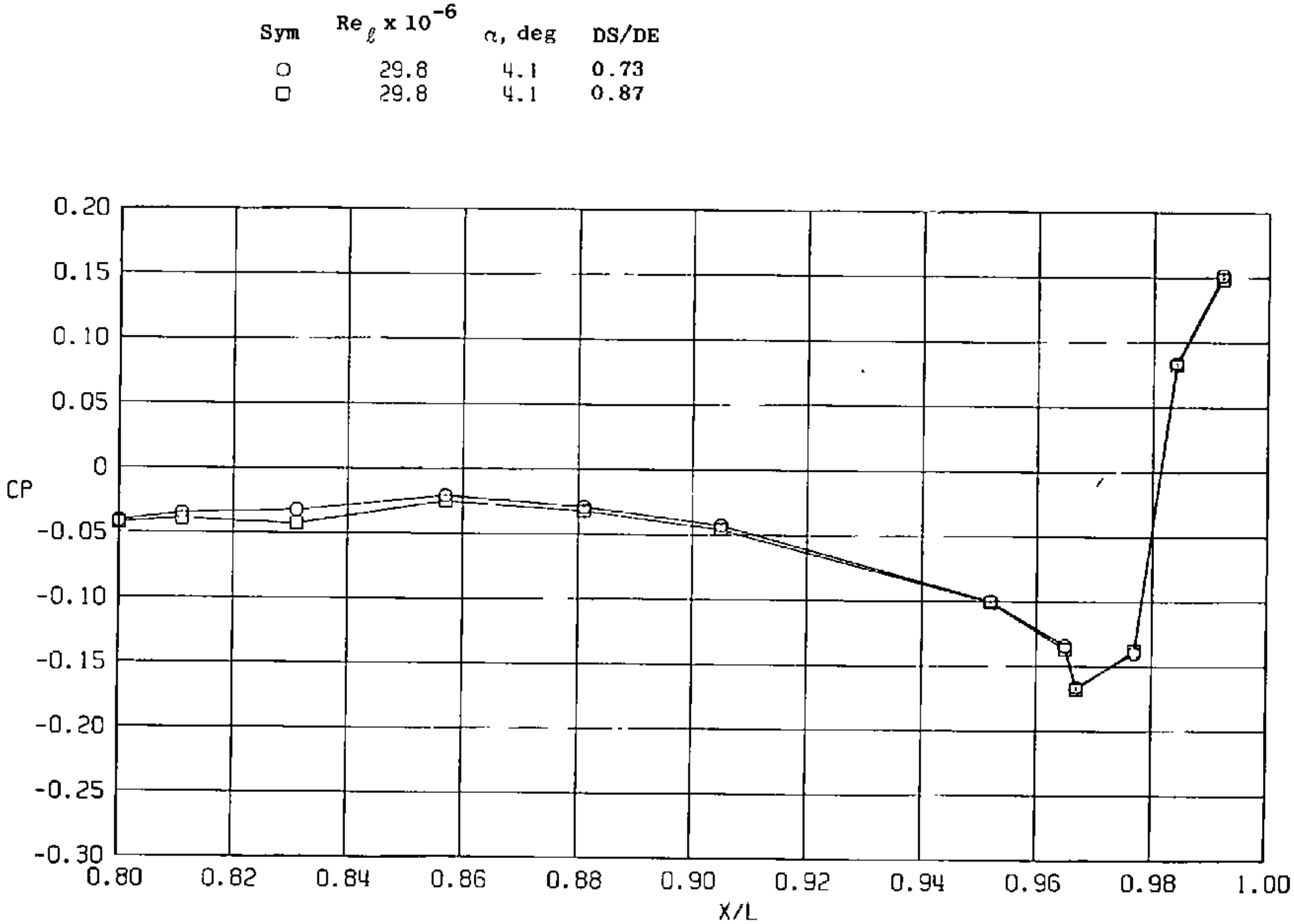

d. ϕ = 180 deg

Figure 29. Continued.

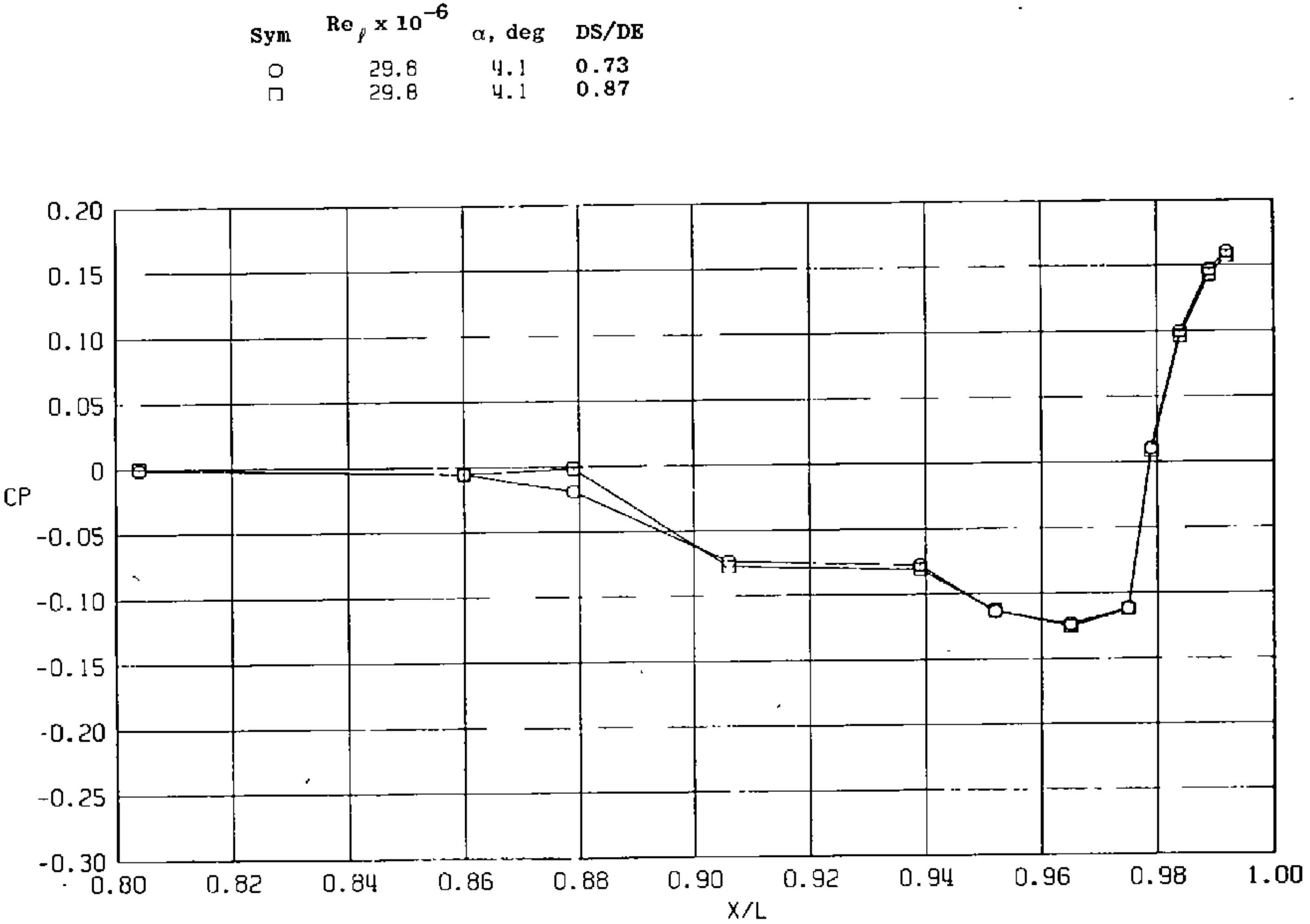

e. ϕ = 225 deg
Figure 29. Continued.

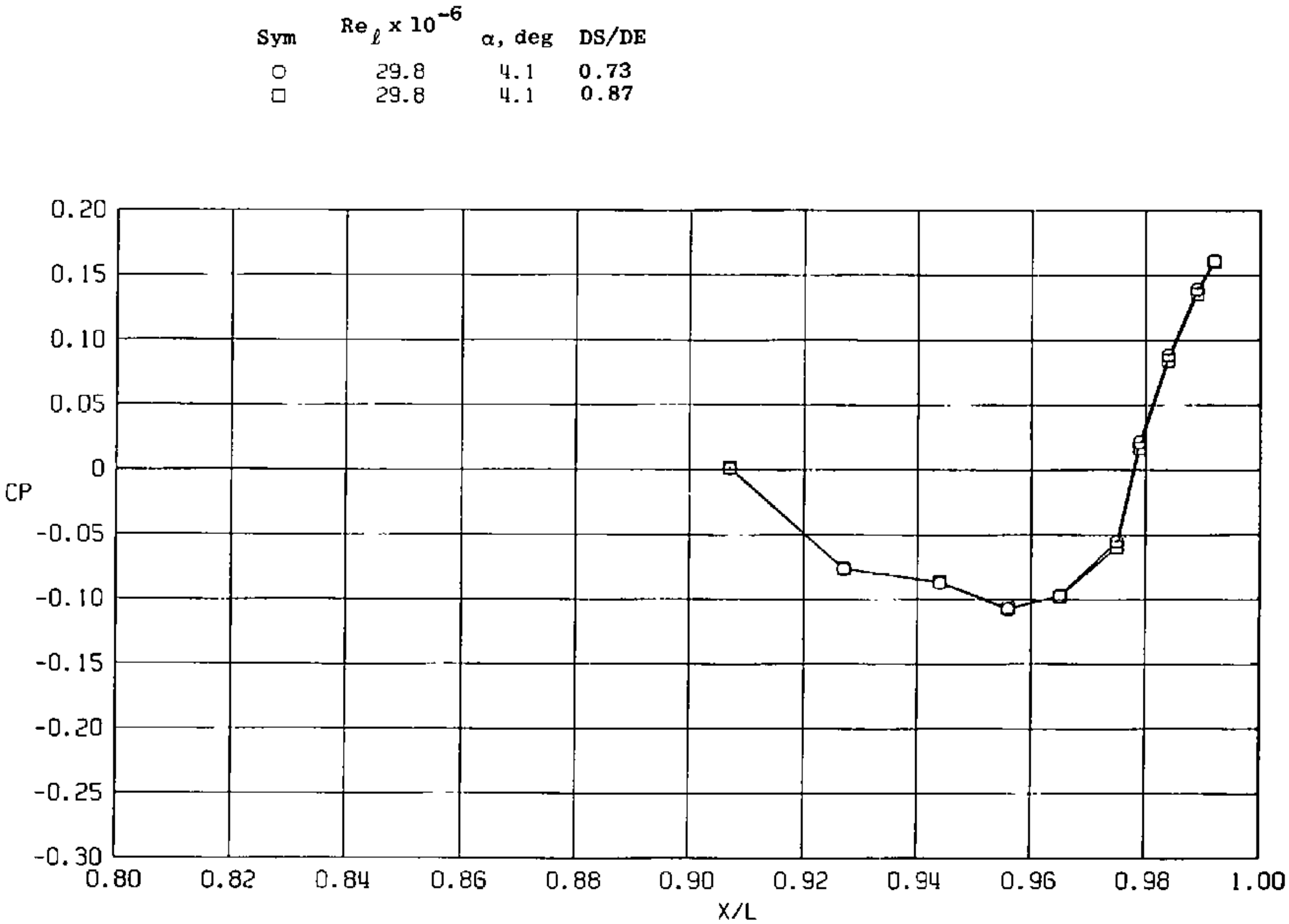

f. ϕ = 315 deg
Figure 29. Concluded.

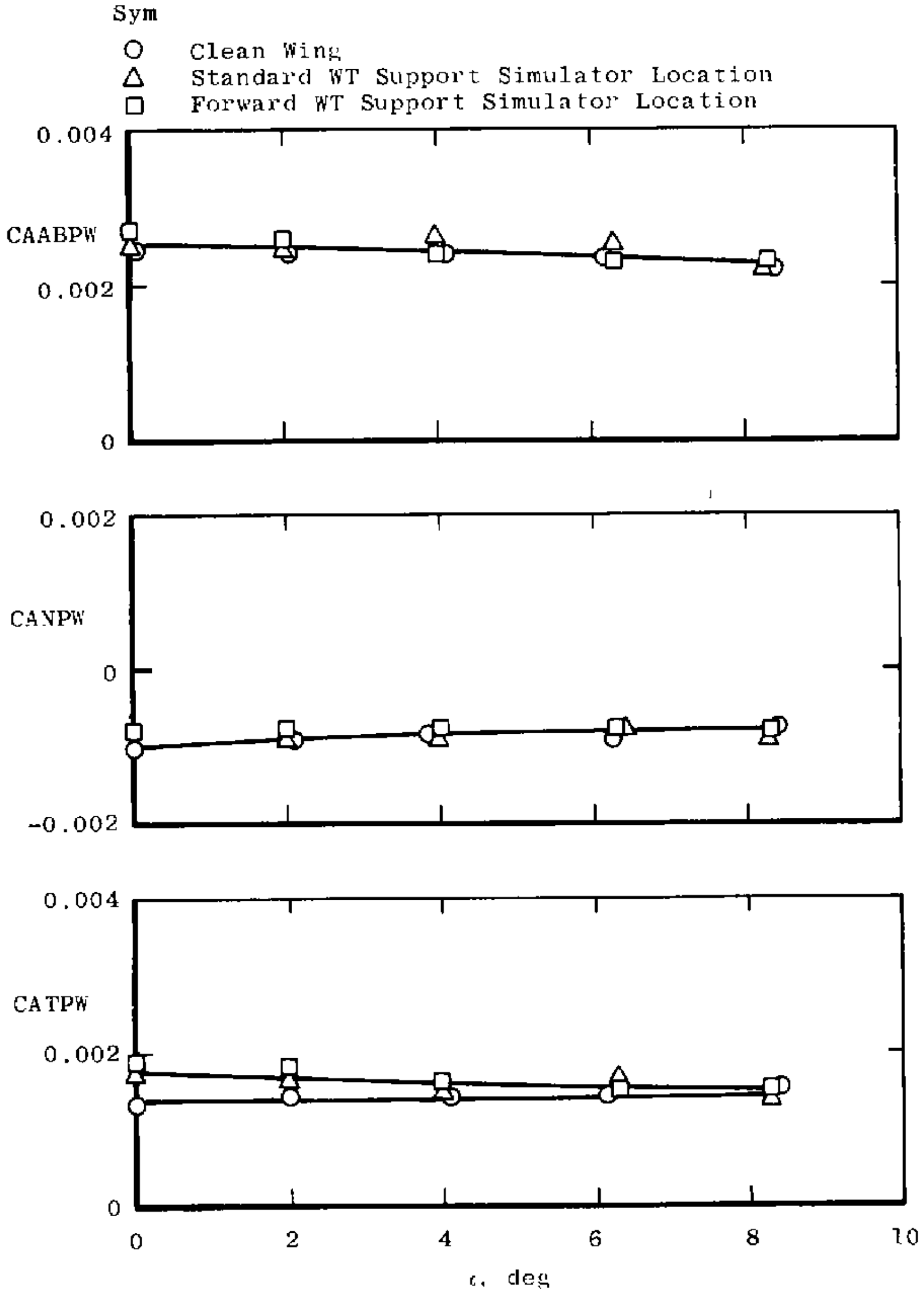

a. M = 0.6

Figure 30. Wingtip support system simulation effects on axial force coefficients, A8 = 200 in.^{2} (LS).

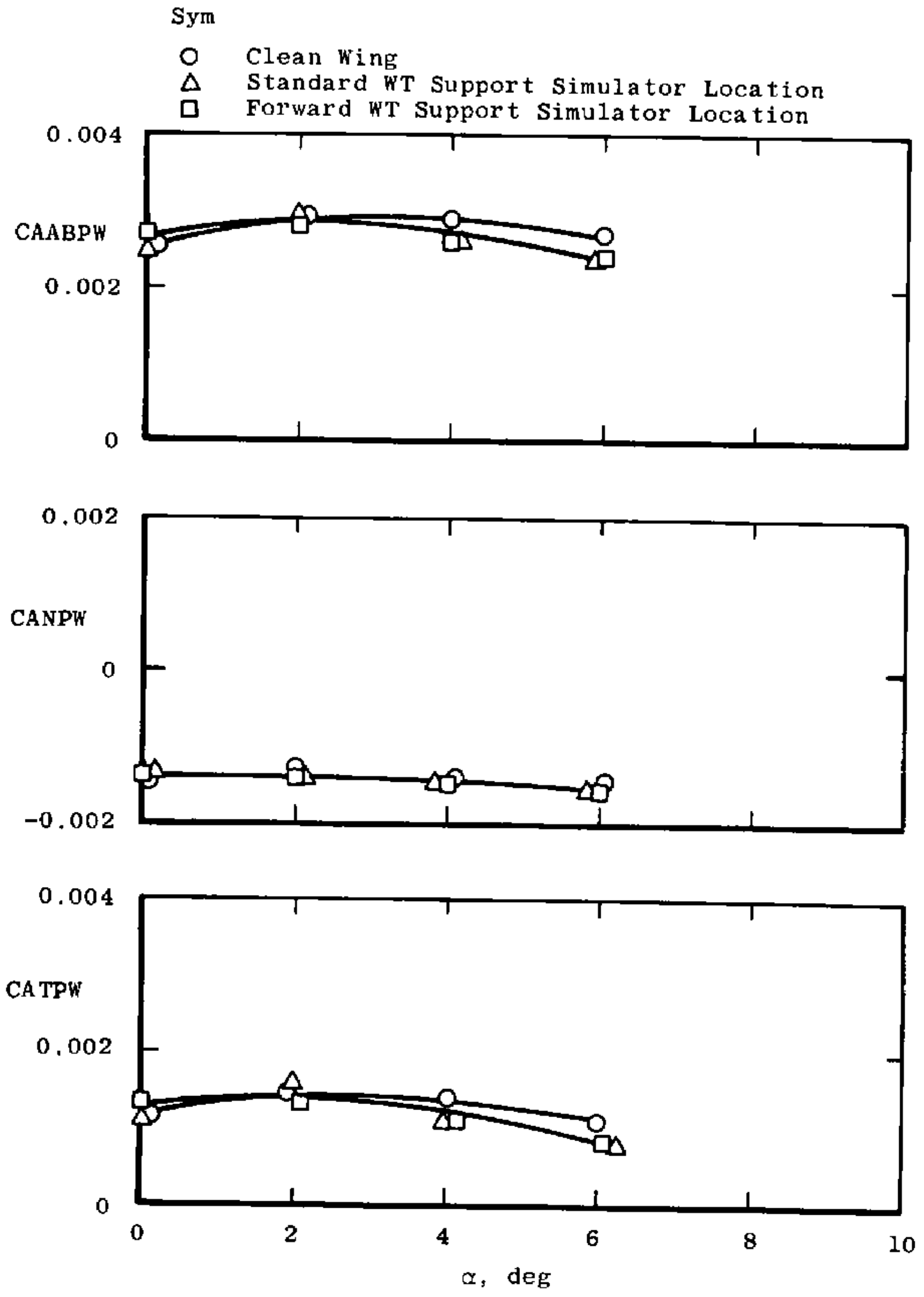

b. M = 0.9
Figure 30. Continued.

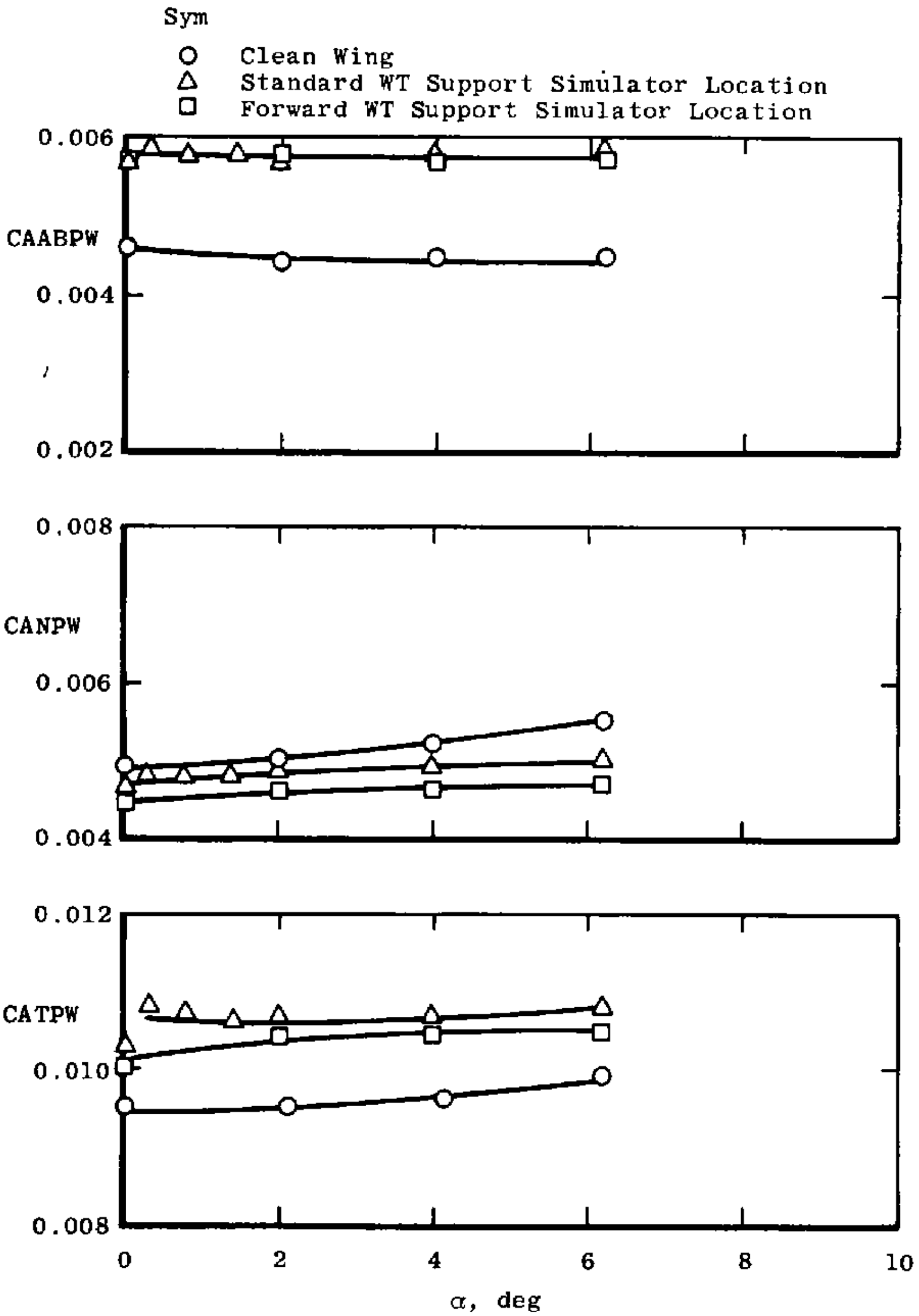

c. M = 1.2
Figure 30. Concluded.

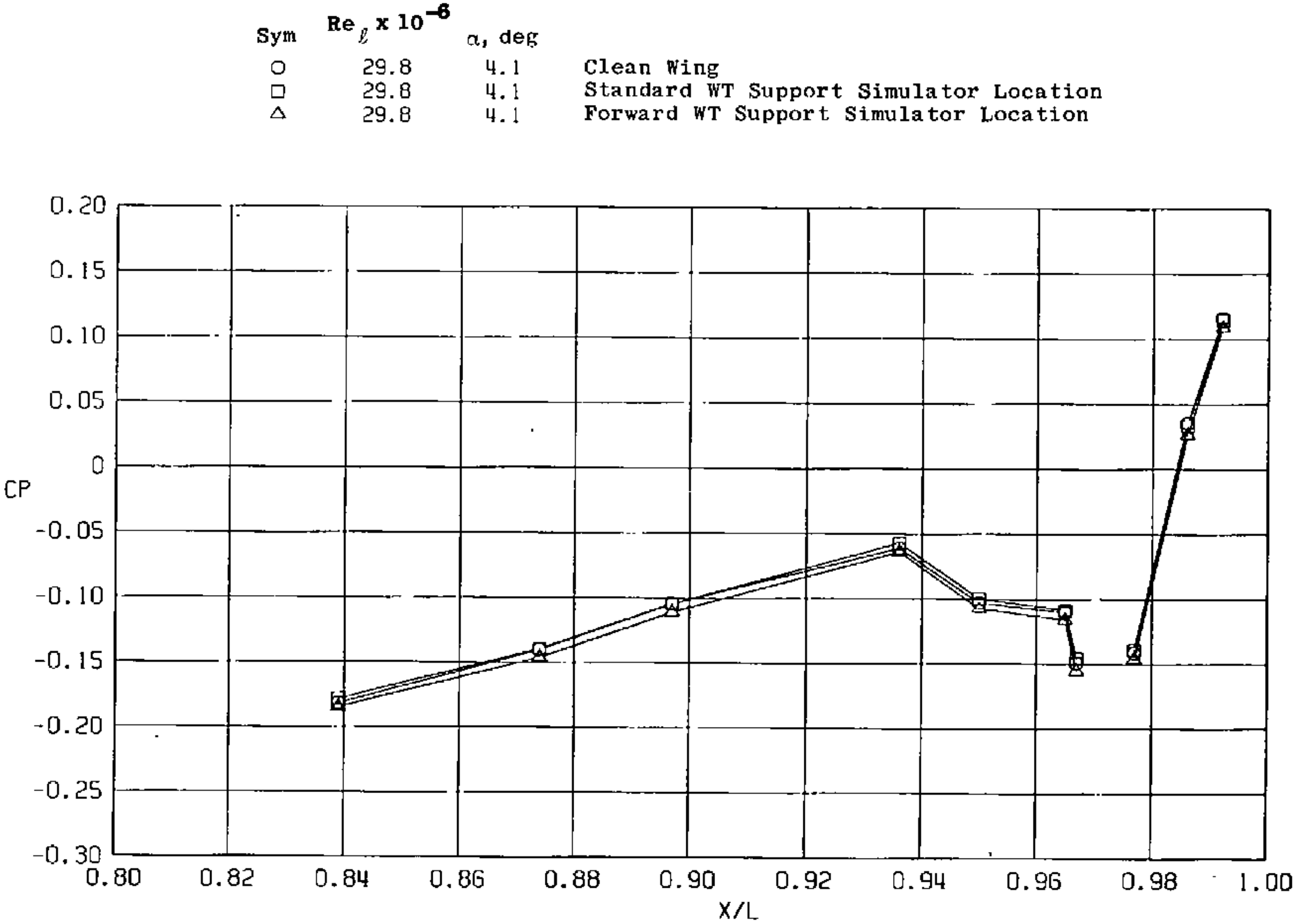

a. $\phi = 0$

Figure 31. Wingtip support simulation effects on surface pressure coefficients, A8 = 200 in.², M = 0.6 (LS), NPR = 1.0.

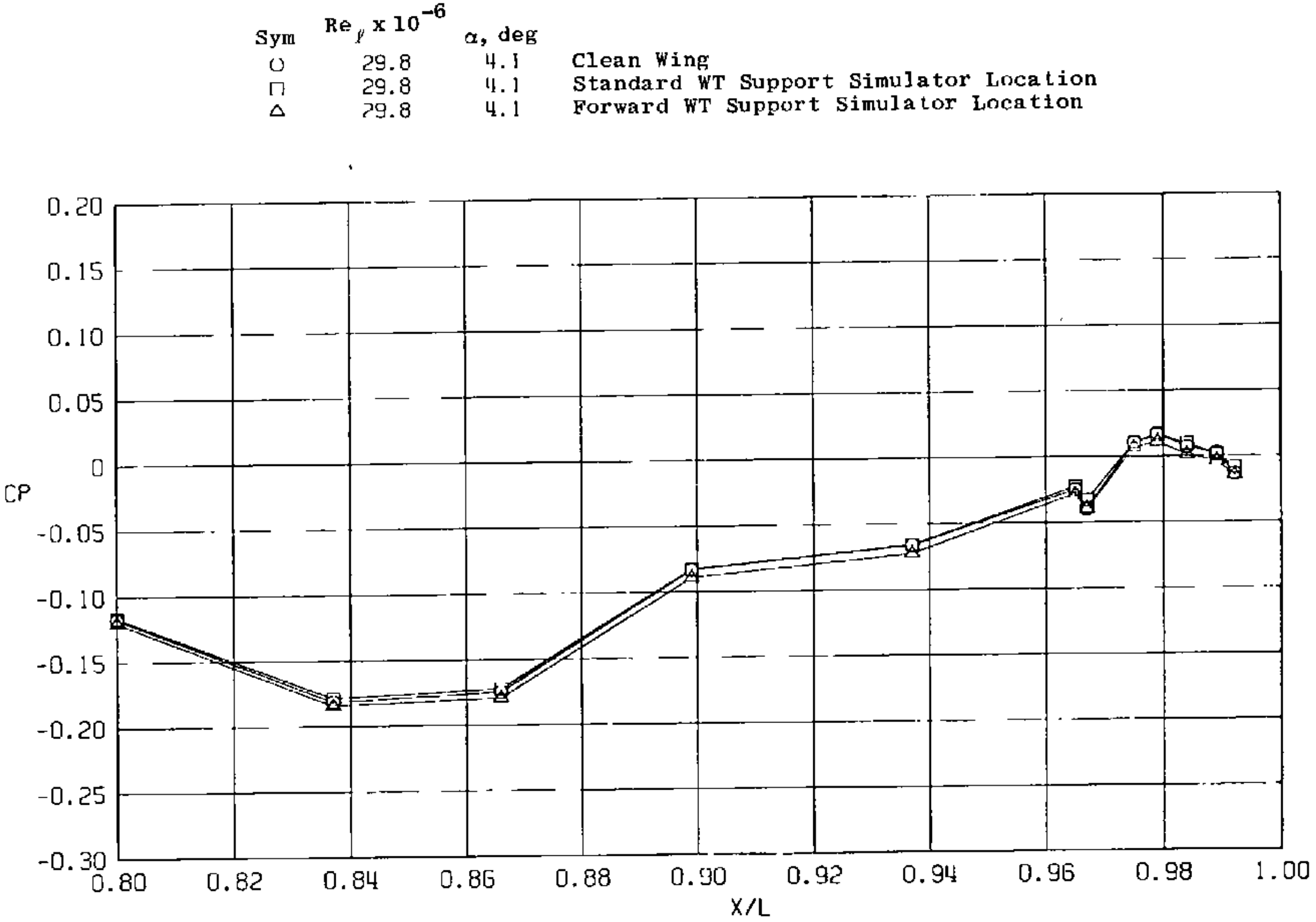

b. ϕ = 45 deg
Figure 31. Continued.

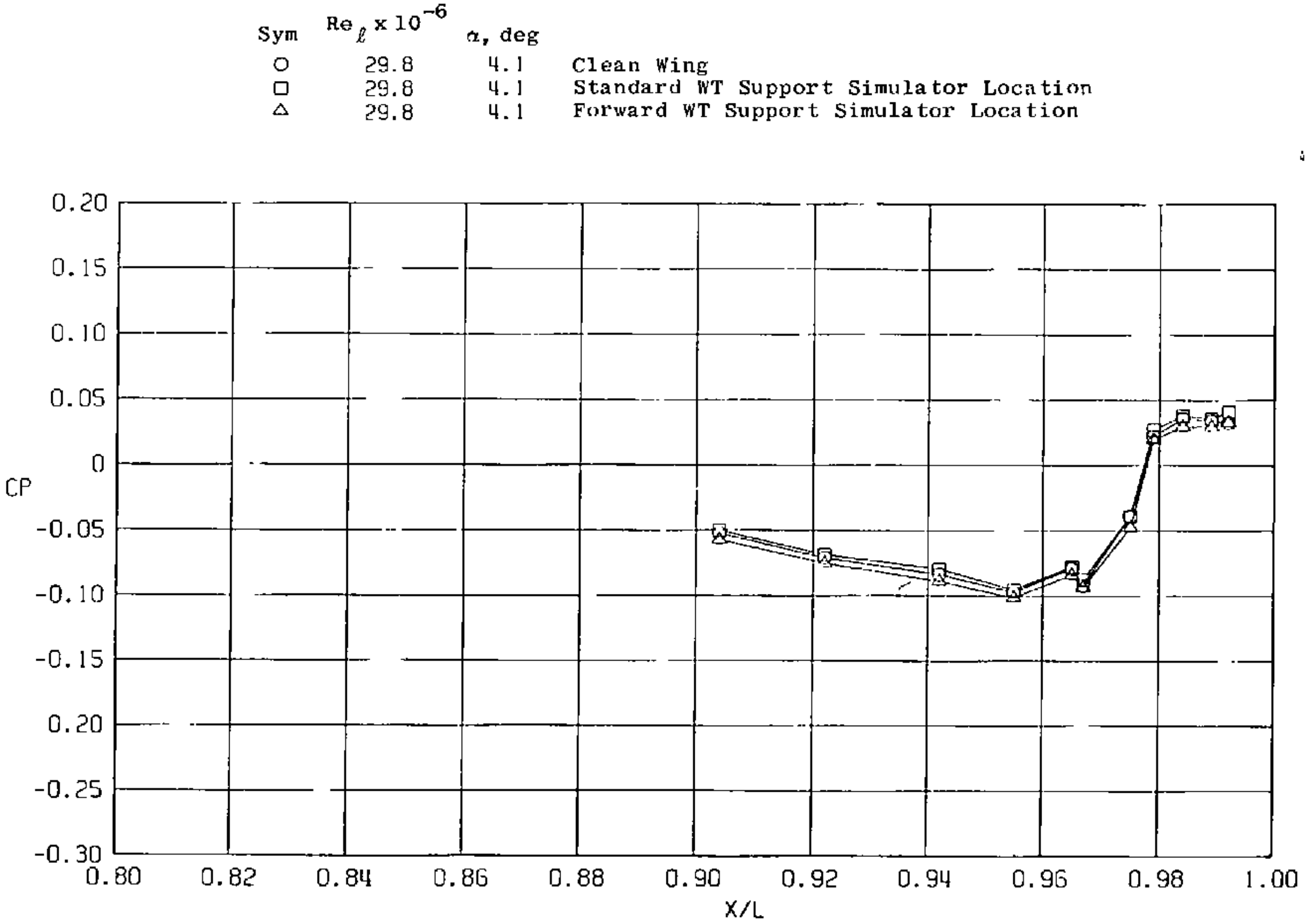

c. ϕ = 135 deg

Figure 31. Continued.

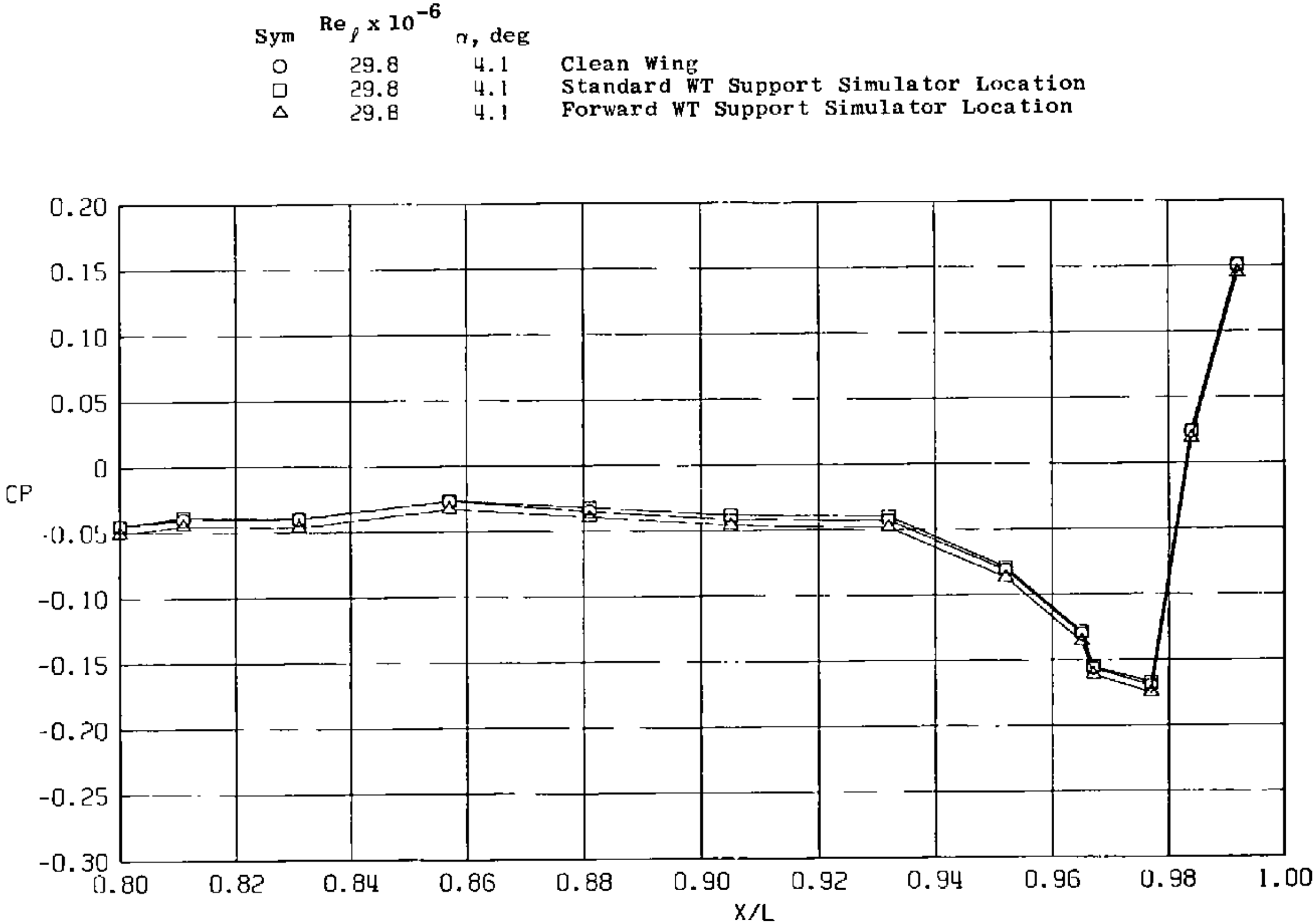

d. ϕ = 180 deg
Figure 31. Continued.

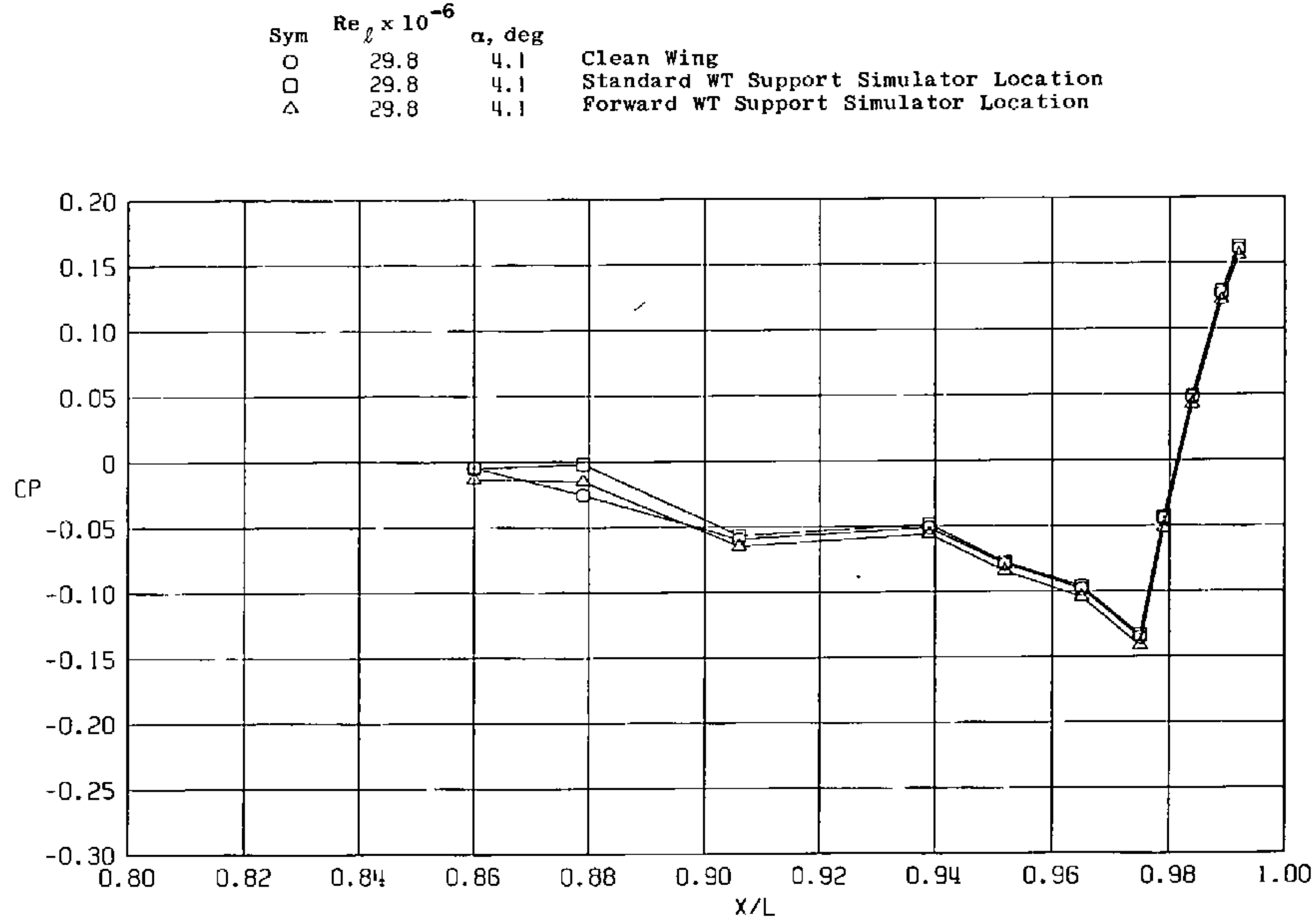

e. ϕ = 225 deg
Figure 31. Continued.

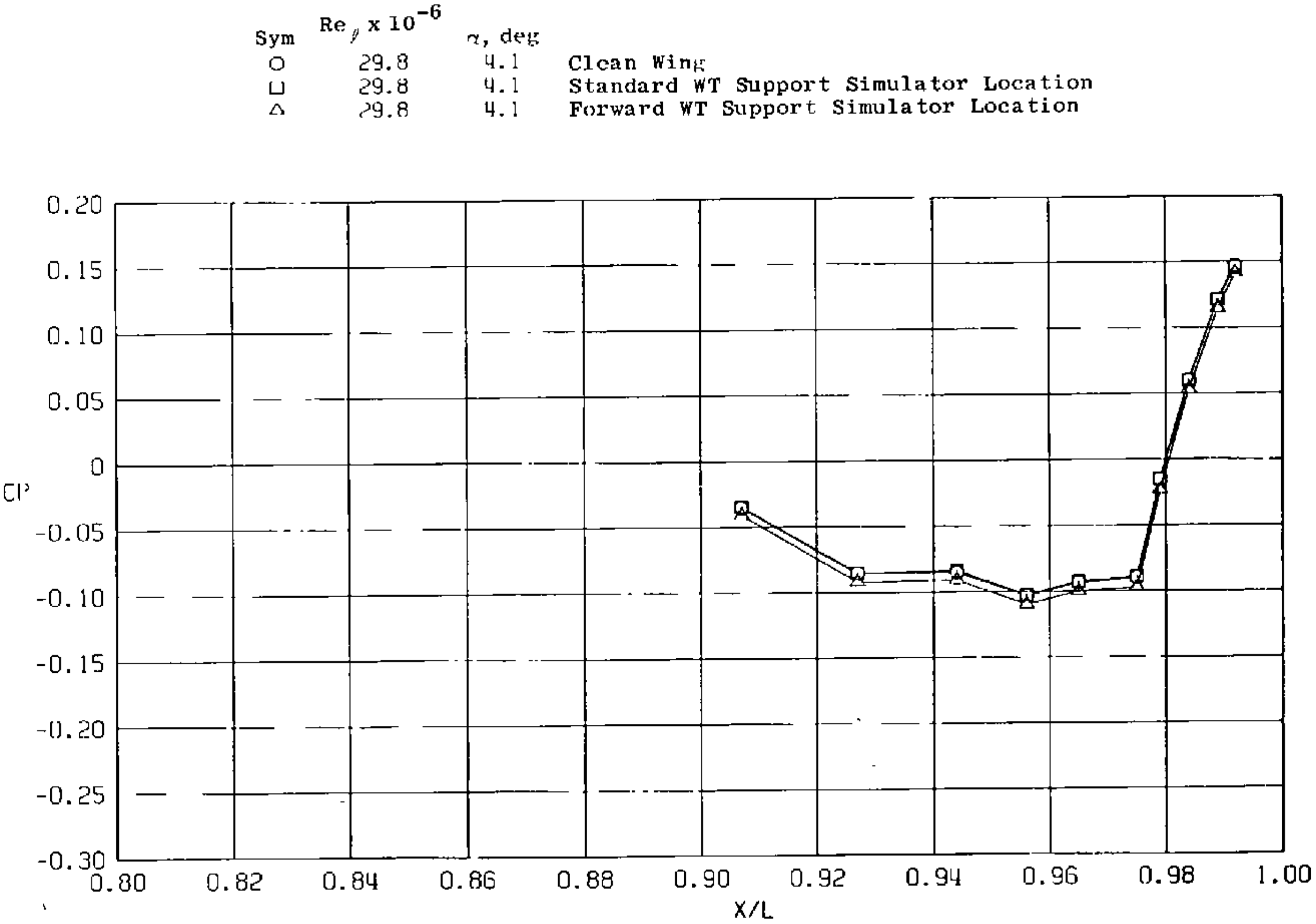

f. ϕ = 315 deg
Figure 31. Concluded.

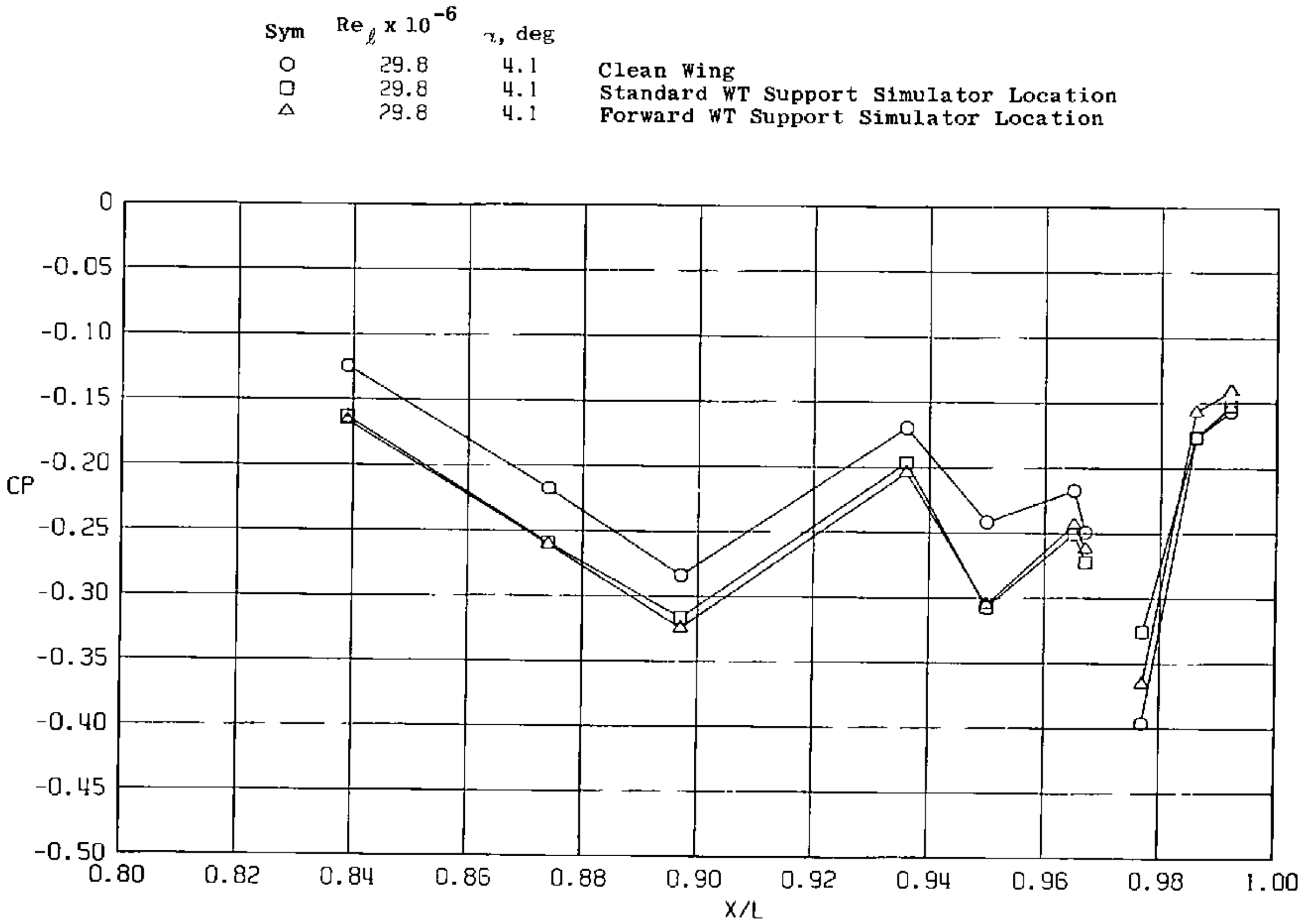

a. $\phi = 0$

Figure 32. Wingtip support simulation effects on surface pressure coefficients, A8 = 200 in.^{2}, M = 1.2 (LS), NPR = 1.0.

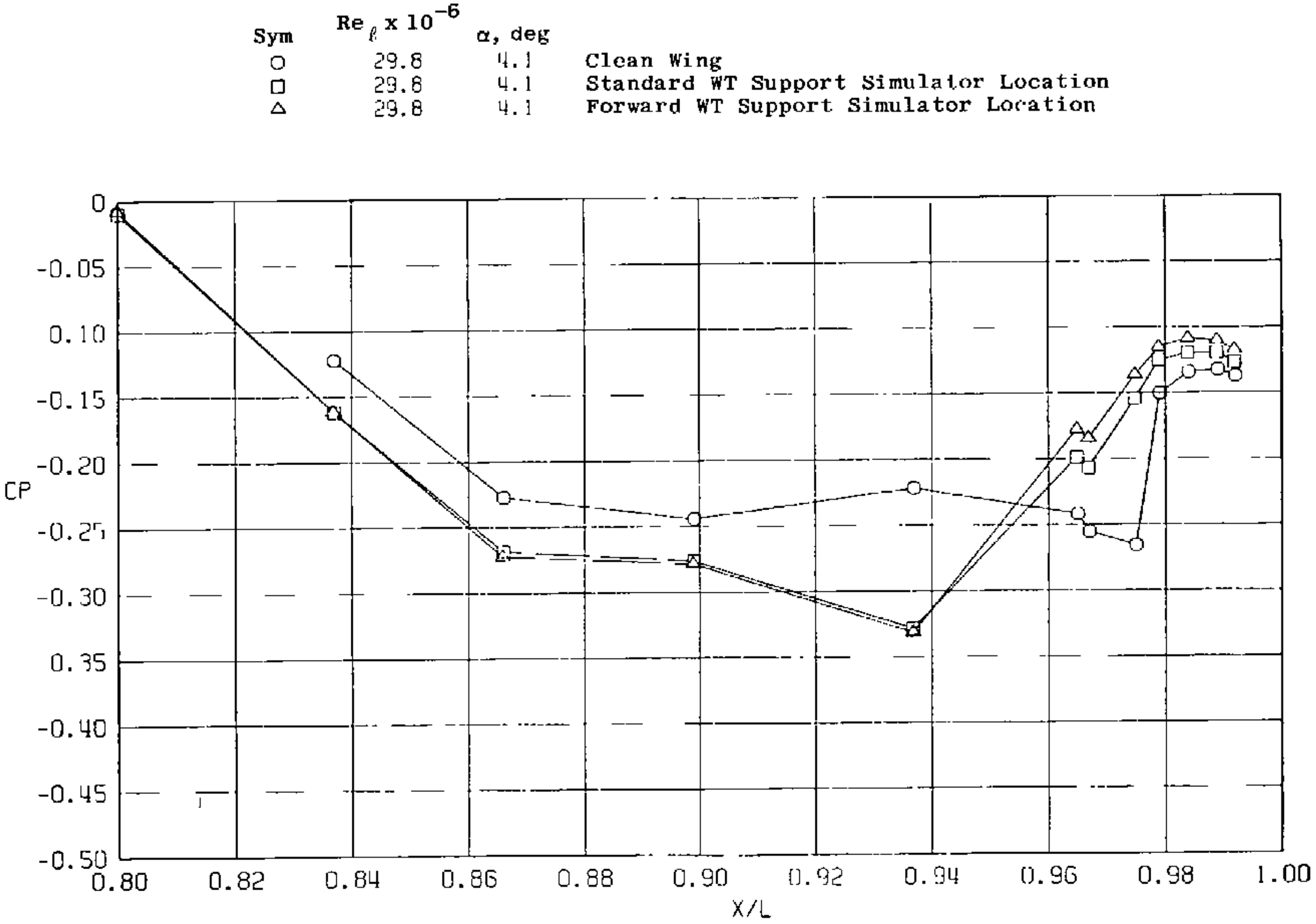

b. ϕ = 45 deg

Figure 32. Continued.

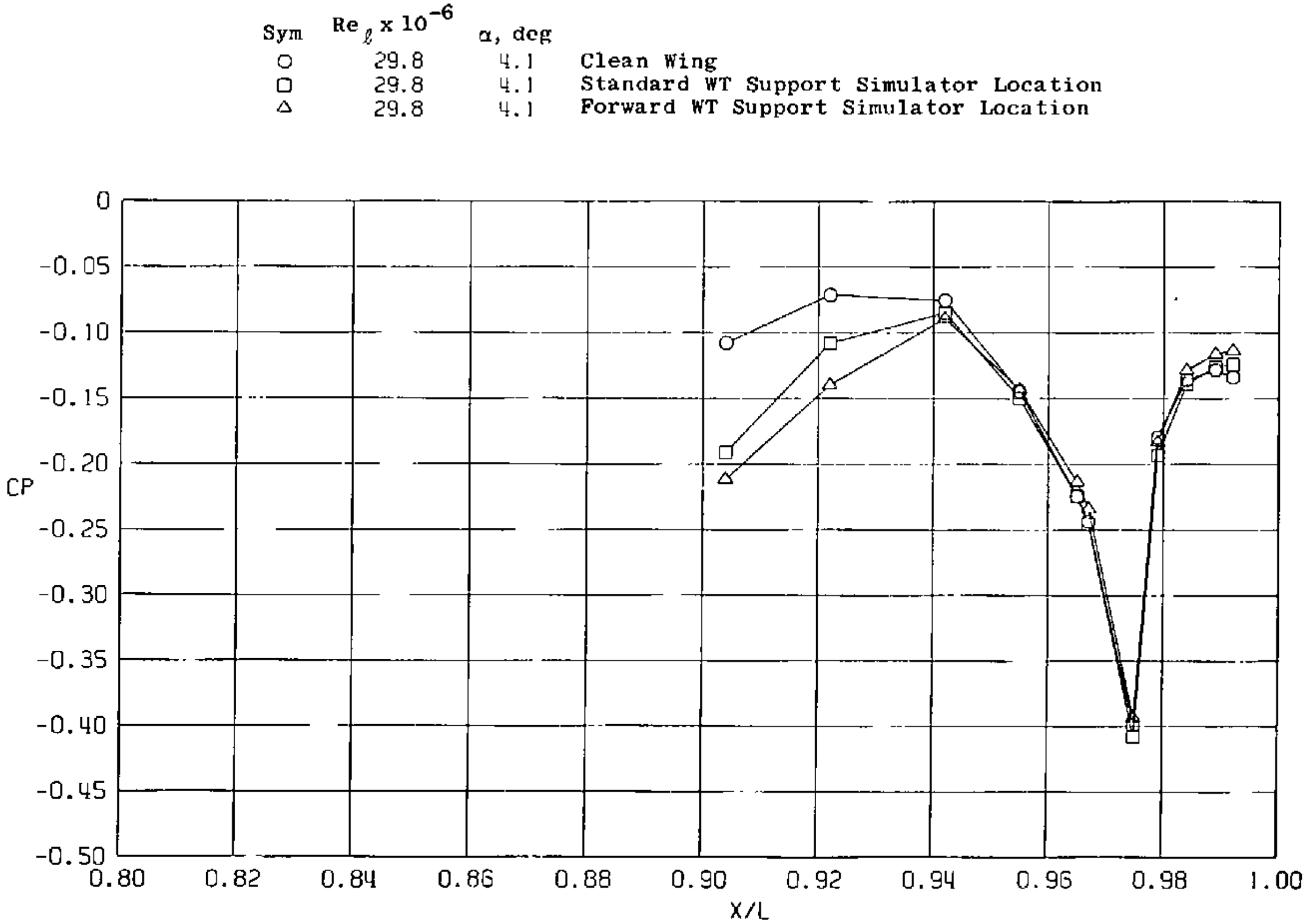

c. ϕ = 135 deg
Figure 32. Continued.

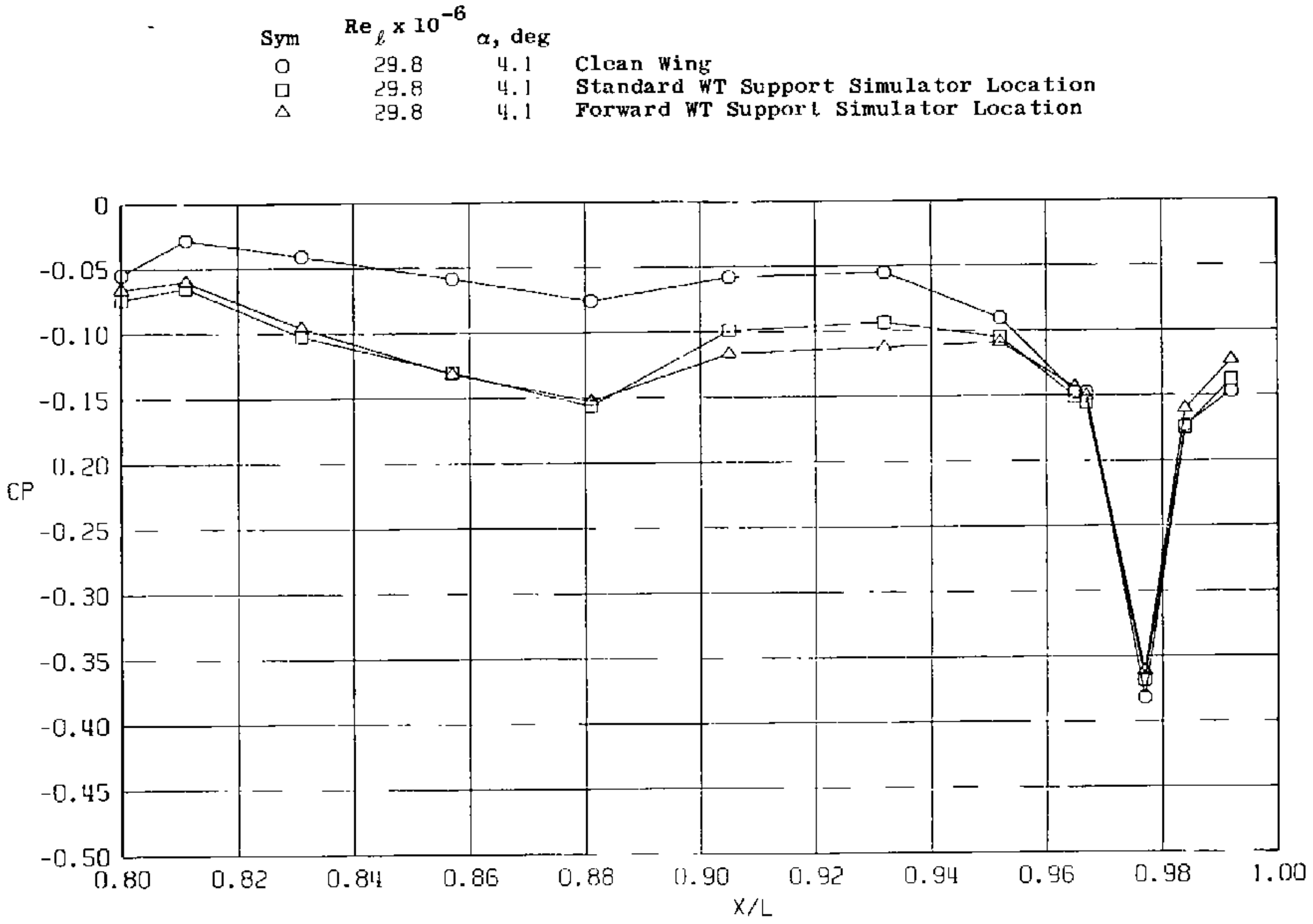

d. ϕ = 180 deg

Figure 32. Continued.

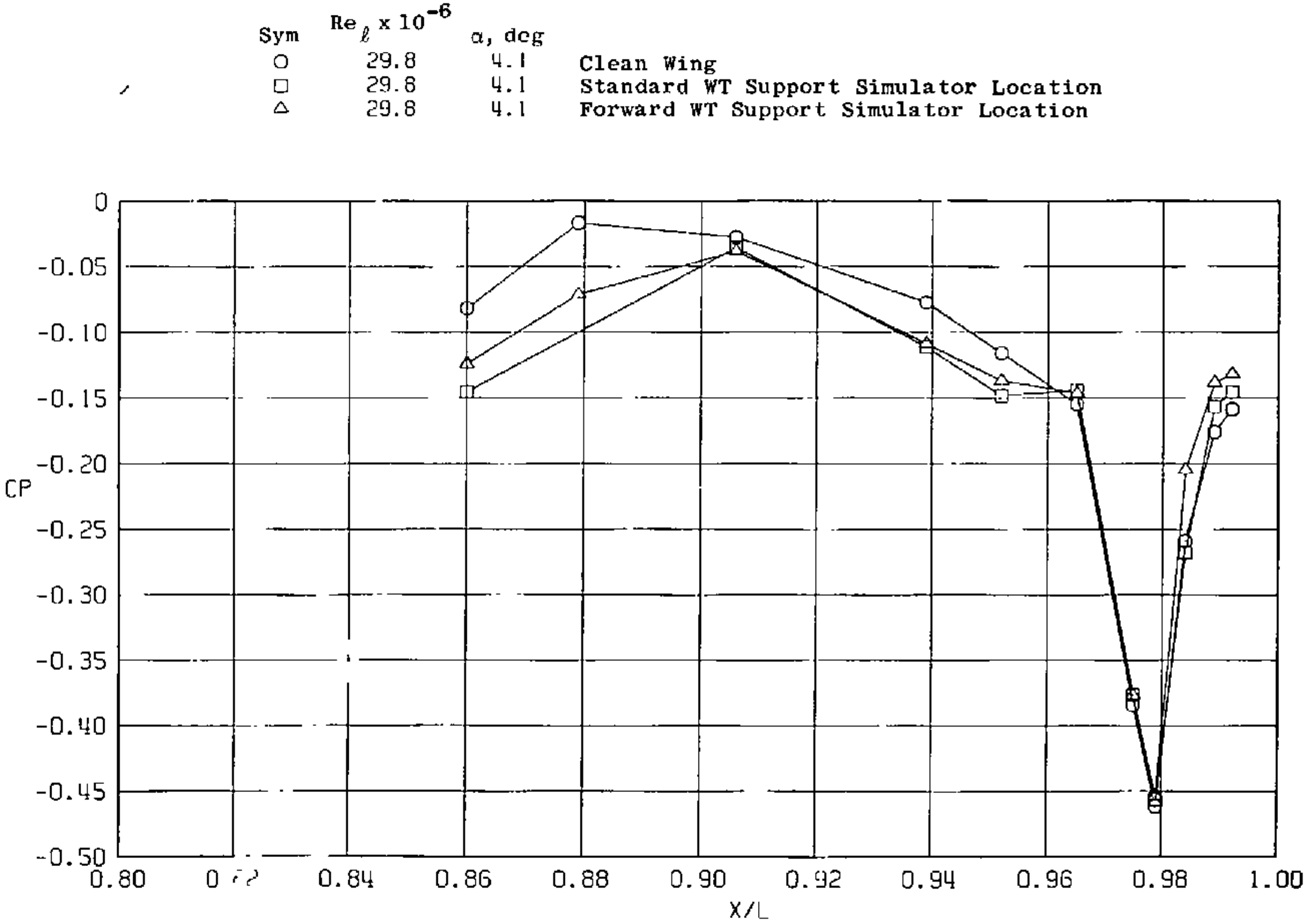

e. ϕ = 225 deg
Figure 32. Continued.

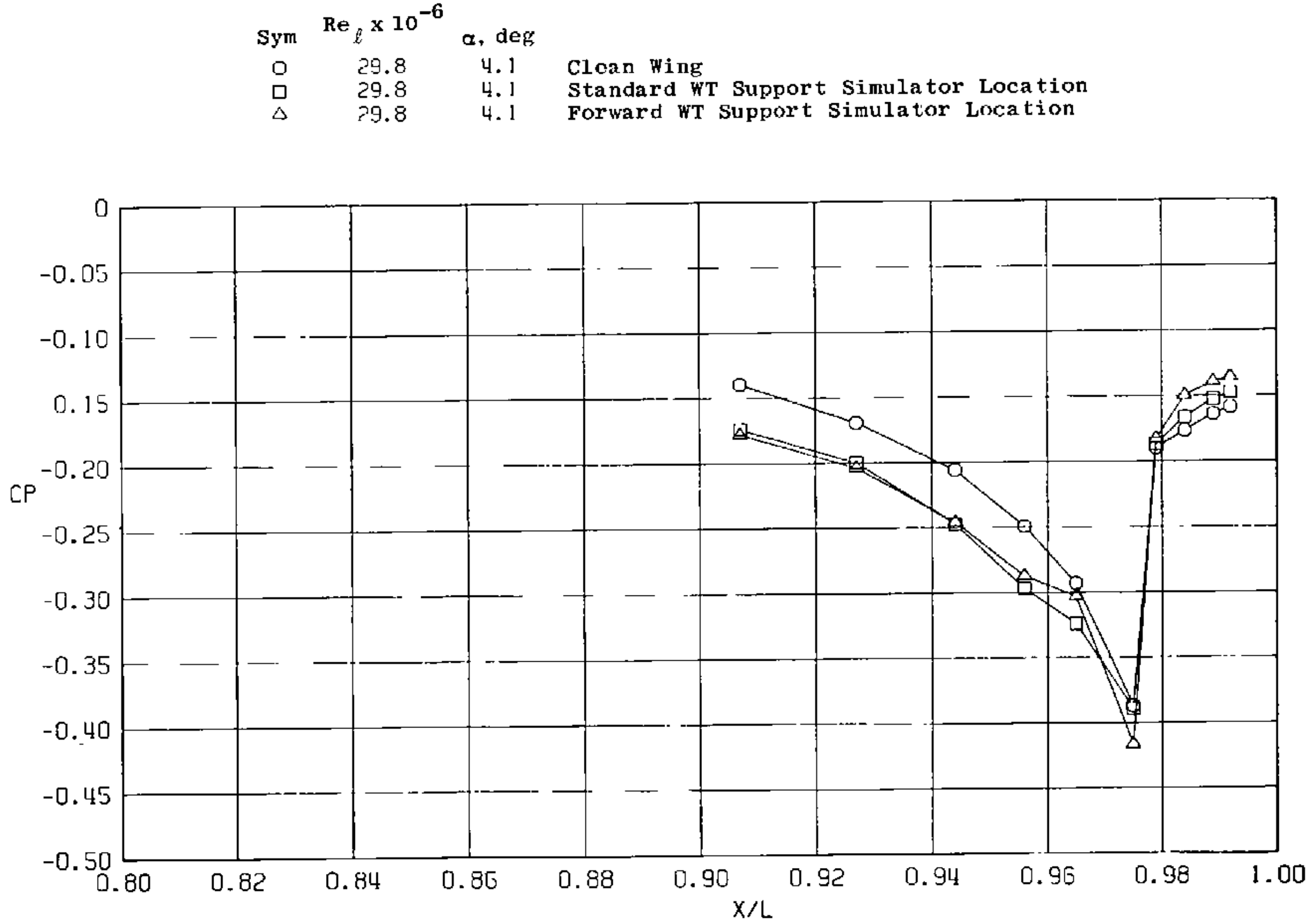

f. ϕ = 315 deg
Figure 32. Concluded.

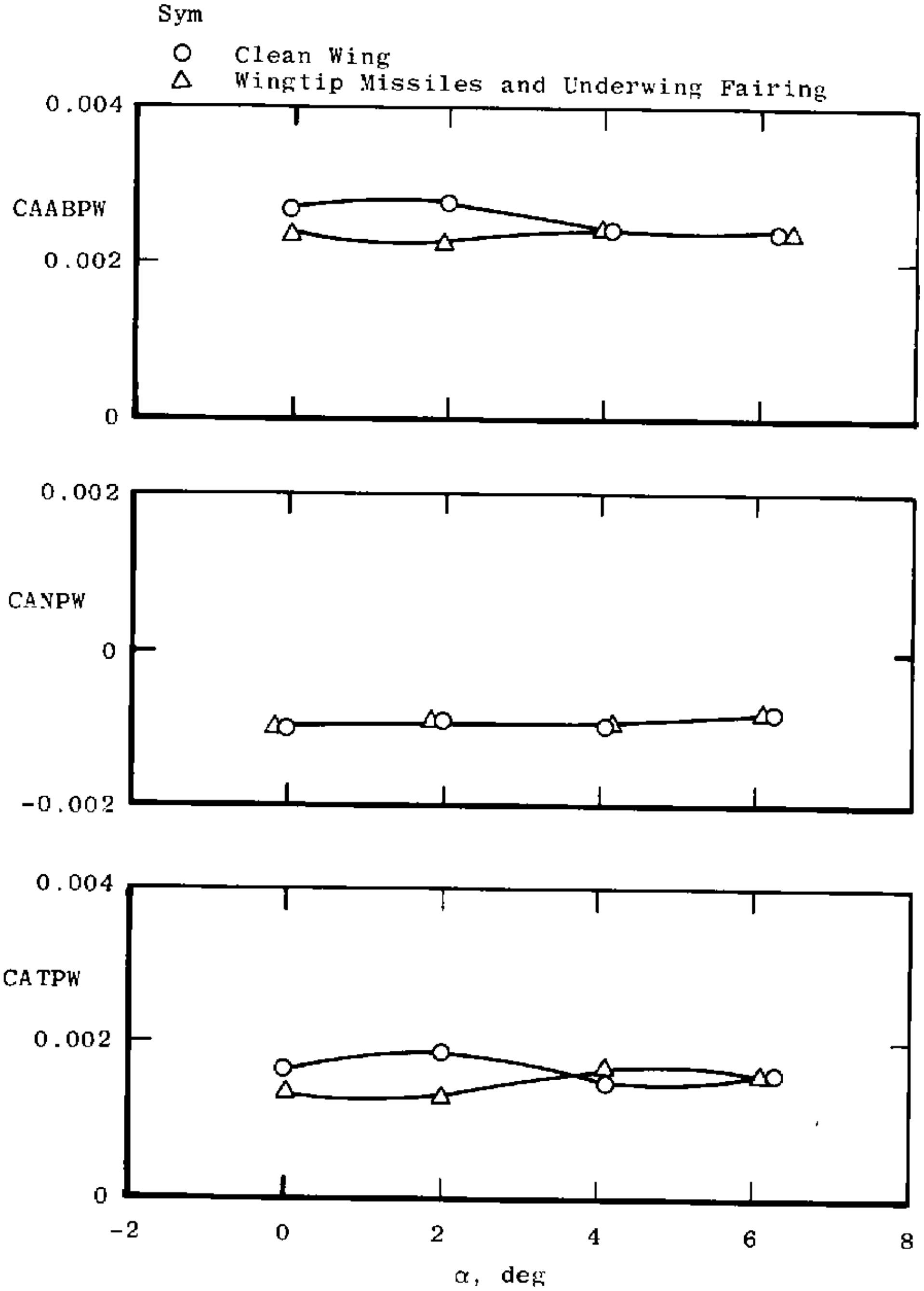

a. M = 0.6, A8 = 200 in.²

Figure 33. Wingtip missile and underwing fairing simulation effects on axial force coefficients (LS).

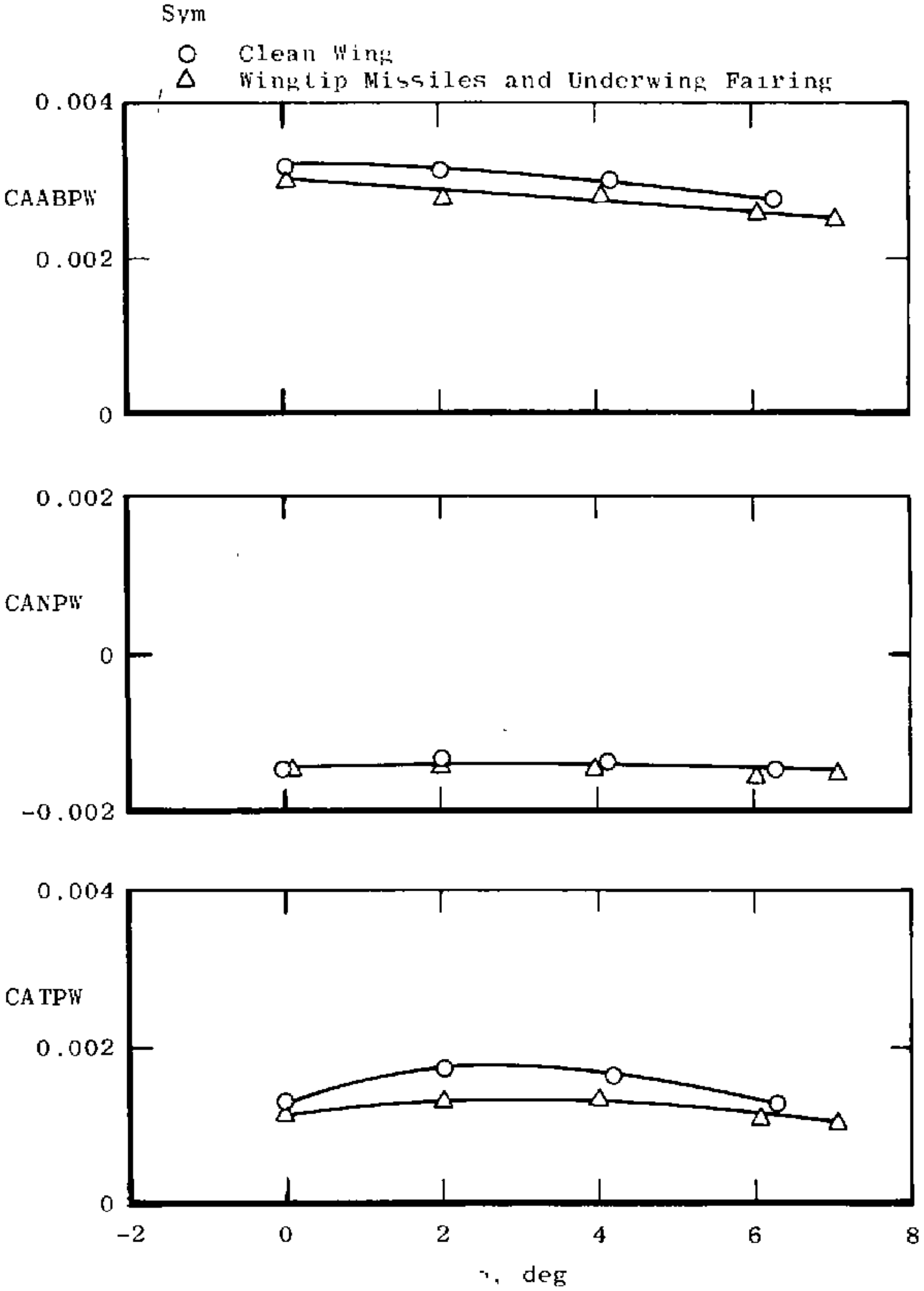

b. M = 0.9, A8 = 200 in.^{2}
Figure 33. Continued.

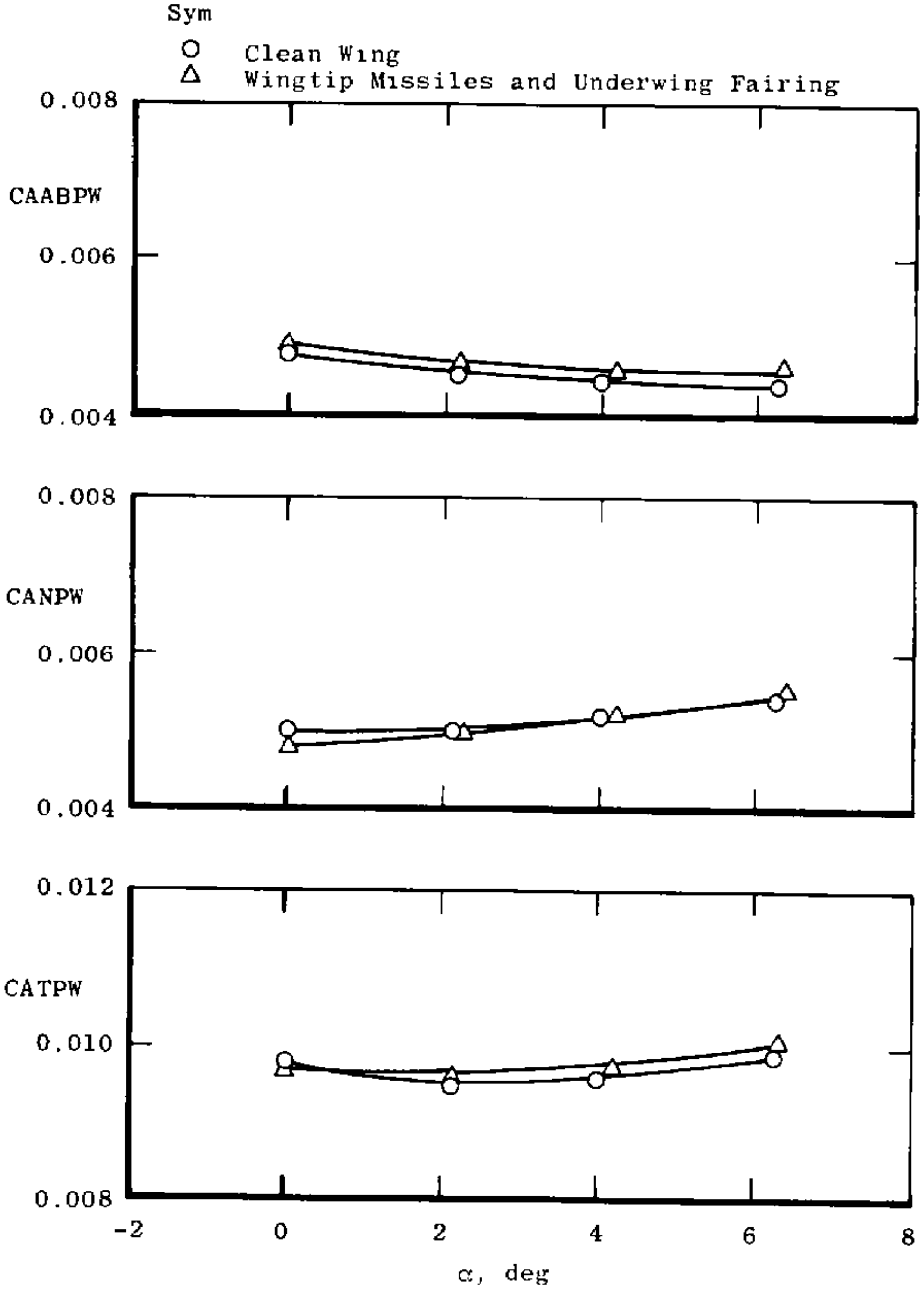

c. M = 1.2, A8 = 200 in.^{2}
Figure 33. Continued.

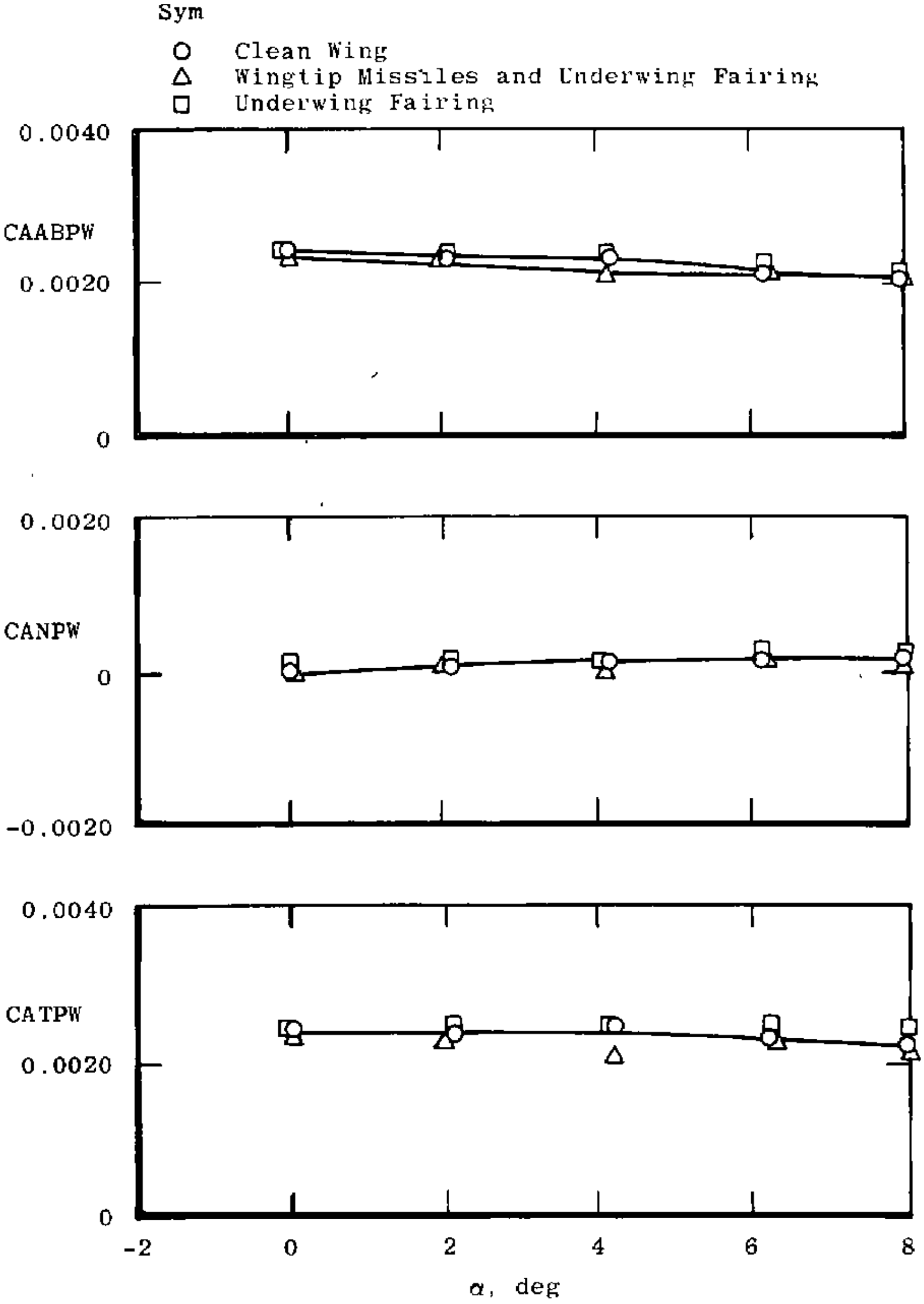

d. M = 0.6, A8 = 300 in.^{2}
Figure 33. Continued.

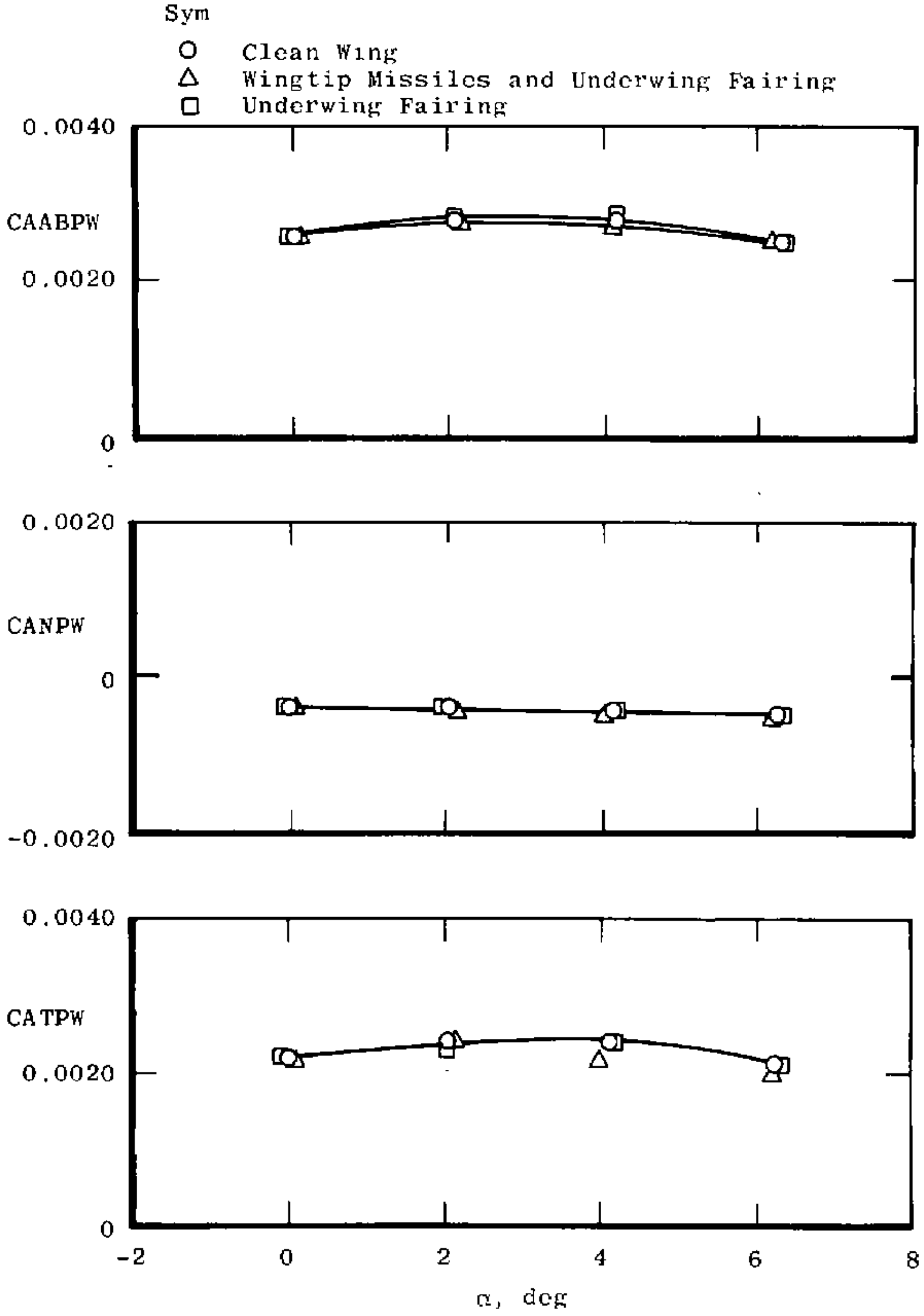

e. M = 0.9, A8 = 300 in.^{2}
Figure 33. Continued.

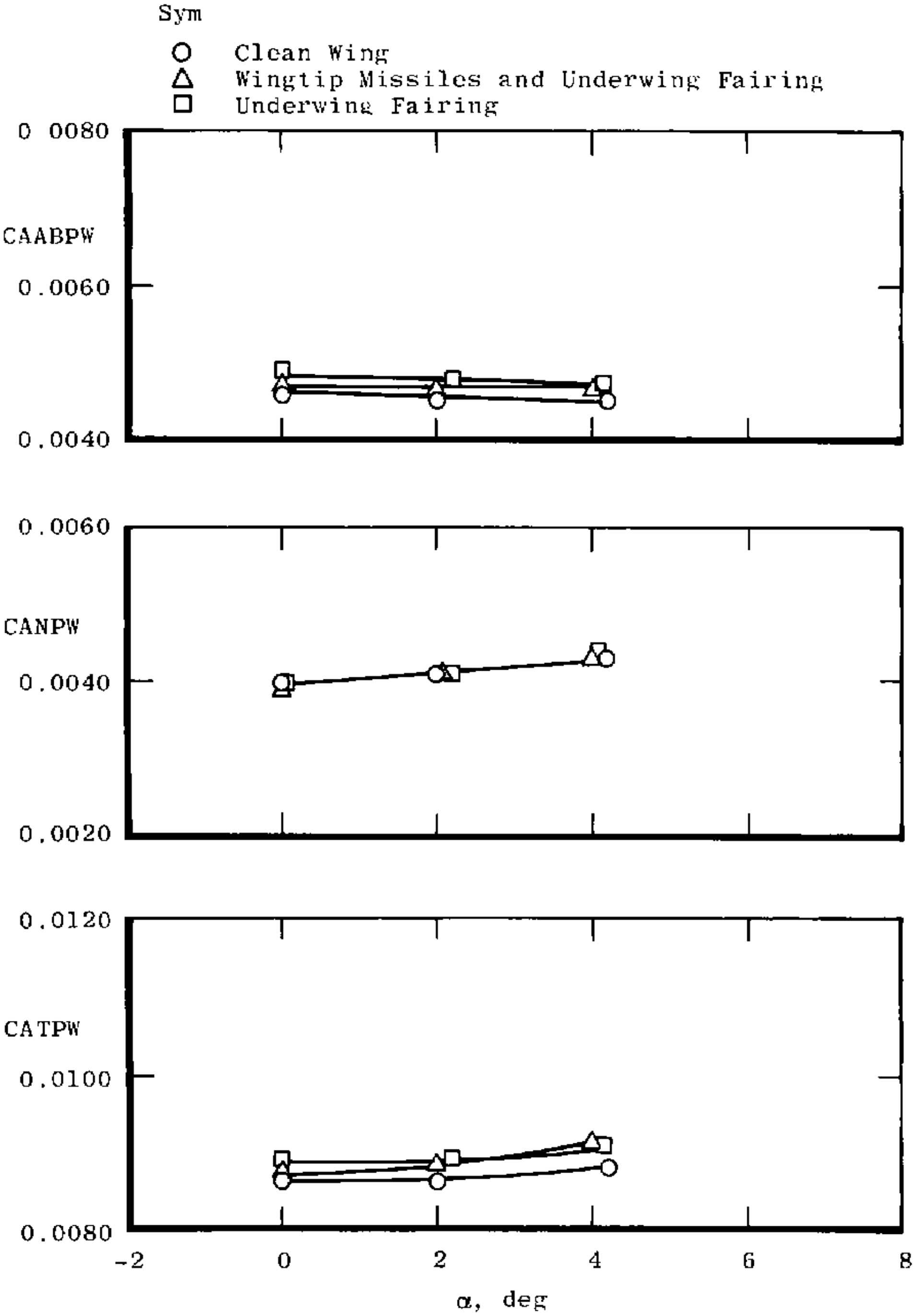

f. M = 1.2, A8 = 300 in.^{2}
Figure 33. Concluded.

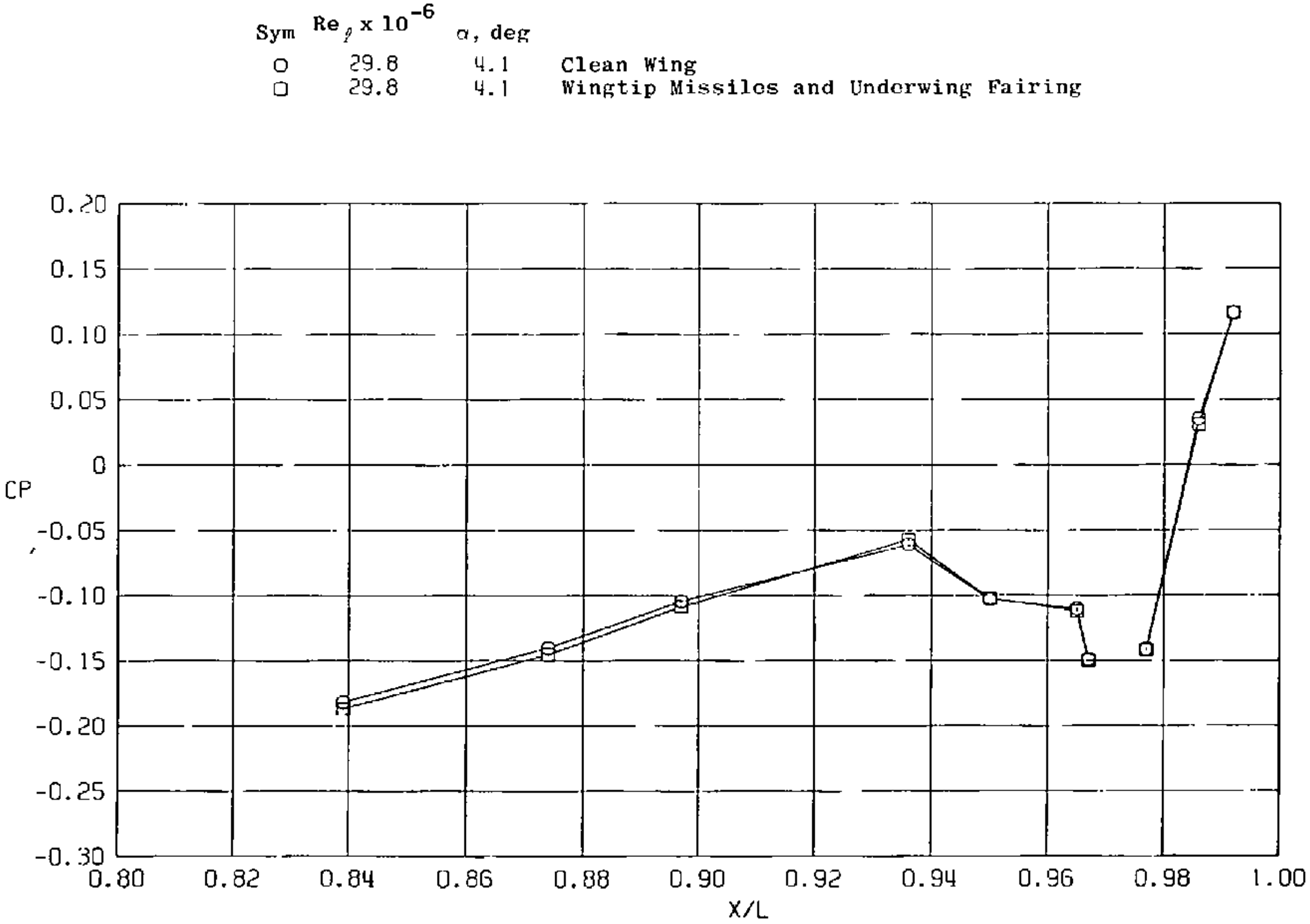

a. $\phi = 0$

Figure 34. Wingtip missile and underwing fairing simulation effects on surface pressure coefficients, A8 = 200 in.², M = 0.6 (LS), NPR = 1.0.

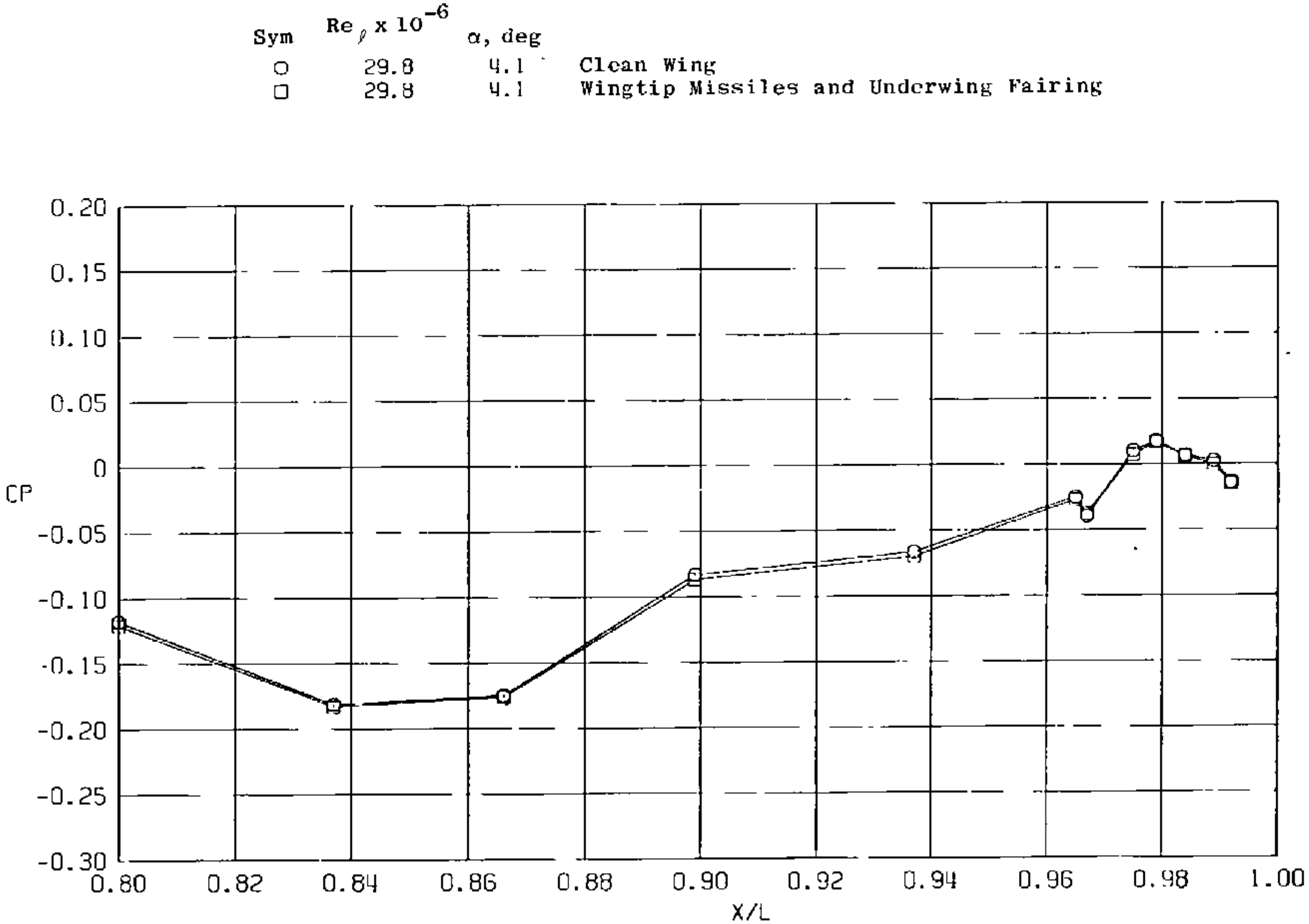

b. ϕ = 45 deg
Figure 34. Continued.

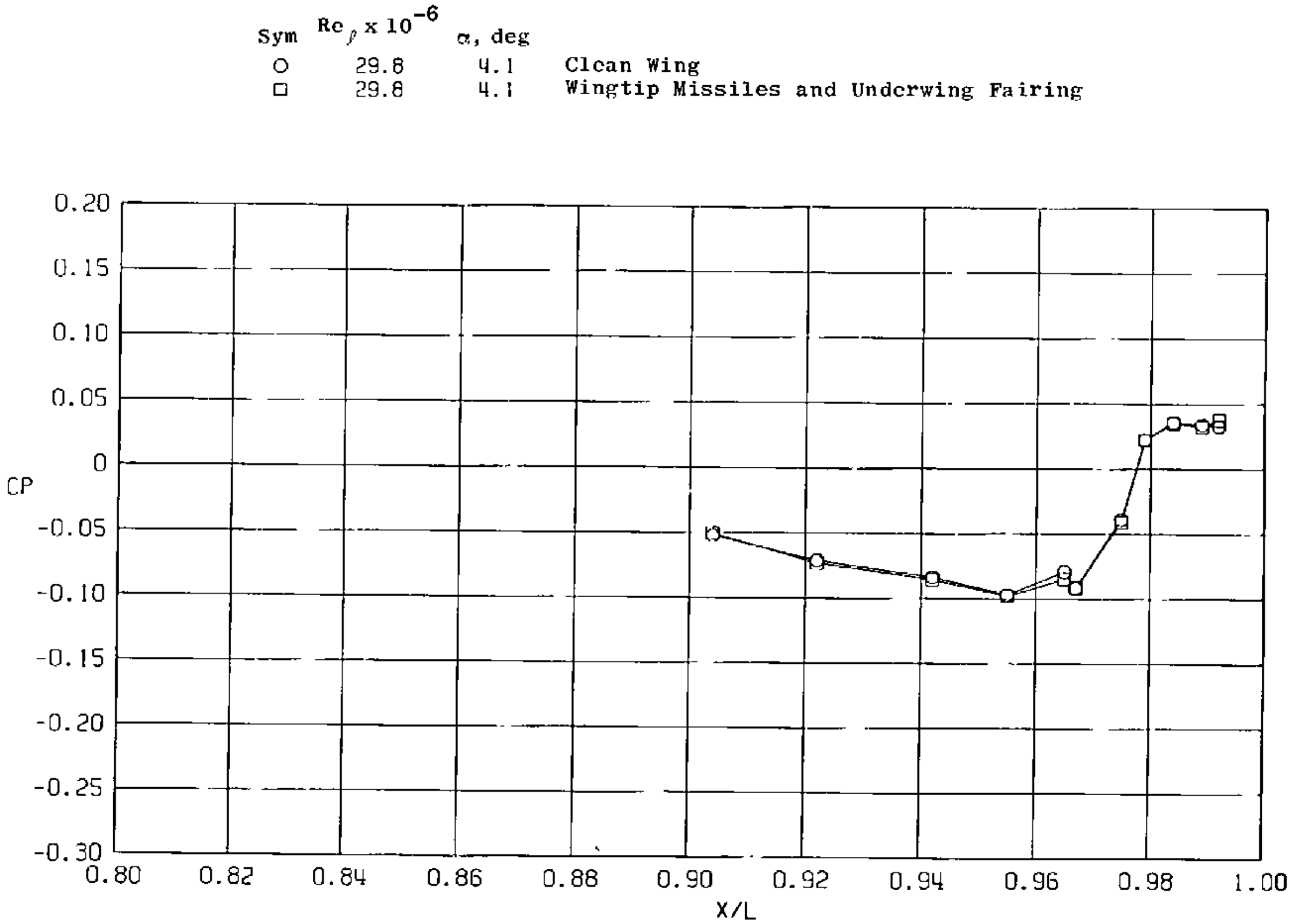

c. ϕ = 135 deg
Figure 34. Continued.

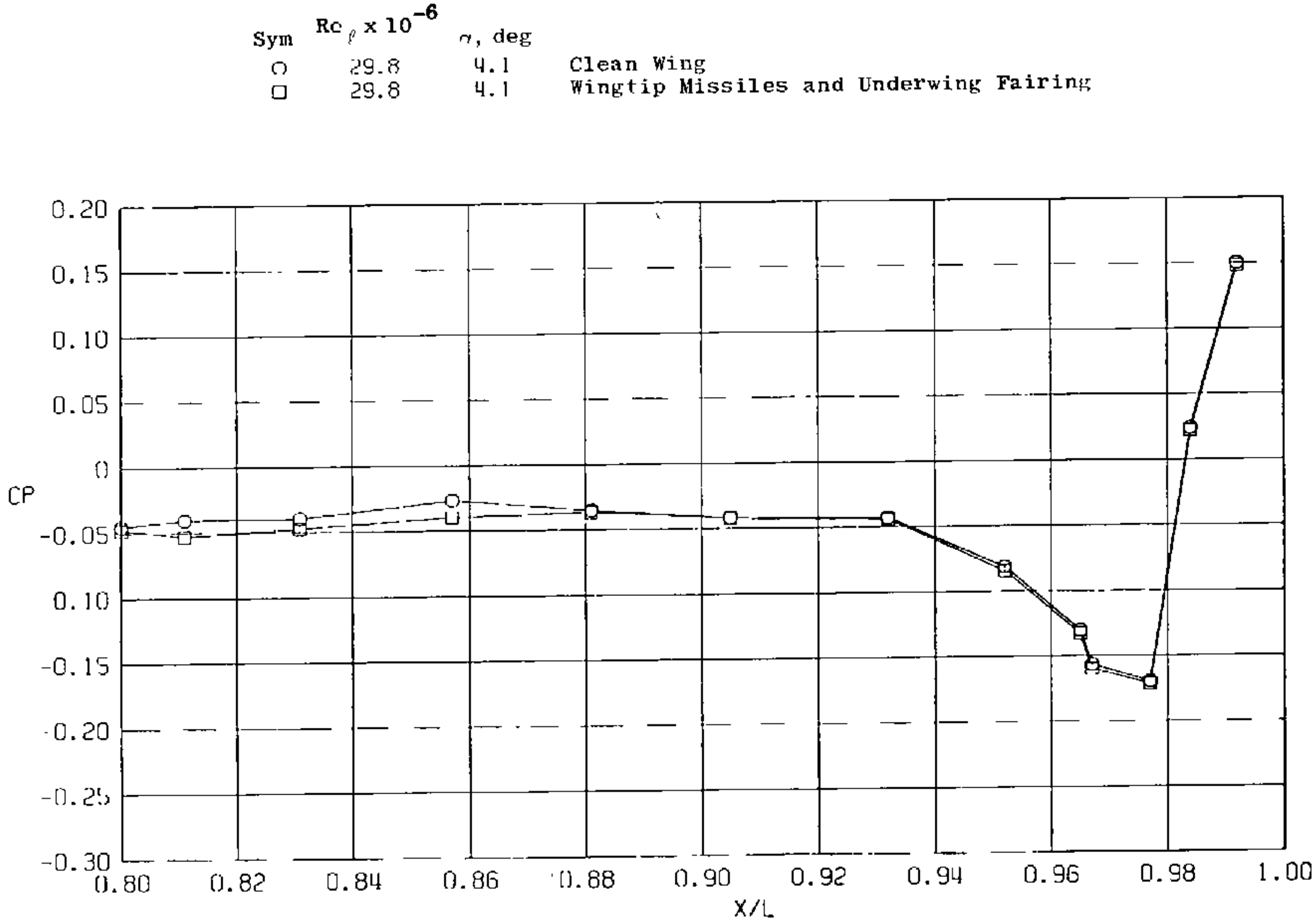

d. ϕ = 180 deg

Figure 34. Continued.

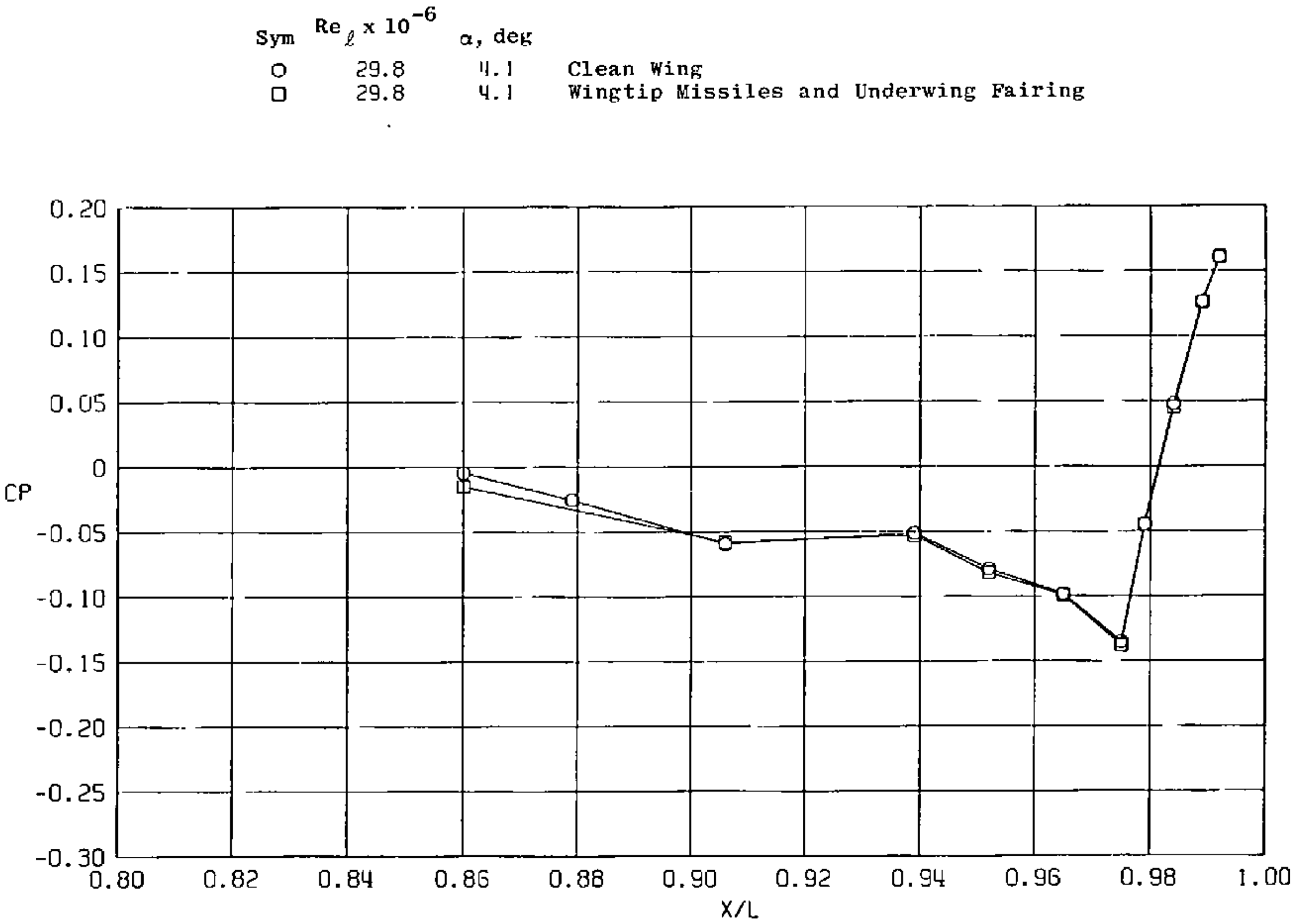

e. ϕ = 225 deg
Figure 34. Continued.

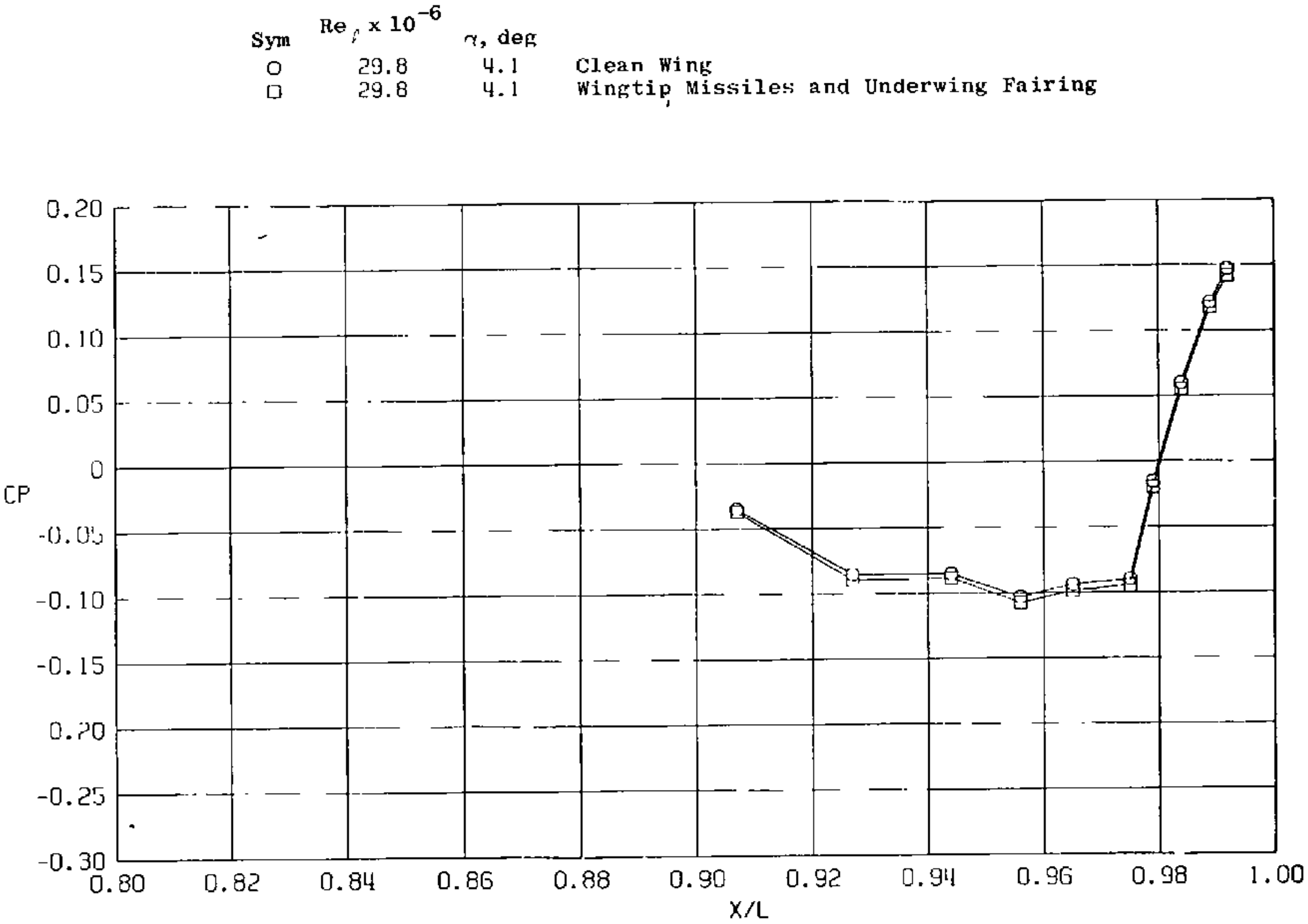

f. ϕ = 315 deg
Figure 34. Concluded.

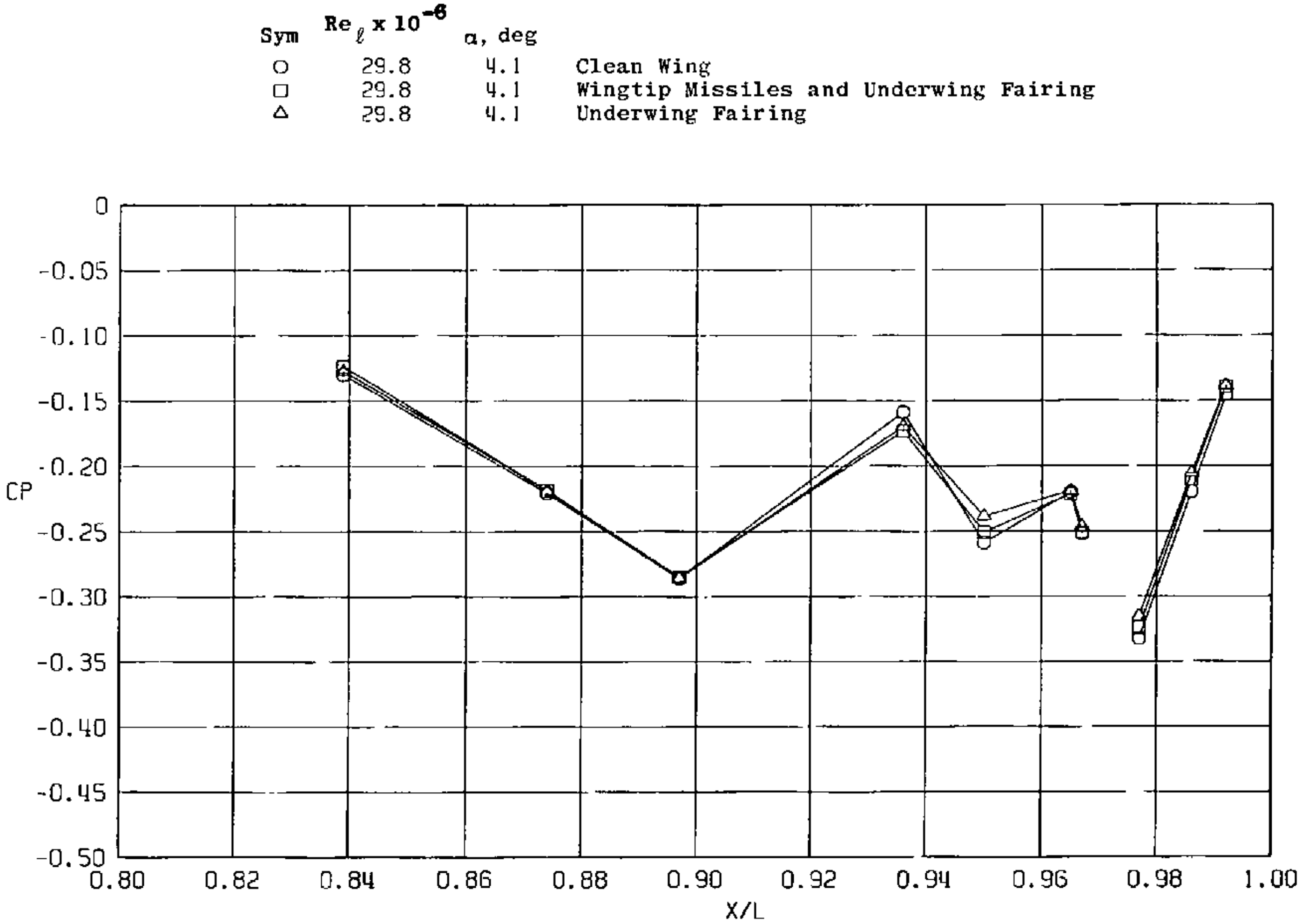

a. $\phi = 0$

Figure 35. Wingtip missile and underwing fairing simulation effects on surface pressure coefficients, A8 = 300 in.^{2}, M = 1.2 (LS), NPR = 1.0.

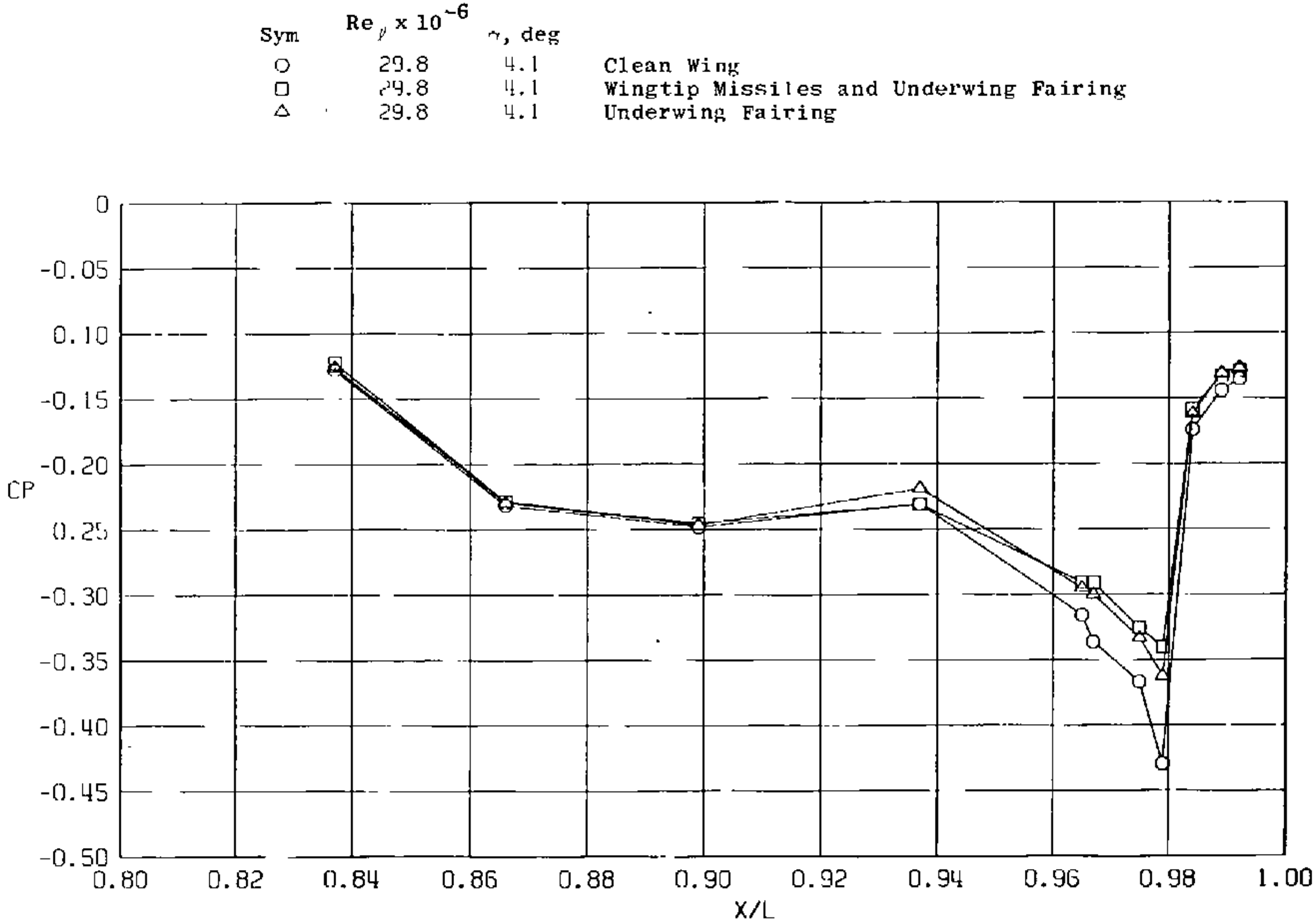

b. ϕ = 45 deg

Figure 35. Continued.

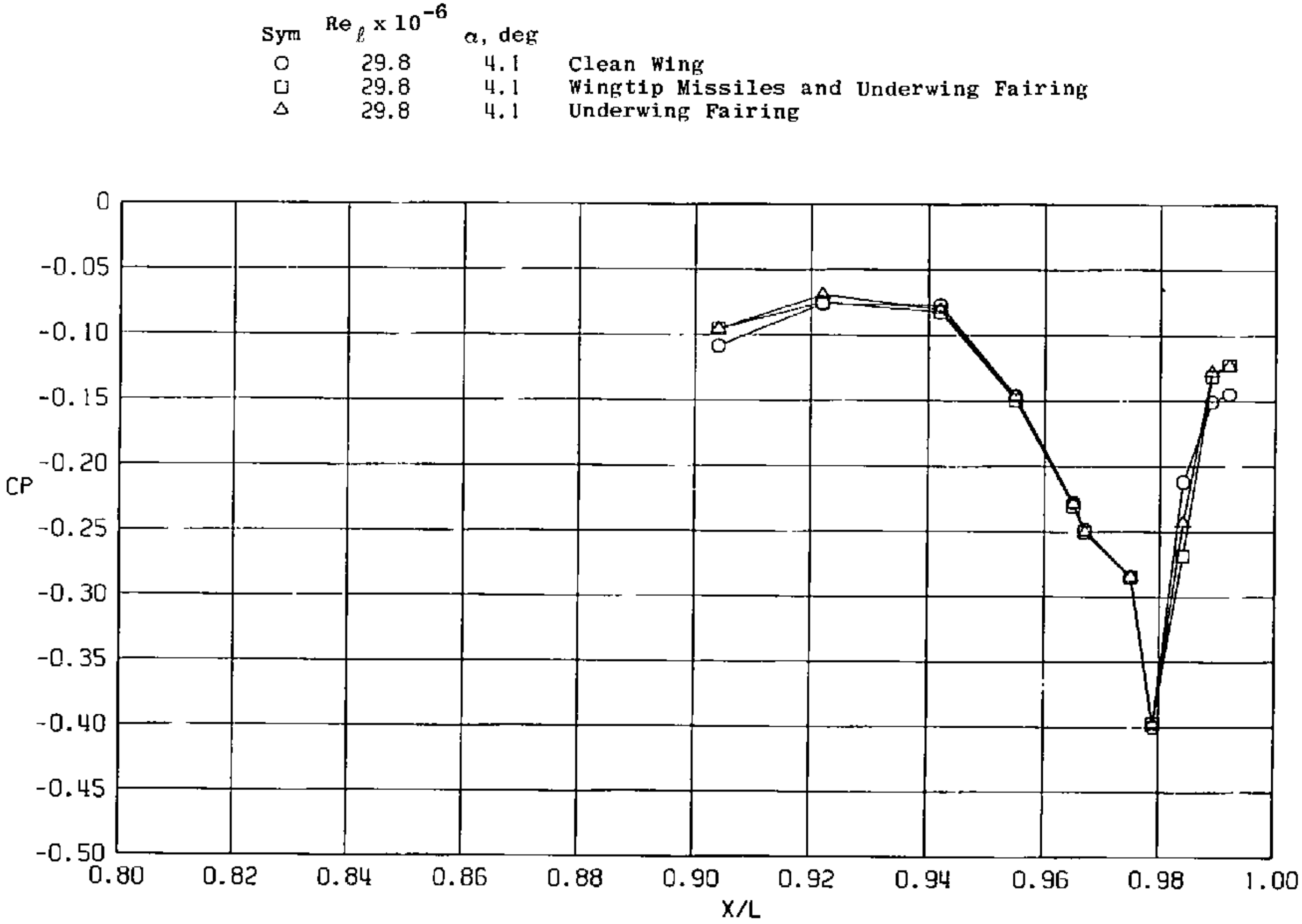

c. ϕ = 135 deg
Figure 35. Continued.

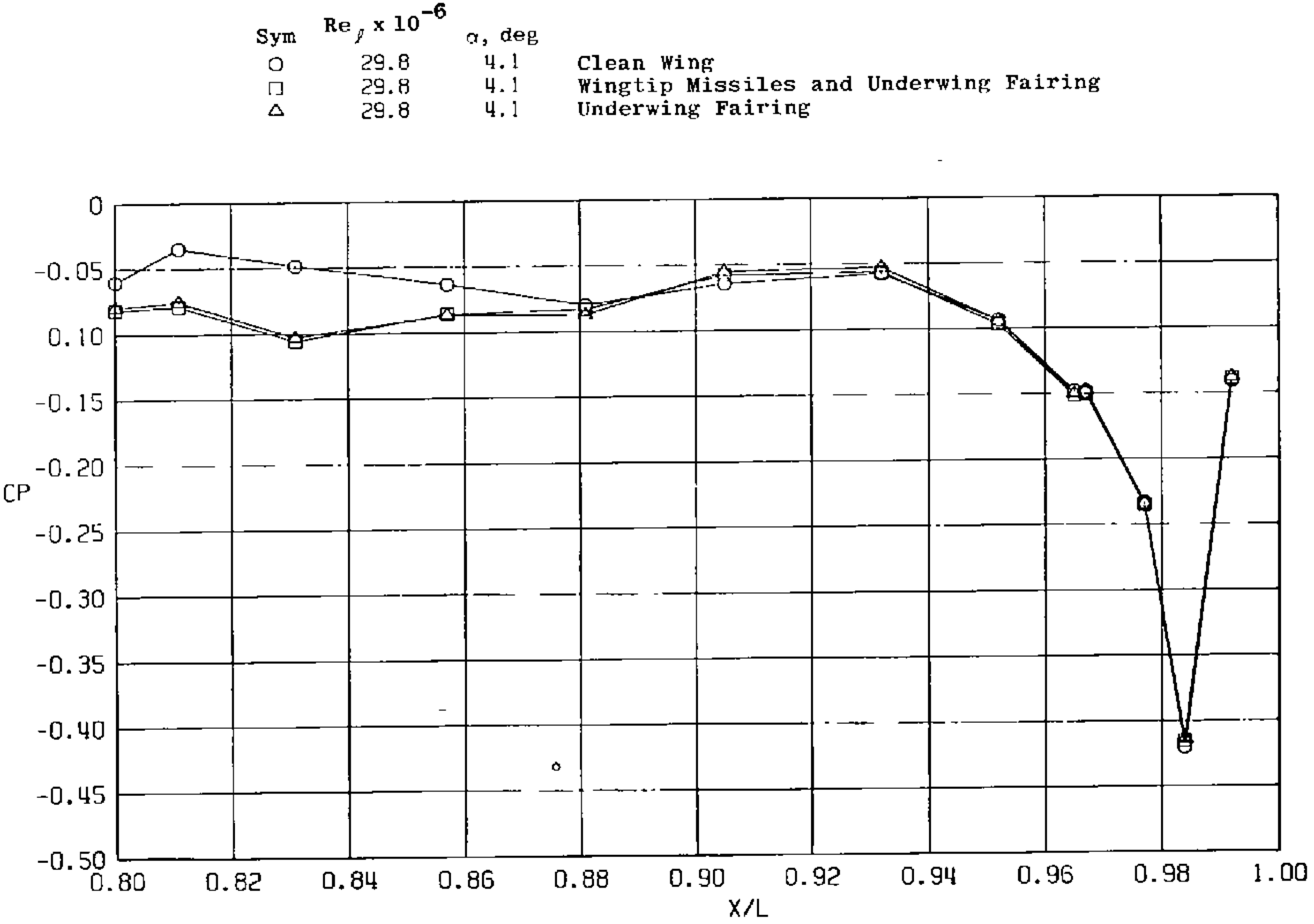

d. ϕ = 180 deg

Figure 35. Continued.

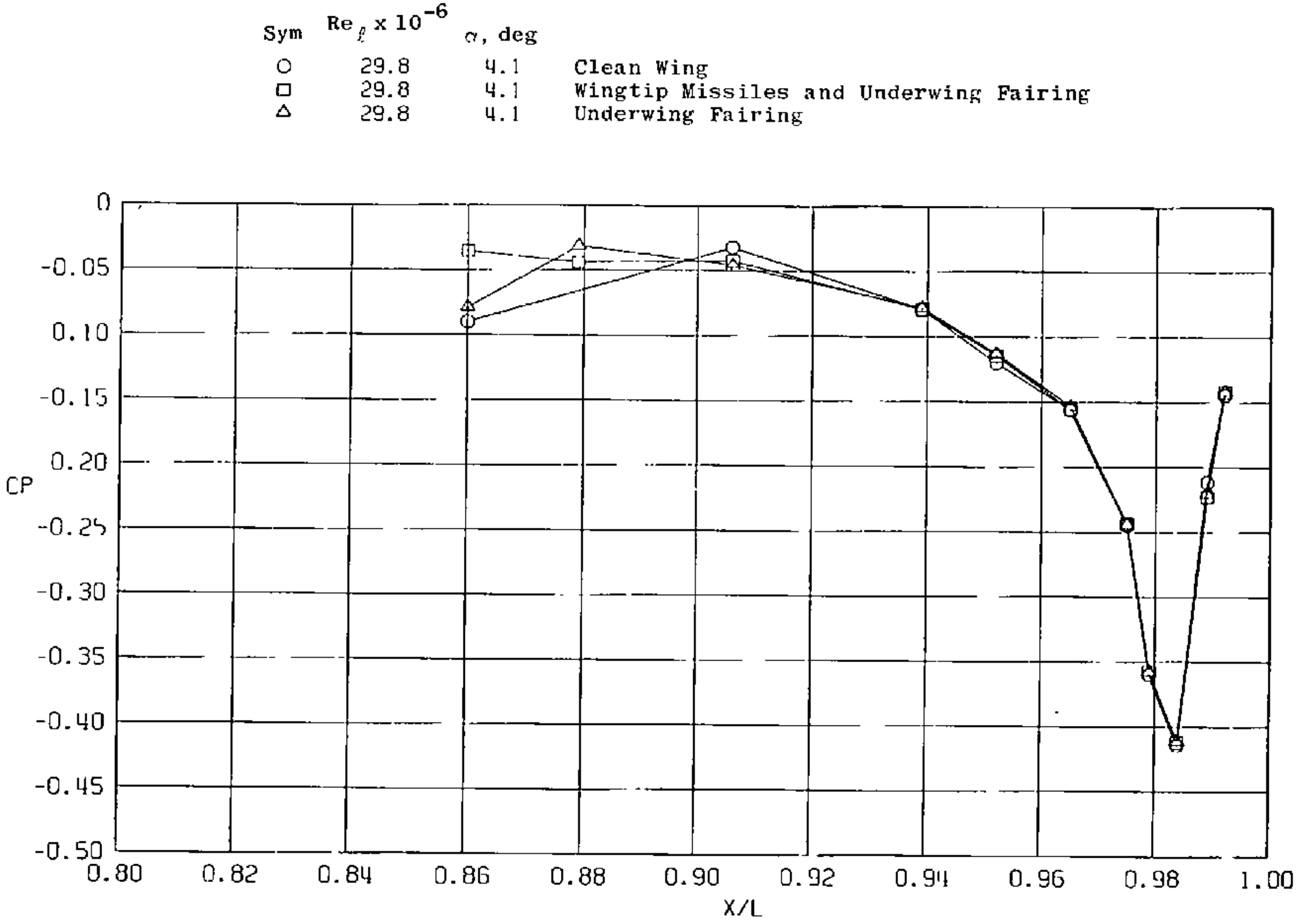

e. ϕ = 225 deg

Figure 35. Continued.

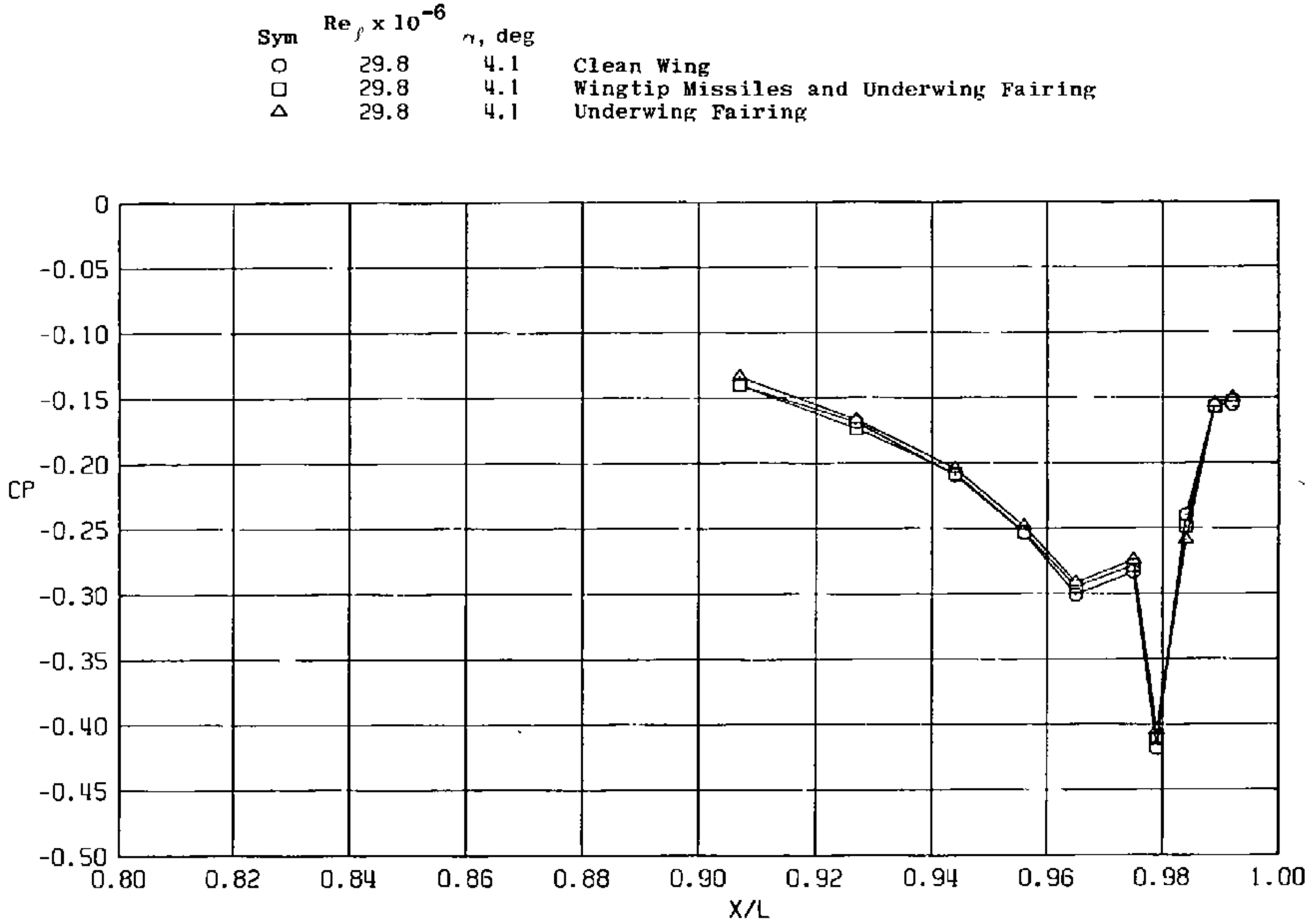

f. ϕ = 315 deg
Figure 35. Concluded.

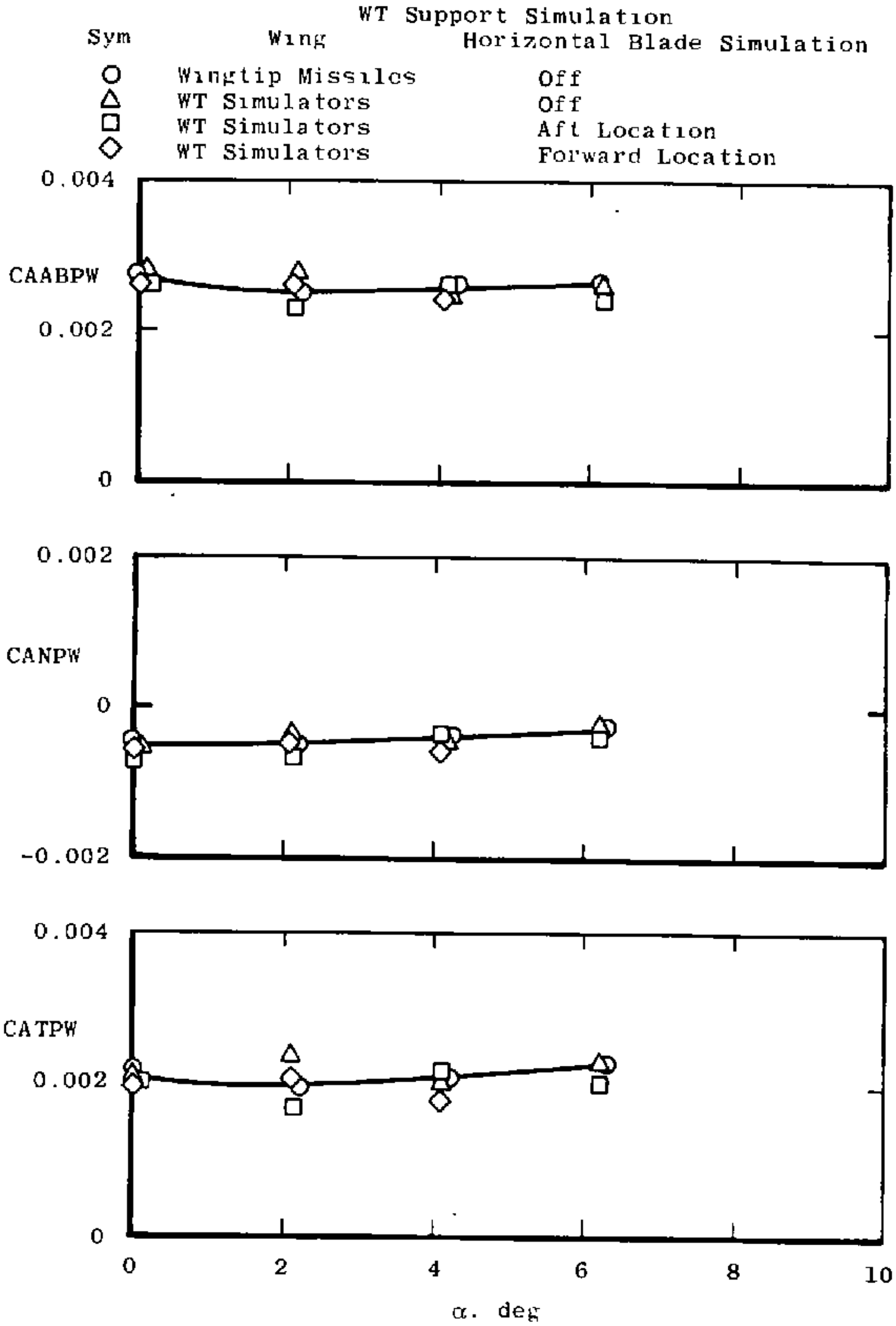

a. M = 0.6, A8 = 200 in.^{2}, NPRE = 3.4

Figure 36. Wingtip support system simulation effects on axial force coefficients (SS).

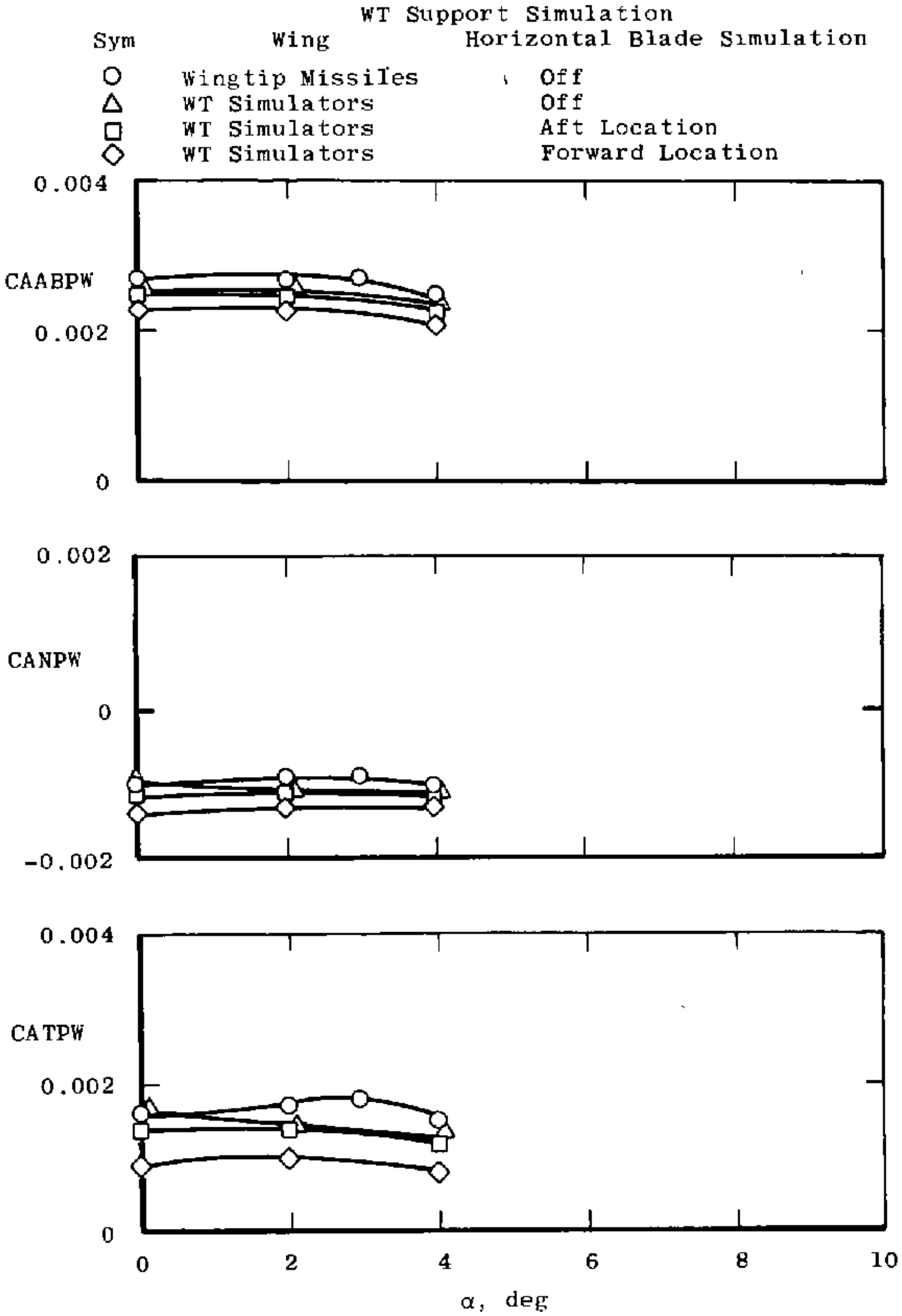

b. M = 0.8, A8 = 200 in.², NPRE = 3.4
Figure 36. Continued.

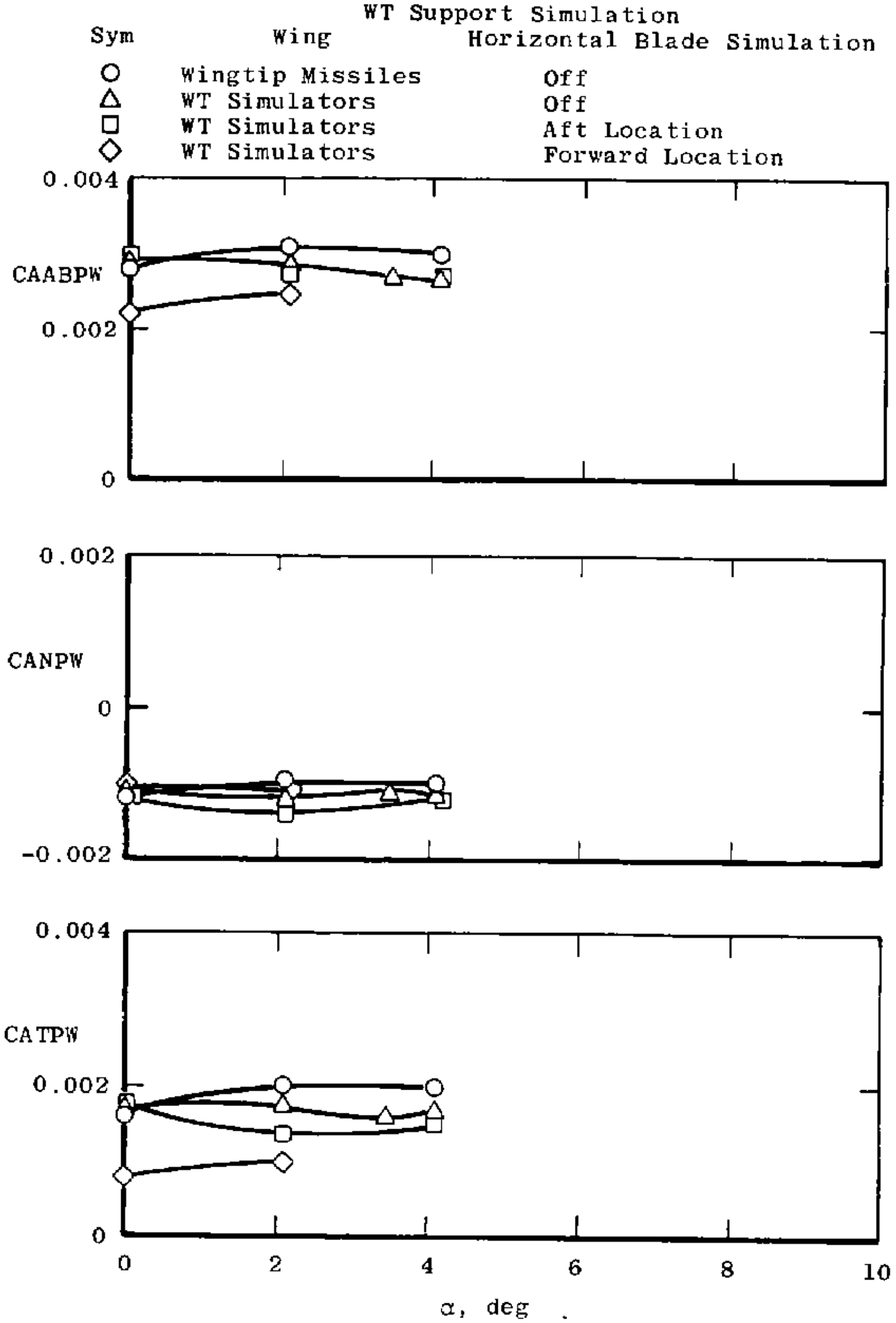

c. M = 0.9, A8 = 200 in.², NPRE = 3.4
Figure 36. Continued.

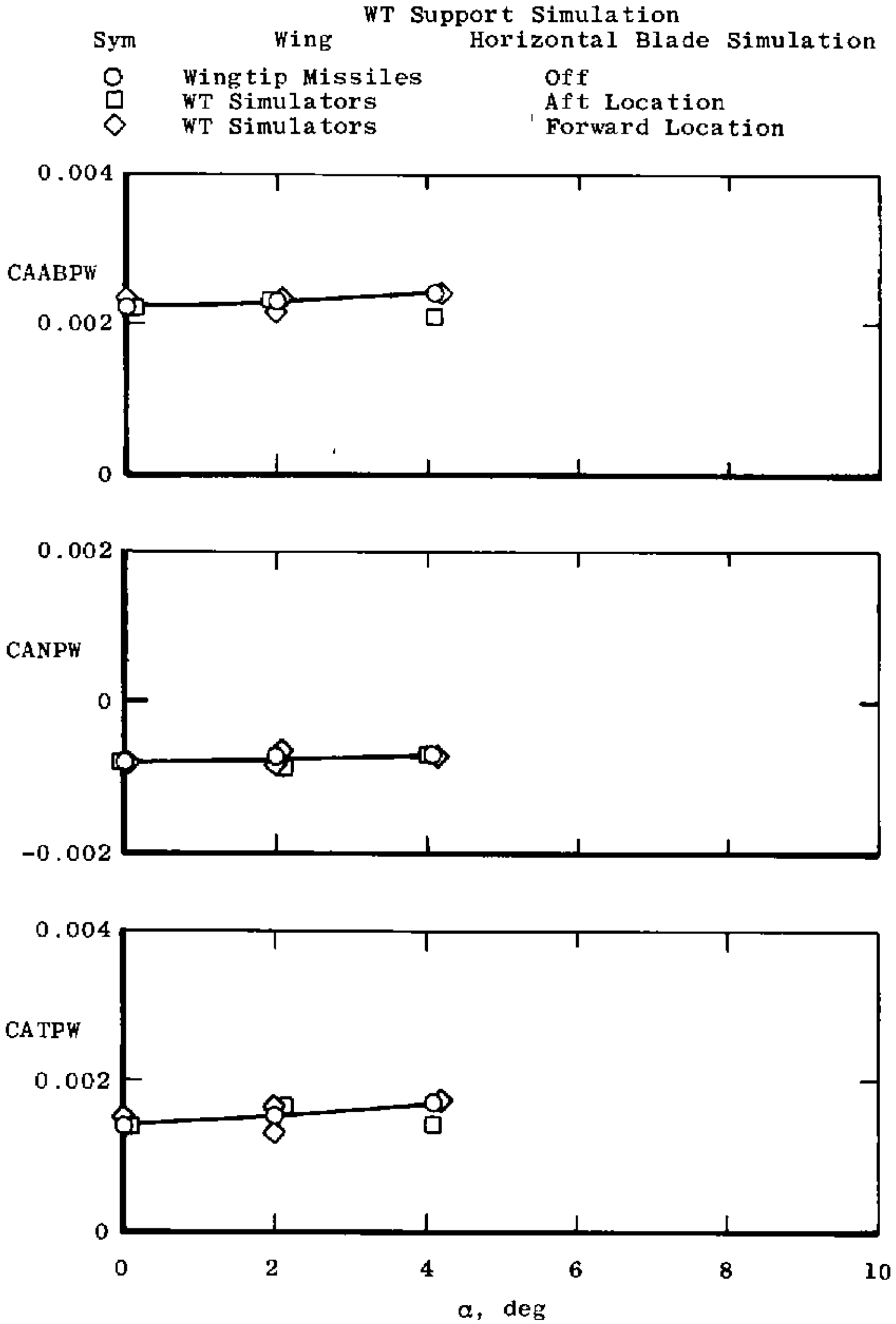

e. M = 0.6, A8 = 300 in.^{2}, NPRE = 5.0
Figure 36. Continued.

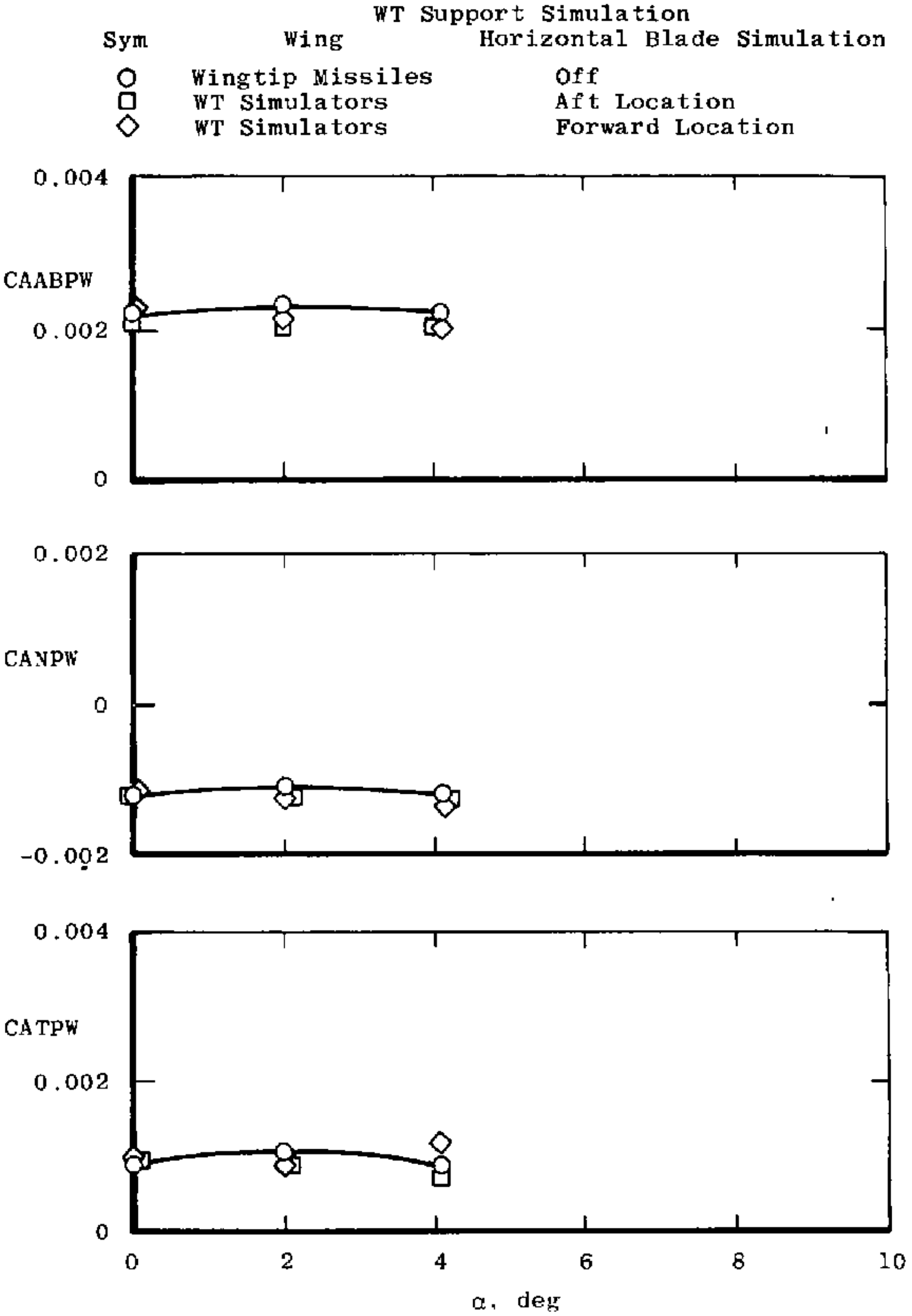

f. M = 0.8, A8 = 300 in.², NPRE = 5.0
Figure 36. Continued.

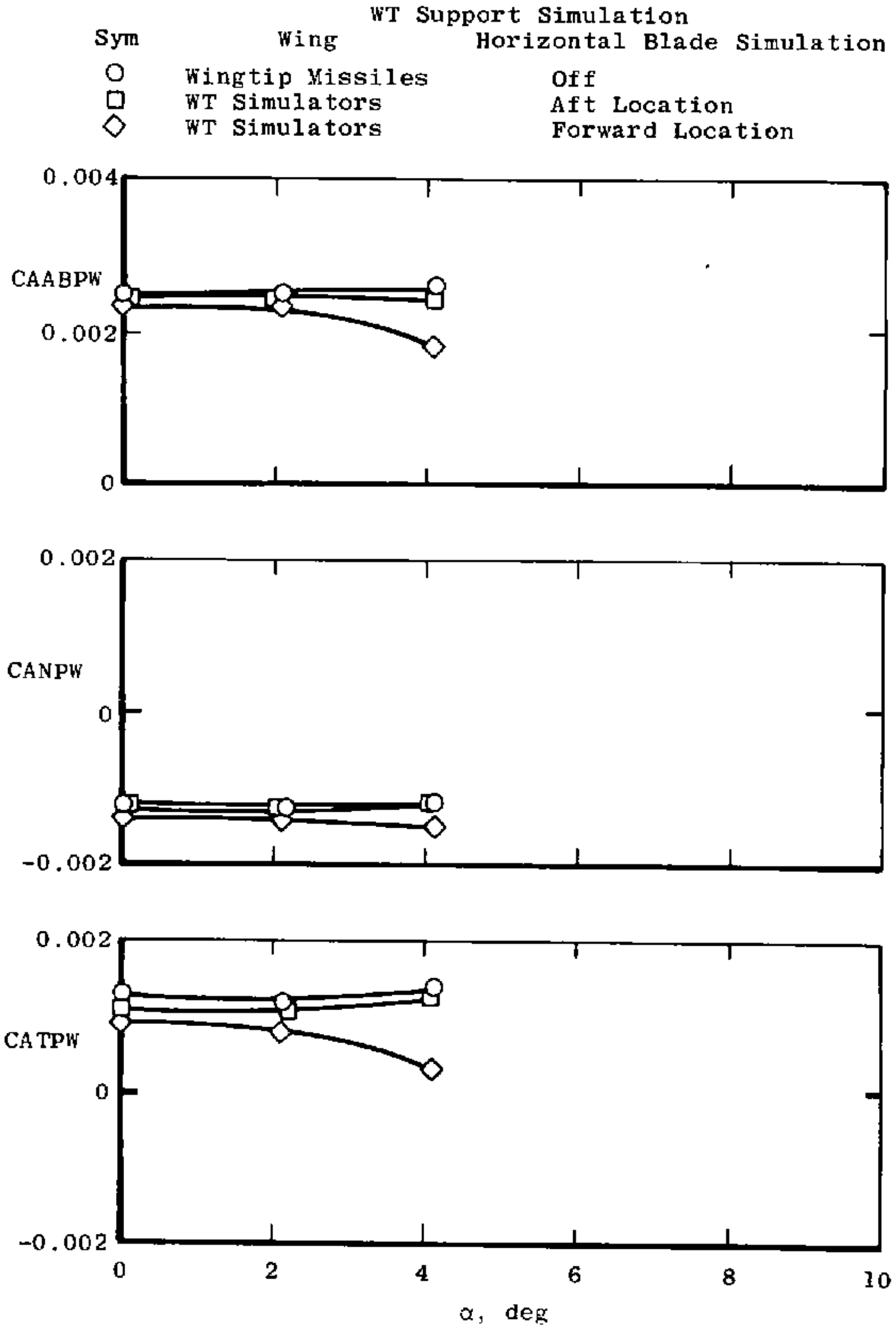

g. M = 0.9, A8 = 300 in.^{2}, NPRE = 5.0
Figure 36. Continued.

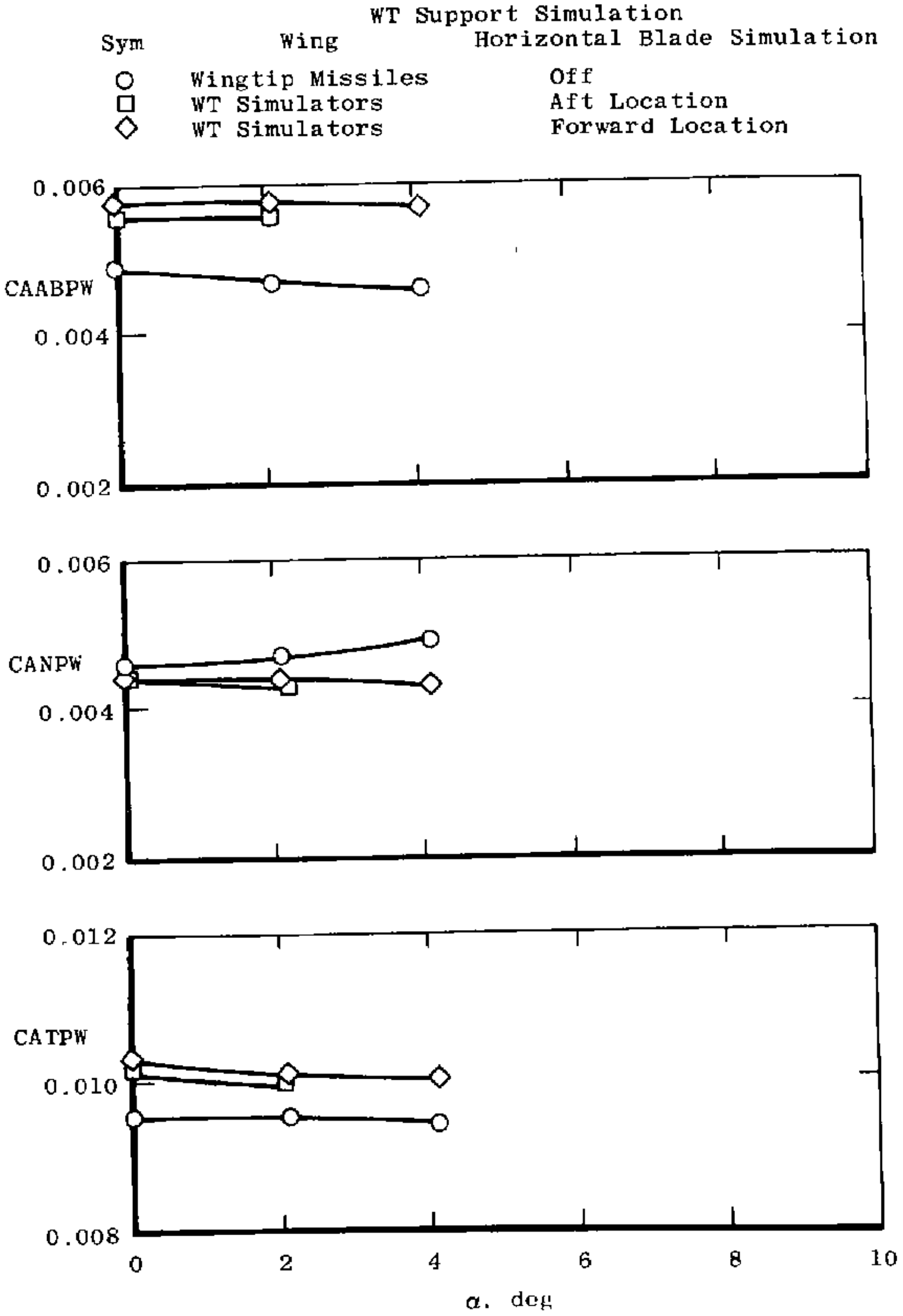

h. M = 1.2, A8 = 300 in.^{2}, NPRE = 5.0
Figure 36. Concluded.

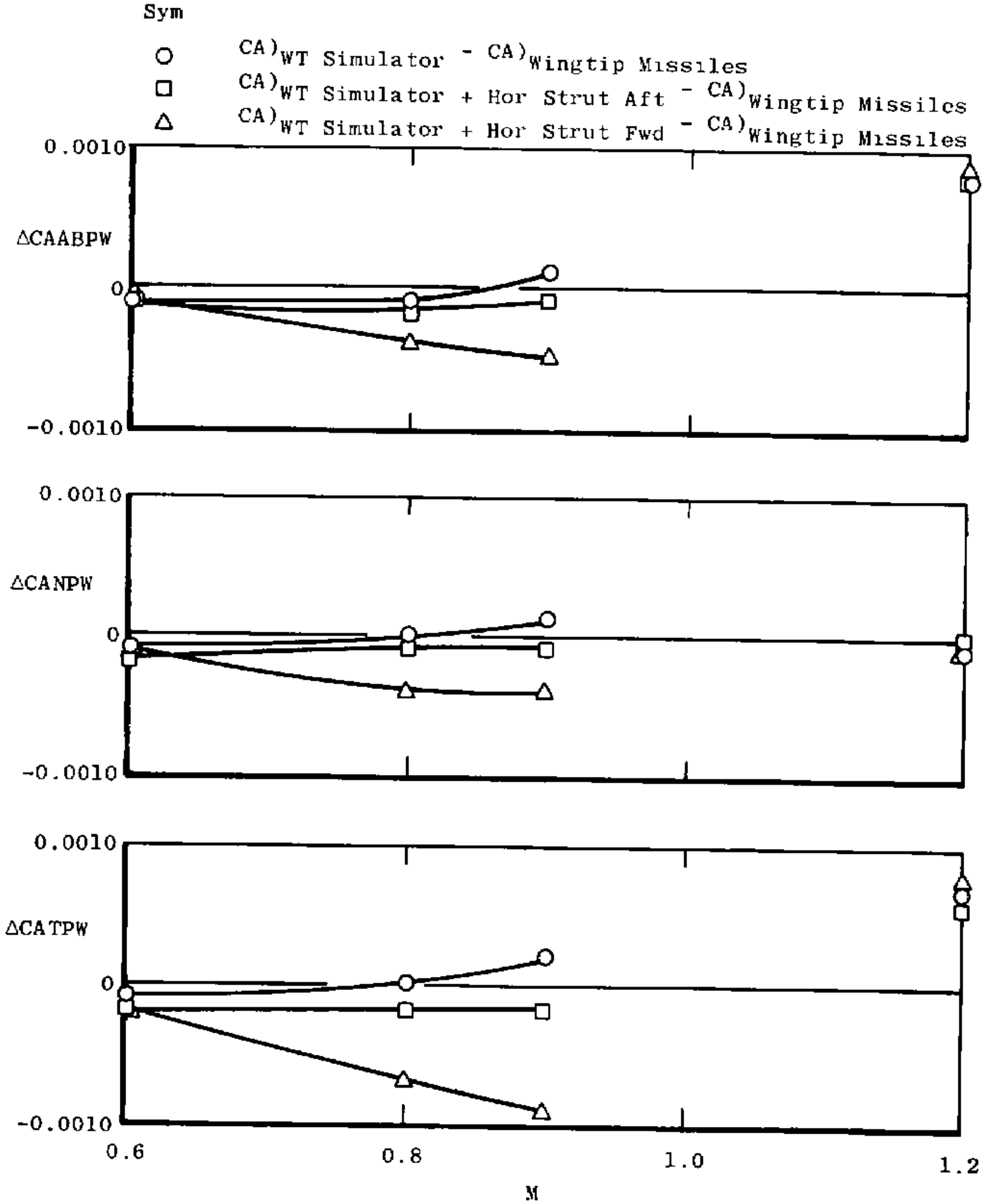

a. A8 = 200 in.^{2}, α = 0, NPRE = 3.4

Figure 37. Wingtip support system simulation incremental effects on axial force coefficients (SS).

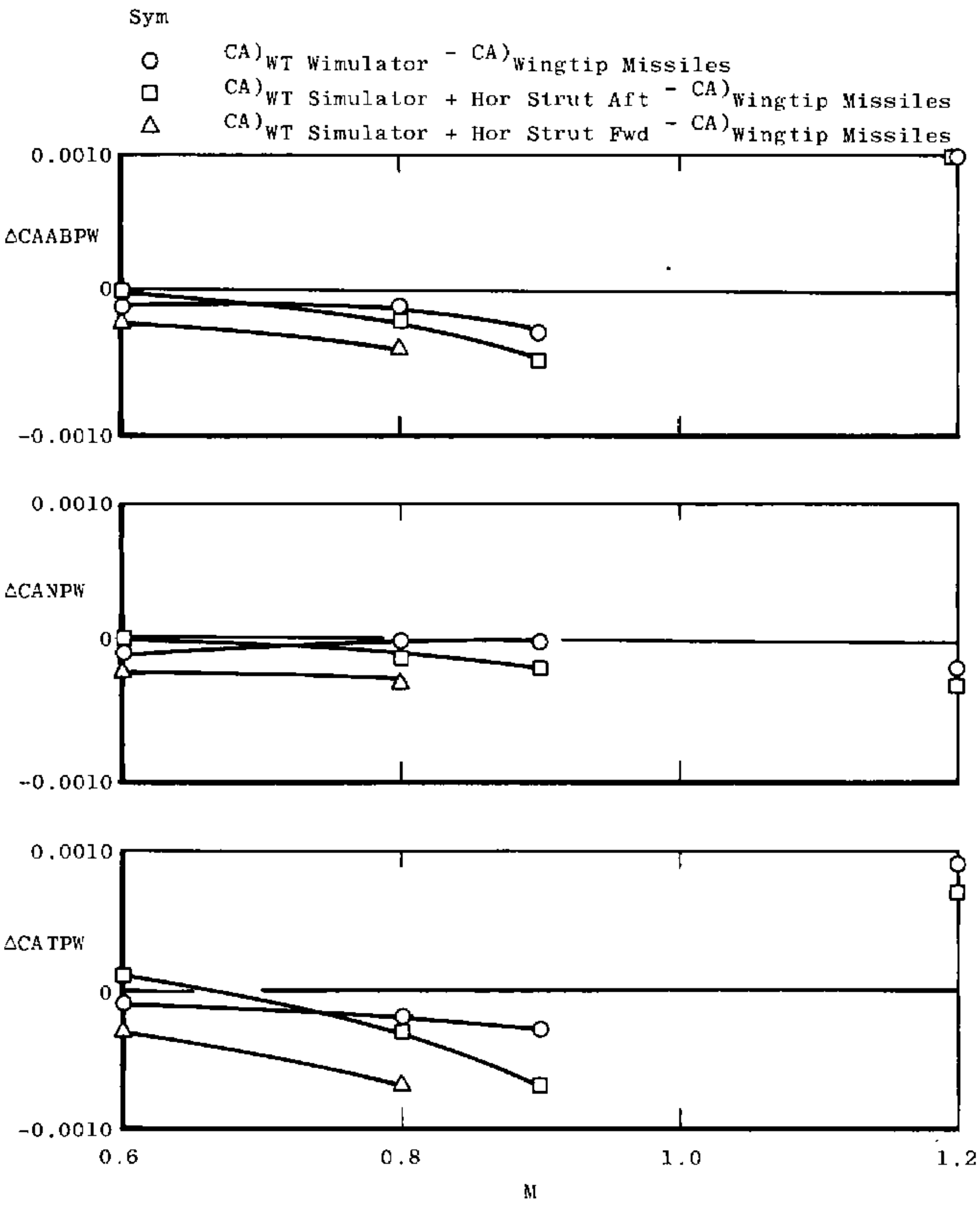

b. A8 = 200 in.^{2}, α = 4.1 deg, NPRE = 3.4
Figure 37. Continued.

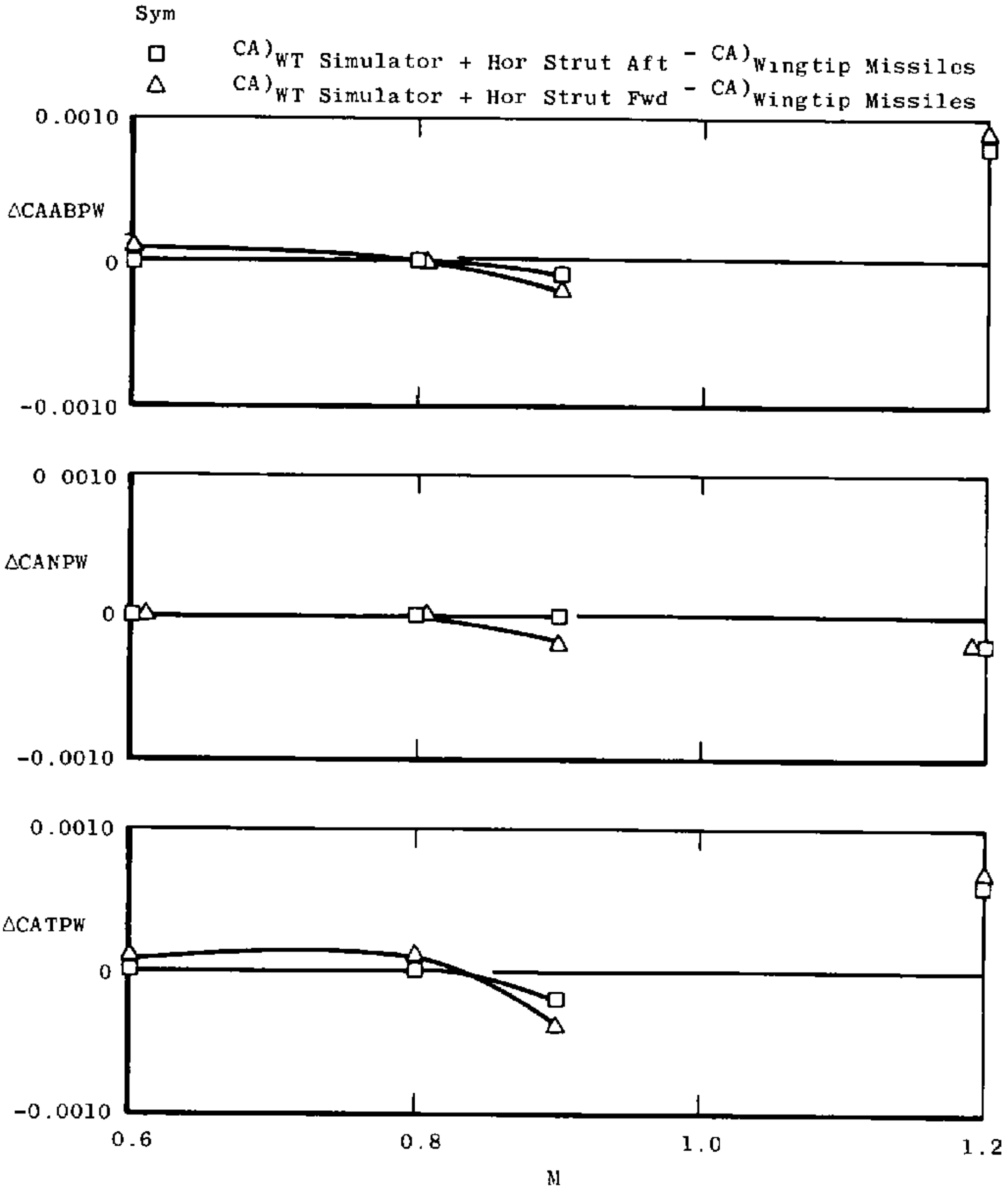

c. A8 = 300 in.^{2}, α = 0, NPRE = 5.0

Figure 37. Continued.

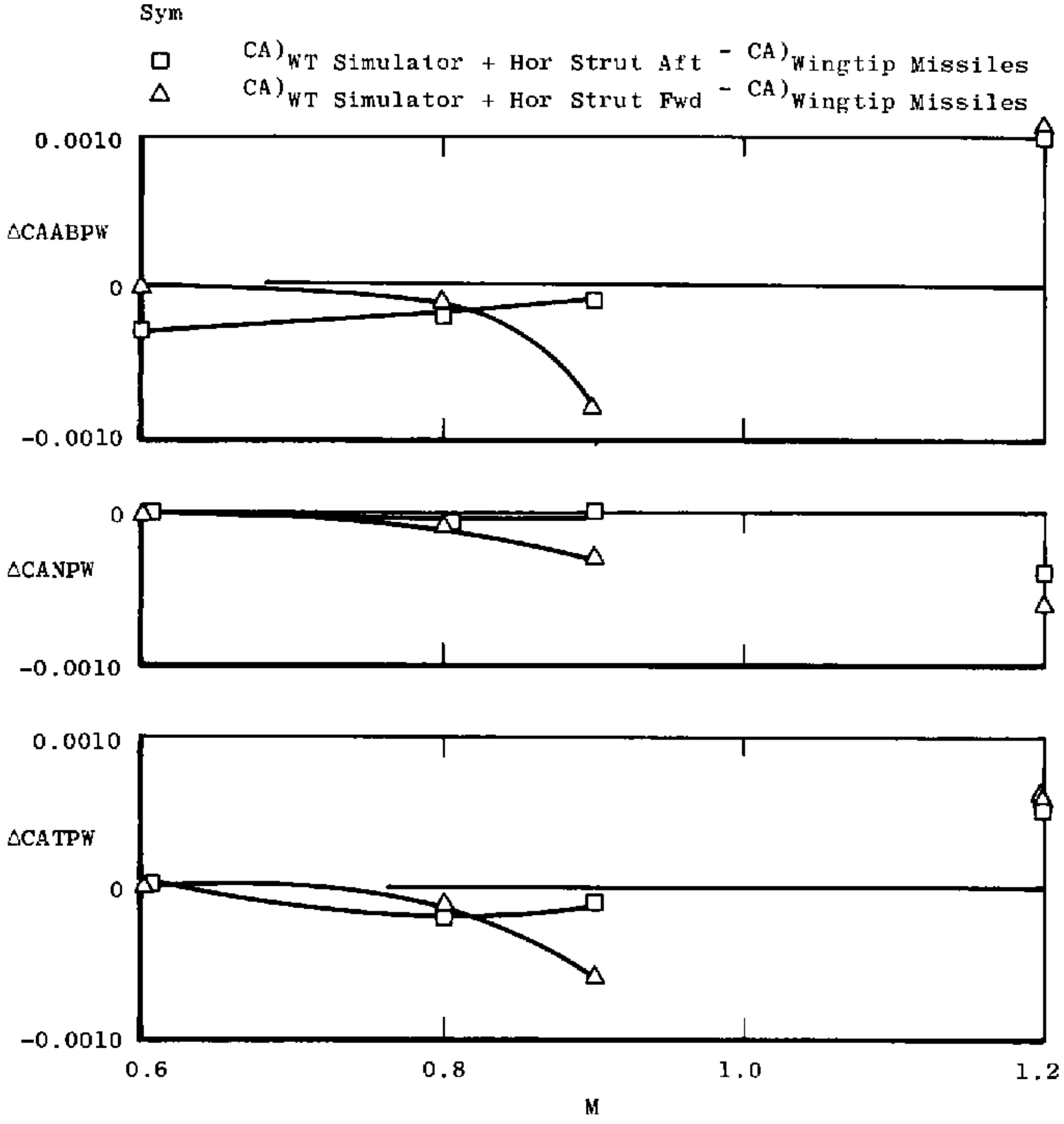

d. A8 = 300 in.², α = 4.1 deg, NPRE = 5.0
Figure 37. Concluded.

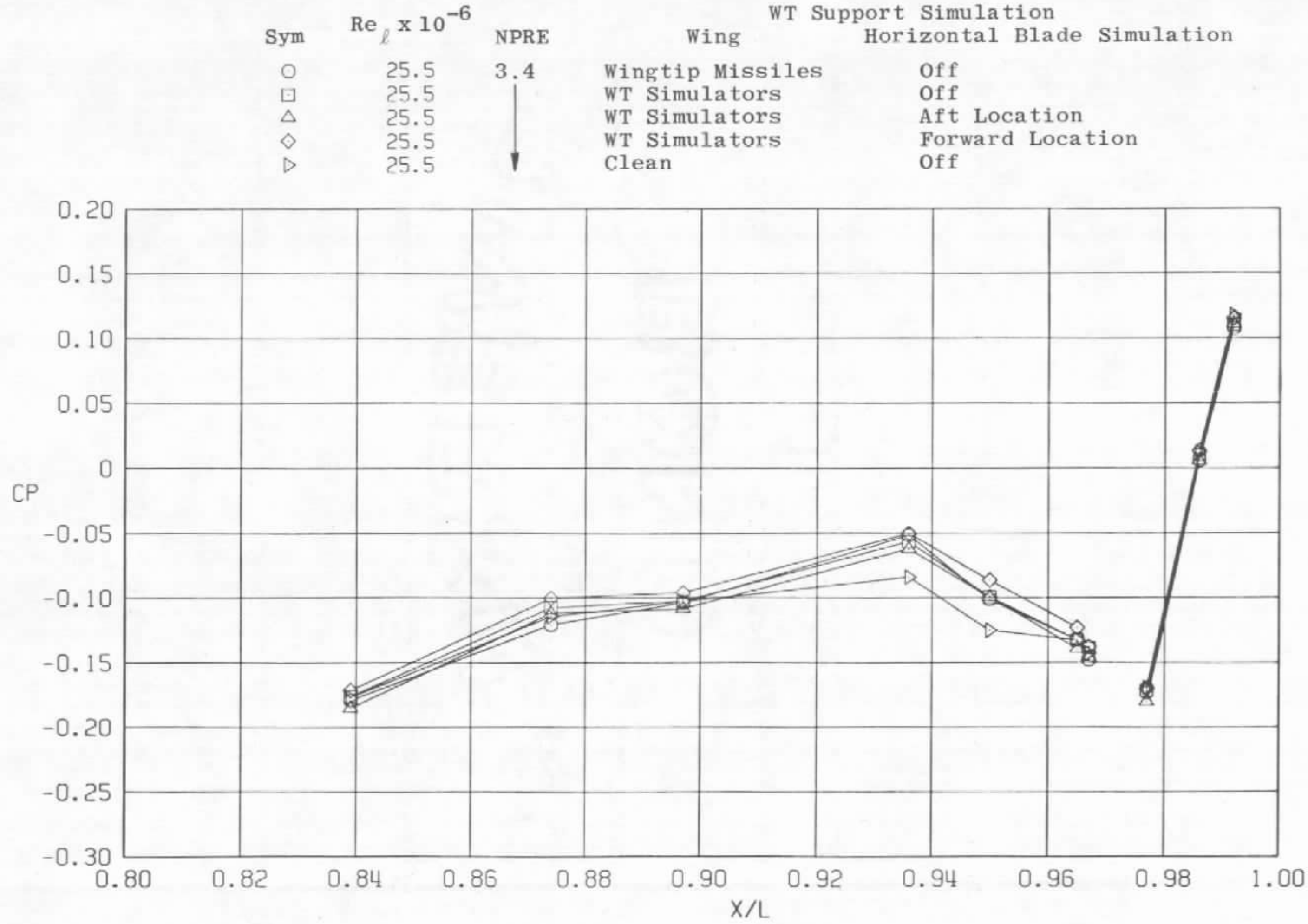

a. $\phi = 0$

Figure 38. Wingtip support system simulation effects on surface pressure coefficients, A8 = 200 in.^{2}, M = 0.6 (SS), α = 4.1 deg.

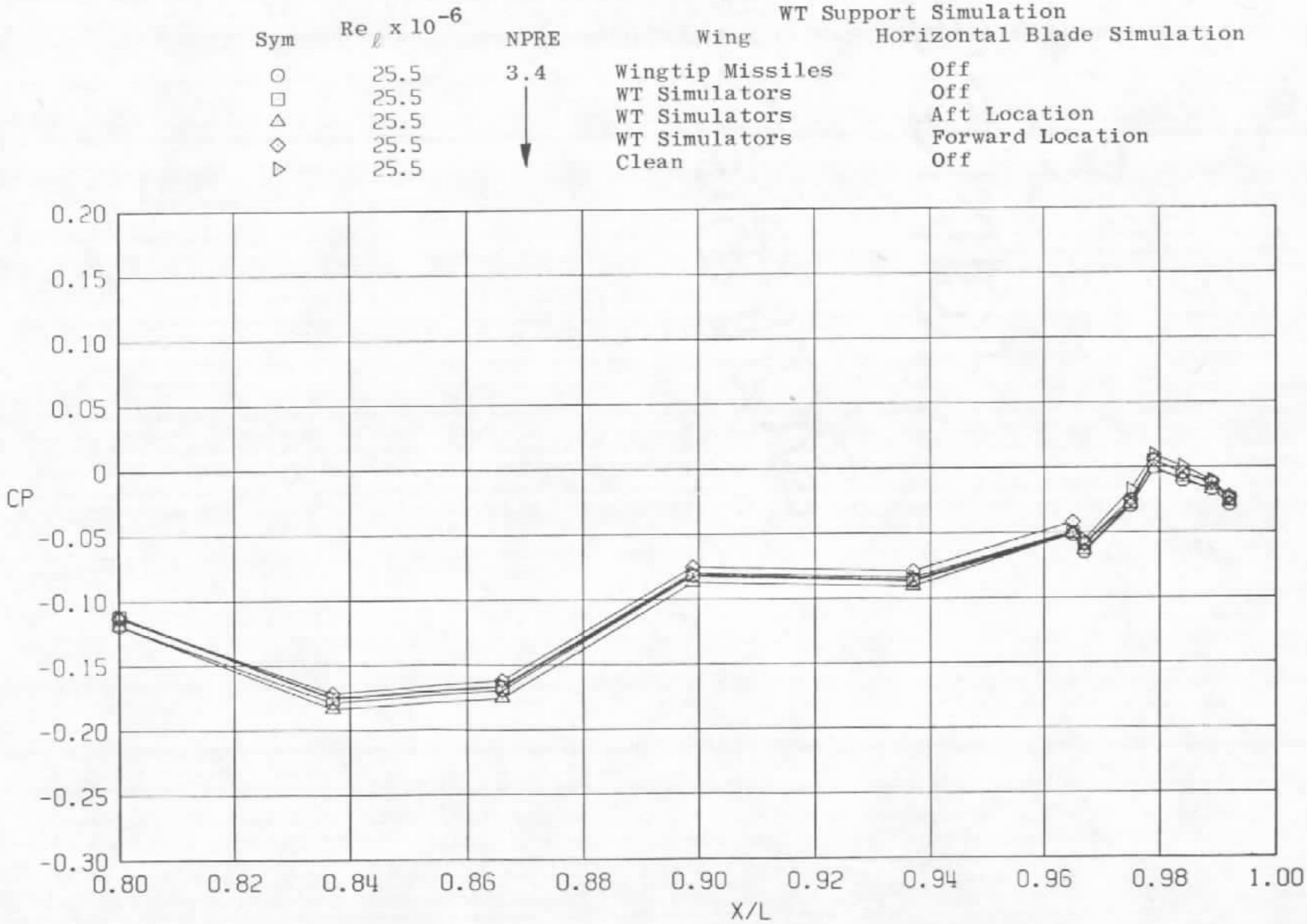

b. ϕ = 45 deg

Figure 38. Continued.

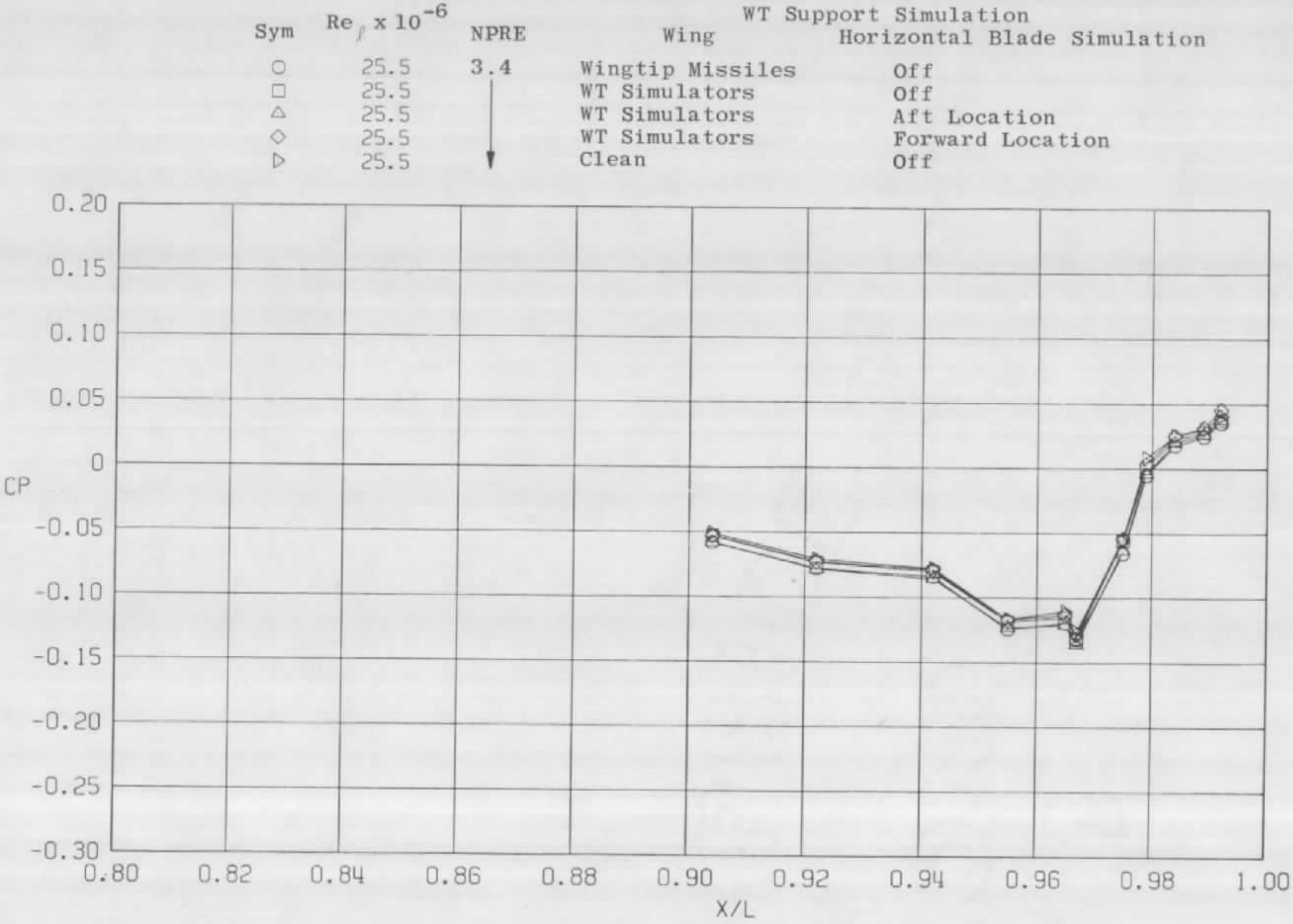

c. ϕ = 135 deg
Figure 38. Continued.

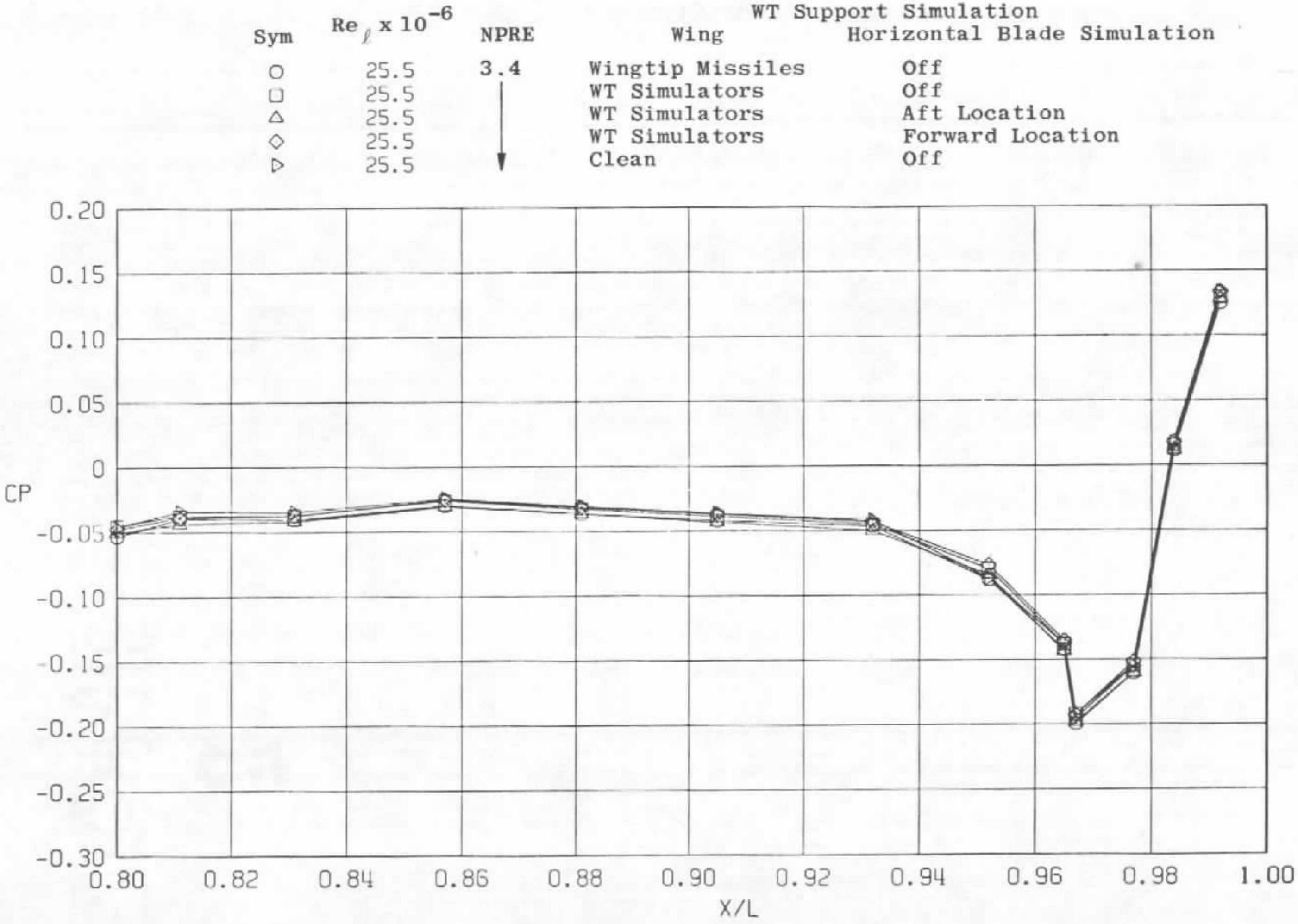

d. ϕ = 180 deg
Figure 38. Continued.

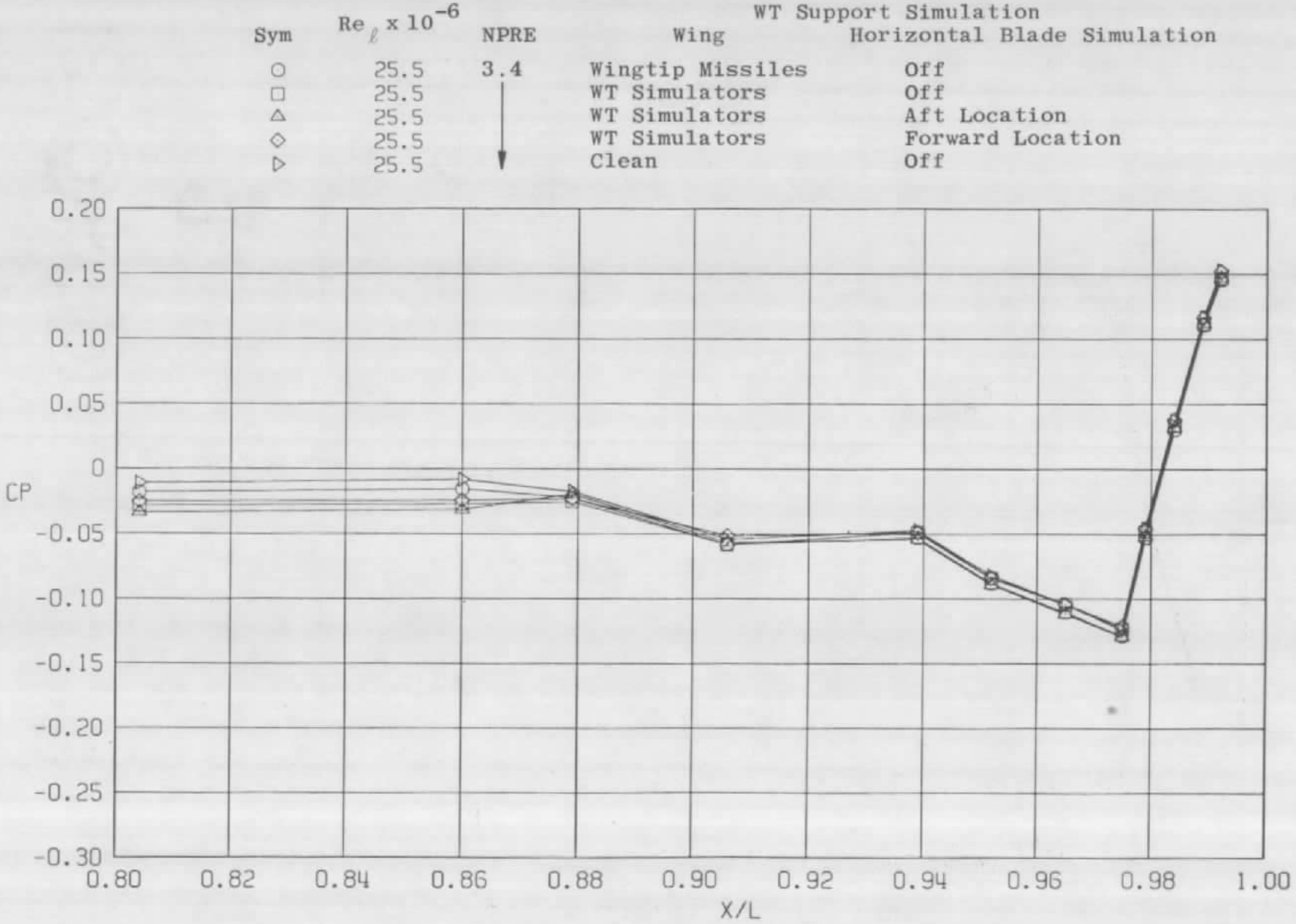

e. ϕ = 225 deg

Figure 38. Continued.

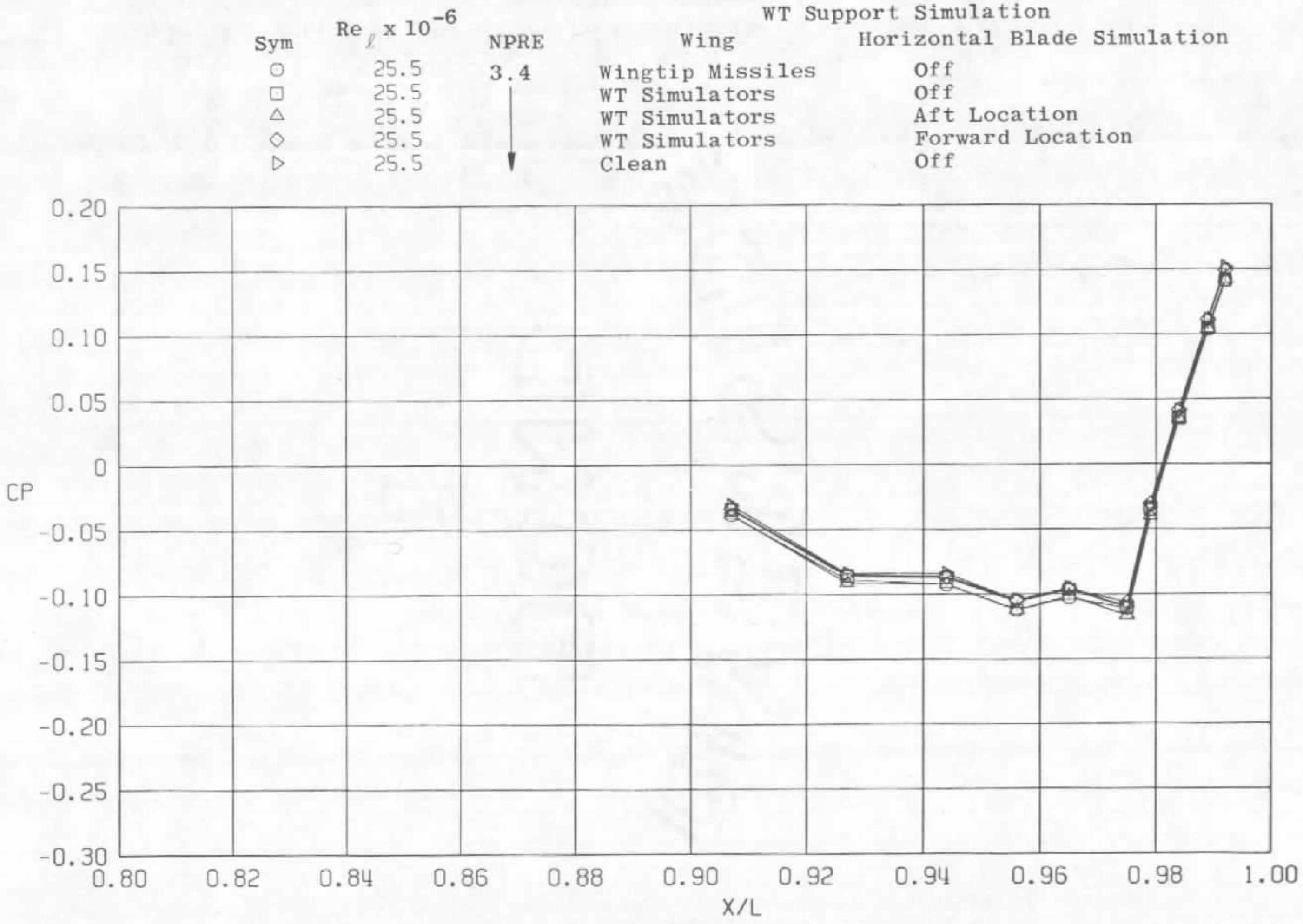

f. ϕ = 315 deg

Figure 38. Concluded.

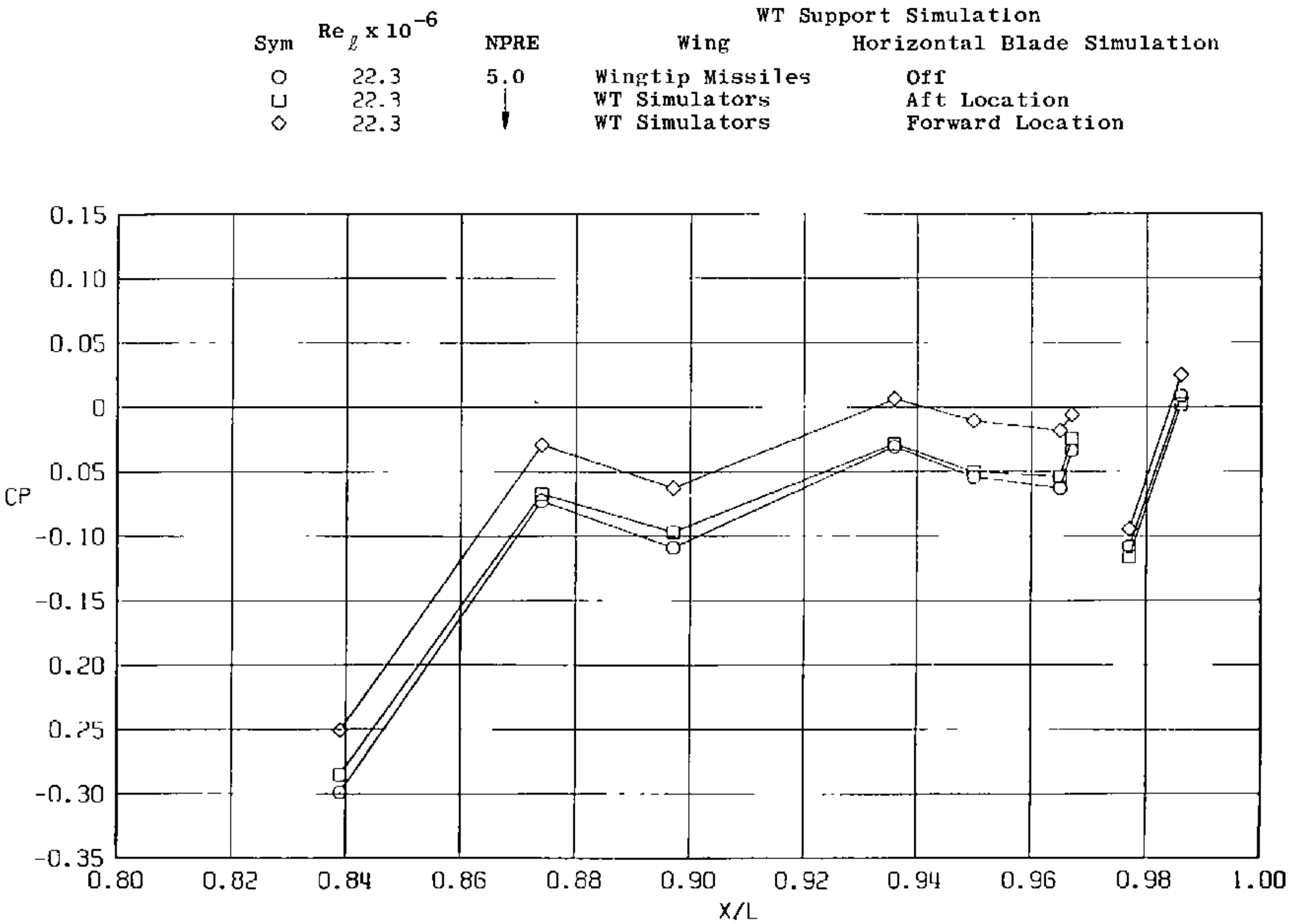

a. $\phi = 0$

Figure 39. Wingtip support system simulation effects on surface pressure coefficients, A8 = 300 in.^{2}, M = 0.9 (SS), α = 4.1 deg.

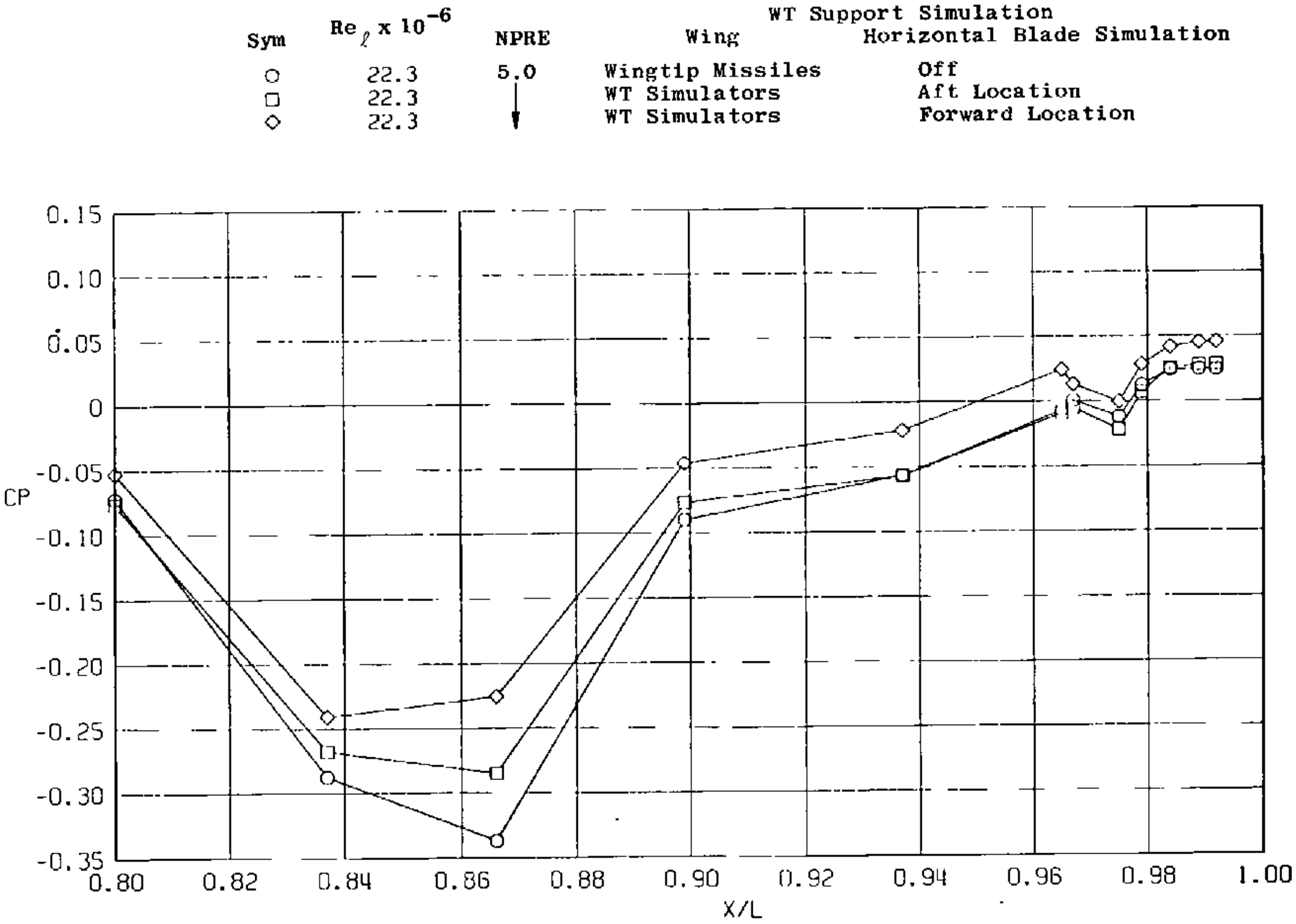

b. ϕ = 45 deg

Figure 39. Continued.

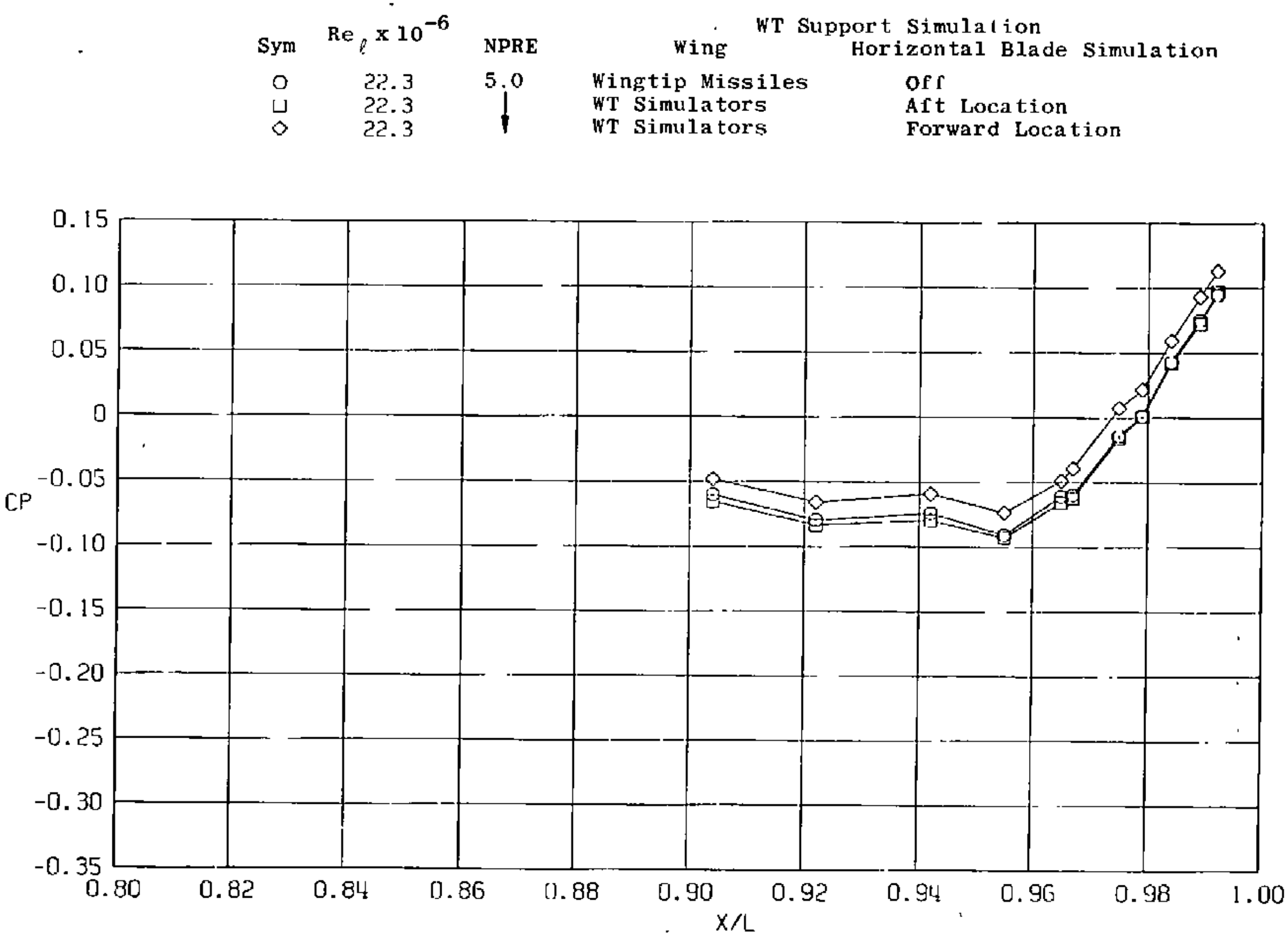

Sym	$Re_\ell \times 10^{-6}$	NPRE	Wing	WT Support Simulation Horizontal Blade Simulation
○	22.3	5.0	Wingtip Missiles	Off
□	22.3	↓	WT Simulators	Aft Location
◇	22.3		WT Simulators	Forward Location

c. ϕ = 135 deg
Figure 39. Continued.

Sym	$Re_{\ell} \times 10^{-6}$	NPRE	Wing	WT Support Simulation Horizontal Blade Simulation
○	22.3	5.0	Wingtip Missiles	Off
□	22.3	↓	WT Simulators	Aft Location
◇	22.3		WT Simulators	Forward Location

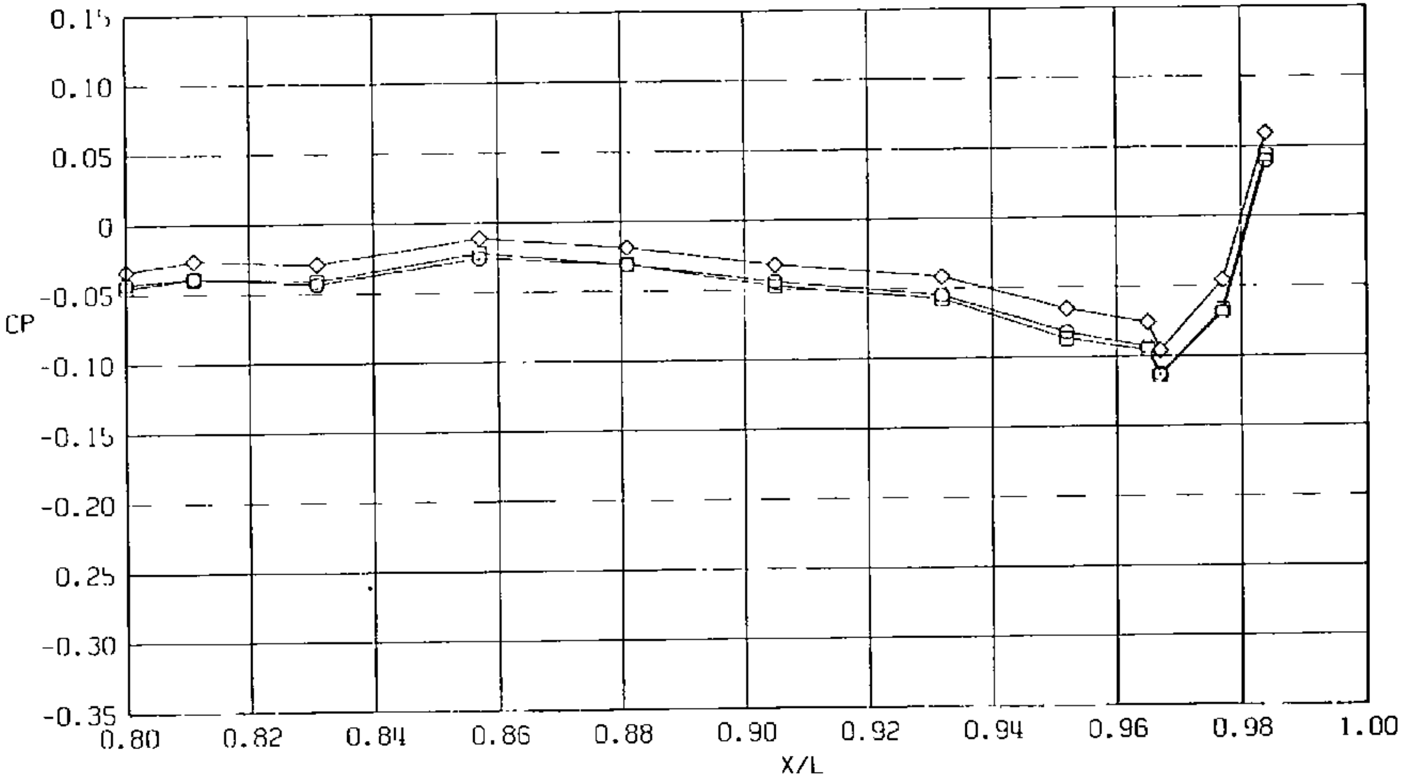

d. ϕ = 180 deg
Figure 39. Continued.

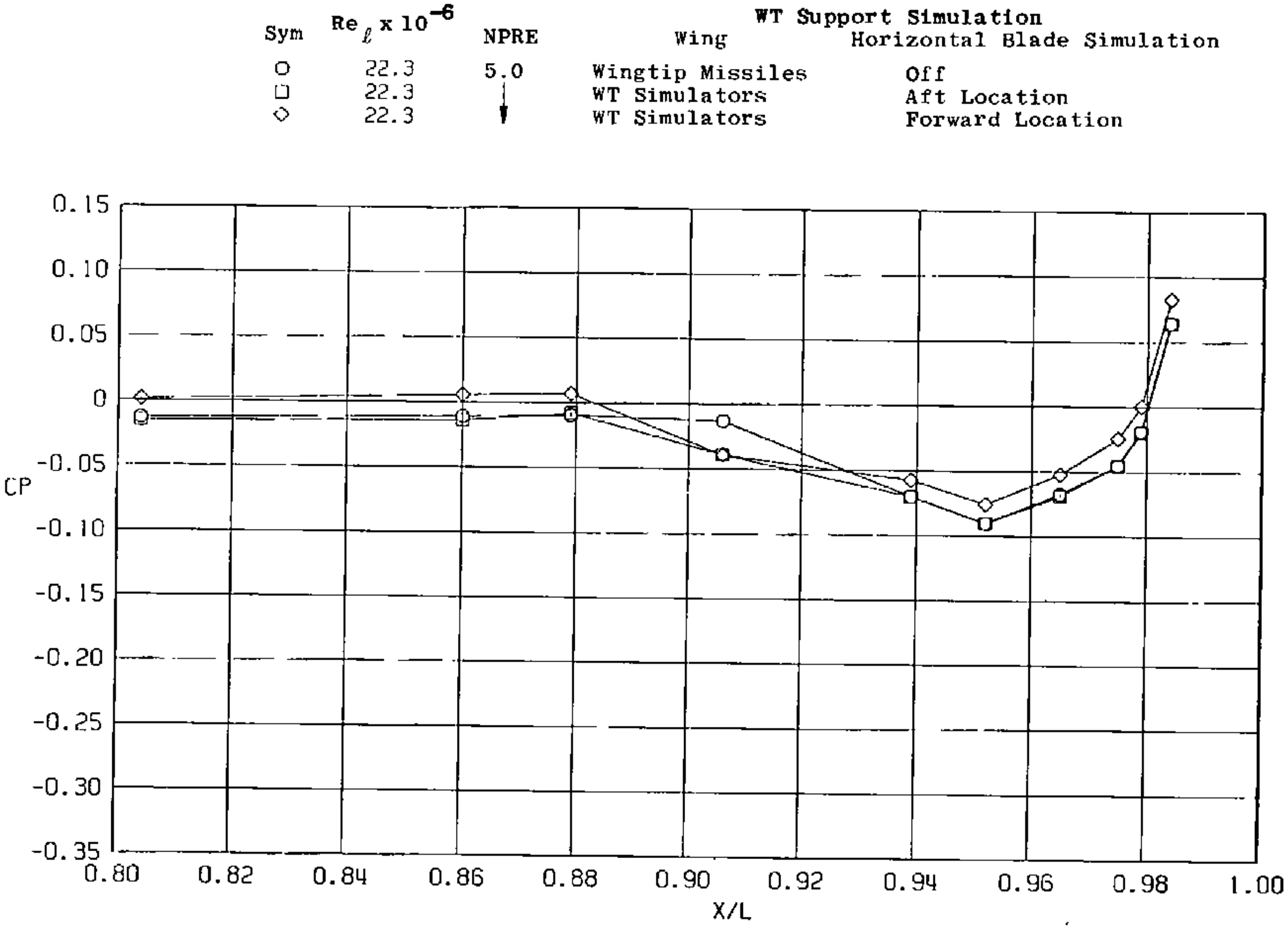

e. ϕ = 225 deg
Figure 39. Continued.

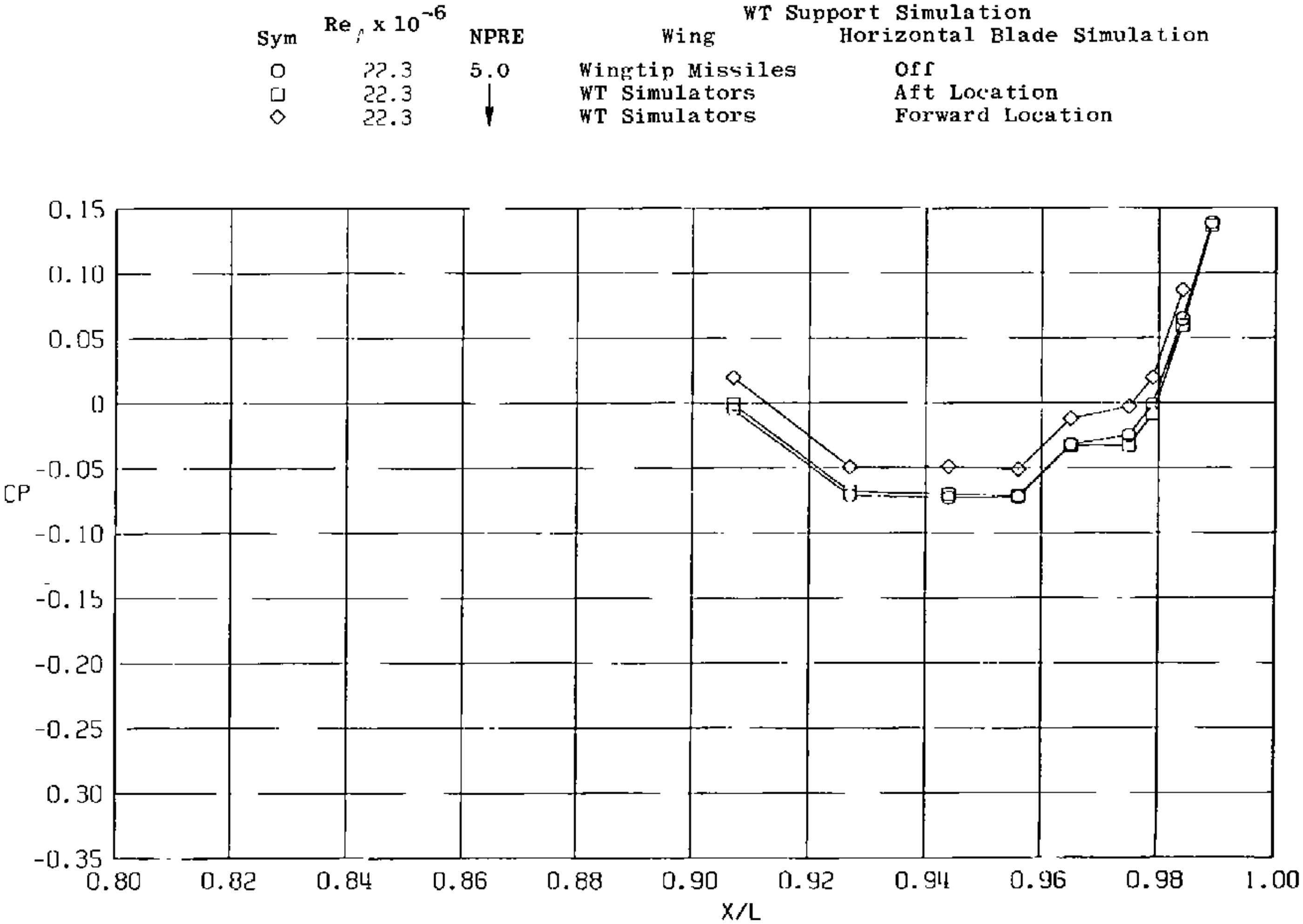

f. ϕ = 315 deg
Figure 39. Concluded.

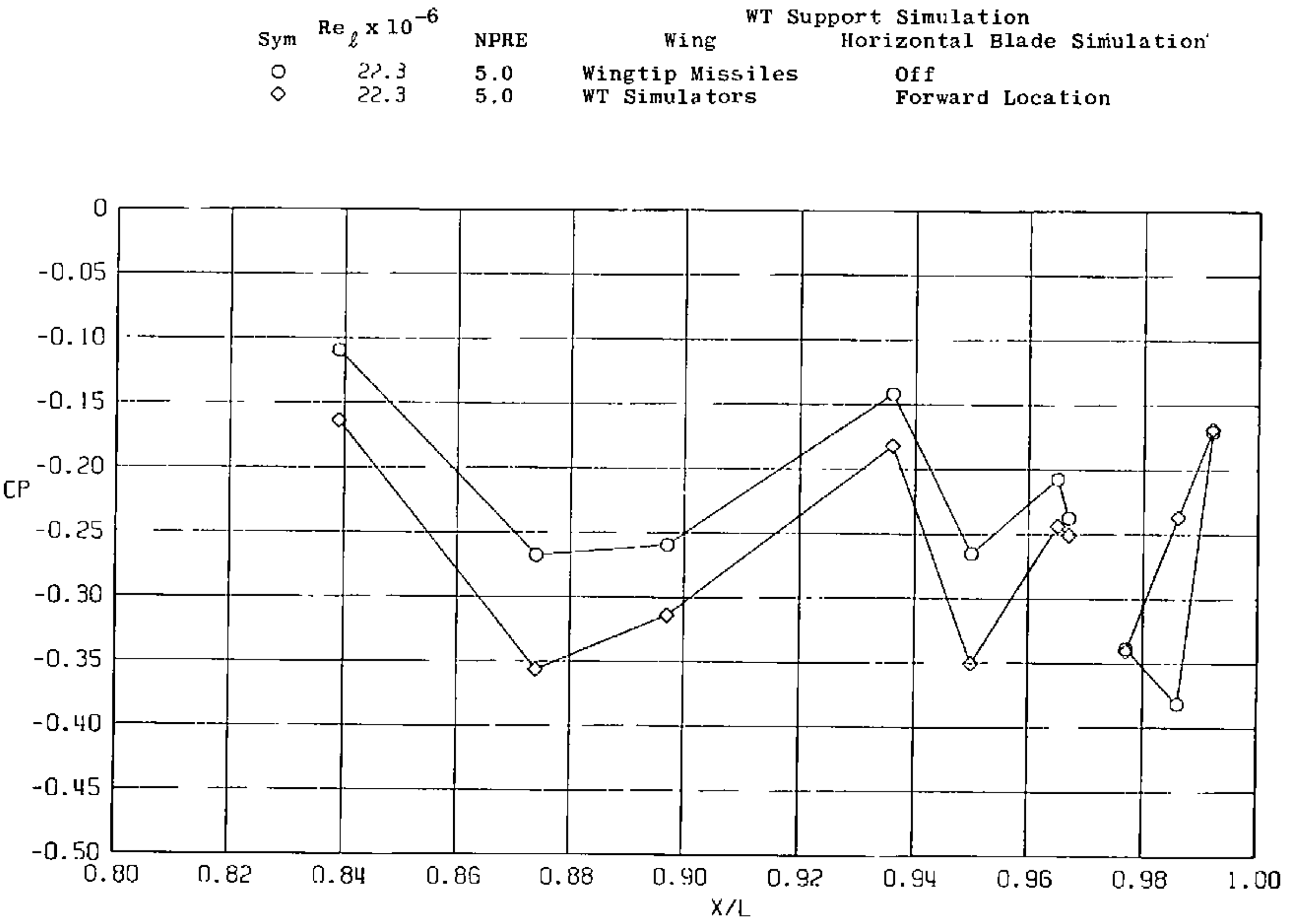

a. $\phi = 0$

Figure 40. Wingtip support system simulation effects on surface pressure coefficients, A8 = 300 in.^{2}, M = 1.2 (SS), α = 4.1 deg.

Sym	$Re_{\ell} \times 10^{-6}$	NPRE	WT Support Simulation Wing	Horizontal Blade Simulation
○	22.3	5.0	Wingtip Missiles	Off
◇	22.3	5.0	WT Simulators	Forward Location

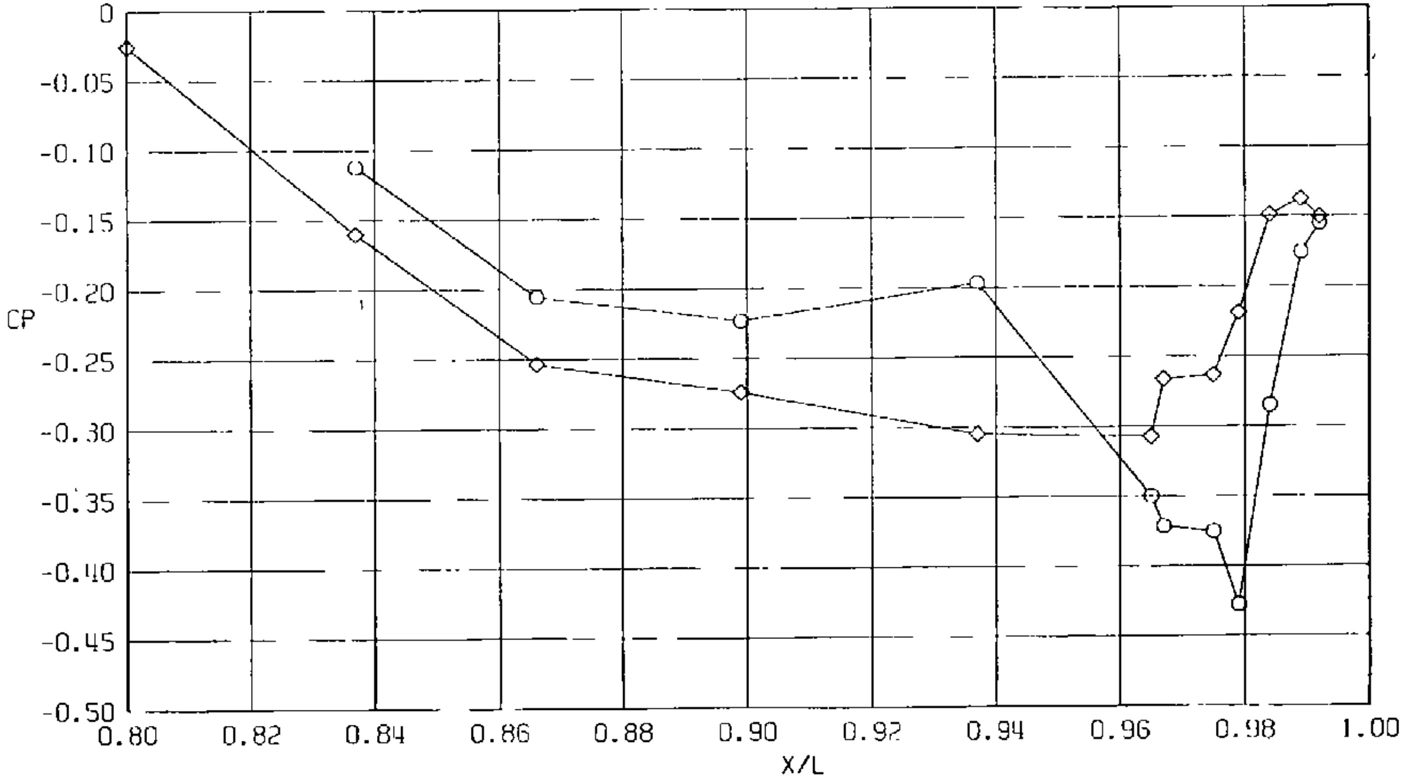

b. ϕ = 45 deg
Figure 40. Continued.

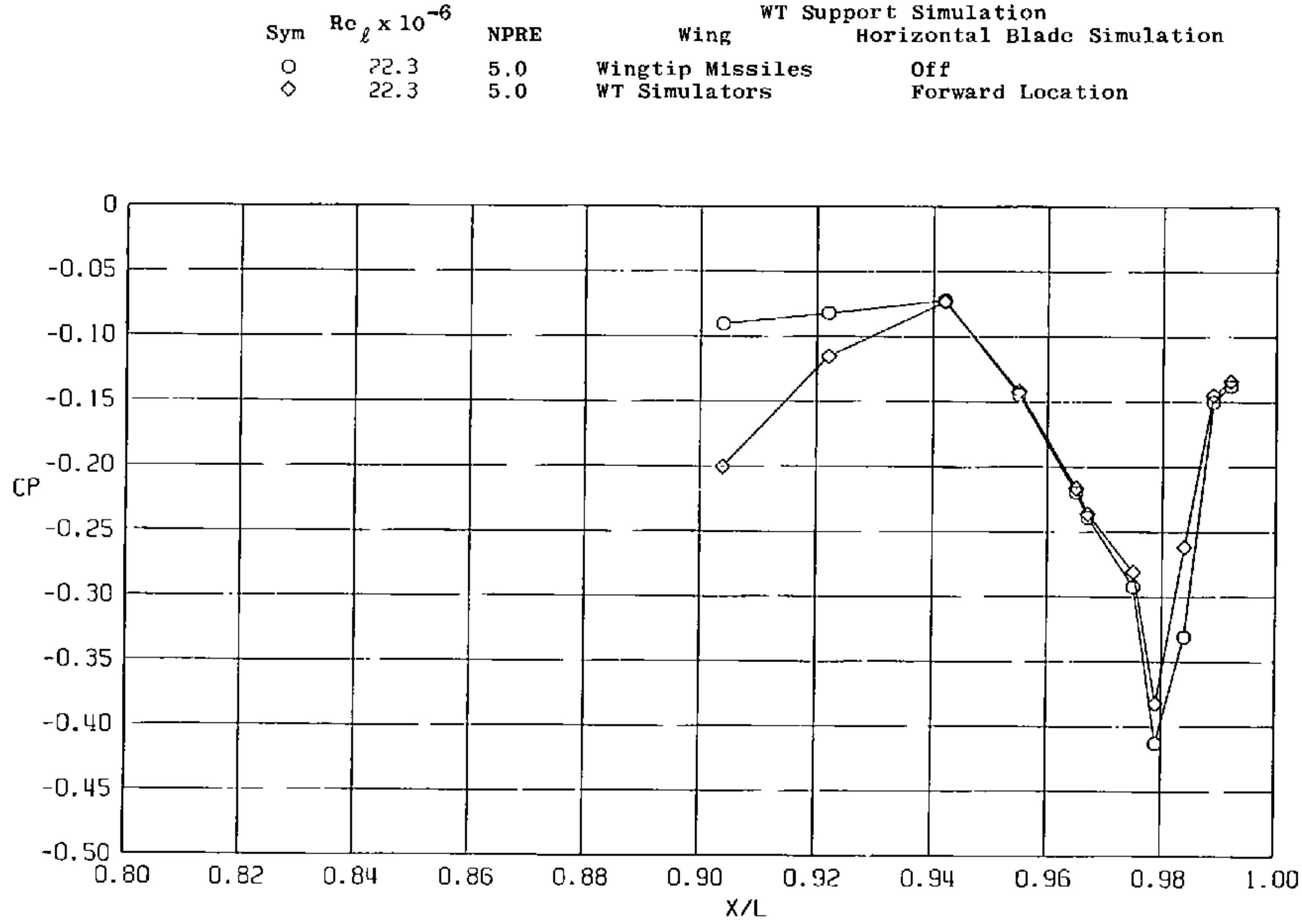

c. ϕ = 135 deg
Figure 40. Continued.

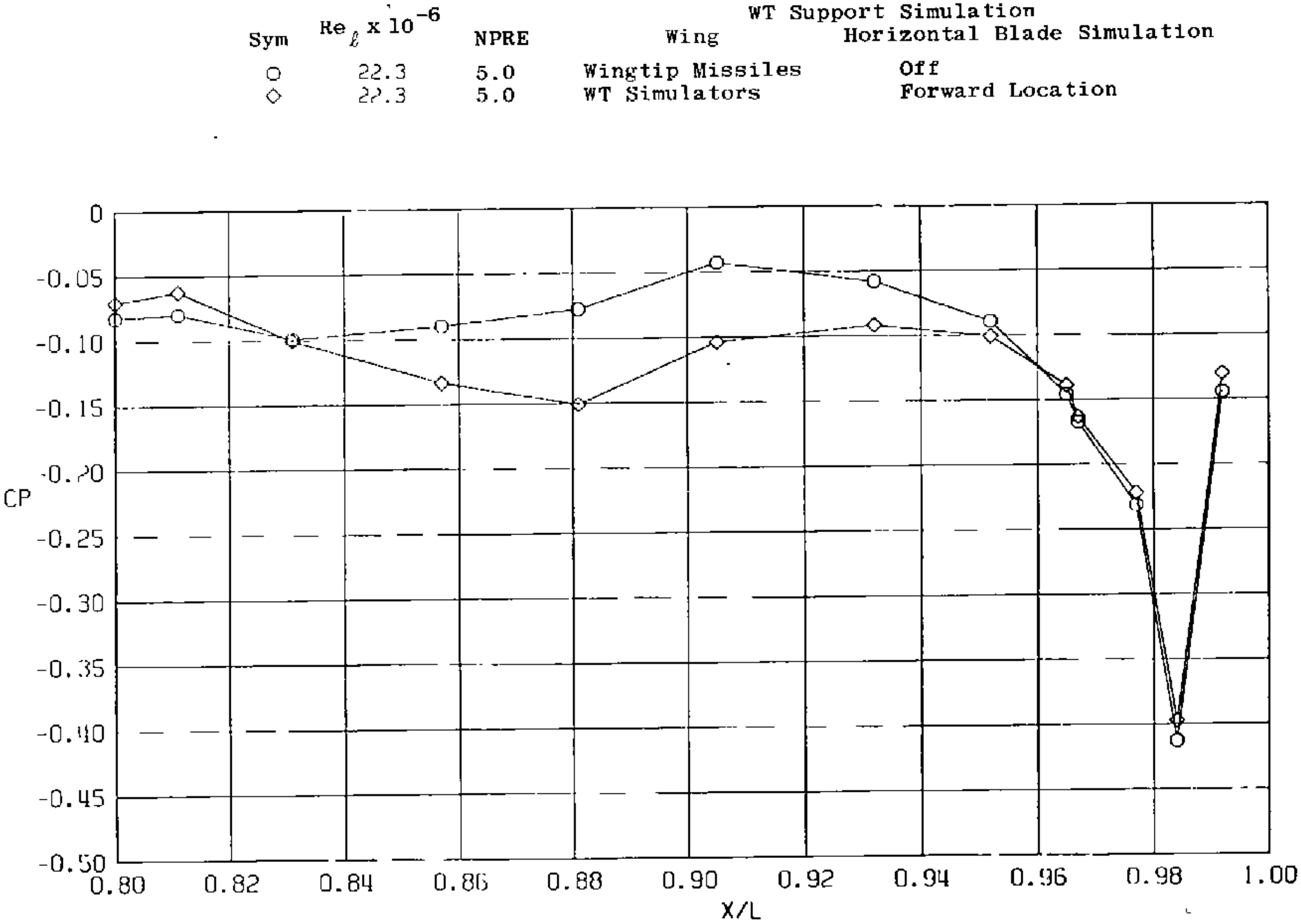

d. ϕ = 180 deg

Figure 40. Continued.

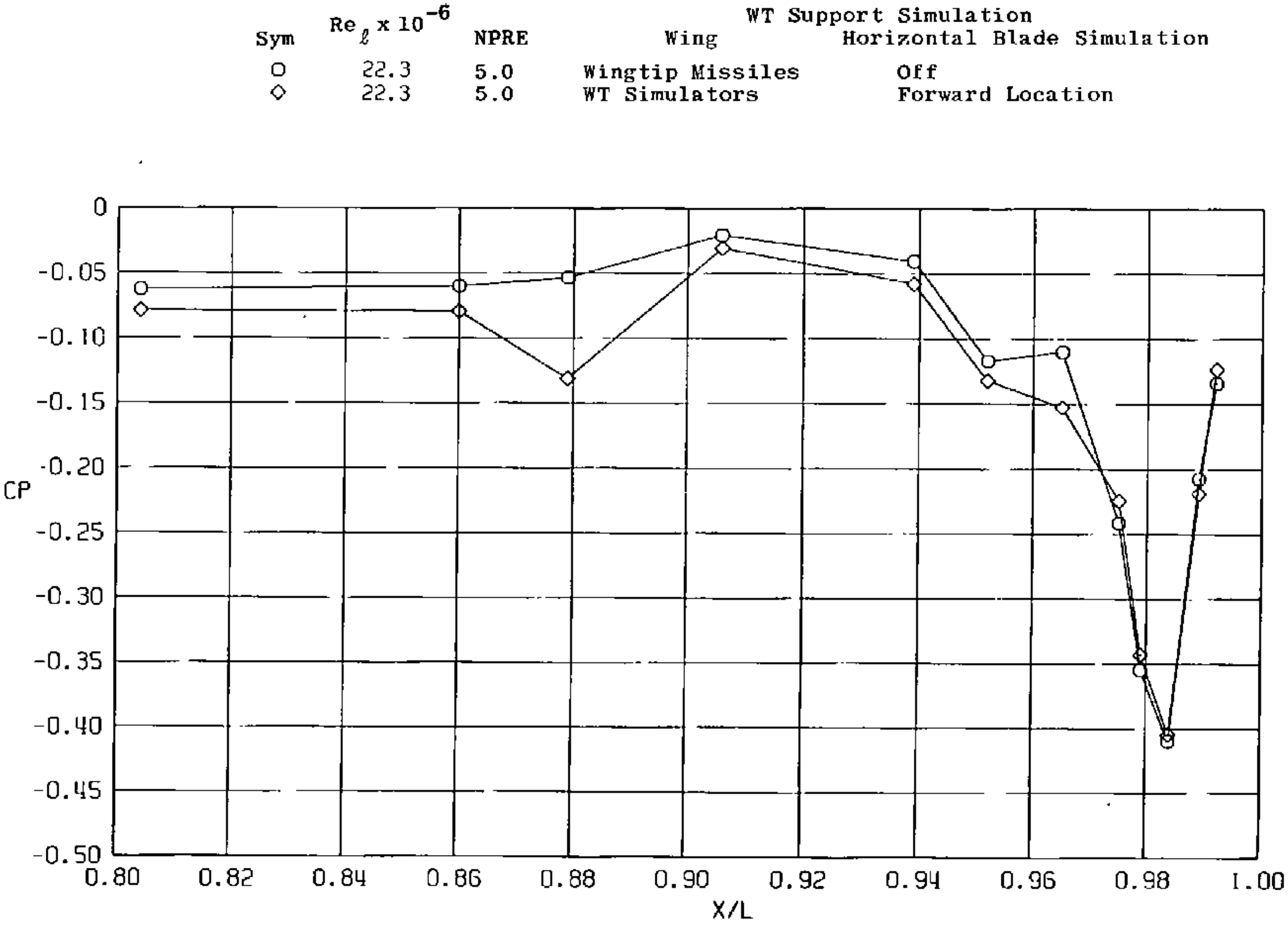

e. ϕ = 225 deg
Figure 40. Continued.

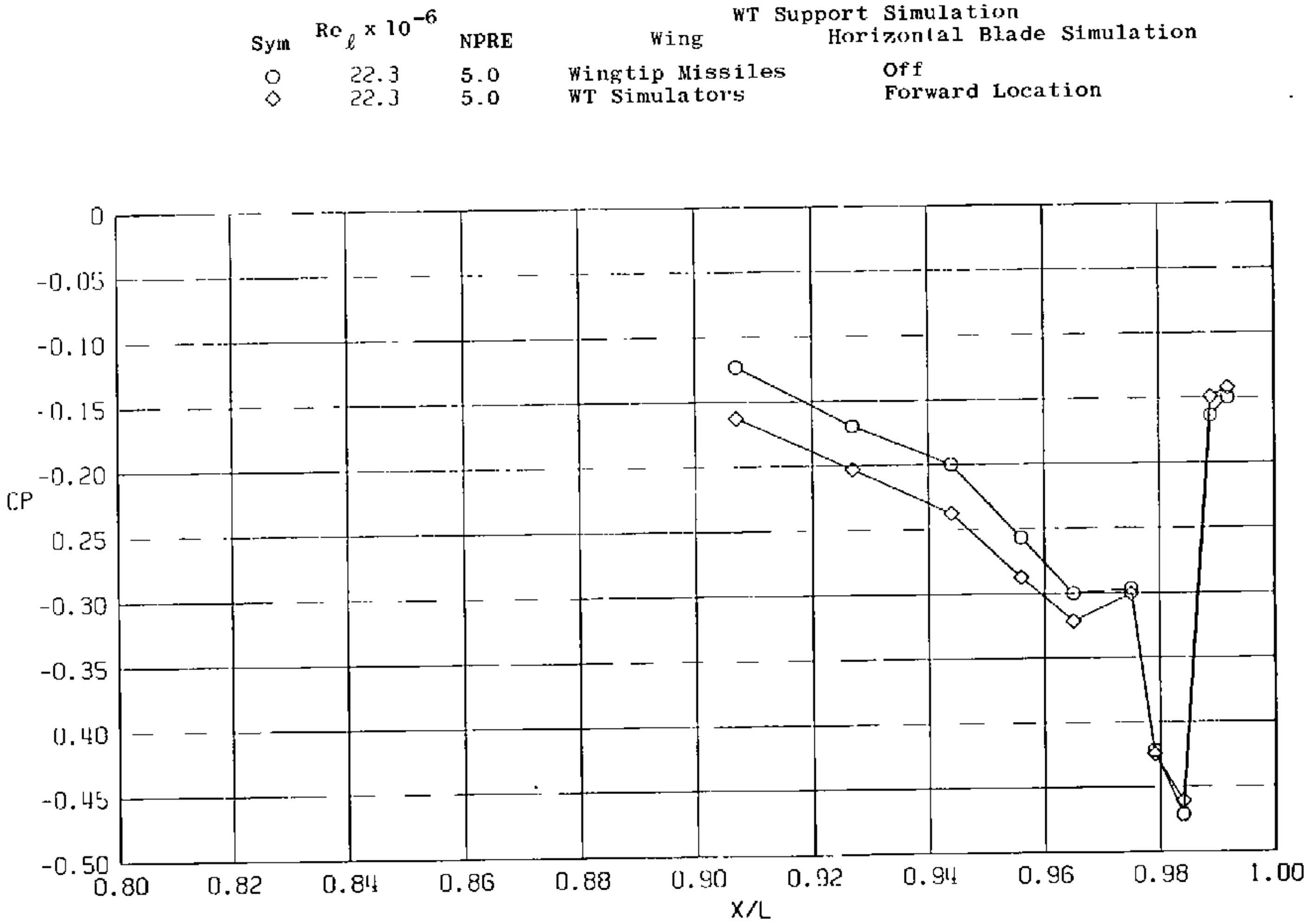

f. ϕ = 315 deg

Figure 40. Concluded.

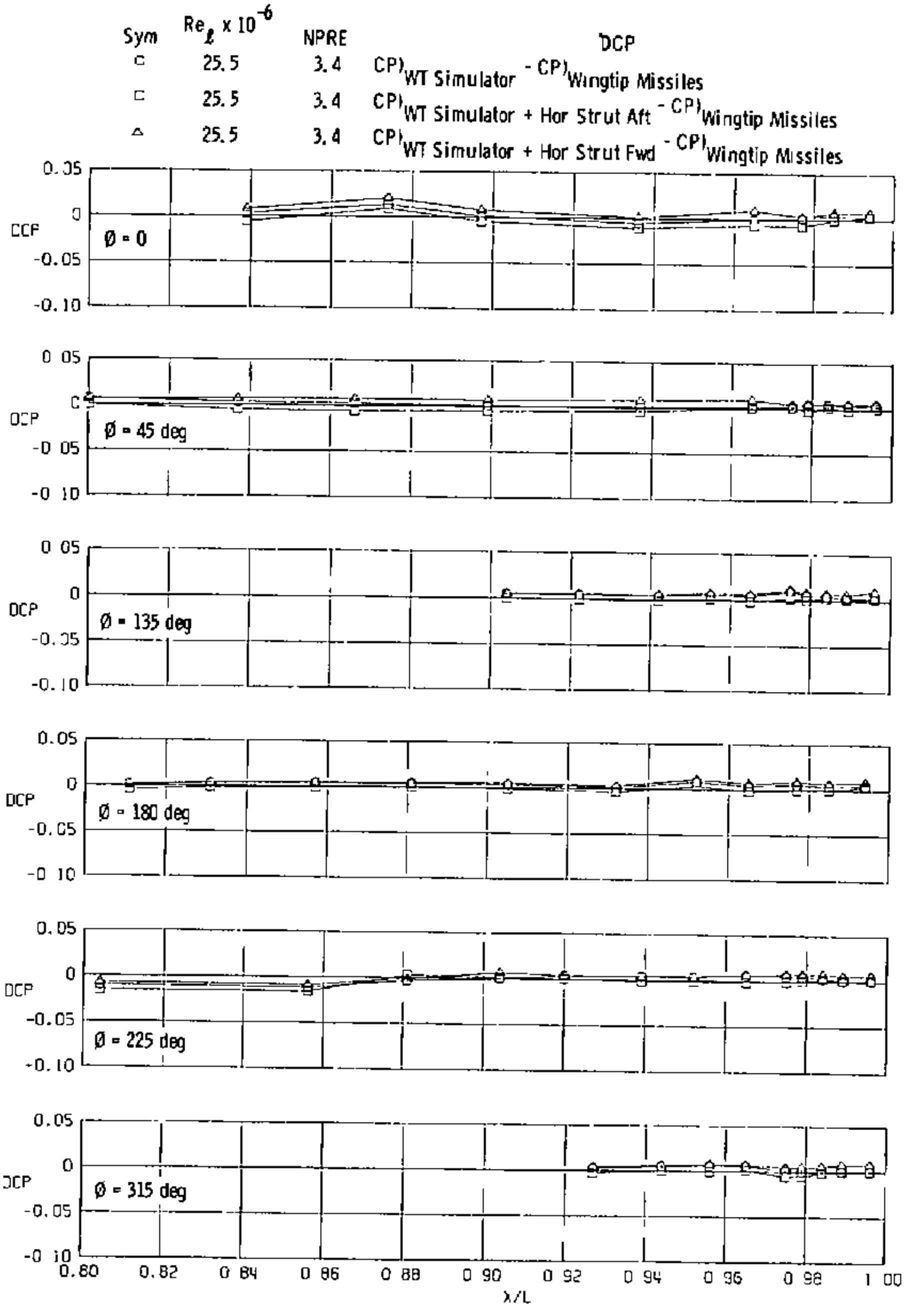

a. A8 = 200 in.², M = 0.6, α = 4.1 deg

Figure 41. Wingtip support system simulation incremental effects on surface pressure coefficients (SS).

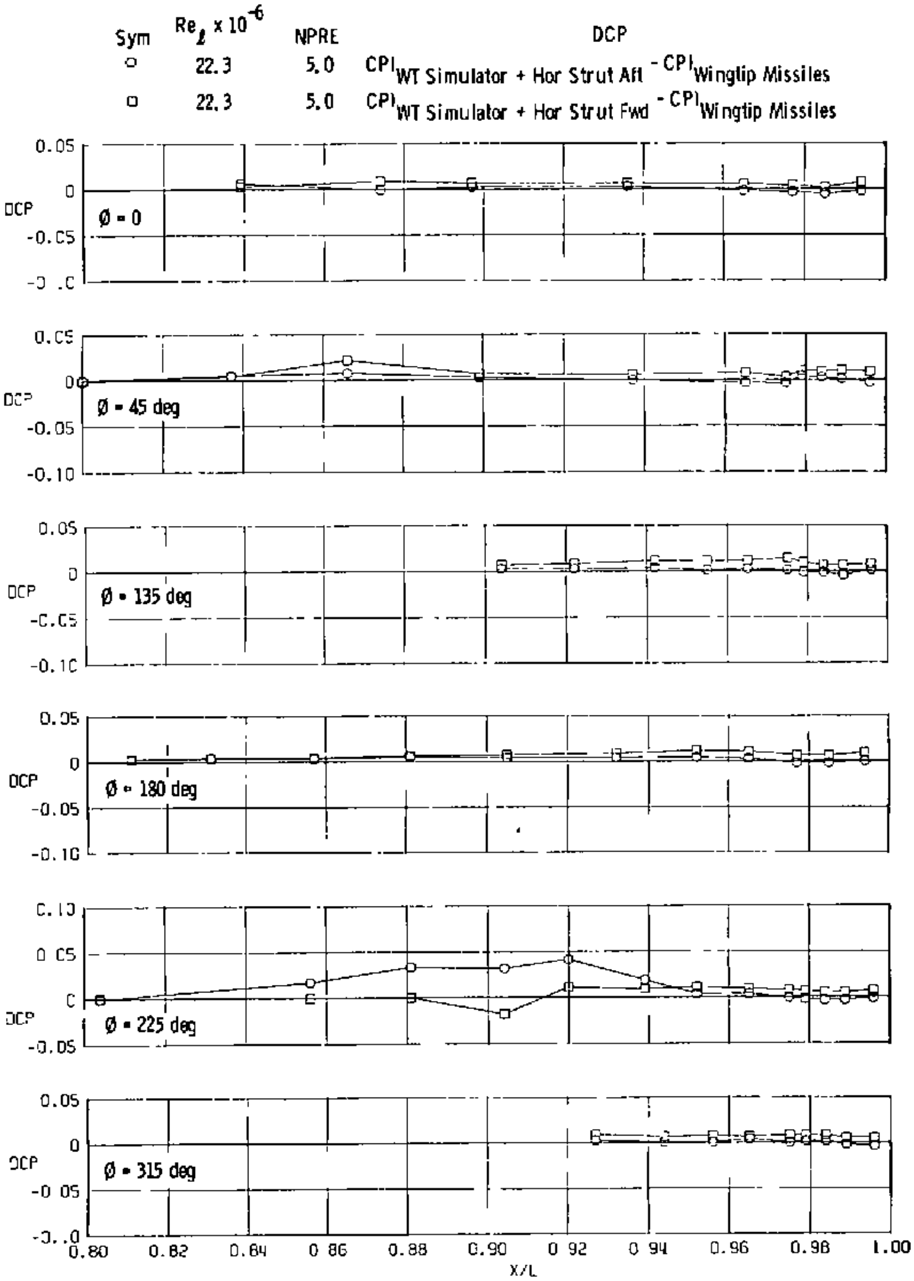

b. A8 = 300 in.², M = 0.6, α = 0
Figure 41. Continued.

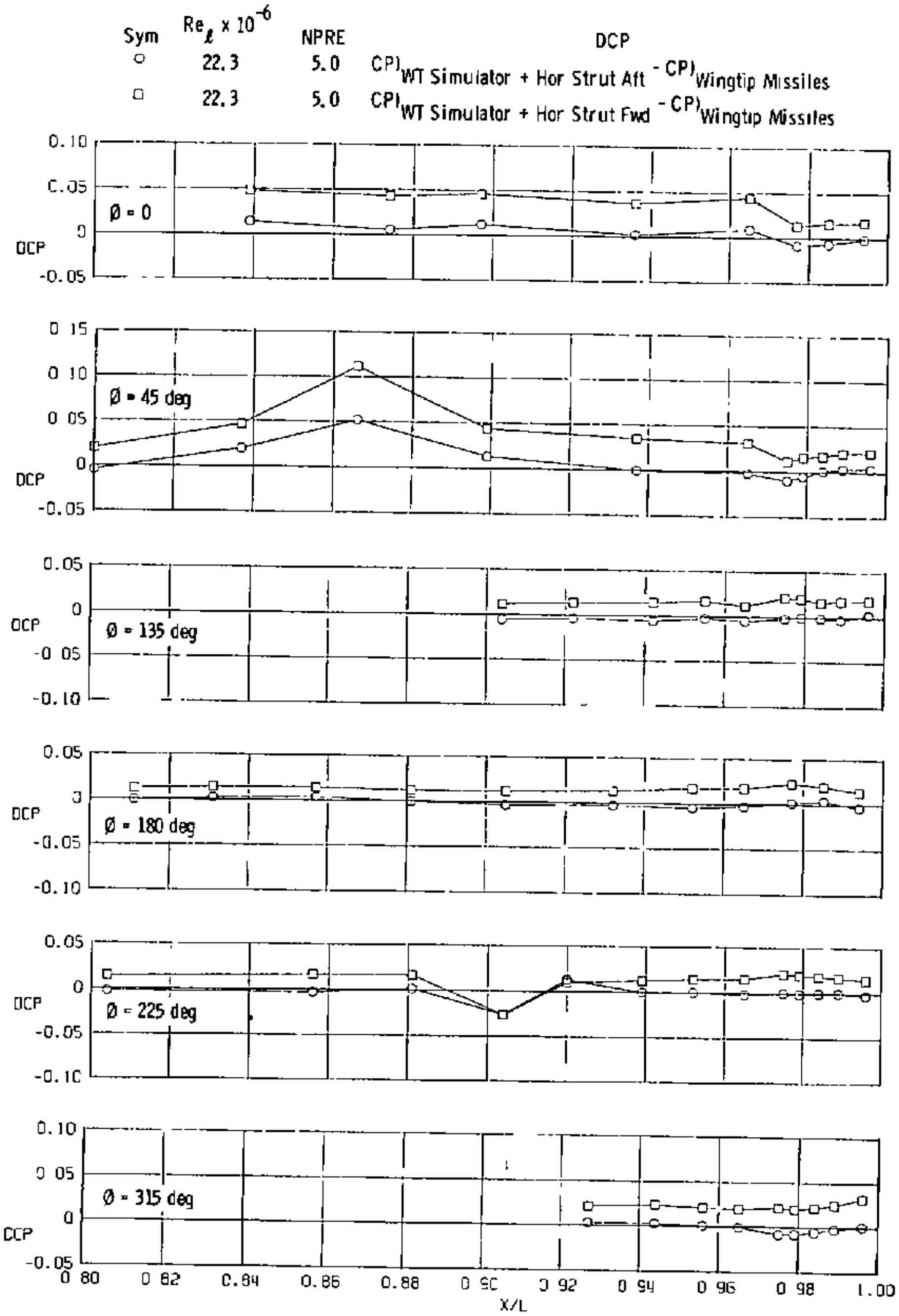

c. A8 = 300 in.², M = 0.9, a = 4.1 deg
Figure 41. Continued.

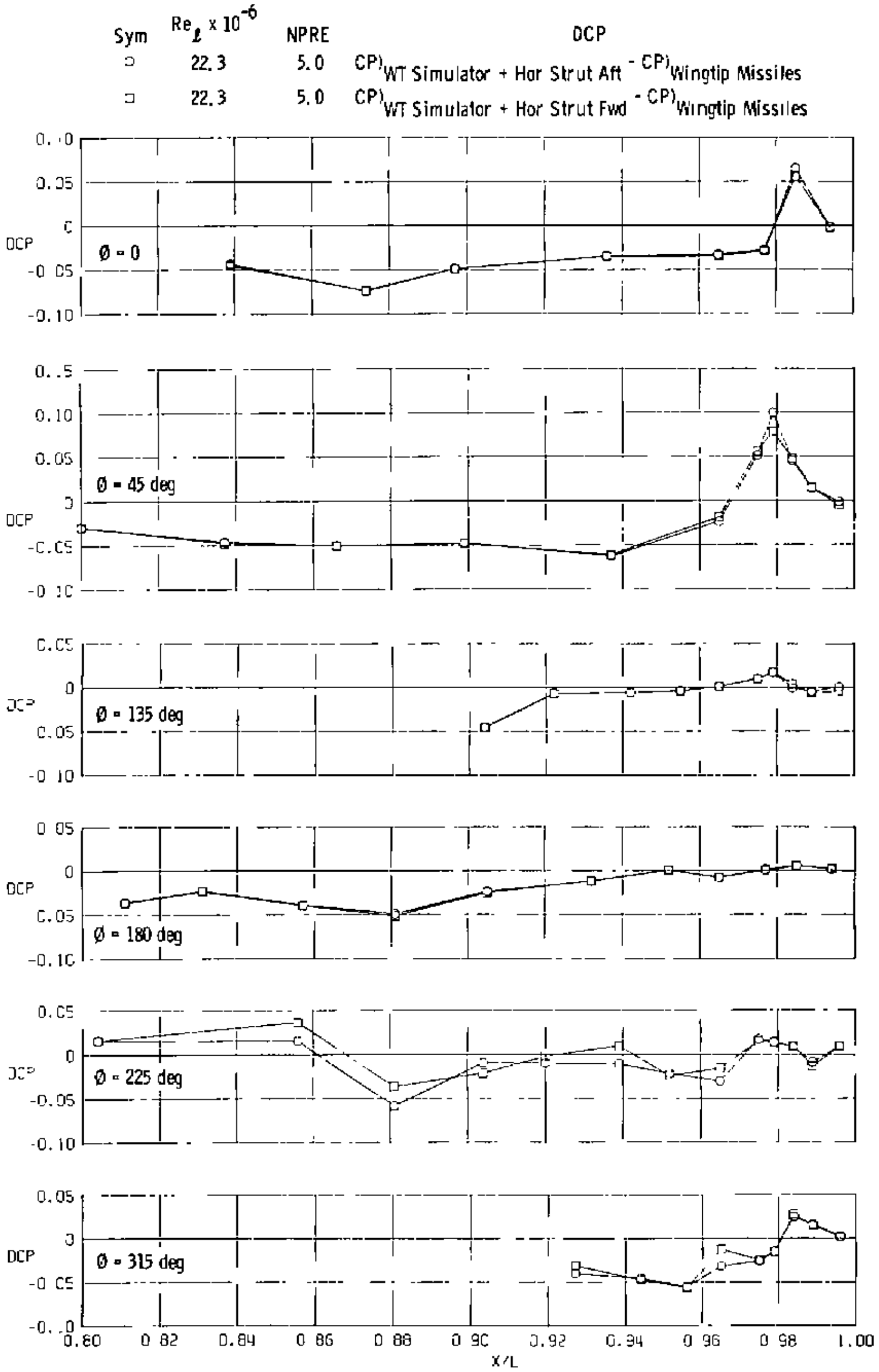

d. A8 = 300 in.², M = 1.2, α = 0
Figure 41. Concluded.

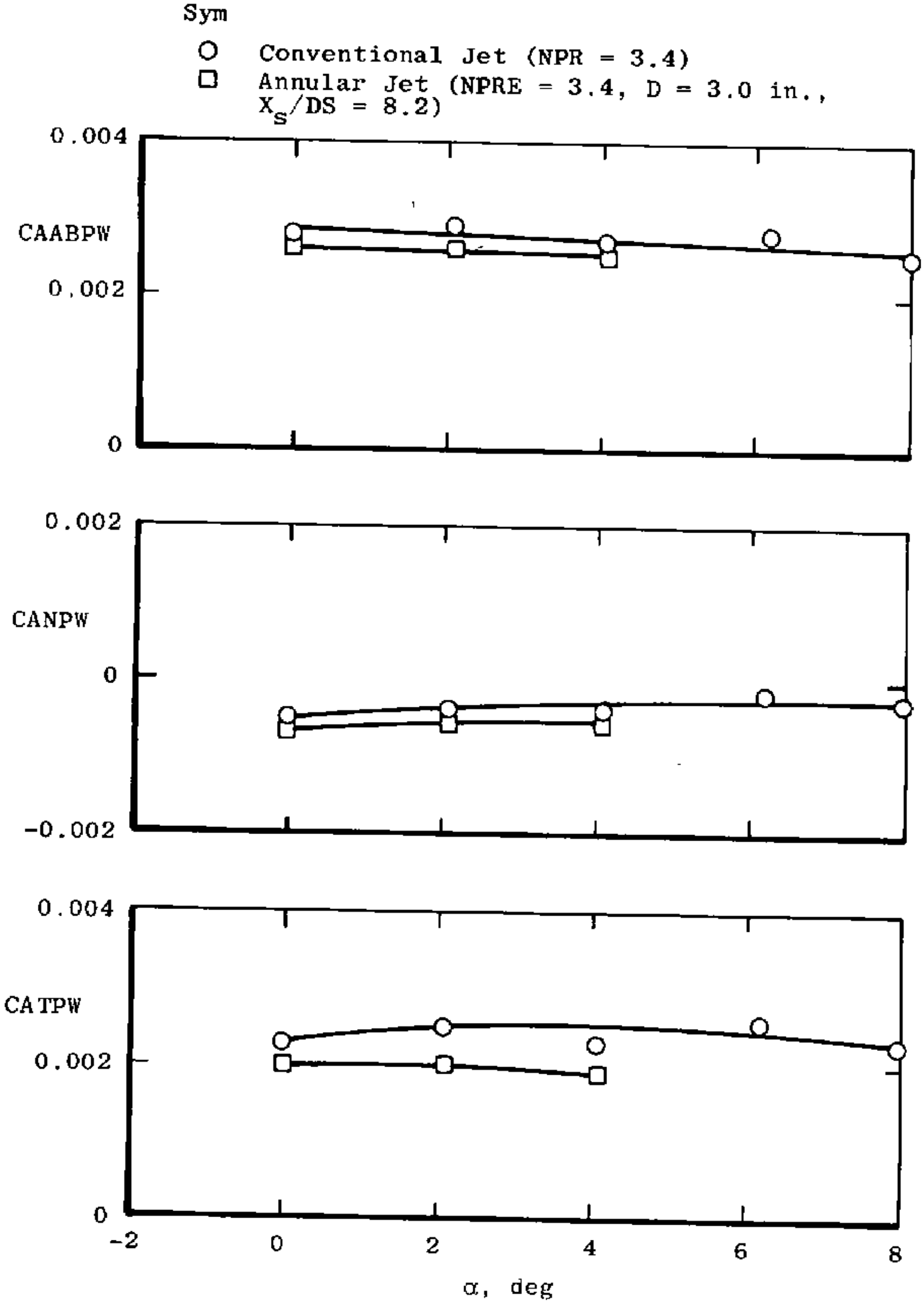

a. A8 = 200 in.^{2}, M = 0.6

Figure 42. Comparison of annular-jet and conventional jet effects on axial force coefficients (WT).

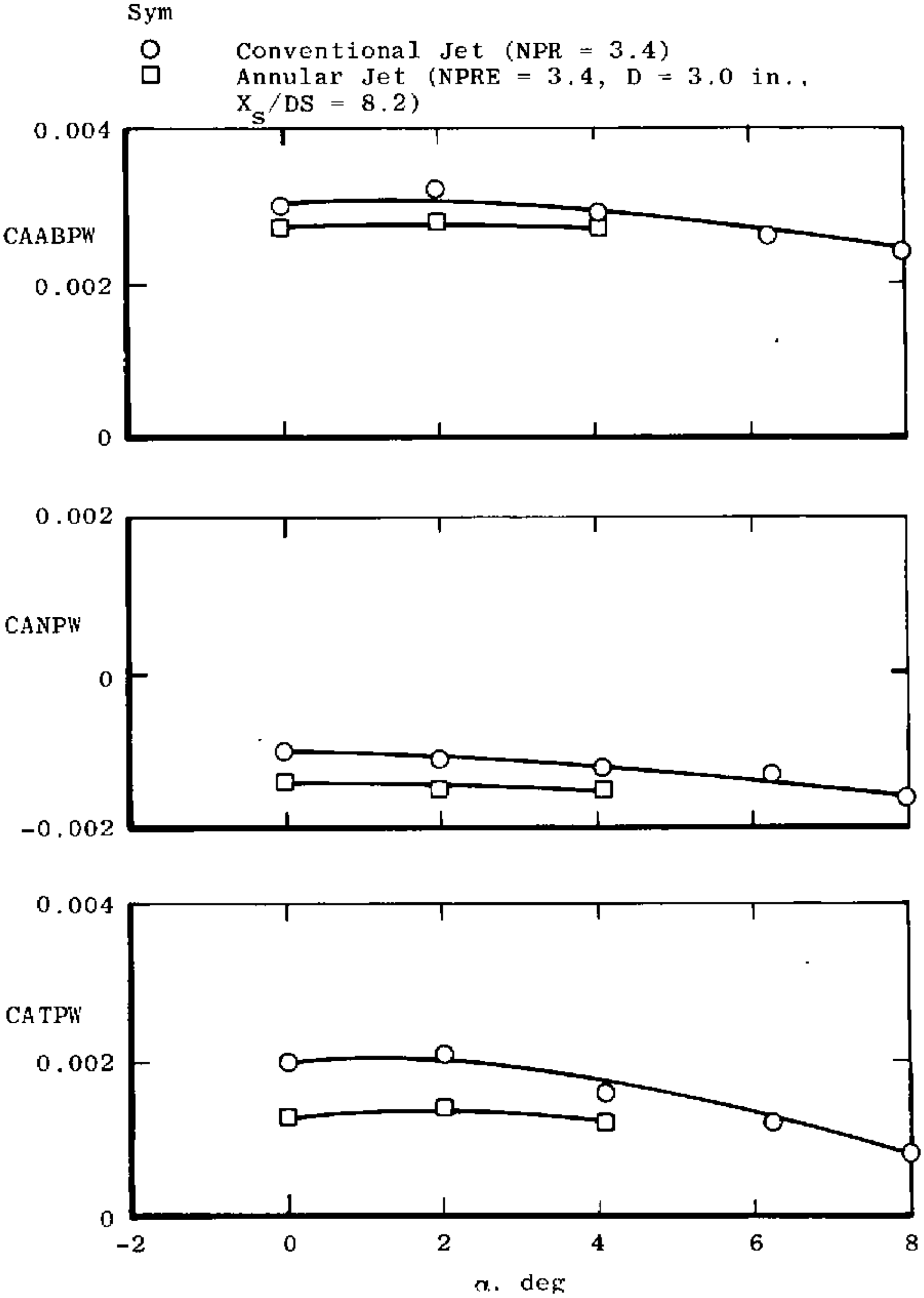

b. A8 = 200 in.², M = 0.9
Figure 42. Continued.

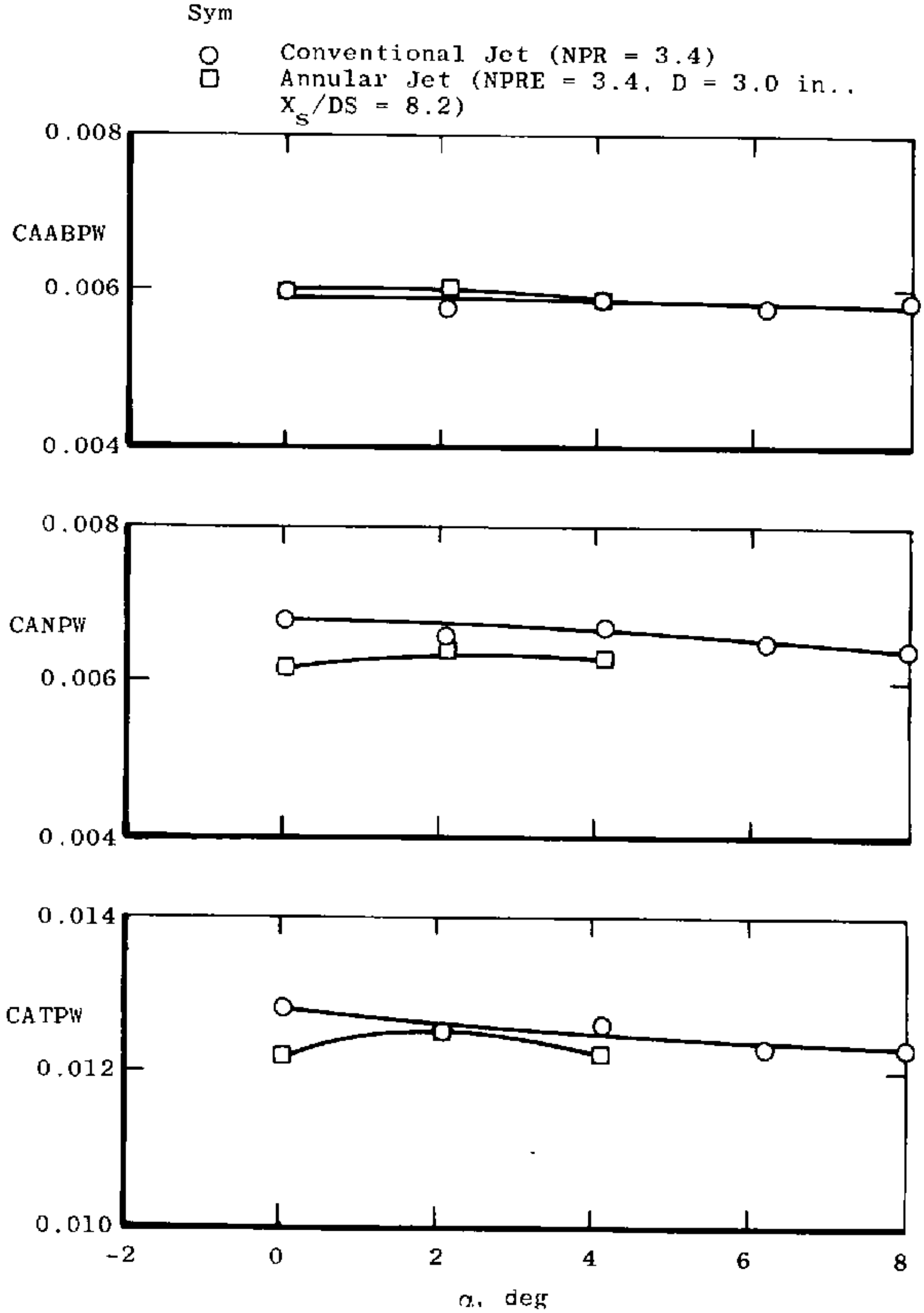

c. A8 = 200 in.^{2}, M = 1.2
Figure 42. Continued.

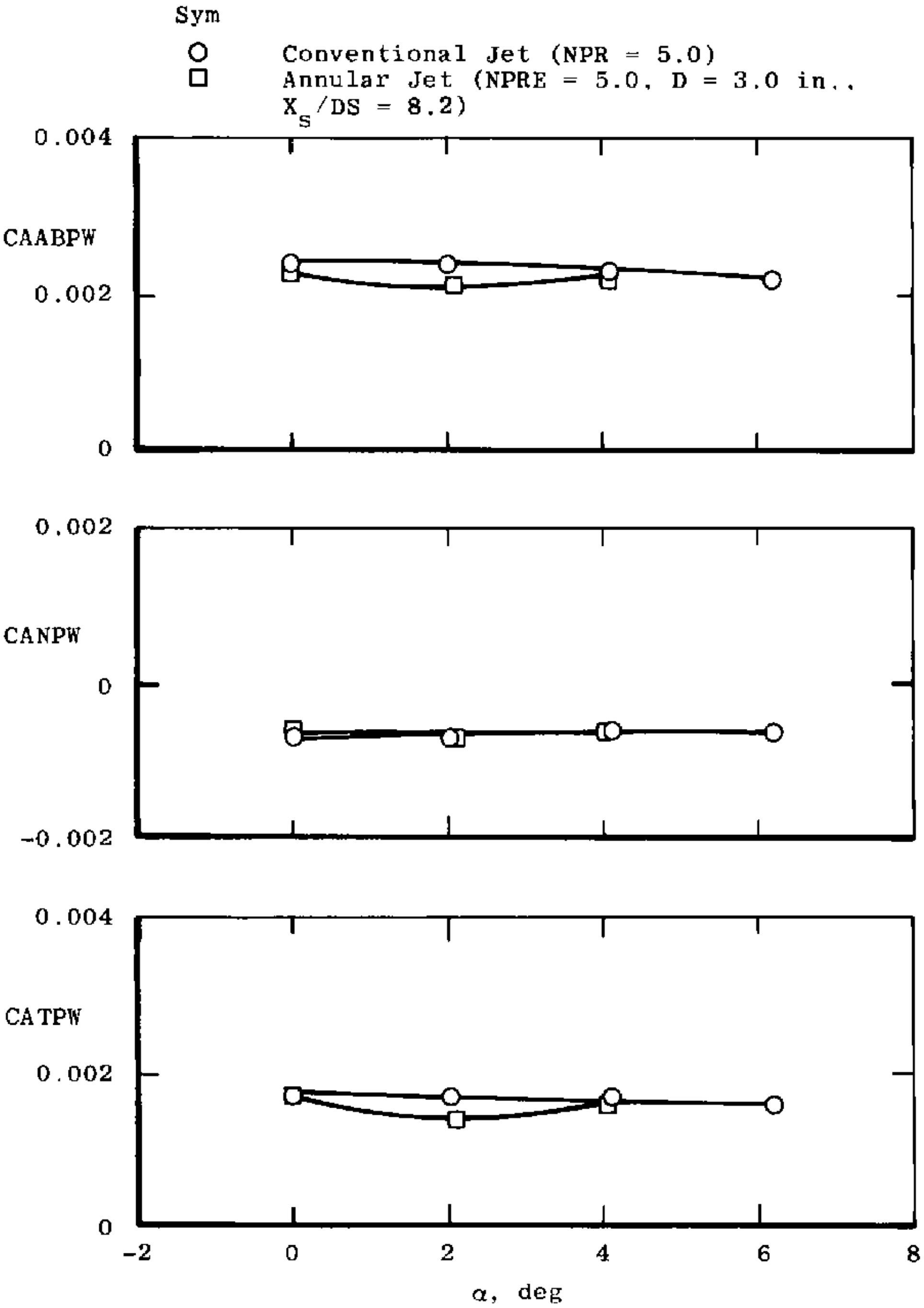

d. A8 = 300 in.², M = 0.6

Figure 42. Continued.

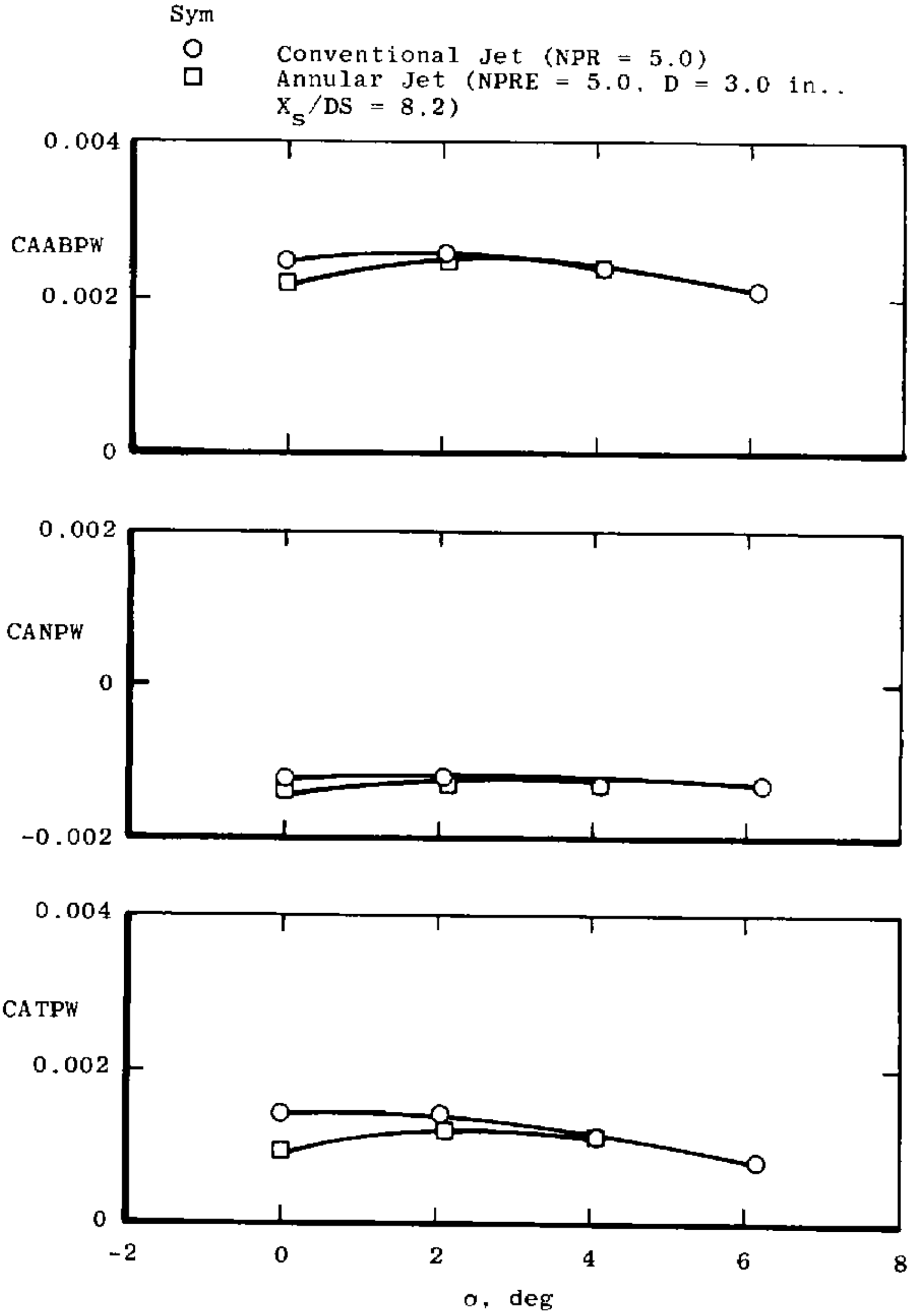

e. A8 = 300 in.², M = 0.9
Figure 42. Continued.

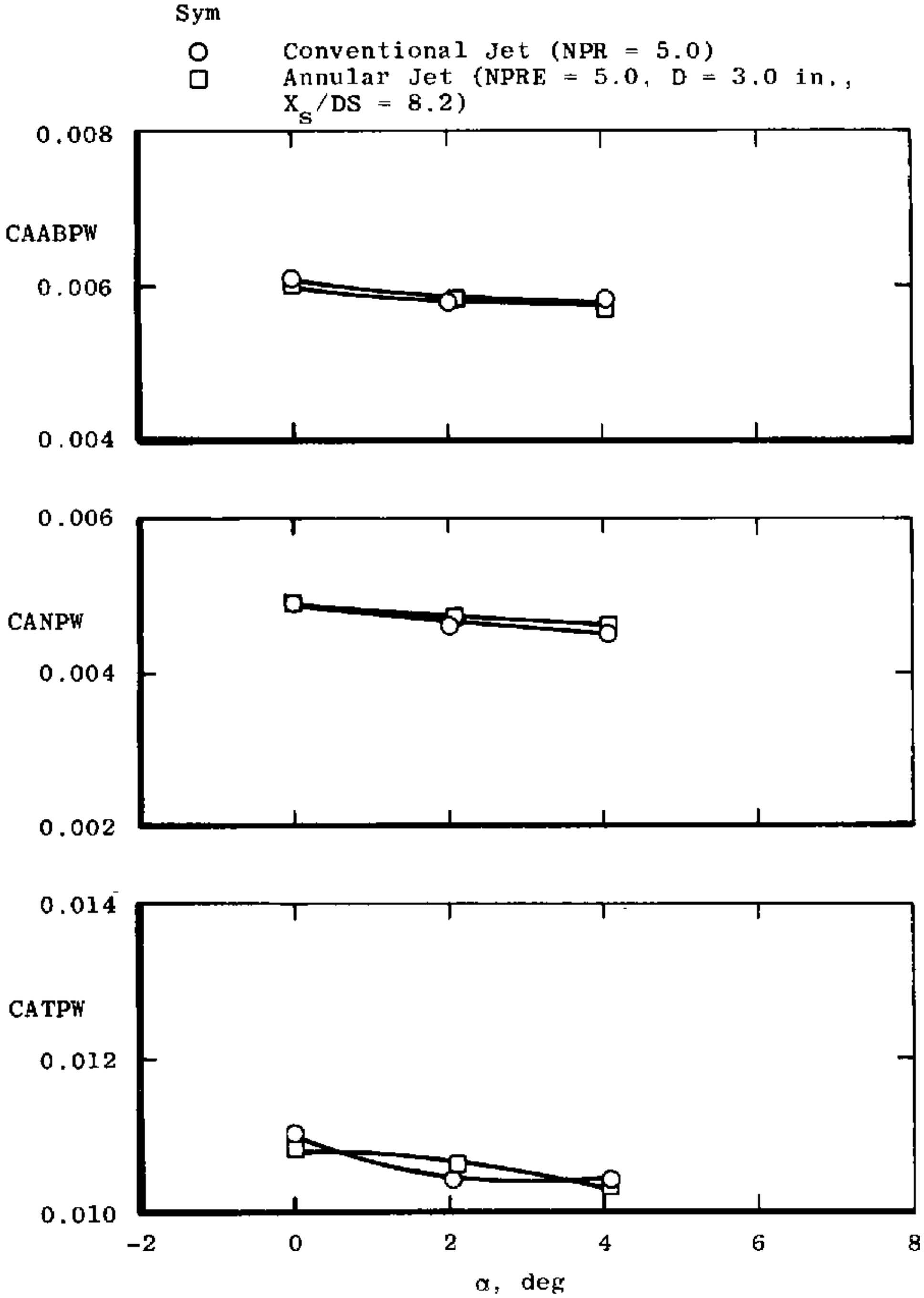

f. A8 = 300 in.^{2}, M = 1.2
Figure 42. Concluded.

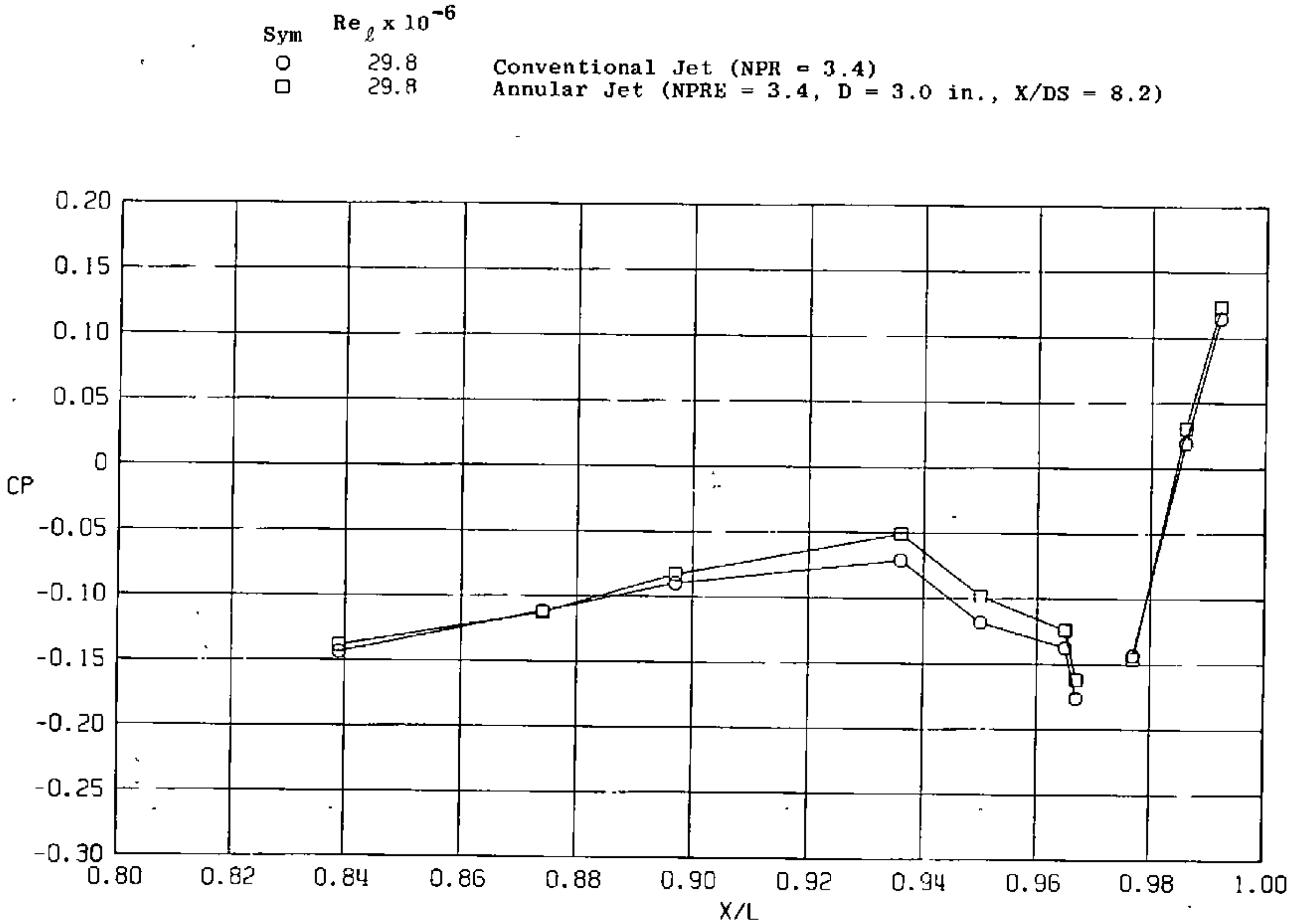

a. $\phi = 0$

Figure 43. Comparison of annular-jet and conventional jet effects on surface pressure coefficients, A8 = 200 in.^{2}, M = 0.6, α = 0 (WT).

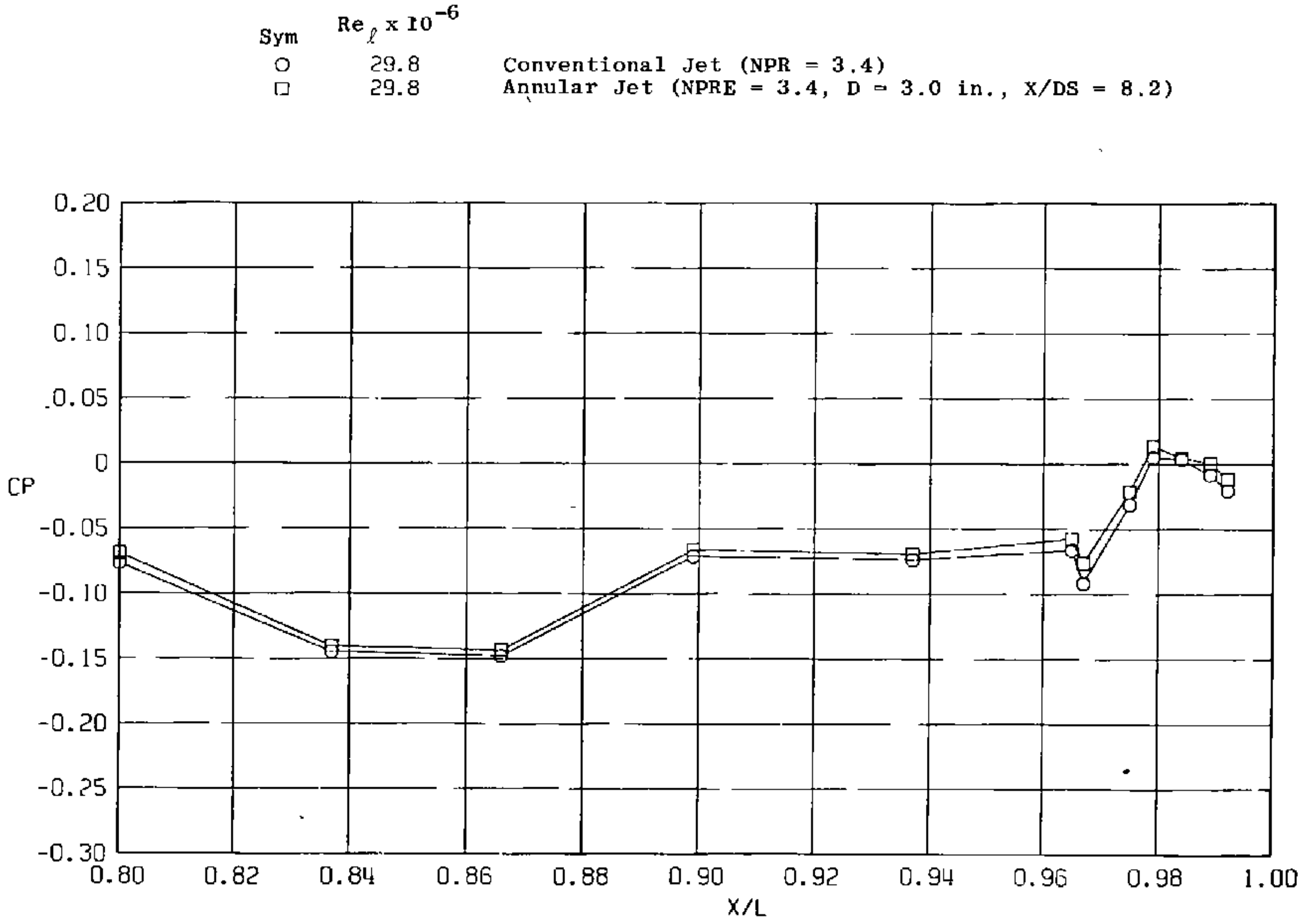

b. ϕ = 45 deg

Figure 43. Continued.

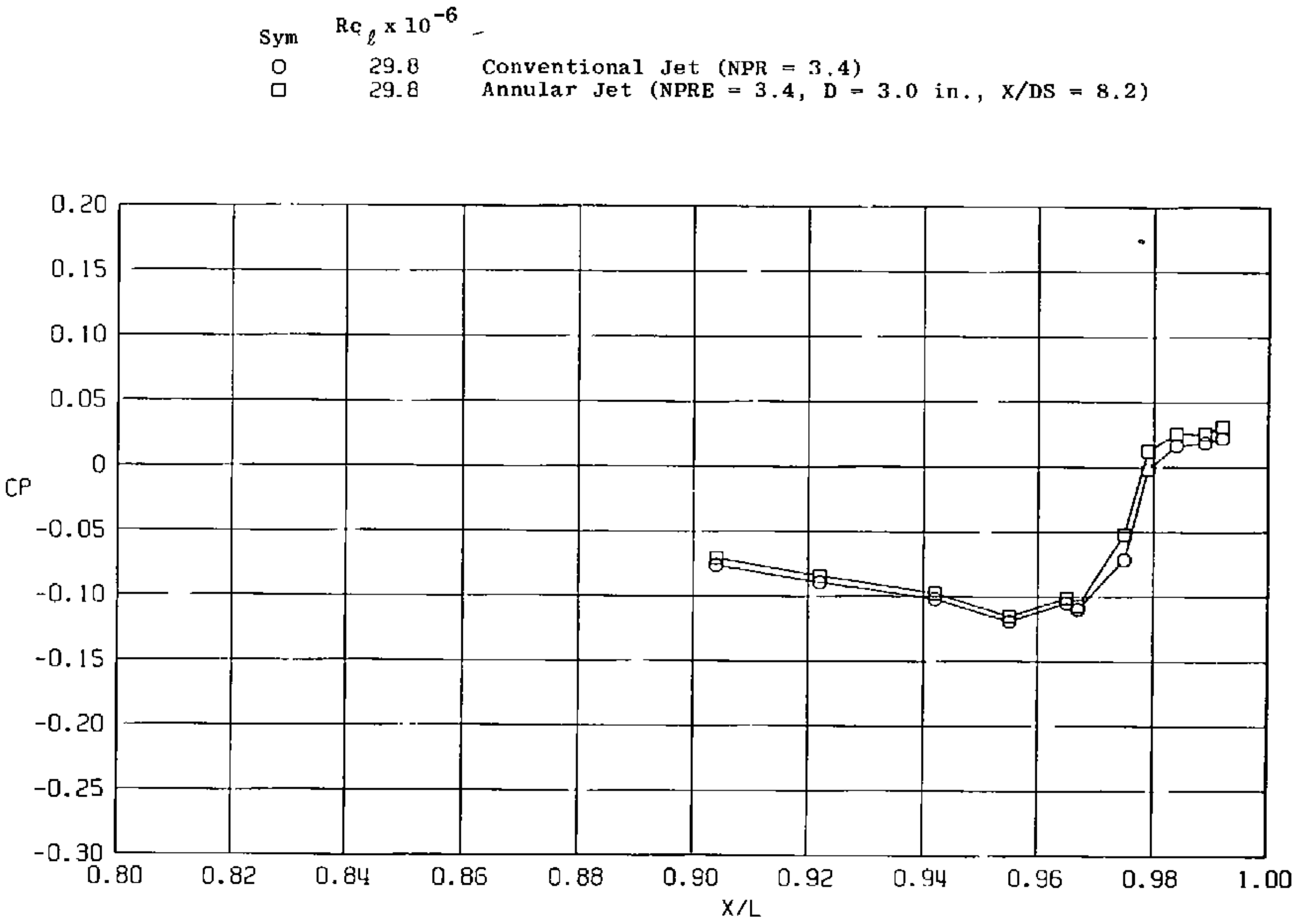

c. ϕ = 135 deg

Figure 43. Continued.

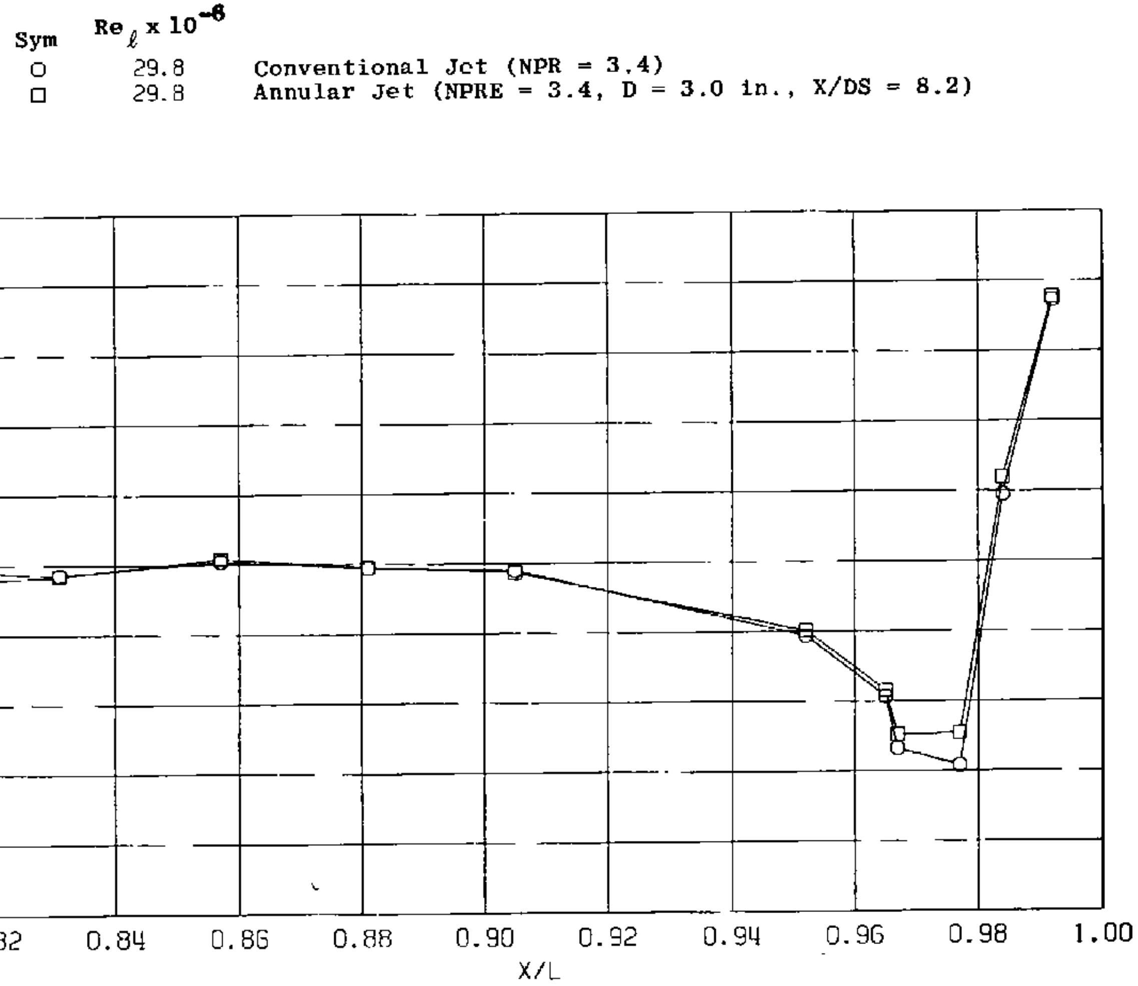

d. ϕ = 180 deg
Figure 43. Continued.

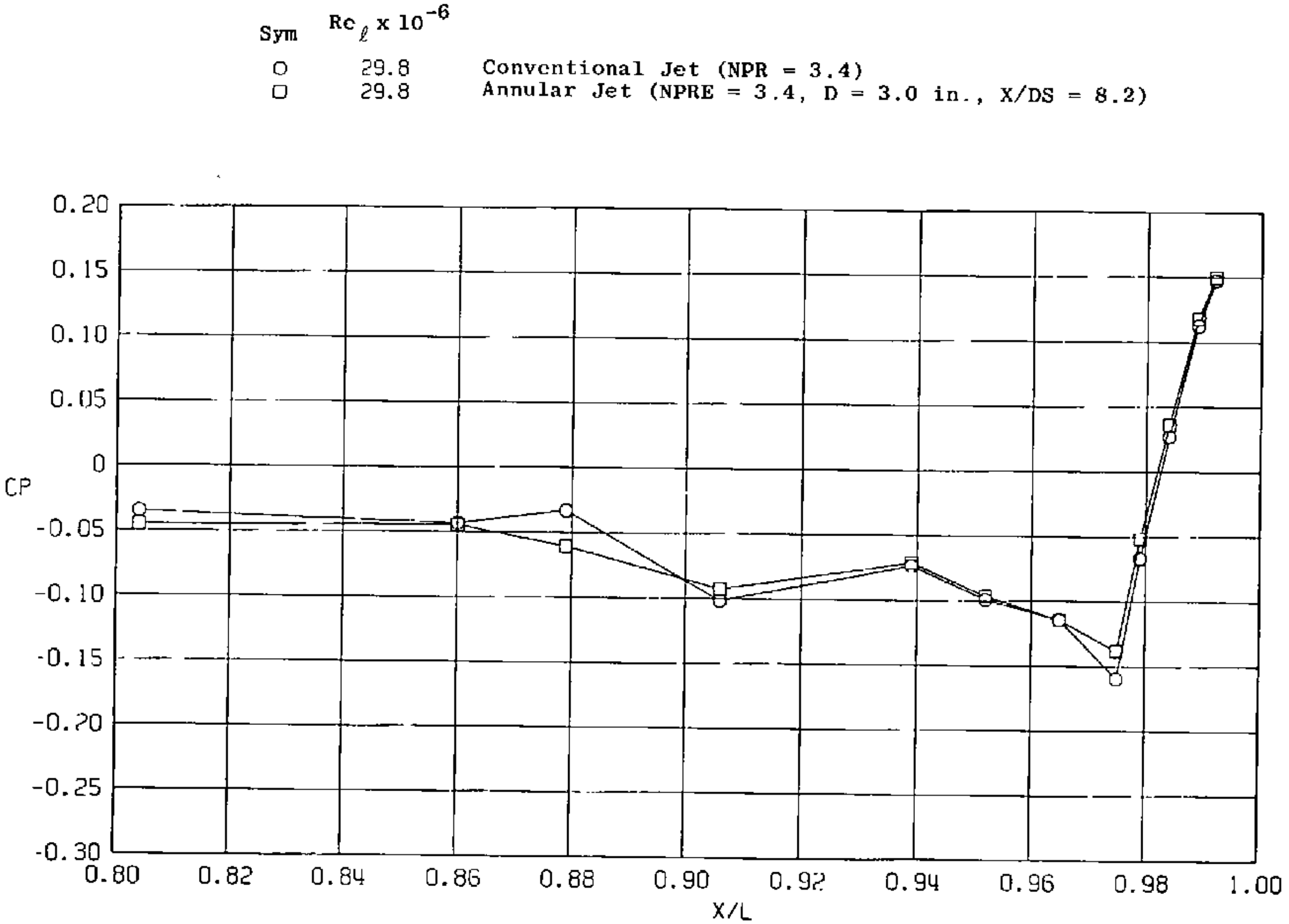

e. ϕ = 225 deg
Figure 43. Continued.

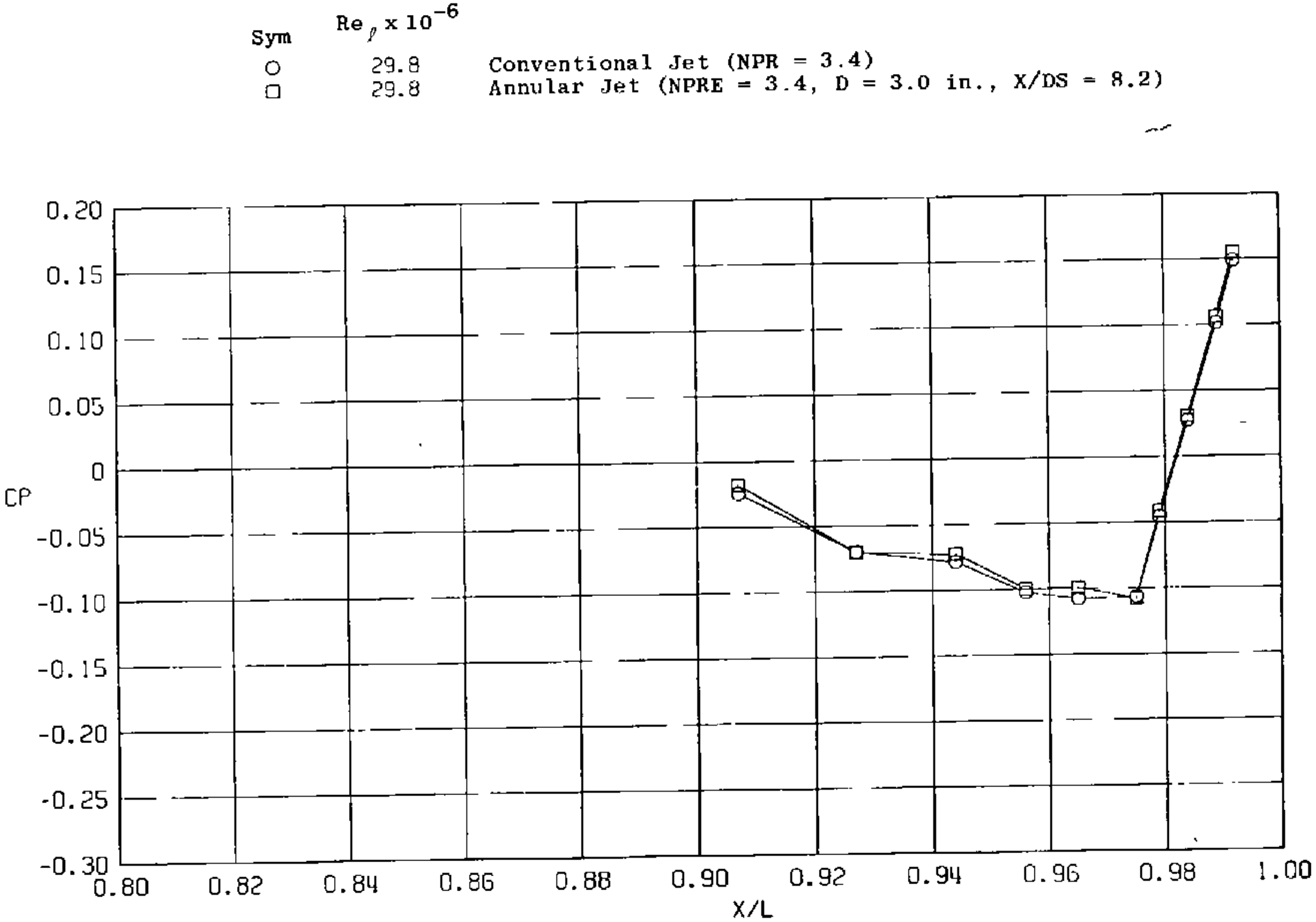

f. ϕ = 315 deg
Figure 43. Concluded.

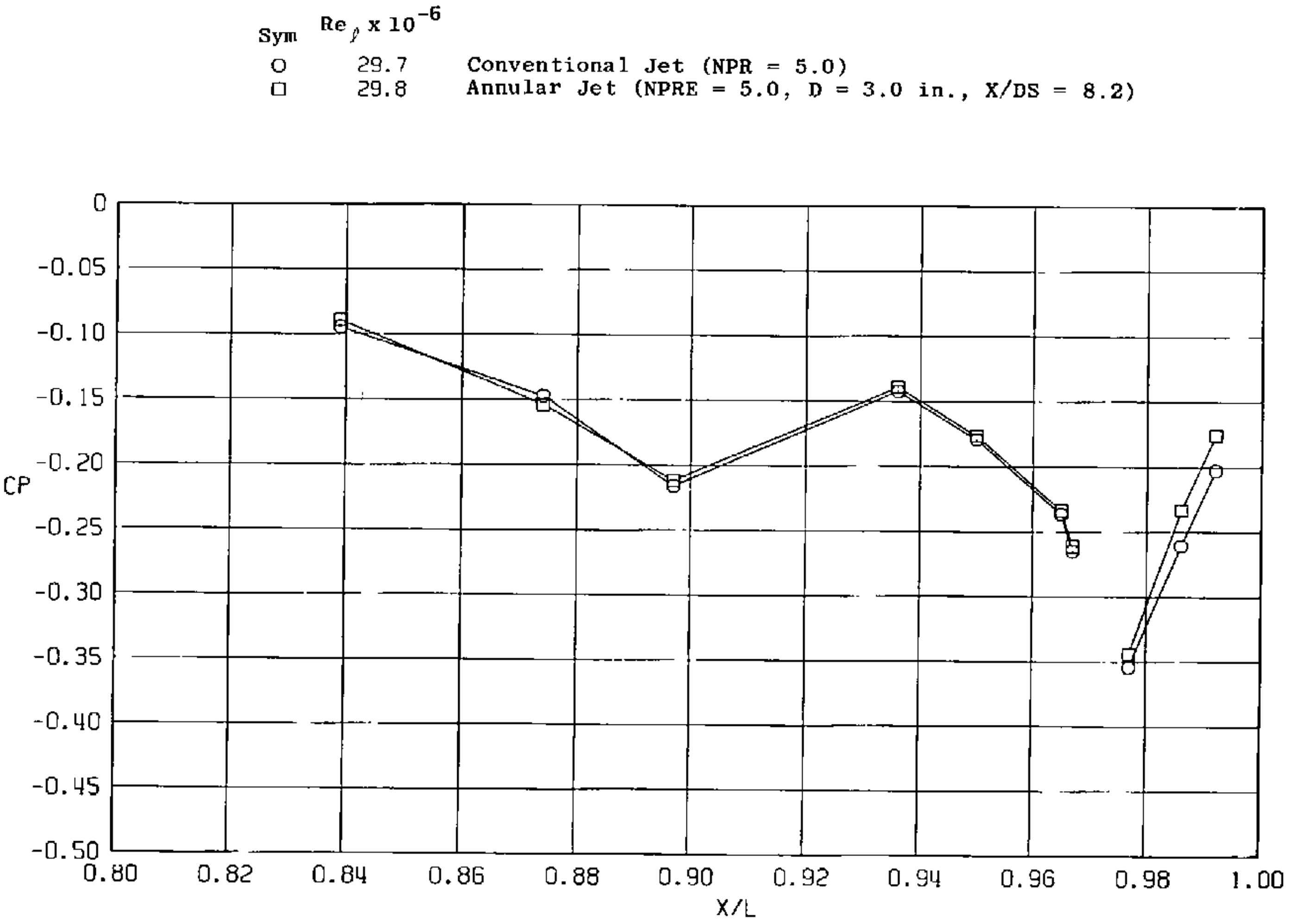

a. $\phi = 0$

Figure 44. Comparison of annular-jet and conventional jet effects on surface pressure coefficients, A8 = 300 in.^{2}, M = 1.2, α = 0 (WT).

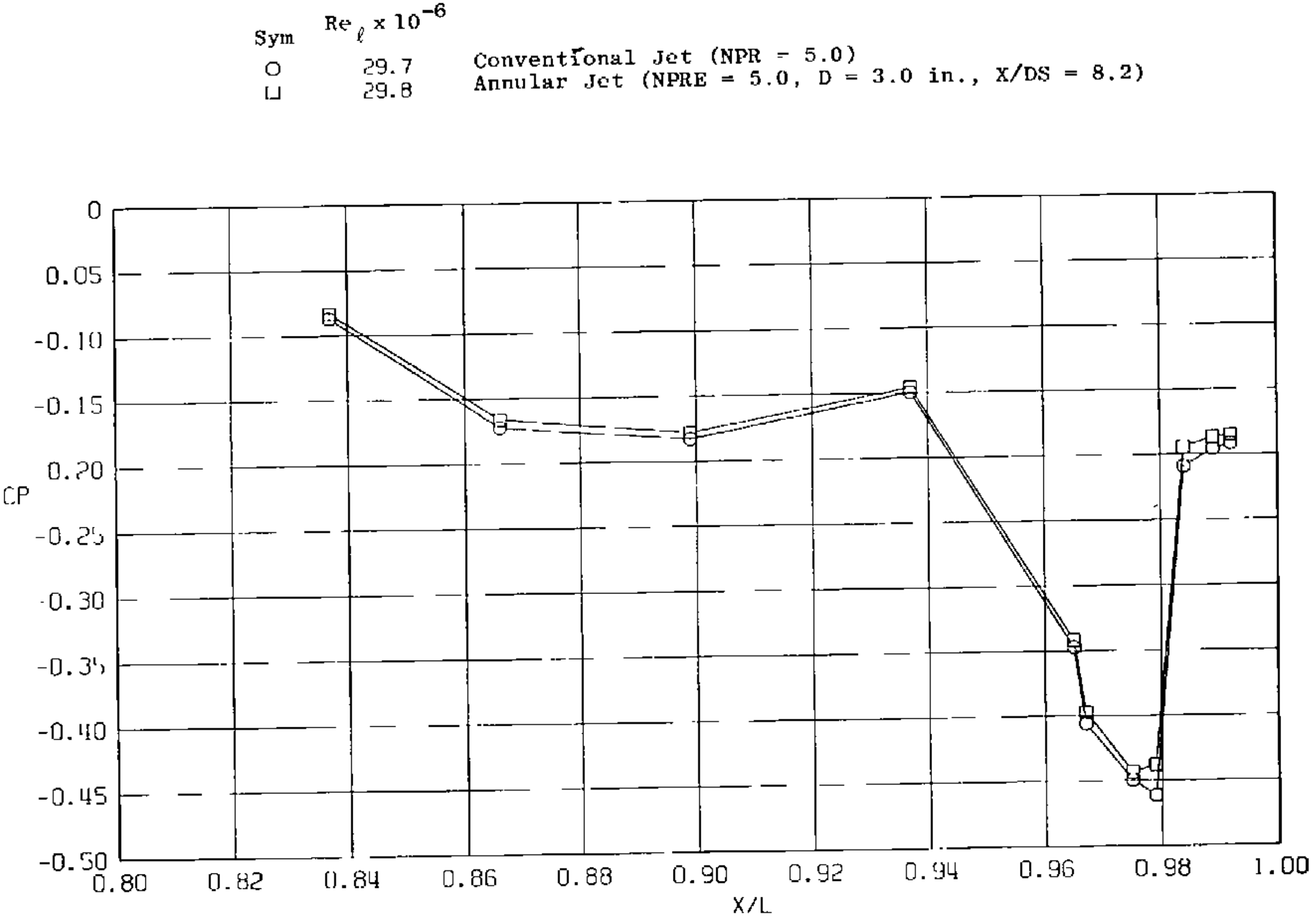

b. ϕ = 45 deg
Figure 44. Continued.

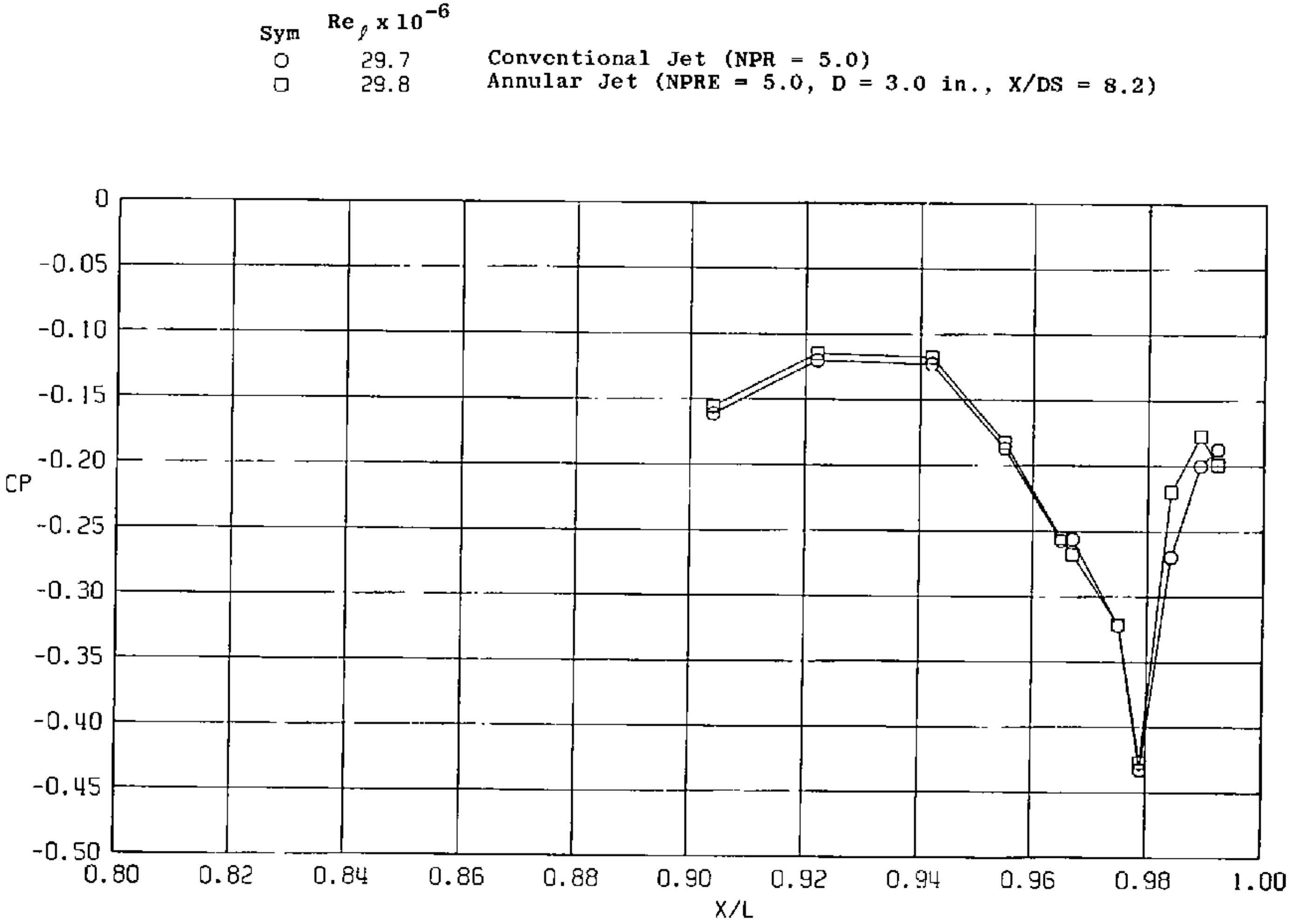

c. ϕ = 135 deg

Figure 44. Continued.

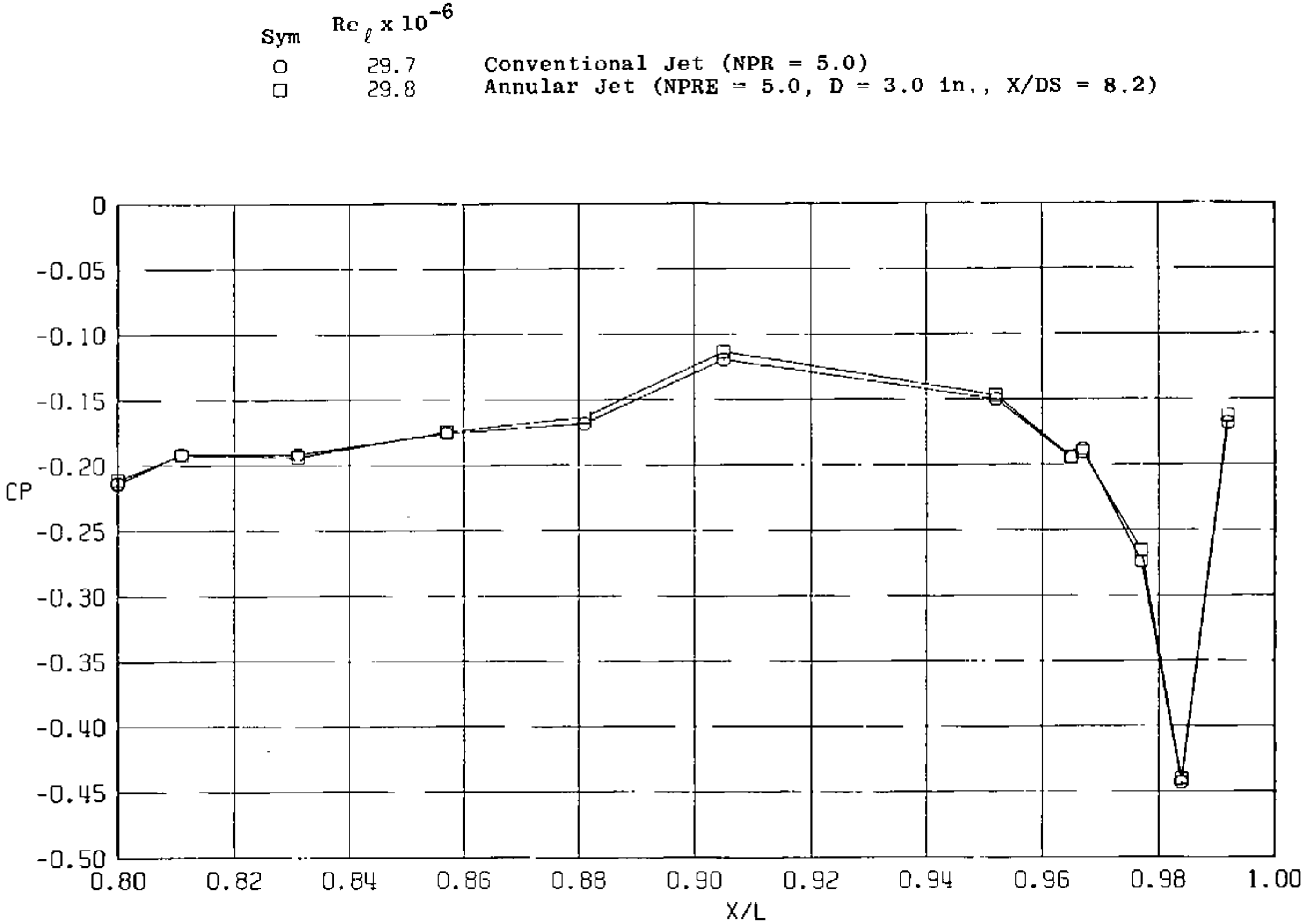

d. ϕ = 180 deg

Figure 44. Continued.

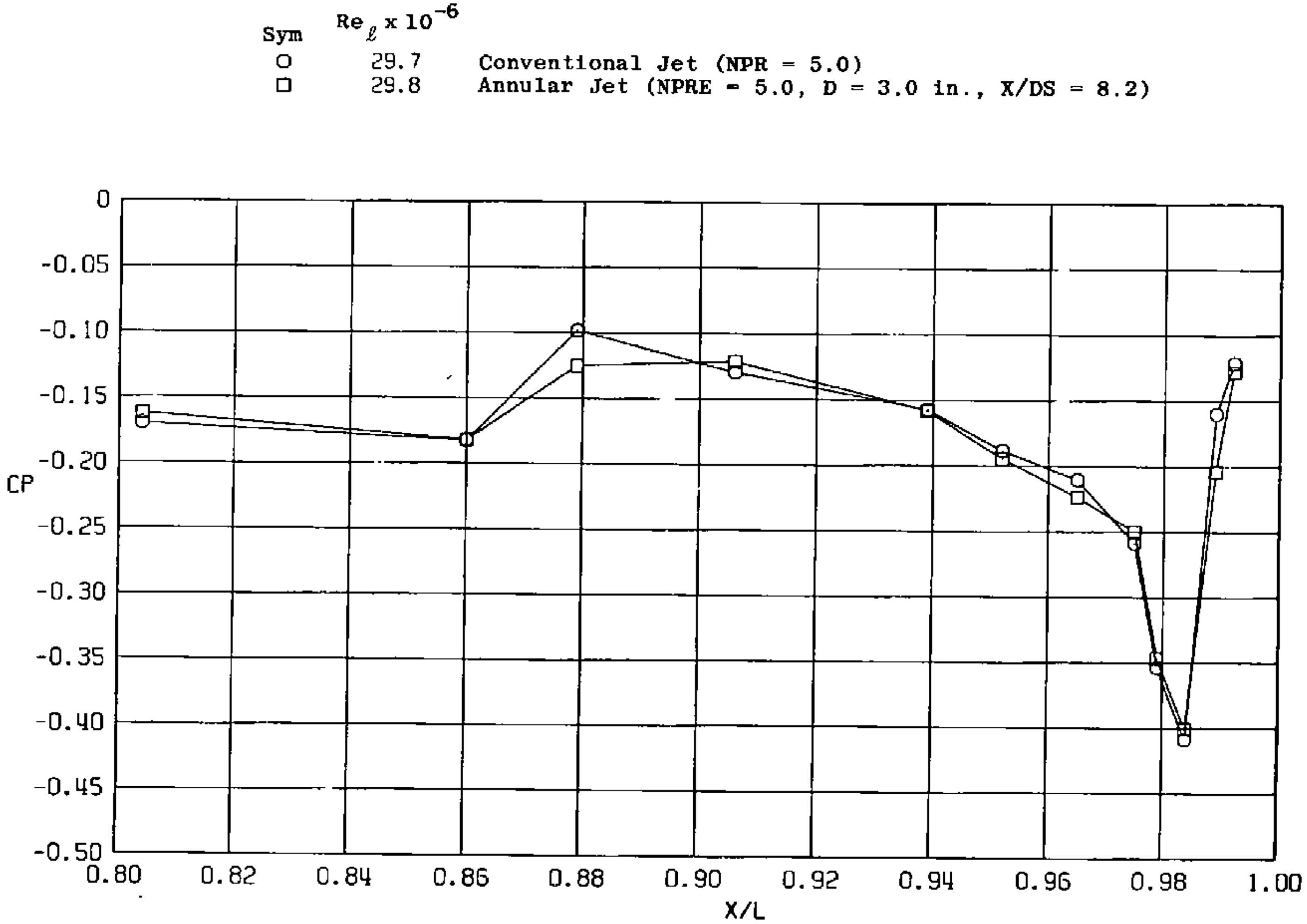

e. ϕ = 225 deg
Figure 44. Continued.

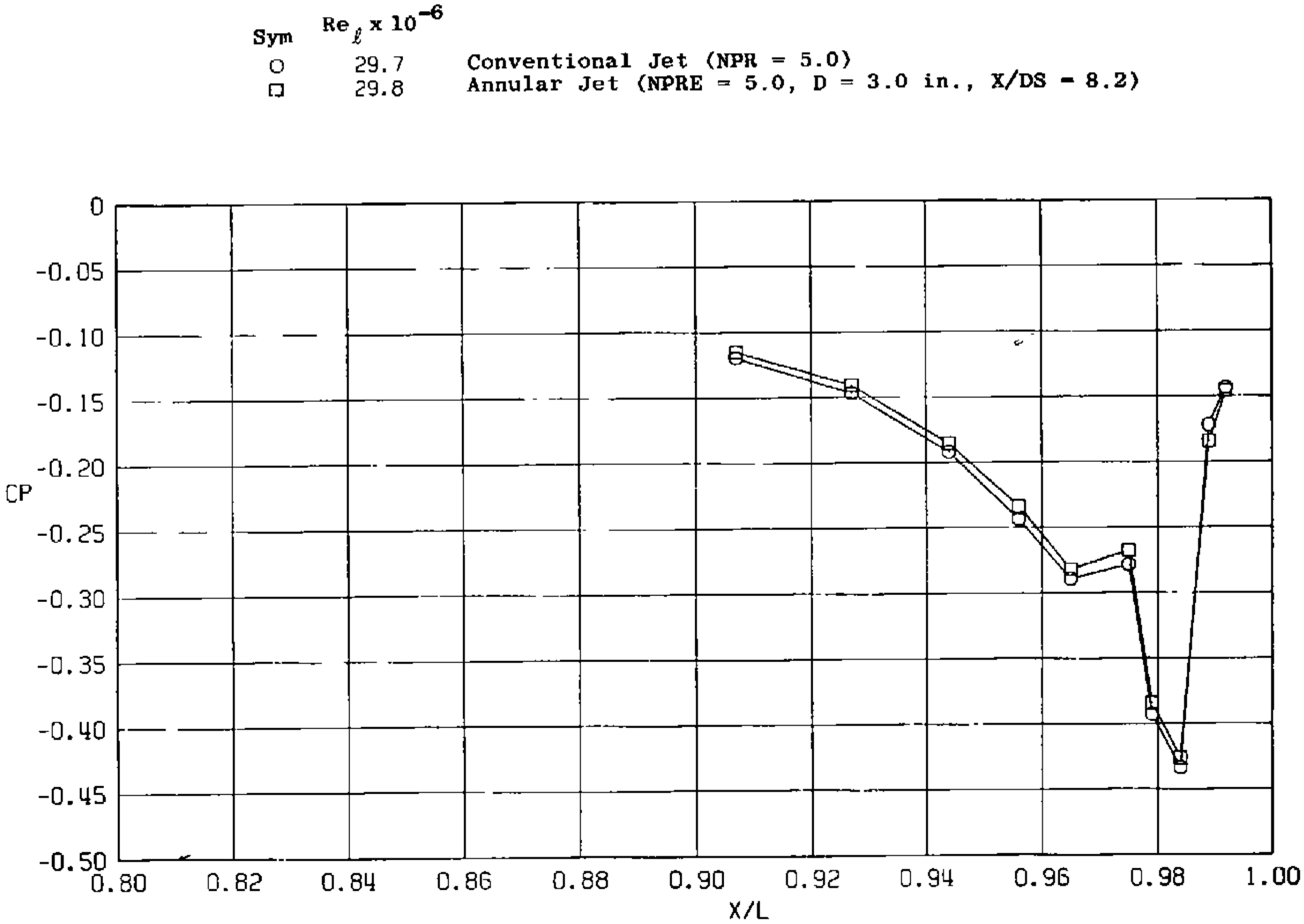

f. ϕ = 315 deg
Figure 44. Concluded.

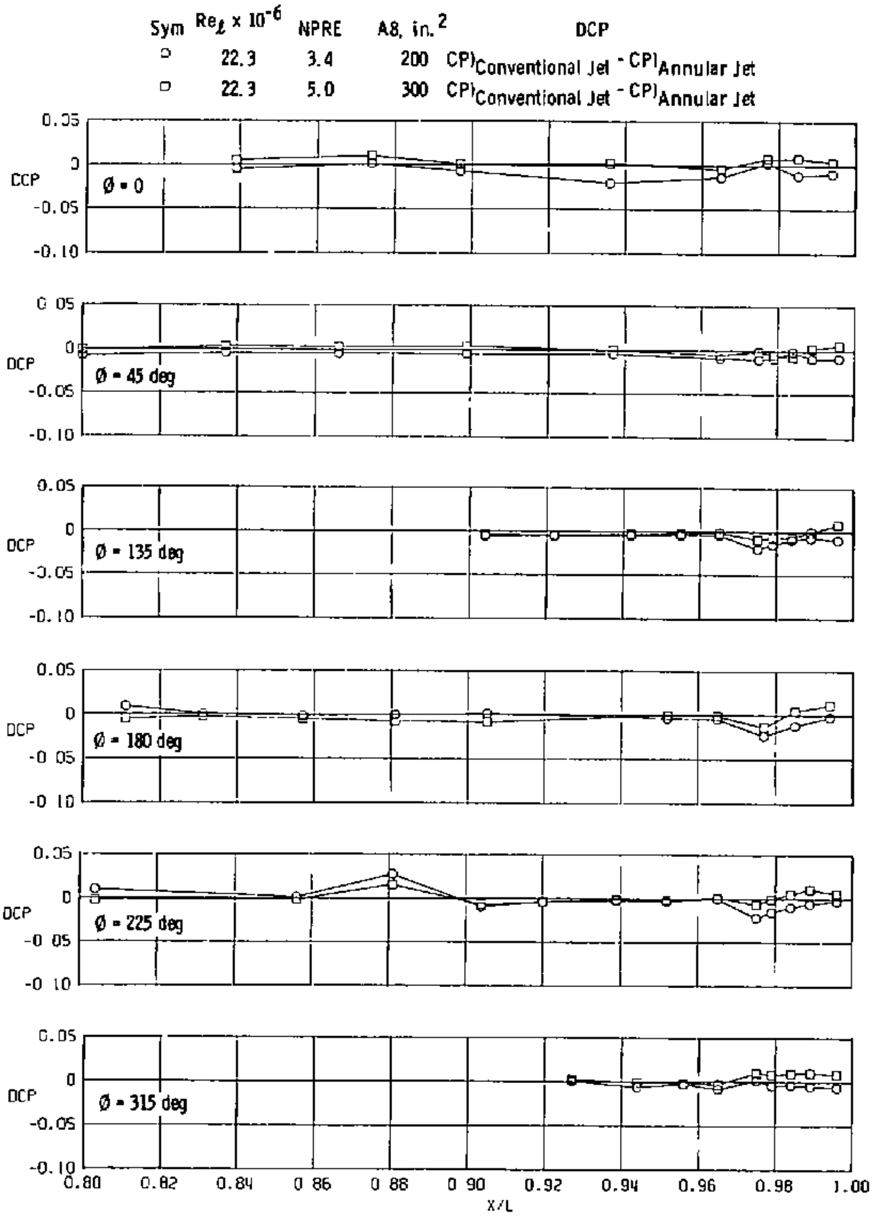

a. M = 0.6, α = 0

Figure 45. Comparison of annular-jet and conventional jet incremental effects on surface pressure coefficients (WT).

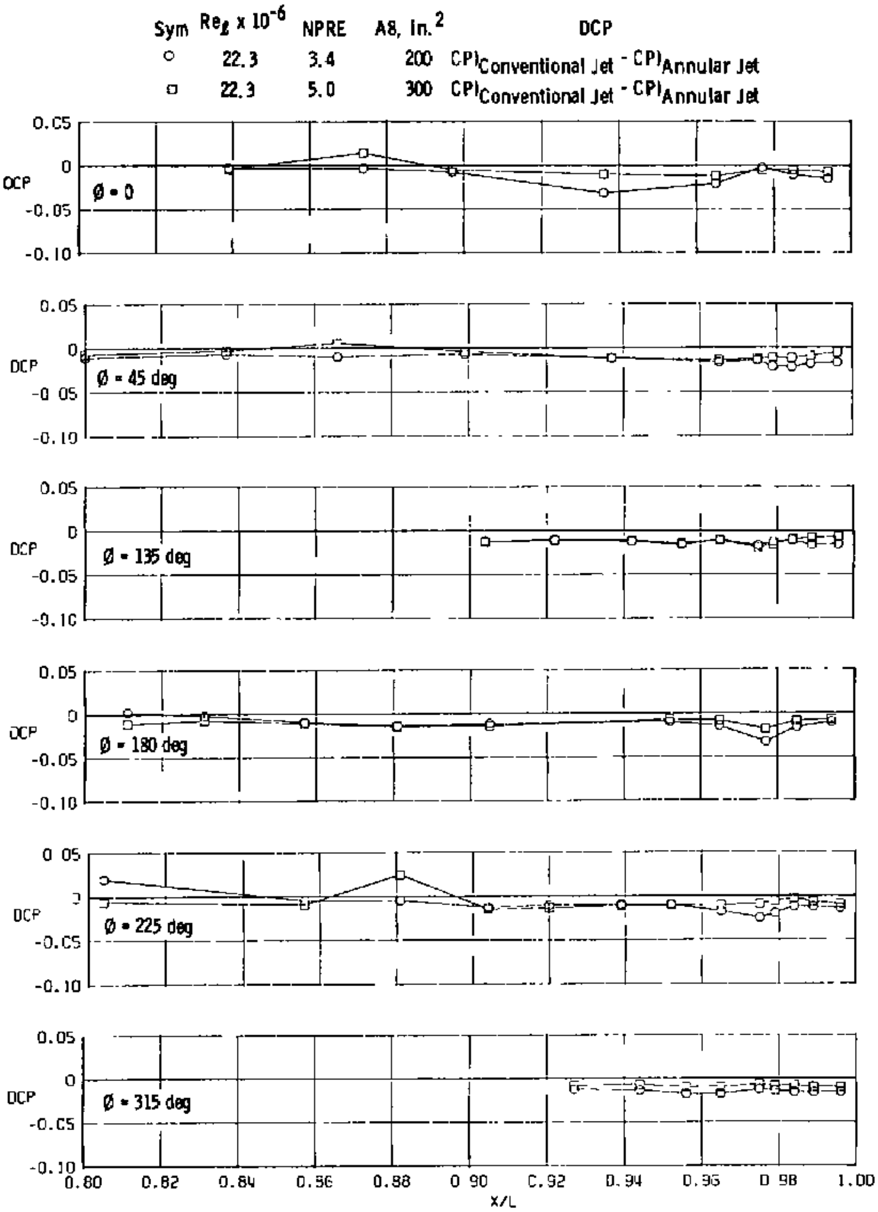

b. M = 0.9, a = 0

Figure 45. Continued.

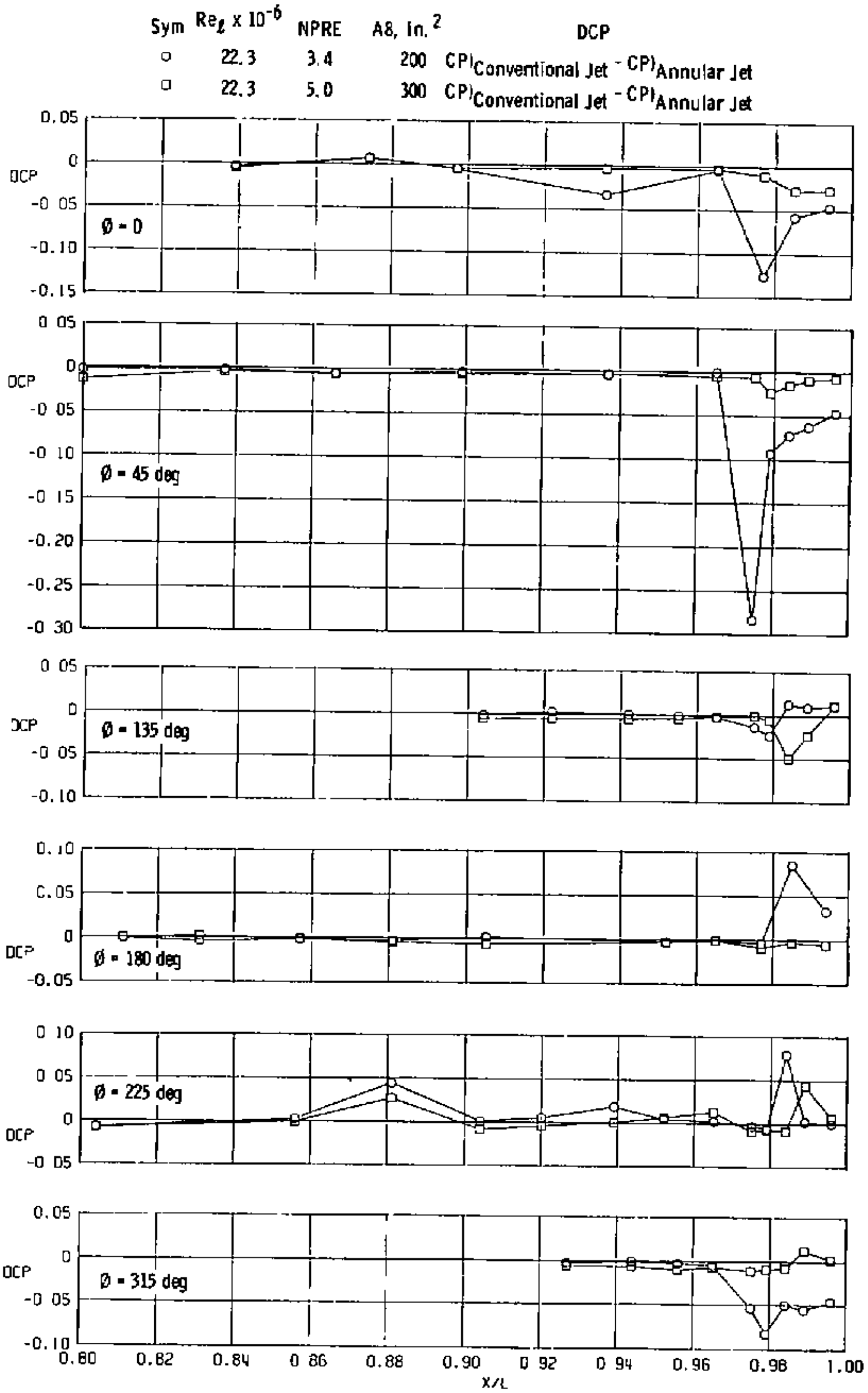

c. M = 1.2, α = 0
Figure 45. Concluded.

Table 1. Test Matrix Summary, Wingtip Support Phase

Nozzle	δ_H, deg	Simulated Stings		Notes (Bay Purge)	M	0.6					0.8			0.9					1.2					1.5
		X_s, in.	Diam, in.		R_e x 10^{-6}/ft	1.4	2.1	2.8	4.2	5.6	1.4	2.8	4.2	1.4	2.8	4.2	5.2	5.6	1.4	2.1	2.8	4.2	4.8	2.8
					Variable																			
200	0			Closed	NPR	x	x	x	x	x		x		x	x	x		x	x		x	x		x
	↓			↓	α	x		x	x		x	x	x	x	x	x		x			x			x
	-2.0				NPR	x		x						x	x	x		x	x		x	x	x	
	↓				α			x				x			x	x		x			x			
	-1.25				α			x							x						x			
	-1.75				α	x		x		x					x			√			√			
	-1.5			Screens 0.44-in.-diam Inlet	α			x		√				x	x	x		x			x			
	↓				α			x		√					x						x			
					α			x							x						x			
	-1.0			Closed	NPR			x							x						x			
	↓			↓	α			x							x						x			
230	-2.0				NPR			x							x						x			
	↓				α			x						x	x	x		x			x			
	0				NPR			x							x						x			x
	↓				α			x							x						x			x
300	0				NPR	x		x				x		x	x	x	x			√	x			x
	↓				α	x		x				x			x	x				x	x			x
	-2.0				NPR			x						x	x						x			
	↓				α			x							x						x			
360	0				NPR			x				x			x						x			x
	↓				α			x				x			x						x			x
	-2.0				NPR			x							x						x			
	↓				α			x							x						x			

x – One or More Data Part Numbers

√ – Single Data Point

Table 1. Concluded.

Nozzle	δ_H, deg	Simulated Stings		Notes	M	0.6					0.8			0.9					1.2					1.5
		X_s, in.	Diam, in.		$R_e \times 10^{-6}$/ft	1.4	2.1	2.8	4.2	5.6	1.4	2.8	4.2	1.4	2.8	4.2	5.2	5.6	1.4	2.1	2.8	4.2	4.8	2.8
					Variable																			
200	0	28	2.5		NPR			x							x						x			x
					α			x							√						√			√
		28	3.0		NPR			x							x						x			x
					α			x							x						x			x
		47	3.0		NPR			√							√						√			
					α			√							√						√			
		28	3.43*		α			x	x			x			x	√					x			x
	−2.0	28	3.0		NPR			x							x						x			
					α			√							√						√			
		28	3.43*		α			x	x						x	√					x			x
300	0	28	3.0		NPR			x							x						x			x
					α			x							x						x			x
		28	3.43		α			√	x			x			√	x					x			x
	−2.0	28	3.43		α			x	x						x	√					x			

x – One or More Data Part Numbers √ – Single Data Point

* – 3.43-in.-diam Sting Fills the 200 Nozzle Exit (No Jet Plume Flow)

Table 2. Test Matrix Summary, Large-Sting Support Phase

Nozzle	δ_H, deg	Notes	M	0.6						0.7	0.8			0.9				0.95	1.0	1.1	1.2						1.3	1.4	1.5		
			$R_e \times 10^{-6}$/ft	1.25	1.4	2.1	2.8	4.2	5.6	2.8	1.4	2.8	4.2	1.4	2.8	3.5	4.2	2.8	2.8	2.8	1.25	1.4	2.1	2.8	3.5	4.2	2.8	2.8	1.25	1.4	2.8
200	0	Clean Wing		x	x	x	x	x	x	x	x	x	x	x	x	x	x	x	x	x	x	x		x	x		x	x	x	x	x
	-1.0	↓					x								x									x							
	-1.25						x								x									x							
	-1.5						x								x									x							
	-1.5*						x								x									x							
	-1.75				x		x	x	x						x		x							x							
	-2.0				x		x		x			x			x							x		x							x
	-3.5						x					x			x									x							x
	0	Simulated Missile Underwing Fairing					x	x							x		x							x							x
	0	STD Boom Location					x			x		x			x			x		x				x			x	x			x
	-2.0	↓					x								x									x							
	-3.5						x								x									x							x
	0	Fwd Boom Location					x					x			x									x			x				x
	-2.0	↓					x					x			x									x							
	0	Mid Boom Location					x					x			x									x			x				x
230	0	Clean Wing					x					x			x									x							x
	-2.0	↓					x					x			x									x							x

* Bay Purge Investigation (Inlet = 0.44-in. Diam)

Table 2. Concluded.

Nozzle	δ_H, deg	Notes	M	0.6						0.7	0.8			0.9				0.95	1.0	1.1	1.2						1.3	1.4	1.5		
			$R_e \times 10^{-6}$/ft	1.25	1.4	2.1	2.6	4.2	5.6	2.8	1.4	2.8	4.2	1.4	2.8	3.5	4.2	2.8	2.8	2.8	1.25	1.4	2.1	2.8	3.5	4.2	2.8	2.6	1.25	1.4	2.6
300	0	Clean Wing			x		x	x	x			x		x	x		x			x	x	x	x	x	x		x	x			x
	-2.0	↓		x			x			x		x		x	x					x	x			x			x	x			x
	0	Underwing Fairing					x								x									x							x
	0	Simulated Missiles Underwing Fairing					x	x							x		x							x							x
	0	STD Boom Locations					x					x			x					x				x			x	x			x
	-2.0	↓					x			x		x			x					x				x			x	x			x
360	0	Clean Wing					x			x		x		x	x		x			x				x			x	x			x
	-2.0						x					x			x									x							x
	-3.5	↓					x					x			x									x							x
	0	Wingtip Glove					x					x			x									x			x	x			x
	0	STD Boom Location					x			x		x			x					x				x			x	x			x
	-2.0						x					x			x									x							x
	-3.5	↓					x					x			x									x							x

Table 3. Test Matrix Summary, Small-Sting Support Phase

Configuration					M	0.6								0.8				0.9						1.2				1.5	
Nozzle	δ_H, deg	Wingtip Booms	Horizontal Blade	Notes	$R_e \times 10^{-6}$/ft	1.4		2.1		2.4		2.8		1.4		2.4		1.4		2.1		2.4		1.4		2.1		1.8	
					Vary	α	NPR	α	NPR	α	NPR	α	NPR	α	NPR	α	NPR	α	NPR	α	NPR	α	NPR	α	NPR	α	NPR	α	NPR
200	0	Off	Off	No Missiles		x	x	x	x	x	x	x		x		x	x												
↓	0	↓	↓	WT Missiles						x	x					x	x	x	x	x		x	x		x	x	x		
↓	−2	↓	↓	↓			x			x	x					x				x	x					x	x		
↓	−1.5	↓	↓	↓						x								x		x						x			
↓	−1.0	↓	↓	↓						x						x				x						x			
↓	−1.75	↓	↓	↓		x				x	x									x	x						5.2		
↓	−1.25	↓	↓	↓						x	x									x	x						3.3		
↓	0	On	↓	No Missiles						x						x				x						x			
↓	0	↓	Aft	↓						x						x				x	x					x			
↓	0	↓	Fwd	↓						x						x				x						x			
↓	−4	↓	Aft	↓						x						x				x						x			
230	0	↓	Fwd	↓						x						x				x						x	x		
↓	−2	Off	Off	WT Missiles						x	x							x		x	x					x	x		
↓	0	↓	↓	↓						x	x					x	x			x	x					x	x		
300	−2	↓	↓	↓						x	x					x	x		x	x	x			x	x	x	x		
↓	−3.5	↓	↓	↓						x										x						x	x		
↓	0	↓	↓	↓		x	x			x	x					x	x	x	x	x	x					x	x	1.3	1.2
↓	0	On	FWD	No Missiles						x						x				x						x			
↓	0	↓	Aft	↓						x						x				x						x			
↓	−2	↓	↓	↓						x						x				x						x			
360	0	On	Aft	↓						x						x				x						x			
↓	0	Off	Off	WT Missiles						x	x					x	x			x	x					x	x		
↓	−2	↓	↓	↓						x	x					x	x			x	x					x	x		

Table 4. Surface Pressure Orifice Location
a. Forebody

Orifice No.	X/L	φ, deg	R, in.	Y, in.	Z, in.	Comment
502	0.197			0		Upper Surface
503	0.373			0		
504	0.535			0		
505	0.633			0		
506	0.774			0		
507	0.795			0		
508	0.795			2.4		
509	0.795			4.8		
510	0.774			4.8		
511	0.704			4.8		
512	0.266				2.0	
513	0.310				0	
514	0.422				0	↓
515	0.670	225				Lower Surface
516	0.732	225				
517	0.795	225				↓
518	0.795			0.8		Upper Surface
519	0.795	150				Lower Surface
520	0.795			0		↓
604					-2.6	Static Pressure (Pitot-Static Boom)
605	0.531			3.75		Upper Surface
606	0.559			3.5		
607	0.588			3.5		
608	0.599			3.5		
609	0.611			3.5		
610	0.638			3.5		
611	0.704			3.5		
612	0.774			3.5		
613	0.795			3.5		↓
614	0.774			0		Lower Surface
615	0.746			0		
616	0.704			0		
617	0.661			0		
618	0.619			0		
619	0.591			0		↓

Table 4. Continued
a. Concluded.

Orifice No.	X/L	ϕ, deg	R, in.	Y, in.	Z, in.	Comment
620	0.535			0		Lower Surface
621	0.373			0		↓
622	0.197			0		↓
623	0.661	180				
624	0.704	180				
625	0.746	180				
626	0.795	180				
627	0.795	202.5				
628	0.746	202.5				
629	0.704	202.5				
630	0.661	202.5				
631	0.619	202.5				
632	0.591	202.5				
633	0.795	247.5				
634	0.638					0.50 in. above Dorsal Base
635	0.611					↓
636	0.600					↓
637	0.588					↓
638	0.559					↓
639	0.535					↓
640	0.600					1.0 in. above Dorsal Base
641	0.611					↓
642	0.621					↓

Table 4. Continued
b. Afterbody Pressure Instrumentation

Orifice No.	X/L	ϕ, deg	R, in.	Y, in.	Z, in.
221	0.964	90	-	0.06	-
222	0.964	77	-	0	-
223	0.927	-	-	0.25	-
224	0.964	-	-	0.20	
225	0.893	50.06	4.564	0	2.930
226	0.862	43.15	5.118	0	3.734
227	0.831	38.54	5.618	0	4.394
228	0.836	37.52	4.564	0.72	3.620
229	0.866	40.74	4.258	0.72	3.226
230	0.898	45	3.930	0.722	2.779
231	0.937	45	3.700	0.884	2.616
232	0.964	50	-	-	-
233	0.957	22.5	3.574	2.132	3.302
234	0.930	22.5	3.752	2.064	3.466
235	0.899	22.5	3.930	1.996	3.631
236	0.873	22.5	4.094	1.934	3.782
237	0.847	22.5	4.258	1.870	3.934
238	0.839	0	4.258	3.500	4.258
239	0.873	0	4.094	3.500	4.094
240	0.896	0	3.930	3.500	3.930
241	0.936	0	3.700	3.500	3.700
242	0.964	0	-	3.500	-
243	0.950	0	-	3.500	-
302	0.956	340	3.574	4.722	3.358
303	0.929	340	3.800	4.800	3.571
304	0.896	340	4.040	4.882	3.796
305	0.839	340	4.258	4.956	4.001
306	0.839	-	-	6.300	-
307	0.902	326.2	4.258	5.868	3.538
308	0.933	326.2	3.930	5.686	3.266
309	0.959	326.2	3.574	5.488	2.970
310	0.964	315	3.677	6.100	2.600
311	0.955	315	3.700	6.116	2.616
312	0.943	315	3.930	6.278	2.779
313	0.926	315	4.258	6.510	3.011
314	0.907	315	4.564	6.728	3.227
315	0.827	326.2	4.494	6.000	3.734
316	0.830	303.8	4.848	7.528	2.697
317	0.907	303.8	4.564	7.292	2.539
318	0.930	303.8	4.258	7.038	2.369
319	0.946	303.8	3.930	6.766	2.186
320	0.955	303.8	3.700	6.574	2.058
321	0.964	303.8	3.610	6.500	2.008
322	0.964	292.5	3.615	6.840	1.383
323	0.960	292.5	3.700	6.918	1.416
324	0.927	292.5	3.930	7.130	1.504
325	0.891	292.5	4.258	7.434	1.629

Table 4. Continued
b. Continued

Orifice No.	X/L	ϕ, deg	R, in.	Y, in.	Z, in.
326	0.819	292.5	4.564	7.716	1.747
327	0.852	282	4.258	7.664	0.885
328	0.897	282	3.930	7.344	0.817
329	0.938	282	3.700	7.120	0.769
330	0.964	282	3.578	7.000	.744
331	0.964	272	3.602	7.100	.126
332	0.964	264	3.459	6.940	-.362
333	0.964	252.8	3.454	6.800	-1.021
334	0.940	252.8	3.700	7.034	-1.094
335	0.910	252.8	3.930	7.254	-1.162
336	0.829	252.8	4.258	7.568	-1.259
337	0.808	247.5	4.564	7.716	-1.747
338	0.883	247.5	4.258	7.434	-1.629
339	0.928	247.5	3.930	7.130	-1.504
340	0.964	247.5			
341	0.935	236.2	3.930	6.766	-2.186
342	0.897	236.2	4.564	7.292	-2.539
402	0.804	225	5.374	7.300	-3.800
403	0.860	225			
404	0.878	225			
405	0.905	225			
406	0.920	225			
407	0.939	225			
408	0.951	225	3.700	6.116	-2.616
409	0.964	215			
410	0.964	220			
411	0.964	213.8			
412	0.938	213.8	3.930	5.686	-3.266
413	0.899	213.8	4.564	6.038	-3.793
414	0.866	213.8	5.118	6.347	-4.253
415	0.829	202.5	5.374	5.556	-4.965
416	0.856	202.5	5.118	5.459	-4.728
417	0.875	202.5	4.848	5.355	-4.479
418	0.895	202.5	4.564	5.247	-4.217
419	0.915	202.5	4.258	5.129	-3.934
420	0.935	202.5	3.930	5.004	-3.631
421	0.959	202.5	3.574	4.868	-3.302
422	0.961	191.2	3.930	4.263	-3.855
423	0.926	191.2	4.564	4.386	-4.477
424	0.839	191.2	5.118	4.494	-5.021
425	0.810	180	5.374	3.500	-5.374
426	0.831	180	5.118	3.500	-5.118
427	0.856	180	4.848	3.500	-4.848
428	0.880	180	4.564	3.500	-4.564
429	0.904	180	4.258	3.500	-4.258
430	0.931	180	3.930	3.500	-3.930

Table 4. Continued
b. Concluded.

Orifice No.	X/L	ϕ, deg	R, in.	Y, in.	Z, in.
431	0.952	180	3.700	3.500	-3.700
432	0.964	180	-	3.500	-
433	0.938	168.8	3.930	2.737	-3.855
434	0.887	168.8	4.564	2.614	-4.477
435	0.837	168.8	5.118	2.506	-5.021
436	0.809	157.5	5.618	1.350	-5.190
437	0.832	157.5	5.374	1.443	-4.965
438	0.855	157.5	5.118	1.541	-4.728
439	0.878	157.5	4.848	1.645	-4.479
440	0.900	157.5	4.564	1.753	-4.217
441	0.921	157.5	4.258	1.871	-3.934
442	0.941	157.5	3.930	1.996	-3.631
521	0.956	157.5	3.700	2.084	-3.418
522	0.964	157.5	-	2.16	-
523	0.964	145	-	1.5	-
524	0.942	145	3.930	1.246	-3.219
525	0.923	145	4.258	1.058	-3.488
526	0.904	142.5	4.564	0.720	-3.620
527	0.873	145	4.848	0.720	-3.972
528	0.867	147.1	5.118	0.720	-4.298
529	0.842	148.8	5.374	0.720	-4.600
530	0.818	150.3	5.618	0.720	-4.882
531	0.825	-	-	0.750	-
532	0.875	136.85	5.118	0	-3.734
533	0.909	-	-	0.350	-
534	0.921	139.2	4.258	0.720	-3.226
535	0.941	135	3.930	0.721	-2.779
536	0.955	135	3.700	0.884	-2.616
537	0.964	135	-	-	-
538	0.952	123.8	3.700	0.425	-2.058
539	0.944	-	-	0.450	-
540	0.964	112.5	-	-	-
541	0.967	0	-	-	-
542	0.967	320	-	-	-
543	0.967	215	-	-	-
544	0.967	135	-	-	-
602	0.967	50	-	-	-
603	0.967	180	-	-	-

Table 4. Continued
c. 200-in.^{2} Nozzle

Nozzle: 200-in.^{2} Throat

Orifice No.	X/L	ϕ, deg	R, in.	Y, in.	Z, in.
102	0.974	0	3.24	3.5	
103	0.984	0	2.81	3.5	
104	0.992	0	2.24	3.5	
105	0.994	22.5	2.118	2.6895	
106	0.984	22.5	2.81	2.4247	
107	0.974	22.5	3.24	2.260	
108	0.974	45	3.24	1.209	
109	0.978	45	3.07	1.329	
110	0.984	45	2.81	1.513	
111	0.988	45	2.504	1.729	
112	0.992	45	2.24	1.916	
113	1.000 Exit Static	45	1.746	2.265	
114	0.994	67.5	2.118	1.543	
115	0.985	67.5	2.717	0.9898	
116	0.976	67.5	3.174	0.5676	
117	0.974	90	3.24	0.260	
118	0.984	90	2.717	0.783	
119	0.992	90	2.24	1.26	
120	0.994	112.5	2.118	1.543	
121	0.985	112.5	2.717	0.9898	
122	0.976	112.5	3.174	0.5676	
123	0.974	135	3.24	1.209	
124	0.979	135	3.042	1.349	
125	0.984	135	2.810	1.513	
126	0.988	135	2.518	1.7195	
127	0.992	135	2.240	1.916	
128	1.000 Exit Static	135	1.746	2.265	
129	0.994	157.5	2.118	2.6895	
130	0.984	157.5	2.810	2.4247	
131	0.974	157.5	3.24	2.260	
132	0.974	180	3.24	3.50	
133	0.984	180	2.810	3.50	
134	0.992	180	2.24	3.50	
135	0.994	202.5	2.118	4.310	

Table 4. Continued
c. Concluded

NOZZLE: 200-in.^{2} Throat

Orifice No.	X/L	ϕ, deg	R, in.	Y, in.	Z, in.
136	0.985	202.5	2.717	4.5398	
137	0.974	202.5	3.24	4.7399	
138	0.974	225	3.24	5.791	
139	0.979	225	3.042	5.651	
140	0.984	225	2.810	5.487	
141	0.988	225	2.518	5.2805	
142	0.992	225	2.240	5.0839	
143	0.977	181	3.140	3.5548	
202	1.000 Exit Static	225	1.746	4.7346	
203	0.994	247.5	2.118	5.4568	
204	0.985	247.5	2.717	6.010	
205	0.976	247.5	3.174	6.432	
206	0.976	270	3.174	6.674	
207	0.985	270	2.717	6.217	
208	0.994	270	2.118	5.618	
209	0.994	292.5	2.118	5.4568	
210	0.985	292.5	2.717	6.010	
211	0.976	292.5	3.174	6.432	
212	0.974	315	3.24	5.791	
213	0.979	315	3.042	5.651	
214	0.984	315	2.810	5.487	
215	0.988	315	2.518	5.280	
216	0.992	315	2.240	5.0839	
217	1.000 Exit Static	315	1.746	4.7346	
218	0.994	337.5	2.118	4.310	
219	0.985	337.5	2.717	4.5398	
220	0.976	337.5	3.174	4.7146	

Table 4. Continued
d. 230-in.^{2} Nozzle

NOZZLE: 230-in.^{2} Throat

Orifice No.	X/L	φ, deg	R, in.	Y, in.	Z, in.
102	0.975	0	3.262	3.5	
103	0.985	0	2.865	3.5	
104	0.993	0	2.330	3.5	
105	0.995	22.5	2.218	2.651	
106	0.985	22.5	2.865	2.404	
107	0.975	22.5	3.262	2.252	
108	0.975	45	3.262	1.193	
109	0.979	45	3.099	1.309	
110	0.985	45	2.865	1.474	
111	0.989	45	2.580	1.676	
112	0.993	45	2.330	1.852	
113	1.000 Exit Static	45	1.925	2.139	
114	0.995	67.5	2.218	1.451	
115	0.986	67.5	2.783	0.929	
116	0.977	67.5	3.198	0.545	
117	0.975	90	3.262	0.238	
118	0.986	90	2.783	0.717	
119	0.993	90	2.330	1.170	
120	0.995	112.5	2.218	1.451	
121	0.986	112.5	2.783	0.929	
122	0.977	112.5	3.198	0.545	
123	0.975	135	3.262	1.193	
124	0.980	135	3.08	1.322	
125	0.985	135	2.865	1.474	
126	0.989	135	2.593	1.666	
127	0.993	135	2.330	1.852	
128	1.000 Exit Static	135	1.925	2.139	
129	0.995	157.5	2.218	2.651	
130	0.985	157.5	2.865	2.404	
131	0.975	157.5	3.262	2.252	
132	0.975	180	3.262	3.5	
133	0.985	180	2.865	3.5	
134	0.993	180	2.33	3.5	
135	0.995	202.5	2.218	4.349	

Table 4. Continued
d. Concluded

NOZZLE: 230-in.^{2} Throat

Orifice No.	X/L	φ, deg	R, in.	Y, in.	Z, in.
136	0.986	202.5	2.783	4.565	
137	0.975	202.5	3.262	4.748	
138	0.975	225.0	3.262	5.807	
139	0.980	225	3.080	5.678	
140	0.985	225	2.865	5.526	
141	0.989	225	2.593	5.334	
142	0.993	225	2.330	5.148	
143	0.978	181	3.17	3.555	
202	1.000 Exit Static	225	1.925	4.861	
203	0.995	247.5	2.218	5.549	
204	0.986	247.5	2.783	6.071	
205	0.977	247.5	3.198	6.455	
206	0.977	270	3.198	6.698	
207	0.986	270	2.783	6.283	
208	0.995	270	2.218	5.718	
209	0.995	292.5	2.218	5.549	
210	0.986	292.5	2.783	6.071	
211	0.977	292.5	3.198	6.455	
212	0.975	315	3.262	5.807	
213	0.980	315	3.08	5.678	
214	0.985	315	2.865	5.526	
215	0.989	315	2.593	5.334	
216	0.993	315	2.330	5.148	
217	1.000 Exit Static	315	1.925	4.861	
218	0.995	337.5	2.218	4.349	
219	0.986	337.5	2.783	4.565	
220	0.977	337.5	3.198	4.724	

Table 4. Continued
e. 300-in.^{2} Nozzle

NOZZLE: 300-in.^{2} Throat

Orifice No.	X/L	φ, deg	R, in.	Y, in.	Z, in.
102	0.977	0	3.295	3.5	
103	0.987	0	2.990	3.5	
104	0.996	0	2.538	3.5	
105	0.995	22.5	2.577	2.514	
106	0.987	22.5	2.990	2.356	
107	0.977	22.5	3.295	2.239	
108	0.977	45	3.295	1.170	
109	0.982	45	3.18	1.252	
110	0.987	45	2.990	1.386	
111	0.992	45	2.758	1.550	
112	0.996	45	2.538	1.705	
113	1.000	45	2.304	1.871	
	Exit Static				
114	0.995	67.5	2.577	1.119	
115	0.988	67.5	2.933	0.790	
116	0.980	67.5	3.234	0.512	
117	0.977	90	3.295	0.205	
118	0.988	90	2.933	0.567	
119	0.996	90	2.538	0.962	
120	0.995	112.5	2.577	1.119	
121	0.988	112.5	2.933	0.790	
122	0.980	112.5	3.234	0.512	
123	0.977	135	3.295	1.170	
124	0.982	135	3.160	1.266	
125	0.987	135	2.990	1.386	
126	0.992	135	2.760	1.548	
127	0.996	135	2.538	1.705	
128	1.000	135	2.304	1.871	
	Exit Static				
129	0.995	157.5	2.577	2.514	
130	0.987	157.5	2.990	2.356	
131	0.977	157.5	3.295	2.239	

Table 4. Continued
e. Concluded

NOZZLE: 300-in.^{2} Throat

Orifice No.	X/L	ϕ, deg	R, in.	Y, in.	Z, in.
132	0.977	180	3.295	3.5	
133	0.987	180	2.990	3.5	
134	0.996	180	2.538	3.5	
135	0.995	202.5	2.577	4.486	
136	0.988	202.5	2.933	4.622	
137	0.977	202.5	3.295	4.761	
138	0.977	225	3.295	5.830	
139	0.982	225	3.16	5.734	
140	0.987	225	2.99	5.614	
141	0.992	225	2.760	5.452	
142	0.996	225	2,538	5.295	
143	0,980	181	3,230	3.556	
202	1.000 Exit Static	225	2.304	5.129	
203	0,995	247.5	2.577	5.881	
204	0,988	247.5	2.933	6.21	
205	0,980	247.5	3.234	6.488	
206	0.980	270	3.234	6.734	
207	0.988	270	2.933	6.493	
208	0.995	270	2.577	6,077	
209	0.995	292.5	2.577	5.881	
210	0.988	292.5	2.933	6.210	
211	0.980	292,5	3.234	6.488	
212	0.977	315	3.295	5.830	
213	0.982	315	3.16	5.734	
214	0.987	315	2.990	5.614	
215	0.992	315	2.760	5.452	
216	0.996	315	2.538	5.295	
217	1.000 Exit Static	315	2.304	5.129	
218	0.995	337.5	2.577	4.486	
219	0.988	337.5	2.933	4.622	
220	0.980	337.5	3.234	4.738	

Table 4. Continued
f. 360-in.^{2} Nozzle

NOZZLE: 360-in.^{2} Throat

Orifice No.	X/L	ϕ, deg	R, in.	Y, in.	Z, in.
102	0.979	0	3.333	3.5	
103	0.989	0	3.098	3.5	
104	0.998	0	2.720	3.5	
105	0.999	22.5	2.658	2.483	
106	0.989	22.5	3.098	2.314	
107	0.979	22.5	3.333	2.225	
108	0.979	45	3.333	1.143	
109	0.983	45	3.258	1.196	
110	0.989	45	3.098	1.309	
111	0.994	45	2.910	1.442	
112	0.998	45	2.720	1.577	
113	1.000 Exit Static	45	2.589	1.669	
114	0.999	67.5	2.658	1.044	
115	0.990	67.5	3.046	0.686	
116	0.981	67.5	3.303	0.448	
117	0.979	90	3.333	0.167	
118	0.990	90	3.046	0.454	
119	0.998	90	2.720	0.78	
120	0.999	112.5	2.658	1.044	
121	0.990	112.5	3.046	.686	
122	0.981	112.5	3.303	.448	
123	0.979	135	3.333	1.143	
124	0.984	135	3.240	1.209	
125	0.989	135	3.098	1.309	
126	0.994	135	2.920	1.435	
127	0.998	135	2.720	1.577	
128	1.000 Exit Static	135	2.589	1.669	
129	0.999	157.5	2.658	2.483	
130	0.989	157.5	3.098	2.314	
131	0.979	157.5	3.333	2.225	
132	0.979	180	3.333	3.5	
133	0.989	180	3.098	3.5	
134	0.998	180	2.720	3.5	

Table 4. Concluded
f. Concluded

NOZZLE: 360-in.^{2} Throat

Orifice No.	X/L	ϕ, deg	R, in.	Y, in.	Z, in.
135	0.999	202.5	2.658	4.517	
136	0.990	202.5	3.046	4.666	
137	0.979	202.5	3.333	4.775	
138	0.979	225	3.333	5.857	
139	0.984	225	3.240	5.791	
140	0.989	225	3.098	5.691	
141	0.994	225	2.920	5.565	
142	0.998	225	2.720	5.423	
143	0.982	181	3.292	3.557	
202	1.000 Exit Static	225	2.589	5.331	
203	0.999	247.5	2.658	5.956	
204	0.990	247.5	3.046	6.314	
205	0.981	247.5	3.303	6.552	
206	0.981	270	3.303	6.803	
207	0.990	270	3.046	6.546	
208	0.999	270	2.658	6.158	
209	0.999	292.5	2.658	5.956	
210	0.990	292.5	3.046	6.314	
211	0.981	292.5	3.303	6.552	
212	0.979	315	3.333	5.857	
213	0.984	315	3.240	5.791	
214	0.989	315	3.098	5.691	
215	0.994	315	2.920	5.565	
216	0.998	315	2.720	5.423	
217	1.000 Exit Static	315	2.589	5.331	
218	0.999	337.5	2.658	4.517	
219	0.990	337.5	3.046	4.666	
220	0.981	337.5	3.303	4.764	

NOMENCLATURE

Ai	Incremental areas used in pressure integration, in.^{2}
A8	Full-scale nozzle throat area, in.^{2} (see Fig. 4)
CAABPW	Afterbody integrated pressure axial force coefficient Σ(CPi) (Ai)/S,i = 221 to 442, and 522 to 603 (see Table 4)
CANPW	Nozzle integrated pressure axial force coefficient Σ(CPi) (Ai)/S,i = 102 to 220 (see Table 4)
CATPW	Total aft end (nozzle plus afterbody) integrated pressure axial force coefficient, CAABPW + CANPW
CPxx	Surface pressure coefficient, (Pi-P)/Q, along orifice ray at ϕ = xx
D	Sting diameter, in.
DCPxx	Pressure coefficient differences (WT - SS) on orifice ray at ϕ = xx
DE	Nozzle exit diameter, in. (see Fig. 4)
DS	Maximum sting diameter, (3.43 in.)
FS	Model fuselage station, in. (see Fig. 2)
L	Model length, 142.1 in.
ℓ	Body length, 126.6 in. (10.55 ft)
LS	Large-sting support system
M	Free-stream Mach number
NPR	Nozzle pressure ratio (model nozzle total pressure/free-stream static pressure)
NPRE	Equivalent nozzle pressure ratio (Ref. 5)
P	Free-stream static pressure, psfa
Pi	Model surface pressure, psfa (see Fig. 7 and Table 4)
PT	Free-stream total pressure, psfa

Q	Free-stream dynamic pressure, psfa
R	Nozzle and afterbody outer surface radius, in. (See Figs. 4b through e and Table 4)
Re	Free-stream unit Reynolds number, per foot
Re_{ℓ}	Characteristic Reynolds number based on body length
r	Nozzle internal surface radius, in. (see Figs. 4b through e)
S	Wing + fuselage planform area (2,020 in.^{2})
SS	Small-sting support system (annular-jet test)
TS	Wind tunnel station, in.
UCPi	Uncertainty in surface pressure coefficient i
WT	Wingtip support system
X	Model axial station, in.
X_n	Nozzle axial station, in. (see Figs. 4b through e)
X_s	Distance between nozzle exit and beginning of sting taper, in. (see Table 1)
Y	Lateral location of pressure orifice (see Fig. 7)
Z	Vertical location of pressure orifice (see Fig. 7)
α	Model angle of attack, deg
Δ	Differential of components for conditions indicated (see Fig. 37)
δ_H	Horizontal tail deflection angle, deg (positive leading edge up)
ϕ	Angular location of pressure orifice, deg (see Fig. 7b)
Part Number	Data part number (a data subset containing variations of only one independent parameter)
Data Point	Data point number (a single record of all test parameters)